Investigation of Undersea Sour Gas Well Blowouts using Multiphase Computational Fluid Dynamics

by

Devin O'Malley

Submitted in partial fulfilment of the requirements
for the degree of Doctor of Philosophy

at

Dalhousie University
Halifax, Nova Scotia
April 2018

This thesis is dedicated to my family, who have stood by and supported me through my life.

Table of Contents

iv

List of Tables

List of Figures

Abstract

The production of natural gas requires the removal of carbon dioxide and hydrogen sulfide during processing, resulting in a waste stream typically called acid gas. In offshore natural gas production, the disposal of these undesirable by-products is more challenging than during onshore production. One viable option is to reinject the acid gas into a depleted portion of the reservoir. This option effectively sequesters the waste stream and helps to maintain the production well pressure. However, the downside is the increased need to transport and store this toxic gas, which increases the risk posed by a potential catastrophic failure and subsequent release of the gas. Although such a failure may be unlikely, the prediction of the resulting gas plume is the first step towards developing an emergency response plan.

During this work, a model was developed to predict the behaviour of a released acid gas stream in the water column following a shallow water release. The physical situation for such a release can be divided into three distinct regions: the momentum-driven jet in the near field, the buoyancy driven plume region in the far field, and the free surface between the sea and the atmosphere. Only the first two zones were considered in this work. The developed multiscale computational fluid dynamics model employed an interface capturing model for the near field, since the flow of gas was expected to be continuous. A drift-flux model was used to capture the behaviour of the far field as a plume of uniformly sized bubbles.

The development of each portion of the model is described in detail. An approach to facilitate direct numerical predictions of heat and mass transfer within incompressible and compressible interface capturing approaches was developed and tested. The effect of computational mesh refinement on the ability of the interface capturing approach to resolve gas jet behaviour was studied. The multiscale modeling approach was developed and tested through comparison to published small-scale experimental data. The model was used to simulate a realistic scenario involving the release of acid gas from a ruptured reinjection well.

List of Abbreviations and Symbols Used

Abbreviations

ALE	Arbitrary Lagrangian Eulerian
CFD	Computational Fluid Dynamics
CICSAM	Compressive Interface Capturing Scheme for Arbitrary Meshes
CVOFLS	Coupled Volume-of-Fluid and Level-set
DF	Drift-Flux
DNS	Direct Numerical Simulation
DSM	Discrete Singularity Model
E-E	Eulerian-Eulerian
E-L	Eulerian-Lagrangian
FCT	Flux Corrected Transport
FT	Front-tracking
IT	Interface Tracking
LES	Large Eddy Simulation
LPT	Lagrangian Particle Tracking
LS	Level-set
MAC	Marker and Cell
MULES	Multidimensional Universal Limiter with Explicit Solution
PLIC	Piecewise Linear Interface Reconstruction
PROST	Parabolic Reconstruction of Surface Tension (for Volume-of-Fluid)
QMOM	Quadrature Method of Moments
QUICK	Quadratic Upstream Interpolation of Convective Kinematics
RANS	Reynolds Averaged Navier-Stokes

RSM	Reynolds Stress Model
SLIC	Simple Linear Interface Reconstruction
VLES	Very Large Eddy Simulation
VOF	Volume-of-Fluid
VOF-IR	Volume-of-Fluid with Interface Reconstruction

Symbols

A	Area (m^2)
$\vec{A}_f$	Face area vectors (m^2)
a	Area density (m^{-1})
C	Concentration (kg m^{-3})
C_{BIT}	Bubble induced turbulence coefficient
C_D	Drag coefficient
C_l	Lift coefficient
C_{vm}	Virtual mass coefficient
C_{TD}	Turbulent dispersion coefficient
Co_{local}	Local Courant number
c_p	Specific heat capacity at constant pressure (J kg^{-1} K^{-1})
c_v	Specific heat capacity at constant volume (J kg^{-1} K^{-1})
$D_{i,jM}$	Effective diffusion coefficient between the mixture and component j in phase i (m^2 s^{-1})
d	Diameter (m)
E_k	Kinetic energy (J kg^{-1})
Eo	Eötvös number
e	Internal energy (J kg^{-1})

$\vec{F}$	Force Vector (N m^{-3})
f	Fugacity (Pa)
$\vec{g}$	Gravity vector (m s^{-2})
H^*	Henry's law coefficient (varies)
h	Enthalpy (J kg^{-1})
$\vec{h}$	Height vector (m)
h_c	Convective heat transfer coefficient (W m^{-2} K^{-1})
$\boldsymbol{I}$	Identity matrix
$\vec{j}$	Mass flux (kg m^{-2} s^{-1})
K	Mass transfer coefficient (s^{-1})
k	Turbulent kinetic energy
m	Mass (kg)
$\dot{m}$	Mass flow rate (kg/s)
Nu	Nusselt number
P	Pressure (Pa)
Pr	Prandtl number
$\vec{q}$	Heat flux (W m^{-2})
R	Universal gas constant (J mol^{-1} K^{-1})
Re	Reynolds number
S	Continuity source (s^{-1})
S_E	Energy source (W m^{-3})
S_M	Mass source (kg m^{-3} s^{-1})
Sc	Schmidt number
Sh	Sherwood number

T	Temperature (K)
t	Time (s)
$\vec{u}$	Velocity vector (m/s)
V	Volume (m^3)
$\hat{V}$	Molar or specific volume (m^3 mol^{-1} or m^3 kg^{-1})
Y	Mass fraction

Greek

α	Phase fraction (-)
γ	Old VOF indicator
ϵ	Turbulent dissipation
ζ	Plane constant
K	Thermal conductivity (W m^{-1} K^{-1})
κ	Surface curvature
λ	Time constant (s)
μ	Dynamic Viscosity (Pa s)
ν	Kinematic Viscosity (m^2 s^{-1})
ρ	Density (kg/m^3)
σ	Surface tension (N/m)
τ	Viscous stress tensor
Φ	Face volume flux (m s^{-1})
χ	Transitional filter
φ	Level-set parameter
Ψ	Phase compressibility

Subscripts

BIT	Bubble induced turbulence
b	Bubble or dispersed phase
DF	Drift-flux
EXP	Explicit
eff	Effective
f	Face
G	Gas phase
i	Phase index/general index
IMP	Implicit
int	Interfacial
j	Species index
L	Liquid phase
m	Mass averaged
N	Normal
p	Primary phase (continuous phase)
R	Relative
SGS	Sub-grid scale
SN	Surface normal
ST	Surface tension
sol	Solubility or solubility limit
t	Turbulent
VOF	Volume-of-fluid

Superscripts

N	Current time/position
sat	Saturation
T	Transpose

Acknowledgements

Chapter 1

Introduction

Although renewable energy sources such as hydroelectric, wind, solar, biomass and tidal power are being rapidly developed, oil and gas still account for a large portion of the energy market. In 2010, Canada produced 41.4% of its primary energy from oil, and an additional 36.5% and 9.2% from natural gas and coal, respectively (Natural Resources Canada, 2016). Therefore, 77.9% of primary energy was produced using oil and gas. In terms of Canada's GDP, oil and gas was worth 6.8% for both power production and export in 2010 (Natural Resources Canada, 2016). In 2015, Canada was ranked third for crude oil and seventeenth for natural gas in proved capacity, and fourth and fifth for production (Natural Resources Canada, 2017). For the same year, Canada's total GDP reliance had increased to 10.8% on both direct and indirect sources of oil and gas. Through export and power production this industry accounted for approximately 5% of total employment in 2015. On a world scale, the need for energy is expected to increase by 31% by 2040, and it is anticipated that hydrocarbons will account for 71% of this need (Canadian Association of Petroleum Engineers, 2017). Based on predictions from the International Energy Agency (2016), despite an increasing trend to move away from fossil fuels, in part due to the Paris Accord, natural gas will fare the best among fossil fuels and increase consumption by 50%. Additionally, although renewables will account for 60% of all projected new energy (International Energy Agency, 2016), this necessarily means that the industry will still need to maintain and increase oil and natural gas related infrastructure.

Nearly 30% of produced crude oil and natural gas comes from offshore resources, according to the U.S. Energy Information Administration (EIA) (2016) as well as numbers from Planete Energies (2015). The U.S. EIA also mentions that most offshore production is found in shallow waters due to lower costs for construction and maintenance (Schaefer, 2016), although deep water projects have been developed. Schaefer (2016) proposes the same ratio of shallow to deep water projects, which has kept up even though total

production continues to increase, with a majority in shelf and shallow water production and a decreasing quantity of deep water production. Planete Energies (2015) has states that from the 1950s, offshore was limited to depths of up to 200 m, and more than half of the vessels were fixed to the sea bed until around the 1970s when the world slipped into an oil crisis. Since the 1990s, companies have completed wells up to depths of 3 000 m due to the need to move farther offshore, and deepwater now accounts for up to 6% of the total oil and natural gas share. Schaefer (2016) indicated that investments are currently decreasing, especially for deep water, largely due to the downturn in oil prices. However, given that oil and gas production are projected to increase overall, and that much of the world's new energy needs cannot be provided by renewables in the short term, it is safe to assume oil and gas production will continue. Increases in efficiency may prolong onshore reserves, but currently up to 30% of production is offshore, a number that will likely have to increase if petroleum is to be used in the future. Given that natural gas consumption may rise to become the new dominant fuel source, the safety of such onshore and offshore projects is very important.

Geographically, the predominant regions for offshore activity are the Gulf of Mexico, the North Sea, the Barents Sea, the Santos Basin (off the coast of Brazil), off the coast of Nigeria and Angola, the Persian Gulf, off the coast of China and India, and off the coast of Australia, maintaining a worldwide presence across all major continents (Offshore Technology, 2017). The relative production of oil to natural gas varies sharply by region, with natural gas being more common in the North Sea and Barents Sea, as well as South African, Chinese, Indian and Australian waters.

Although wells range in depth, the overwhelming majority remain closer to the coast, in depths to 200 m. Considering the number of wells, accidental releases and blowouts occur relatively infrequently. Nonetheless, such events can have devastating environmental consequences and pose a serious threat to safety. It is therefore important to be able to accurately predict the near-field and far-field fate of released components when such accidents occur. Tamim et al. (2017), have developed a framework for leading indicators of drillwell blowouts. Within their work they have uncovered that for the Gulf of Mexico, one of the largest production zones for both the U.S. and Mexico (Meng, 2017), there were

77 blowouts and 32 major release events between 1980 and 2011. The average then is 2 blowouts and 1 major release per year since 1980 related to drilling or well-related activities that have led to uncontrolled releases. One of the most vexing problems is the apparent spontaneity of the events, as noted for the Macondo (Deepwater Horizon) spill that happened just after a seven year period of no personal injury (Skogdalen et al., 2011). Tamim et al. (2017) concluded that lagging events reporting and subsequent decision making are a primary concern, but that would be true whether oil or natural gas are being produced. Catastrophic events have a chance of happening in both types of fields.

In 1988, the oil rig known as Piper Alpha exploded and eventually sank (Hendershot, 2013), in part due to the low levels of procedural safety. While not explicitly a well blowout, the sinking of a rig may produce strain upon the wellbore below, as well as associated pipelines. For Mumbai High North, it was another vessel that ultimately caused the abandonment of the platform (Daley, 2013). A ship struck the risers, causing a gas leak and ultimately setting the rig on fire. Unlike many of the accidents in the Gulf of Mexico, neither of these were directly blowouts, the goal is instead to highlight alternative means of structural damage that may affect the entire infrastructure of the rig. As more oil rigs come on line and others are decommissioned, it is important that routine checks be done to see if capped wells are leaking, as they will have to persist long after the oil or gas has been exhausted.

There are numerous other examples, such as the Alexander L. Kielland in the North Sea, the Ocean Ranger Oil Rig, the Atlantis Deepwater, and the Enchova blowout. In 2001, a rig off the coast of Freeport, Texas had its well blow out while drilling the exploratory bore (Daily GPI, 2001). The 2013 blowout at the Hercules 265 rig left natural gas flowing from the well for 13 hours with the rig platform itself on fire (Offshore Post, 2015). Current natural gas rigs might have better safety protocols learned from these lessons of the past, but no mechanical device is without a chance of failure, despite the best engineering. Therefore, it is both ethical and pragmatic to develop emergency response plans with the best possible predictive tools, and to try to improve these tools.

In any offshore oil and/or gas production process, there are undesirable components in the produced gas that must be removed prior to transportation or use. For natural gas, the common contaminants are carbon dioxide and sulfur containing compounds. According to Carroll (2009), most of the sulphur containing compounds are in low quantities, except for hydrogen sulfide. Carroll (2009) makes the distinction between sour gas and acid gas, the latter usually being used to refer solely to mixtures of carbon dioxide and hydrogen sulfide. Onshore, injection of produced acid gas into depleted wells is relatively common. However, offshore reinjection of acid gas to drive the natural gas production process is relatively rare due to higher costs. In 2009, offshore acid gas reinjection had only been developed at the West Sleipner and Deep Panuke projects.

In principle, acid gas reinjection is beneficial to the environment and operation of the production facility because it prevents the release of greenhouse gases to the atmosphere. However, reinjection also implies maintaining a higher inventory of toxic hydrogen sulfide gas, which poses an additional threat to safety and the environment. Data on the risk of accidents for reinjection wells is not available but, given the safety concerns, emergency response plans must be developed using the best possible predictions about fate of released gases. Considering that many rigs operate in shallow waters, the severity of the consequences of an acid gas release could be significant.

For emergency response planning, mathematical models are usually used to predict risks posed by various scenarios. All such models have inherent limitations and it is therefore important to refine them periodically to ensure that best practices are used. To accurately describe gas dispersion in the atmosphere it is important to characterize underwater gas plume behaviour, since the underwater behaviour of the plume directly affects the concentration, quantity and potentially the location of gas entering the atmosphere. The primary focus of this research project was the development of an improved modeling approach, based on multiphase computational fluid dynamics (CFD), to characterize the underwater behaviour of gas released during a blowout event. The specific focus was on the development of a model that could be used to predict the fate of a shallow underwater release of acid gas. Since carbon dioxide and hydrogen sulfide are quite soluble in seawater, the dissolution rates of these gases in the surrounding water would be expected

to have a significant effect on the atmospheric release rate during such an event. Therefore, a substantial emphasis was placed on developing a method for predicting dissolution rates for the released gas.

Underwater gas plumes represent a difficult modeling challenge due to the high number of interacting factors. If gas is released under water from a high-pressure source, it will form a jet that immediately begins to lose its momentum to the surrounding liquid and starts to break up and disperse. Upon expansion, the gas will cool, and phase change may occur. Once the gas jet has transferred sufficient momentum to the liquid, the gas forms a dispersed bubble plume that rises through the water column primarily driven by buoyancy forces. If the gas is not released at a sufficient depth, a buoyancy-driven plume may not be formed and the gas jet itself may reach the ocean surface. Additionally, as the gas plume rises through the water column, a variety of physicochemical interactions can occur. Typically, some of the chemical constituents of the gas will dissolve in the liquid to varying degrees and at varying rates. Further, if the gas release occurs at sufficient depth and sufficiently low temperature, natural gas hydrates or even ice can form. Each of these processes has different governing length and time scales, making it difficult to incorporate them into a single plume model. A conceptual representation of an underwater release is shown in Figure 1.1. As described above, it can be divided into three primary regions of interest: the momentum-driven jet region, the buoyancy-driven plume region, and the surface region, which is influenced by ocean-atmosphere interactions.
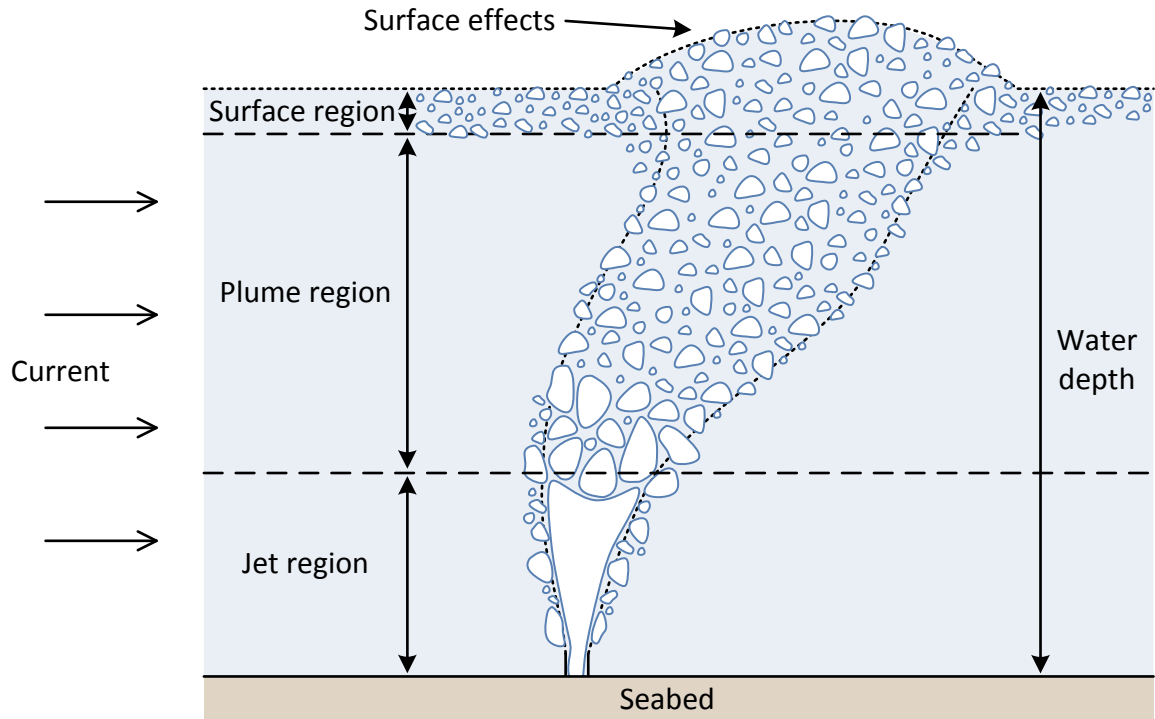
Figure 1.1 Schematic representation of a gas well blowout scenario.

1.1 Objectives

The primary objective of this thesis is to develop a model to predict the emission rate of acid/sour gas to the atmosphere during an accidental release using computational fluid dynamics. Within the context of this objective, it was necessary to:

- Investigate the feasibility of using direct numerical simulation DNS of heat and mass transfer to simulate dissolution in jet region.
- Study the possibility of using interface tracking for prediction of interfacial area and hydrodynamics in the jet region.
- Review modeling approaches for both the jet and plume regions.
- Develop, test and validate a multiscale modeling approach to simulate the entire release.
- Apply the multiscale model to predict emission rates for a realistic release scenario.

The proposed model also had to have manageable computational resource demands in order to be effective, as a number of potential case studies may need to be performed to adequately quantify the release.

1.2 Thesis Structure

Several studies were performed to develop and validate a numerical method to simulate the near-field behaviour of an underwater gas jet. The model was then extended to consider both the jet and bubble plume regions. Gas fluid dynamics as well as heat and mass transfer were considered, and the method was applied to analyze a large-scale release scenario. To organize the various studies, this dissertation has been divided into two sections and eight chapters. The first chapter in each section introduces important theoretical considerations and reviews relevant literature.

1.2.1 Section I. Development of Methods for the Numerical Simulation of Underwater Gas Jets

The first section, which includes chapters 2, 3 and 4, introduces the concept of interface tracking as a method for simulating the jet region. Chapter 2 examines methods for simulating multiphase flows. In particular, the chapter focuses on interface tracking as a methodology applicable to quantifying interfacial heat and mass transfer. Methodologies are categorized based on their computational efficiency and speed, as well as their ability to predict a sharp interface.

Chapter 3 focuses on the use of a compressible volume-of-fluid (VOF) solver for simulating interphase heat and mass transfer. The justification for this work was the inability of an incompressible solver to accurately calculate the change in volume as a result of transfer from one phase to another, without adjusting to very low time step sizes. Interphase heat and mass fluxes were calculated using direct interfacial area and normal concentration gradient estimates. The resulting fluxes were converted to volumetric source terms and added to the conservation equations as immersed boundary conditions. The solver was tested on three validation cases: a 1D Stefan tube diffusion problem, and a 3D evaporating droplet in microgravity, both with and without the phase transfer source term. These cases strategically tested the ability of the solver to calculate interphase transport

rates under stationary conditions, estimate interfacial area, and estimate interphase transport rates under moving interface conditions.

Chapter 4 evaluates the ability of the VOF method to predict the hydrodynamics of gas jet releases. By applying the compressible VOF solver to a horizontal jet test case with three successive mesh refinements, the ability of the solver to predict both the momentum length and capture the interface were tested. It was shown that, although the trajectory of the jet was accurately predicted, the surface area of the interface was severely underpredicted in the coarsest case. This conclusion did not support a direct implementation of the method discussed in Chapter 3 to simulate large-scale cases due to a lack of refinement present in the near-field mesh. Therefore, a novel method had to be developed to tackle the multiscale problem.

1.2.2   Section II. Numerical Simulation of Undersea Sour Gas Releases

The second section, which includes chapters 5, 6 and 7, provides the results for large-scale modeling. Chapter 5 provides an overview of approaches that are currently applied in offshore gas/oil release modeling. Computational fluid dynamics methods are the minority when compared to integral models. In integral models, equations for bubble plumes can be integrated in time by performing a mechanistic balance of forces. The models are simpler, but based on assumptions about flow profiles that have to be known a priori. CFD models that exist are primarily two phase models, but such formulations neglect the continuous, momentum-driven jet region. Depending on the release rate, the momentum-driven region varies in size, which would impact overall fluid dynamics and other transfer rates. It may therefore be inaccurate to discount the momentum region for particularly large release rates, which is something that the CFD model can correct.

Chapter 6 focuses on the development of a multiscale model to predict fluid dynamics and mass transfer in large-scale cases. The area construction algorithm is faster than advecting the interface directly but was still slow and difficult to formulate in varied cell geometries. Since a sufficiently high mesh resolution to resolve interfacial area and dynamics outside of the jet region is usually infeasible, the model had to be extended using semi-empirical sub-grid scale models. Using penetration theory, a mass transfer model was constructed in

the band near the interface. The aim of this model is to design a unified mass transfer model that can be changed depending on the region. This model provides continuous blending between a VOF formulation and the drift-flux approximation with an assumed bubble size. Since sufficient mesh resolution cannot be maintained in the plume region to use VOF and direct estimation of mass transfer rates, the mixture model is used in place of the VOF algorithm for cells with sufficiently dispersed phase fraction. A bubble size is assumed and applied to the mass transfer term. The multiscale model was tested by comparison to published laboratory data for horizontally injected gas bubbles in a variety of phase fraction ranges. The turbulent dispersion force model was empirically tuned using published experimental results from a vertical air plume.

Chapter 7 describes the scenario used to study the ability of the model to predict the behaviour of a full-scale acid gas release. A water depth of 45 m was assumed. The gas was assumed to be pre-expanded and therefore an equivalent inlet diameter to maintain the a reasonable momentum and velocity was calculated. A mesh was built to focus refinement in the ten meters closest to the release point in order to benefit from the strengths of the VOF approach in the continuous gas region. The inlet velocity of gas was approximately 22 m/s at steady state, with 86.5% carbon dioxide and 13.5% hydrogen sulfide by mass. Mesh dependence, sensitivity to the chosen mass transfer model in the plume region, and sensitivity to chosen bubble size in the plume region were studied. The results indicated convergence to a constant steady-state dissolution rate prediction for a relatively coarse mesh. However, it was also determined that significantly higher resolutions would be required to fully resolve the jet region.

Chapter 8 summarizes the main conclusions stemming from each of the chapters. Suggestions for possible model extensions in future work are also provided.

SECTION I. DEVELOPMENT OF METHODS FOR THE NUMERICAL SIMULATION OF UNDERWATER GAS JETS

Chapter 2

Simulation of Underwater Gas Jets: A Review of

Applicable Multiphase CFD Methods

2.1 Introduction

Subsea gas releases involve many complicated multiphase flow phenomena. A released gas jet is expected to form a continuous gas-liquid interface that will eventually break up into a bubbly plume. One approach for modeling this system is to apply an interface tracking/capturing approach to the jet region and a dispersed flow model to the plume region. A review of current methodologies for modeling gas plumes is found in Chapter 6. This chapter provides an overview of commonly used interface tracking/capturing methods. The objective is to facilitate the selection of a model that can provide the necessary continuous phase tracking in the near-field region of the release. Since the selected near-field model will be coupled with the selected far-field model, ease of coupling must be considered as one of the selection criteria.

During an underwater gas release, gas will expand rapidly as it leaves the punctured pipe or wellhead. Once expanded, the momentum-driven jet will result in a distinguishable boundary between phases. By contrast, the plume region will be governed by the bulk motion of buoyant bubbles as they drift towards the surface. As shown in Figure 2.1, there are different ways to simulate multiphase flows. In general, interface tracking requires knowledge about the positions of markers that are connected to form a continuous interface. Ideally, a large number of points should be used to increase accuracy. However, due to computational constraints, this number is chosen to provide a good representation of the interface's shape. Computational requirements for these types of solution procedures are high. To reduce computational requirements, interface capturing methods only predict the motion of the phase volume fractions. An interfacial representation can be fitted using the captured volume fractions. The advantages are a gain in computational speed, while sacrificing information about the interfacial area.

Dispersed phase models do not attempt to track or capture the deforming interface. Typically, the cell size is larger than the dispersed particles, and therefore the interfacial shape is assumed in the closure laws for the model. This is particularly useful when large-scale bubbly flows, or large-scale droplet laden flows are considered. The computational time to resolve each particle becomes limiting, and the phase can be modeled by a representative average particle diameter (or distribution of diameters). However, it should be noted that these models also require further closure laws to represent other transport processes (such as heat and mass transfer) since the interfacial area is not directly estimated. Therefore, the boundary layer and property gradients across the interface are also not resolved.
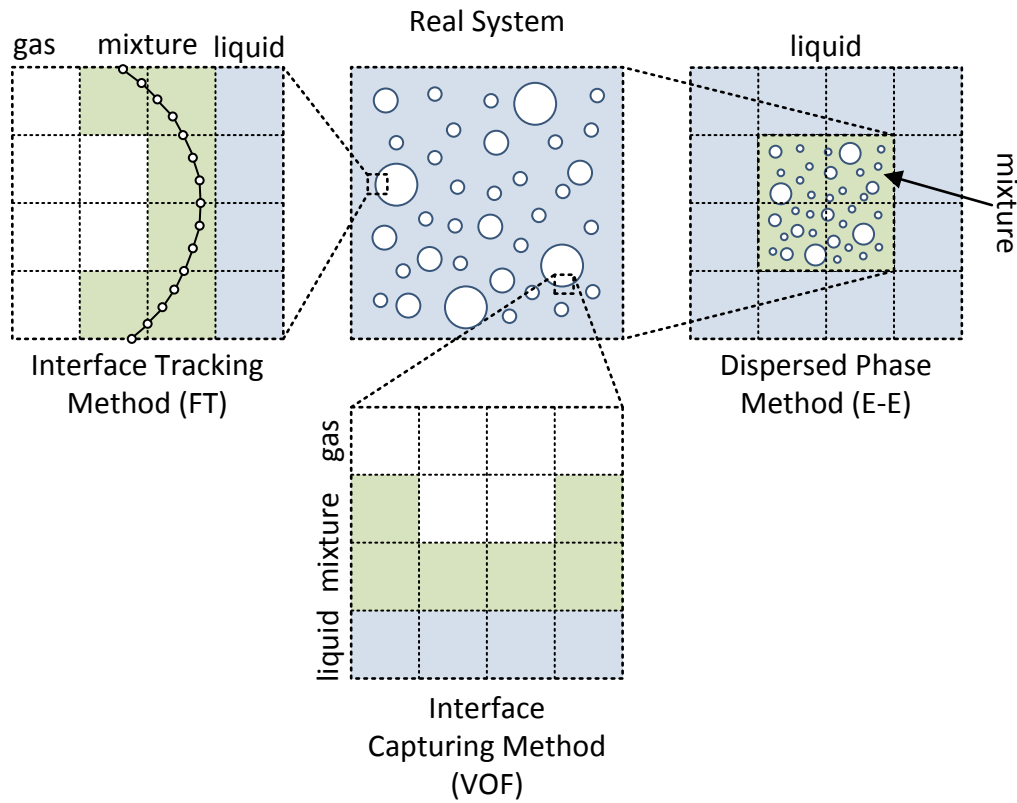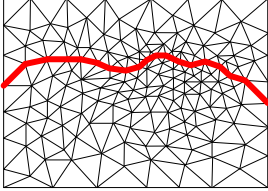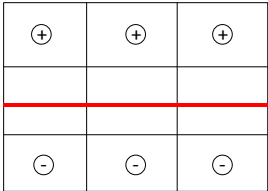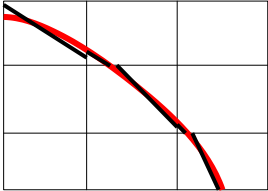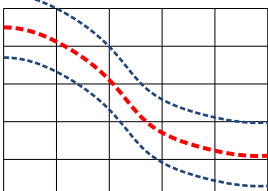
Figure 2.1 The difference between interface tracking, capturing and dispersed phase methods.

As shown in the first image in Figure 2.2, the simplest method of ensuring that the interface location is strictly known is to ensure that the interface is aligned with the computational mesh boundaries. In this method, commonly called arbitrary Lagrangian-Eulerian (ALE)

modeling or moving mesh methods, the mesh itself deforms such that cell boundaries always match the location of the interface (Wörner, 2012, Hirt et al., 1972). As stated by Quan and Schmidt (2007) and Quan (2011), the fact that no cell can contain more than one phase removes the need to average the properties and thus possesses theoretical advantages over other interface tracking methods. A derived benefit for heat and mass transfer is that the interfacial area and gradients are directly known, which makes application of boundary conditions straightforward.

While easy to understand in theory, in practice ALE suffers from several drawbacks. Notable among them is the need to recalculate the mesh position at every timestep. As time advances, the cells need to stay consistent with the interfacial contour. This process can be both arduous and computationally intensive for highly deforming meshes. The changing of cell volumes requires additional source terms in the governing equations to ensure global conservation. A consequence of these cell volume changes are oddly shaped cells that can worsen over time. For these situations careful attention must be paid to the choice of discretization scheme, and higher order schemes might be required for particularly skewed cells. The alternatives are methods to re-mesh the domain periodically to remove such cells. Another concern is that moving mesh method also does not directly handle break up and coalescence, and Quan and Schmidt (2007) introduced a detaching mesh method to resolve this at the cost of another computational step (refined in Quan et al., 2009). Due to these disadvantages many practical applications use Eulerian approaches, though moving mesh methods are still used (Charin et al., 2017). However, ALE methods are unlikely to be a good choice for modeling gas jet dynamics due to their inability to simulate complex breakup processes efficiently.

Lagrangian	Zero Interface Thickness	Moving Mesh	Mesh moves with grid (unstructured).
		Front Tracking	Lagrangian particles move within grid.
Eulerian		Level Set	Equation equal to signed distance from interface.
		Volume of Fluid with IR	Piecewise reconstruction of each contour plane.
		Volume of Fluid with CI	Color function and compressive schemes to bound interface.

Figure 2.2 Methods for interface tracking/capturing.

Dispersed phase models are commonly employed for bubbly flow and multiphase calculations. In an Eulerian framework, multi-fluid models rely on the interpenetrating theory of phases (Wörner, 2012, Ishii and Hibiki, 2010). Like ALE methods, transport equations are solved separately for each phase. Unlike ALE methods, the split equations are not rigidly separated by a mesh boundary, and so the phases can interpenetrate on the same Eulerian grid. Phase coupling is maintained through source terms in the phase transport equations, and closure models are required since the phase boundaries are not directly resolved. The ensemble average enforces either a priori knowledge of the dispersed

phase diameter, or an additional model to manage and track the size distribution of the dispersed particles. Closure models for coupling between the phases are often based on empirical relationships that are derived from dispersed flow experiments. For the modeling of near-field jets, the practical application of dispersed phase models are unsatisfactory due to the lack of interfacial resolution.

Another group of dispersed flow models, Lagrangian particle tracking (LPT) methods, track each bubble or drop as a point that can both interact and are acted on by the surrounding continuous domain. In this formulation, the continuous phase is modeled on an Eulerian grid, but LPT methods share many of the same problems as E-E methods in general. While these models are especially applicable to a dispersed far-field region, they are not sufficient for the continuous near-field region. Due to the multiscale nature of release modeling, these models are revisited in Chapter 6 in detail, given their candidacy for coupling to a near-field model.

Since dispersed phase modeling is not the best option for continuous phases with rapidly changing interfaces, only interface tracking and interface capturing methods remain. The remainder of this chapter therefore focuses on the objective of analyzing interface tracking and interface capturing methods to simulate continuous phases with a potential for break up. Many methodologies are based upon evolutions of the marker and cell (MAC) method proposed by Harlow and Welch (1965). This method used physical markers in cells containing a phase, and used these particles and the surrounding field to advect the phases with a free surface. As pointed out by Rudman (1997), the MAC method, while an initial and helpful foray into multiphase fluid dynamics, suffered from the relatively low tracker densities which resulted in incorrect predictions of void regions under high shear. Nonetheless, the MAC method has led to the development of other one-fluid approximations. The one-fluid model is:

$$\frac{\partial}{\partial t}(\rho) + \nabla \cdot (\rho \, \vec{u}) = 0 \tag{2.1}$$

$$\frac{\partial}{\partial t}(\alpha_i \rho_i) + \nabla \cdot (\alpha_i \rho_i \, \vec{u}_i) = 0 \tag{2.2}$$

$$\frac{\partial}{\partial t}(\rho \, \vec{u}) + \nabla \cdot (\rho \, \vec{u} \, \vec{u}) = -\nabla P + \nabla \cdot \mu (\nabla \vec{u} + (\nabla \vec{u})^T) + \rho \vec{g} + \vec{F} \tag{2.3}$$

where ρ is the mixture density ($\sum_i \alpha_i \rho_i$), $\vec{u}$ is the mixture or mass-averaged velocity, α_i is the phase fraction of phase i, P is the pressure field, μ is the dynamic viscosity, $\vec{g}$ is the gravitational vector, and $\vec{F}$ are the applied body forces. These equations are written with no mass sources, as that is the subject of later chapters.

A primary benefit to these methods is the ability to use a simple background grid and still retain reasonable accuracy (Günther et al., 2014). This simplification may come at the expense of artificially smoothing the flow properties in the vicinity of the interface, losing the sharp transition in favor of fewer equations to solve. Still, some models can accurately estimate the interfacial position with a continuous line. These methods are known as possessing a zero-thickness interface (which is assured in ALE methods). While some interface capturing methods also ensure zero-thickness, it is not guaranteed, and it can therefore be more difficult to accurately determine the surface tension force and to maintain sharp properties across the interface.

The remainder of this chapter is dedicated to the discussion of three primary interface tracking/capturing methodologies. The most common Lagrangian method, front-tracking (FT) is discussed, followed by a description of the most common Eulerian methods, level-set (LS) and volume-of-fluid. Methods are compared based on their inherent properties as they apply to the desired type of model.

2.2 Front-Tracking Method (FT)

Front-tracking is the most prominent Lagrangian IT method (Wörner, 2012). Like all interface tracking methods, it employs a zero-thickness technique by embedding node points on a background Eulerian field that tracks discrete phase fractions (Unverdi and Tryggvason, 1992). Therefore, the interface is directly tracked by a number of interconnected Lagrangian nodes, submerged within the mesh cells that form the stationary grid. The interconnected nodes act as a moving mesh to track the exact location at all times. These embedded sets of nodes form a front, where adjacent nodes (2D) or triplets of nodes (3D) form the boundaries of elements. Elements know of their points, but the points know only of themselves. This allows the interface to behave in a natural way, similar to the moving mesh methods. Following the one-fluid technique, the phase fraction is used to

average transport properties across the interface and only one set of volume-averaged conservation equations is solved to determine the velocity and pressure fields. However, like ALE methods, properties can be better restricted to each phase. The individual shifting of properties naturally transitions from one phase to another, meaning that the correct equations will be used in the bulk fluids.

While originally for incompressible, inviscid flows, FT methods have been extended to compressible, viscid flows as well (Terashima and Tryggvason, 2010). For incompressible flows, a transition region allowed for smoothing of the fluid properties, but for compressible flows care needs to be taken to avoid oscillations near the interface due to the sharp property changes. Thus, for incompressible flow, FT methods had a higher tolerance for diffuse interfaces. This is not the case for compressible flows, where subtle shifts in properties can spur oscillations in the flow field through fluctuations in the pressure field. Terashima and Tryggvason (2010) employed a ghost fluid method, allowing each fluid to perceive a region beyond the interface to smooth out transitional effects by the application of immersed boundary conditions and the use of an exact Riemann solver. The tracked front provides the necessary information to construct the normal gradient for this calculation. The result is higher stability at the expense of extra computational time through additional algorithms.

A notable problem with FT is that the deformation of the interface can lead to poor resolution at the front between fluids. Since the nodes are advected in a Lagrangian way, they rely on movement supplied by the background grid velocity (Wörner, 2012), and they only know of their own location and connectivity. Similar to the ALE method case, this is handled with an adaptive process by which more or less points are taken to resolve the front (Tryggvason et al., 2001). This is a process that requires computational time to assess the situation along the front, before adding or removing the points as necessary to achieve a sufficiently accurate surface representation. If poor planning is made when developing this step of the model, then calculations will suffer as in ALE and may require higher order schemes.

Primarily used to track the movement of bubbles (Unverdi and Tryggvason, 1992), FT does not handle coalescence and break up automatically, but instead requires additional algorithms to detect regions where detachment or attachment should occur (Tryggvason et al., 2001; Gopala and Wachem, 2008). Gopala and Wachem (2008) state that these models are often sub-grid scale, which relies on the translation of marker points and necessarily require prescription to initiate coalescence or break up (Wörner, 2012).

The primary benefit of the FT method is that the interface location and area are known directly from the marker connections. Knowledge of the interfacial linkages, which are retained and reconstructed in time, allow for the exact placement of source terms for a given interfacial area. Even with the small transition region, the implementation of mass and heat transfer is straightforward and arguably more numerically stable if smeared. For continuous regions this is useful, although computationally intensive. Advancing the front is similar to redefining the computational domain, and then break-up and coalescence have to be defined for mesh regions, though this can be handled by filtering the amount of distortion in the links between nodes.

The primary strength of FT methods is also its primary disadvantage. The need to embed the location of nodes and linkages accounts for more data storage that might not scale well to larger domains. Many tests with front-tracking have been limited to swarms with relatively low numbers of bubbles or single bubbles. In these small-scale systems, it is easy to achieve sufficient refinement around the objects of interest (bubbles), and the number of tracking particles can be limited significantly. For these bubbly flows, the number of tracking points can be estimated beforehand and will not change significantly. Conversely, for an underwater gas jet, the number of tracking particles will vary with time. As the release continues, particles must be released into the domain from the inlet, matching the inlet gas fraction as well. FT would be very useful for predicting the surface curvature and interfacial area for heat and mass transfer in the jet region. However, the jet will never truly be stable and the interface will continue to deform, so the exact number of nodes may not be estimated ahead of time. While surface curvature is preserved using this method, as the jet develops, and especially as the momentum region ends, the interface will undergo significant deformation. Pinching effects during break up, which already require additional

algorithms, may be sufficiently captured at the cost of reanalyzing the nodes and their interconnectivity. This is only compounded with additional algorithms to ensure mass conservation during the break up. For this reason, application of FT to the jet region of an underwater gas release, would likely be computationally too expensive.

2.3   Level-set Methods

The level-set (LS) method is a sharp interface method proposed by Osher and Sethian (1988). A tracking function, using the level-set parameter φ, measures the signed distance from the actual interfacial position (Wörner, 2012). However, this signed distance still has to be interpolated to obtain the actual interface location. In doing so, it tracks the direct position of the interface which leads to knowledge of the interfacial area and eases computation of the surface tension forces. Osher and Fedkiw (2001) have designed the tracking parameter (φ) such that:

$$\varphi(x,t) > 0 \quad \text{phase 1}$$
$$\varphi(x,t) < 0 \quad \text{phase 2}$$
$$\varphi(x,t) < 0 \quad \text{interface}$$

To handle the discontinuity at the interface, Sussman et al. (1994) proposed to allow a numerical smearing near the interface, a common trait among one-fluid models. While Sussman et al. (1994) applied their model to solely incompressible flows, the study of bubble dynamics has led to the development of compressible algorithms (see Hänsch et al., 2016; Lee and Son, 2017).

The primary difficulty in LS methods is that the advection of the tracking function does not guarantee mass conservation (Wörner, 2012). This is because of small gradients that develop due to numerical error in the time-dependent advection of the tracking function, and the tracking parameter loses its value as the signed distance and must be re-evaluated. Osher and Fedkiw (2001) note that this approach should allow for direct treatment of the interface. That is to say, the interface should naturally evolve with time, and there should not be a need to apply corrective algorithms to treat break-up and coalescence. While a desired property, the method actually translates these complications into a need to reinitialize the interface. Due to the time evolution of the domain, there is no guarantee that

the original level set will retain its position as a zero indicator for distance from the interface, which can in turn lead to a loss of mass over time in the system.

To handle the issue of reinitializing the level-set function, Sussman et al. (1994) employ a re-initialization after every time step. The associated cost is $O(n^3)$ operations and can become prohibitively expensive over time. This is especially true since solving the system requires approximately $O(n^4)$ operations otherwise, made up of the equations discretized in three dimensions, as well as the original level-set operations (Sethian and Smereka, 2004). A large proportion of this time is spent finding the interface, though Sussman et al. (1994) provide a method that requires less iteration over the level-set parameter. A separate level-set parameter is defined such that the only requirement is that the interface location is along the zero level-set. By solely maintaining this property, it is possible to force the actual level-set function to be zero at the interface, thus keeping its signed distance property. This alternate level-set function acts as a forcing function. This method was further refined in Russo and Smereka (2000), Hartmann et al. (2008) and Ovsyannikov et al. (2010). Another refinement is the method of crossing times, which solves the transport equation for the level set parameter both forward and backward in time to locate the point at which it changes sign. A difficulty with this method is that the zero level-set used may also deviate with time and that too must be handled.

Another approach, highlighted in Sethian and Smereka (2004), is to use a narrow band approach to reduce the number of operations since some of the field is far from the interface, but this reduction is only useful if the interface is confined to one location of interest. Further, Ovsyannikov et al. (2010) have developed another method, known as the extension velocity method. To preserve the identical property of the zero level-set function, a source term can be added in the evolution equation based on a new velocity field such that, outside of the zero level-set region, the distances between different level-sets to the zero level are constant along normal vectors to the zero level isosurface. Ngo and Choi (2017) have instead opted to formulate a direct approach, where the re-initialization is kept to a narrow band near the interface. However, this requires explicit construction of the interface through line segments, which will render it similar to the VOF methodologies

described in the next section. Ngo and Choi (2017) successfully applied their method to unstructured grids.

Günther et al. (2014) have extended LS to multiple phases by employing a set of tracking parameters. This allows for gap tracking and is easily implemented. A combined level-set function is then established to designate the closest interface from a particular point (cell centers, node points, etc.). Further multi-material modeling has been undertaken by Starinshak et al. (2014), and while they mention a robust algorithm that requires less re-initialization, the investigated cases are largely stationary. This would be useful in coalescence and break up, as there is a need to have the ability to define a robust model for many zero level sets to track each breaking portion of the original phase.

More recently, Abu-Al-Saud et al. (2017) have applied level-set methodology to porous media cases to allow accurate prediction of solid surface effects (through the highly accurate resolution of surface curvature). In order to circumvent the need for highly refined meshes, the level set function is used as a filter to determine if a sub-grid scale model should be applied (i.e. if the height returned is less than the grid spacing) for the solution of thin films. Essentially, the level-set function is used to apply a sub-grid scale model if the interface within a cell is near a solid wall. For heat and mass transfer uses, Lee and Son (2017) have captured compressible effects related to bubble growth via phase change. To handle flow oscillations due to property changes near the interface, the ghost fluid method was employed to smooth property transitions from phase to phase.

Overall, the level-set method provides benefits similar to the FT method. By maintaining a level set, the distance function can be used to define an interface location. Moreover, this allows an easier formulation for surface curvature and thus surface tension. However, this is only true if it is possible to keep the level set function as an accurate height function. Due to the evolution of he level-set parameter, there is a tendency for the exponential development of steep gradients in the function that cause it to lose this property. It is for this reason that the method can suffer from lack of mass conservation. However, this not an unsolvable problem. One method is to reinitialize the level set function, but it can be

computational expensive to do so. Another method is to couple level set to another methodology, such as VOF, which compensates for its weaknesses.

If it were applied to underwater gas jet release modeling, LS should be computationally faster than the FT. Since only the evolution of the signed distance is of interest, the computational step forward in time is easier to compute. For deformable interfaces, this method would be particularly applicable and maintains reasonable accuracy for conforming to surface curvature and therefore interfacial area. Still, there are a number of problems that would have to be tackled prior to use. First among these is the inherent problem of mass conversation. The addition of another algorithm to reset the zero level-set is akin to reinitializing the tracking particles in FT methods. Furthermore, the presence of multiple interfacial locations in the region of break-up may require more complicated distancing algorithms as mentioned above.

2.4 Volume-of-Fluid Methods

As written by Hirt and Nichols (1981), the volume-of-fluid method was designed with the mindset of representing multiphase information in one property variable, akin to how other properties are defined on an Eulerian, non-deforming mesh. This type of model is a natural extension of the MAC method developed by Harlow and Welch (1965). The VOF method introduces the volume fraction, or phase fraction α, which is defined by:

$$
\begin{aligned}
\alpha &= 0 & &\text{phase 1} \\
\alpha &= 1 & &\text{phase 2} \\
0 < \alpha &< 1 & &\text{interface}
\end{aligned}
$$

In the VOF method, the movement of the phase fraction is tracked by solving a phase continuity equation. Since the advection algorithm introduces some numerical error, this treatment causes property smearing, which prevents the clear definition of the interface. Hirt and Nichols (1981) presented one of the earliest methods of counteracting this smearing using the donor-acceptor method. This method uses information about α upstream and downstream to compute the flux by constructing an approximation of the interface. This methodology became the current standard for interface reconstruction methods. The benefit of interface reconstruction is the preservation of a zero- thickness interface, even if the stored value of the phase fraction does not inherently contain this

information. The simplest method is simple line interface reconstruction (SLIC) (Noh and Woodward, 1978; Rudman, 1997), where the interface is represented as flat lines parallel to an axis that account for the volume of fluid in the cell. Hirt and Nichols (1981) had adapted this orientation to be chosen based on the normal of the phase fraction gradient estimated using a nine-neighbour stencil.

A logical step forward from this simple approach was to use linear reconstructions of the interface position instead. The linear reconstruction is normally performed such that a drawn plane is both normal to the phase fraction gradient and divides the cell based on the phase fraction such that mass is conserved. This method was employed by Youngs (Youngs, 1982; Rudman, 1997) and is now normally known as piecewise linear interface reconstruction (PLIC). The method requires suitable cube chopping algorithms for structured meshes and complex geometric transformations for unstructured meshes (Scardovelli and Zaleski, 1999, Gueyffier et al., 1999, Pilliod and Puckett, 2004, Fan et al., 2013). More recent examples can employ piecewise parabolic interface reconstruction (PPIC) (Price, 2000), and hyperbolic reconstructions and on a variety of grid types (Rider and Kothe, 1998; Zhang et al., 2014; Xie et al., 2017). For these methods, there is a clear trade off. Better representation and fitting algorithms can be used to improve surface curvature calculations, as well as defining the interfacial area and location. However, higher order reconstruction also requires more resources to initialize and advect the interface at each step. Lower order reconstructions (such as linear and especially simple) will result in interfacial segments that are not guaranteed to line up. This is a problem for maintaining a continuous interface but speeds up computational times.

Intrinsic to reconstructive VOF-based interface tracking is the need to reconstruct the interface geometrically to counteract the smearing of properties before computing the advective fluxes. Once computed, the interface must be advected and then recalibrated to fit the result (Wörner, 2012). A scheme for representing the interface is chosen, and that defines the interface normal. The interface is typically advanced in one of two ways, either using split or un-split schemes. The use of split schemes reformulates the advective step into a series of one-dimensional steps, while unsplit handles the three dimensions at the same time. For split methods, the advective step is done in two parts, updating the interface

in each direction, before a final corrector after the third direction step is complete. The primary advantage for these schemes is stability and mass conservation. Unsplit schemes seek to perform the advection in one step, with only one reconstruction. This saves on computational time but may advect a volume more than once, leading to a required algorithm to prevent mass loss (Wörner, 2012).

An alternative to the geometric method of reconstructing the interface is to use a compressive scheme in the interfacial region to limit the diffusion. These algebraic VOF methods seek to eliminate the complicated step of using reconstruction to define the fluxes, and instead allow the phase fraction equation to be discretized and handled by special source terms at the interface. As written by Qian et al. (2006), this allows the method to be generalized simply to three dimensions. Moreover, this method is inherently easier to apply in unstructured grids (Queutey and Visonneau, 2007). Originally, the method was applied using a fictitious time derivative of pressure in the continuity equation (and therefore the phase continuity equation). However, this required a divergence free solution at every time step for incompressible flows. Otherwise continuity would be violated. Without the interfacial reconstruction, care must be taken when discretizing the phase continuity equation (Gopala and Wachem, 2008).

As mentioned by Gopala and Wachem (2008), a primary difficulty with the VOF method is deciding how to handle the advection term in the phase transport equation. Pure upwind schemes result in highly smeared interfaces, and higher order schemes are unstable. As a result, there had been a number of methods introduced to handle the discretization, such as the flux corrected transport (FCT), or the compressive interface capturing scheme for arbitrary meshes (CICSAM). FCT relies on a lower order monotonic scheme, such as upwind, to provide an initial estimate of the new phase fraction value. CICSAM instead uses the acceptor-donor scheme that is common in interface reconstructive schemes. Gopala and Wachem (2008), utilizes a donor cell with one upwind cell and multiple acceptors surrounding them. The primary face of interest in any calculation is the face between donor and acceptor. The normalization corresponds to the parameter γ, which is another intermediate estimator. A downside of this estimator is that, for a given scheme, fluxes that pass through may produce unrealistic oscillations. Essentially, CICSAM is a

scheme that produces a one-dimensional bounded version of QUICK. Unfortunately, these schemes are inherently diffusive, and so an anti-diffusive flux is defined to counteract the smearing by use of a higher order scheme. A limiter is applied to ensure that the anti-diffusive flux does not cause numerical instability.

Another option to limit the spreading of the interface is to use a LS method (Bonometti and Magnaudet, 2007), which applies a modified velocity at the interface to maintain the gradient of the phase function (or height function from a level-set point of view). The acting point of the velocity is chosen such that it corresponds to the 0.5 contour, or where the interface should be located. Then a fictitious velocity term is applied to counteract the strain rate, and finally the volume fraction is corrected so that mass is not lost.

In Deshpande et al. (2012), another limiting method is used. For the OpenFOAM family of VOF solvers, an algebraic manipulation of the phase continuity equation is used to add a source term that acts at the interface, involving both phase fractions (and therefore is zero in the bulk phases). Since it is not wholly correct to assume a one-fluid approximation near the interface, this formulation applies a source term based on the relative velocity that results directly from manipulation of the independent phase equations. Like a mixture model, this results in a closure term for the replacement of the mixture velocity in the phase continuity equation. The actual scheme used in OpenFOAM also tackles this problem, known as inter-gamma differencing and improves the boundedness (Gopala and Wachem, 2008). Since it is a closure term, the exact form has changed through the various versions of OpenFOAM.

The numerical disadvantage associated with this method is one of spurious currents, which is only exacerbated by a potentially diffuse interface, lower order flux calculation schemes and radical property differences (Renardy and Renardy, 2002; Despande et al, 2012). While one method of handling this problem is to couple VOF with other methods, such as a height function and level set, another is to specifically define the interfacial surface curvature method or to select a scheme above (e.g. CICSAM). The downside for compressive interface methods is that, regardless of scheme choice, the Courant number ($Co = \bar{u}\Delta t/\Delta x$) is always more restrictive (Gopala and Wachem, 2008).

Additionally, although surface tension has been studied, a number of models still rely on the continuum surface force (CSF) model proposed by Brackbill et al. (1992). The phase fraction gradient is used to calculate the surface curvature, which is then related to the surface tension. However, one problem is that the phase fraction is inherently discontinuous, even when reconstructed (Albadawi et al., 2013). For each individual cell, a piecewise function is defined by the gradient of the phase fraction, but there is no guarantee that these join at cell boundaries. Although this issue will theoretically resolve itself as the computational grid gets smaller, runtime will suffer. The PPIC method of Renardy and Renardy (2002), known as PROST, incorporates a parabolic reconstruction and calculation in order to increase the accuracy. A study by Gerlach et al. (2007) proved that for periodic bubble formation PROST performed the best, but coupled methods offered comparable accuracy at reduced computational requirements. However, the use of the CSF model is still prolific (Albadawi et al., 2013; Baltussen et al., 2014), and from the formulation it is clear that for cases of low surface curvature, the model will still give accurate predictions. If bubbly flows are to be simulated, however, a parabolic or coupled method may be more applicable.

Finally, based on the original formulation by Youngs (1982), multiple phase models have also been developed (Benson, 2002; Pathak and Raessi, 2016). A major drawback of these methods is the difficulty in extending them to three dimensions without significant increase in computational power, though they give a zero-thickness interface. Along with this, the interfaces themselves are used to prevent smearing by calculating the movement of the interface construction itself (Gopala and Wachem, 2008). The velocity is integrated over the interface and used as a correction in the one-fluid approximation.

Types of VOF methods can fundamentally be split in two: geometric and compressive. In each method, mass is inherently conserved by a bounded phase fraction function, but the method to do so is different. The geometric method can provide a more accurate model of the exact interface shape, as well as the flux through the interfacial area. Since the interfacial area is already known, adding immersed boundary source terms is far easier. The cost, however, is in the scheme chosen to represent the interface, as well as the need to advect it without losing mass. For applications to underwater jets, the method can

capture highly deforming interfaces due to the background phase fraction function. However, for large interfacial structures the method may become computationally more expensive. Conversely, algebraic VOF methods evolve the interface in a so-called natural way. The phase fraction function itself indirectly tracks the interface through the 0.5 contour. Without the reconstruction to limit the fluxes, the method requires a compressive term at the interface to prevent numerical smearing. This results in either a closure term in the phase continuity equation, or specifically crafted schemes. The primary disadvantages of this method are the choice of closure relation or scheme, since they will affect the numerical stability at the interface as well as the amount of smearing. Additionally, since the interface is not reconstructed, the surface curvature is less accurately predicted. Still, even for reconstructive methods, there is no guarantee that the interface will be continuous without additional computational time. For applications to underwater jet modeling, the faster solution times provided by the algebraic method are useful. Although the interfacial area is not readily available, rather than having multiple reconstructive steps, a simple algebraic estimate based on the reconstructive method can be applied. The accuracy gained is only for estimating immersed boundary conditions and not required for the solution of the flow field. Overall, the ability to naturally move the phase fraction field is necessary for highly deforming interfaces, and this is handled in a simple way.

2.5 Coupled Methods

As alluded to in the previous section, there is another approach that has been explored recently. Since many methods have individual weaknesses that can be mitigated by another method, various coupled methods have been proposed to compensate. For instance, the LS method suffers from a need to be reinitialized, due to an inherent lack of mass conservation. However, it possesses a superior property of calculating surface curvature (perhaps second only to moving mesh or lagrangian methods such as front-tracking). On the other hand, a method like VOF accurately conserves mass but its reconstructive methods do not guarantee a continuous surface function in the absence of diminishing grid size, unless algorithms are implemented to do so. Even so, they are more difficult to implement in three dimensions, whereas the algebraic or compressive variant ignores these weaknesses.

To bypass the issues with surface tension, a number of coupled VOF and LS methods have been proposed. The methods use the VOF algorithm to handle the actual phase transport, while a LS function is defined to approximate the interfacial position and increase the accuracy of surface tension calculations (Albadawi et al., 2013; Ningegowda and Premachandran, 2014). Similar to the interface reconstructive methods, the LS parameter is updated at every timestep in order to ensure the amount of contained volume is accurate, which bypasses the weakness of the LS method on its own (Sethian and Smereka, 2004). This is of interest for algebraic VOF methods, as it still allows a quick solution to the surrounding volume fraction field. The method improves accuracy in correcting the fluxes at the interface to reduce spurious currents, at the cost of maintaining the level-set function. However, an additional flaw pointed out by Ningegowda and Premachandran (2014) is the current lack of effective and computationally efficient multidirectional advection schemes to advance the VOF and LS functions simultaneously.

2.6   Conclusions

This chapter analyzed the applicability of current interface tracking/capturing techniques for the simulation of gas-liquid flows. The discussion highlighted that the choice of a particular methodology should seek to maximize its strengths compared to the needs of the application, while minimizing its weaknesses. For resolving continuous domains and free surfaces, such as the jet region of a gas phase release, methods such as Eulerian-Eulerian can be neglected due to their ensemble averaging and lack of direct interfacial representation. Theoretically, moving mesh methods offer a lot of advantages because they explicitly resolve the interface at the faces between computational cells. However, this increased accuracy comes at a computational cost, as the mesh needs to be updated at every time step. Moreover, the method does not inherently capture break-up and coalescence without additional models.

Front-tracking methods also suffer from this weakness, as well as the computational effort in maintaining the Lagrangian tracking of particles. Efficient methods may have to reduce the number of sample points along the front and then deal with repair at subsequent time steps. The treatment of the interface allows for simpler implementation of interphase transport. However, the maintenance of the interface in regions of high deformation are

prohibitive. Additional algorithms to deal with coalescence and break-up, as well restructure the nodes make it difficult to use for jet flow.

Level-set was promising, but ultimately both VOF and LS are similar. Both try to track the interface through a tracking function. In the case of level-set, this tracking function follows the motion of the signed distance from the interface. In VOF, this is handled by the phase fraction in the particular cell. The advection of these quantities leads to a potential loss of mass with level-set, whereas VOF tracks the amount of volume directly (for incompressible systems this is sufficient in place of mass) by solving continuity for one phase (and hence the other is known in a binary system). With level-set, one advantage may be the ease of tracking multiple phase boundaries, where different distance functions may be used. For VOF with interface reconstruction, it is apparent that the same problem may arise. While the phase fraction is truly the advection of mass, advecting the constructed interface may disagree with the underlying quantities of fluid and therefore re-initialization also plagues this methodology with computational cost. For this reason, compressive interface schemes apply a small term that acts at the interface to prevent smearing and achieve a finite but small interfacial region as opposed to the sharp interfaces of the other two methods. This is beneficial from a computational standpoint, but from an immersed boundary condition standpoint it does not allow for the accurate representation of interfacial phenomena that must occur across a fixed area defined by the interface itself.

A compressive interface VOF will be used in the proceeding chapters as the method of tracking gas-liquid interfaces and for the jet region of the large-scale release of acid/sour gas. This choice was made due to the relative simplicity of the method, its availability in OpenFOAM, and its natural ability to facilitate breakup and coalescence predictions. While some test cases will be small scale, there will be a necessary lack of resolution in large-scale cases to achieve manageable run times. For compressive interface VOF, the solution times are the quickest, but it is necessary to accept the numerical smearing of the interface. Although the curvature is not predicted with the accuracy of other methods, the interfacial shape is maintained through the evolution of the 0.5 contour. Additionally, this model has the most natural form of break-up and coalescence without the need to redesign the interfacial tracking component. For heat and mass transfer, interface reconstructive

methods can be borrowed to provide interfacial area estimates for the calculation of interphase fluxes.

Chapter 3

Simulation of Interphase Heat and Mass Transfer using an Immersed Boundary Method in OpenFOAM

3.1 Introduction

Multiphase flows involving at least one compressible phase are prevalent in many industrial applications. In many cases such systems also involve non-ideal mixtures, which further complicates analysis. Detailed mathematical models are required for design, analysis and optimization of such systems, and to understand the fundamental physical processes limiting performance. This makes computational fluid dynamics (CFD) an invaluable investigative tool. However, efficient and accurate methods are required to resolve the fluid dynamics in these systems, and further methods are required to model interphase heat and mass transfer.

The choice of CFD model for multiphase flows depends on the complexity of the system and the desired level of insight. As a consequence, multiple methodologies for simulating flows with two or more phases have been developed. Chapter 2 presented an overview of the development and use of multiphase methodologies. Therefore, only an abbreviated summary will be presented in this section to lead to the objectives for the chapter.

Dispersed flow models such as Lagrangian particle tracking (LPT) and the Euler-Euler (E-E) method are commonly used for multiphase flow modeling (Padoin et al., 2014; Messa et al., 2015; Rzehak and Krepper, 2016; Fletcher et al., 2017; Hou et al., 2017). These methods are normally applied to systems that contain too many dispersed particles (droplets or bubbles) to make interface tracking or capturing feasible. The inherent benefit of these approaches is their ability to utilize coarse grids to resolve the average flow, thus saving computational time for large geometries. However, they do not provide direct

information about the continuous phase boundaries, and therefore require empirical closure models.

For interface scales on the same scale as the computational grid, interface-tracking/capturing methods are often employed. Currently, the three most common methods are front-tracking (FT), level-set (LS) and volume-of-fluid (VOF).

Front-tracking methods employ small tracking particles distributed along the interface to track the interfacial location by connections between nodes (Wörner, 2012). While this provides a sharp, deforming interface, the connections between nodes must constantly be evaluated, particularly in regions of break-up and coalescence. As mentioned by Roghair et al. (2016), volume is not conserved by default. Due to the level of local detail provided by FT methods, they are often used to analyze the motion of individual bubbles or droplets in a continuous phase, or to investigate the interactions between small numbers of bubbles or droplets. Toutant et al. (2012) applied FT to study a single bubble rising as part of their validation for a smoothing technique. They mention that FT is computationally intensive, but the resolution of the interface is much smoother than typical Eulerian methods. Additionally, the studies of Aboulhasanzadeh et al. (2012), Burghoff and Kenig (2005), and Roghair et al. (2016) employed FT to investigate bubble swarms. FT is convenient for such studies because the scales at which bubbles would have to be resolved when using Eulerian techniques would result in a mesh with a prohibitively small grid spacing. However, only a finite number of interacting bubbles can be modeled due to the high computational effort. More recently, Irfan and Muradoglu (2017) used FT for the simulation of evaporation. They employed both interfacial temperature and species concentration gradient based models to estimate interface heat and mass transfer fluxes. Irfan and Muradoglu (2017) validated their models through comparison to common test cases, including Stefan diffusion problems as well as evaporating falling droplets.

Level-set methods are based on an Eulerian framework, making them somewhat simpler to implement and generalize than FT methods. Relative to other Eulerian interface capturing methods, their primary benefit is that they maintain a sharp interface approximation (Wörner, 2012). This permits direct computation of the interfacial area in

each cell. The primary disadvantage is related to the computational speed reductions through the re-initialization of the zero-level set to ensure mass conservation. Free surface modeling using LS has been employed by many authors (e.g., Ganguli and Kenig, 2011; Wang et al., 2008; and Kenig et al., 2011). Despite the computational overhead for managing the re-initialization, the ability to maintain a continuous description of the interface allows for accurate surface tension predictions. LS has also been adapted to bubbly flows by Labois and Narayanan (2017), who applied a drift velocity model to correct for the velocity in the dispersed phase, while the level set was used to ensure the global boundary between phases. The primary treatment was 1D, built for columns of known geometry or pipes, although it would be valid in higher dimensions. LS has also been used to model interphase heat and mass transfer in a variety of studies (Deshpande and Zimmerman, 2006; Tanguy et al., 2007; Wang et al., 2008; Kenig et al., 2011; Lakehal and Labois, 2011; Gjennestad and Munkejord, 2015; Shaikh et al., 2016). The zero-thickness interface provides a useful for basis for interphase flux estimation.

Volume-of-fluid methods can be divided into two general categories: compressive interface, and geometric reconstruction (Wörner, 2012). In the latter type, the interface is directly represented by a series of segments to match the volume of a phase in the cell and capture the geometry. The piecewise components can be linear (Mencinger and Žun, 2011; Soh et al., 2016), quadratic (Renardy and Renardy, 2002; Diwakar et al., 2009), or another function. The benefit of geometric reconstruction is the preservation of a sharp interface, but this resolution comes at computational cost due to the overhead associated with the need for iterative reconstruction and advection of the interface. By contrast, compressive interface methods seek to track the phases only by their volume fractions. In this method, the interface is usually smeared over a finite number of cells, controlled by constitutive laws that represent the relative velocity near the interface. Correctors provide both a bounding and compressing step to ensure the smearing effect is minimized.

Due to the simplicity of variable storage, and the ability to include interface deformation naturally, VOF is widely employed in interphase heat and mass transfer simulations (Banerjee, 2007; Banerjee, 2013; Haelssig et al., 2010; Haroun et al., 2012; Marschall et al., 2012; Liu and Yu, 2016). Interphase transport, such as evaporation/condensing of a

pure substance, are readily implemented (Rauschenberger and Weigand, 2015; Samkhaniani and Ansari, 2016). Hassanvand and Hashemabadi (2011) modeled mass transfer through a stagnant film and in stratified flow. Haelssig et al. (2010) used VOF to simulate evaporation and condensation of ethanol-water mixtures in counter-current contacting. VOF has also been applied in the droplet flow regime for heat and mass transfer by Banerjee (2013) and Marschall et al. (2012). Bothe and Fleckenstein (2013) used a VOF method to study evaporation from moving droplets over a range of diameters, which has been expanded upon by Grunding et al. (2016) for reacting flows. Fleckenstein and Bothe (2015) studied single droplet shrinkage. Geometrically complex systems have been modeled by Haroun et al. (2012), who studied absorption of gas in liquid films flowing over structured packing. Several models have employed coupled models involving VOF methodologies, such as Gumulya et al. (2015), who employed level set to calculate the surface curvature during the evaporation of a droplet but solved the VOF conservation equations (additionally by Albadawi et al., 2013; Ningegowda and Premachandran, 2014).

This study presents the development and validation of a VOF solver for two-phase, compressible flow with interphase heat and mass transfer. Although compressible VOF solvers with phase change models are commonly used for modeling cavitation (Roohi et al., 2013; Kadivar et al., 2017; He et al., 2017), and boiling and condensation (Samkhaniani and Ansari, 2016; Dinsenmeyer et al., 2017), fewer studies have investigated concentration gradient driven interphase heat and mass transfer processes. The choice of VOF was made due to the inherent mass conservation, as well as the natural ability to handle coalescence and break-up, particularly for the compressive interface models. The presented solver uses the compressive interface approach to advect the phase fraction. A piecewise linear geometric reconstruction is used to estimate the interfacial area required to perform the interphase energy and mass transfer calculations (Soh et al., 2016; Tryggvason, Scardovelli and Zeleski, 2011). Since VOF employs the one-fluid approximation, interface jump conditions for mass and energy transfer are converted to volumetric source terms for incorporation into the appropriate conservation equations. Three validation cases are presented to demonstrate the solver's performance and verify its accuracy.

Additionally, this chapter provides a basis for the study of heat and mass transfer for the near-field region in an underwater gas release. Therefore, this study acts as an initial test into the capacity of this modeling approach to simulate continuous phase transport with coupled interphase phenomena. This study considers mass transfer from an interphase perspective alone, for the development of a framework upon which further models could be developed.

3.2 Methodology

The model was implemented using OpenFOAM, an open source CFD toolbox (The OpenFOAM Foundation, 2018). The base solver was `compressibleInterFoam`, which is a VOF solver for up to two compressible phases that uses OpenFOAM's thermophysical libraries to estimate temperature and pressure dependent property values. Although the solver did not contain species equations or appropriate mass transfer source terms in the phase fraction, continuity or energy equations, its modularity made it possible to link these additions to many of the pre-defined routines that are used in the solvers that do support species transfer. The following discussion describes the conservation equations and their implementation into the `compressibleInterFoam` solver.

3.2.1 Governing Equations

Following the one-fluid formulation, the continuity equation is:

$$\frac{\partial \rho}{\partial t} + \nabla \cdot (\rho \vec{u}) = 0 \tag{3.1}$$

where $\rho = \sum_i \alpha_i \rho_i$ is the mixture density, α_i is the phase fraction of phase i, and $\vec{u}$ is the velocity of the mixture. The phase continuity equation for any phase i is given by:

$$\frac{\partial (\alpha_i \rho_i)}{\partial t} + \nabla \cdot (\alpha_i \rho_i \vec{u}_i) = S_i \tag{3.2}$$

where S_i represents a mass transfer source/sink term for phase i. The volume-averaged momentum equation is:

$$\frac{\partial (\rho \vec{u})}{\partial t} + \nabla \cdot (\rho \vec{u} \vec{u}) + \nabla \cdot \tau = -\nabla P + \rho \vec{g} + \vec{F}_{ST} \tag{3.3}$$

where $\vec{u} = \sum_i \alpha_i \vec{u}_i$ is the mixture velocity, τ is the viscous stress tensor, P is the pressure field, $\vec{g}$ is the gravitational force, and $\vec{F}_{ST}$ is the surface tension force, which is calculated by the method of Brackbill et al. (1992):

$$\vec{F}_{ST} = \sigma\kappa \cdot \nabla_N \alpha_i \tag{3.4}$$

where σ is the surface tension coefficient, and $\kappa = \nabla \cdot \vec{n}_{int}$ is the surface curvature based on the a normal to the interface (discussed in the proceeding section). The subscript N refers to the normal portion of the gradient. The energy equation can be written as:

$$\frac{\partial(\rho e)}{\partial t} + \nabla \cdot (\rho e\vec{u}) + \frac{\partial(\rho E_k)}{\partial t} + \nabla \cdot (\rho E_k \vec{u}) + \nabla \cdot (\vec{u}P) =$$
$$-\nabla \cdot \vec{q} - \nabla \cdot \left(\sum_j e_j \vec{j}_j\right) + S_E \tag{3.5}$$

where e is the internal energy, E_k is the kinetic energy, S_E is the summation of the energy contributions by phase change, and $\vec{q}$ represents the conduction flux. The conduction flux is given by Fourier's law:

$$\vec{q} = -K\nabla T \tag{3.6}$$

where T is the temperature and K is the thermal conductivity. The internal energy for a given phase is defined as:

$$e_i = c_{v,i}T \tag{3.7}$$

where c_v is the specific heat at constant volume, calculated by:

$$e = \sum_i \alpha_i c_{v,i}T = \left(\alpha_1 c_{v,1} + \alpha_2 c_{v,2}\right)T = c_v T \tag{3.8}$$

The energy equation (equation 3.5) can then be written as:

$$\frac{\partial(\rho c_v T)}{\partial t} + \nabla \cdot (\rho c_v T\vec{u}) + \frac{\partial(\rho E_k)}{\partial t} + \nabla \cdot (\rho E_k \vec{u}) + \nabla \cdot (\vec{u}P) = \nabla \cdot (K\nabla T)$$
$$-\nabla \cdot \left(\sum_j e_j \vec{j}_j\right) + S_E \tag{3.9}$$

The species equation for any phase is:

$$\frac{\partial(\alpha_i \rho_i Y_{i,j})}{\partial t} + \nabla \cdot \left(\alpha_i \rho_i Y_{i,j}\vec{u}\right) = -\nabla \cdot \vec{j}_j + S_{M,j} \tag{3.10}$$

where $Y_{i,j}$ is the mass fraction of species j in phase i, and the term $S_{M,j}$ refers to the mass source for specie j. The diffusive flux, $\vec{j}_j$, can be written for each species using Fick's Law:

$$\vec{j}_j = -\alpha_i \rho_i D_{i,jM} \nabla Y_{i,j} \qquad (3.11)$$

where $D_{i,jM}$ is the diffusion coefficient of species j in phase i with respect to the mixture. In dilute multicomponent systems, this is the effective diffusivity. The diffusion flux could be replaced by Maxwell-Stefan diffusion matrices, in which case this term becomes a sum of contributions relative to the other species' gradients. For the case of binary mixtures, Fick's law is sufficient and $D_{i,jM}$ is simply the binary diffusion coefficient.

The source term for a single transferring species is given by:

$$S_{M,j} = -\frac{\rho_i D_{i,jM} \nabla Y_{i,j}}{1-Y_{i,j}} \left(\frac{A}{V}\right)_{int} \qquad (3.12)$$

where the term $(A/V)_{int}$ is the area density of the interface, which will be discussed later. In this case, the definition of the energy equation source term is:

$$S_E = S_{Mj} \Delta H_{vap,j} \qquad (3.13)$$

where $\Delta H_{vap,j}$ is the latent heat of vaporization of species j, assuming transfer from liquid to gas. The collection of individual sources combine to form the phase source:

$$S_i = \left(\sum_j S_{M,j}\right)_i \qquad (3.14)$$

The subscript i denotes that the source term will be the same in units of mass but change sign for a given phase depending on the direction of transfer. This relationship can be substituted directly into equation 3.2.

3.2.2 Numerical Implementation

For phase continuity, OpenFOAM uses the MULES algorithm (Multidimensional Universal Limiter for Explicit Solution), for which only the incompressible form of the equations is solved. The density change is included through appropriate source terms. The phase continuity equation can be organized into phase fraction and density components:

$$\frac{\partial \alpha_i}{\partial t} + \nabla \cdot (\alpha_i \vec{u}_i) = \frac{S_i}{\rho_i} - \frac{\alpha_i}{\rho_i}\left[\frac{\partial \rho_i}{\partial t} + \vec{u}_i \cdot \nabla \rho_i\right] \qquad (3.15)$$

For a two-phase system, the two phase continuity equations are:

$$\frac{\partial(\alpha_1 \rho_1)}{\partial t} + \nabla \cdot (\alpha_1 \rho_1 \vec{u}_1) = S_1 \qquad (3.16)$$

$$\frac{\partial(\alpha_2\rho_2)}{\partial t} + \nabla \cdot (\alpha_2\rho_2\vec{u}_2) = -S_1 \tag{3.17}$$

Note that the total mass source into one phase must equal the total mass source from the other phase. Written as in equation 3.15, the equations become:

$$\frac{\partial\alpha_1}{\partial t} + \nabla \cdot (\alpha_1\vec{u}_1) = \frac{S_1}{\rho_1} - \frac{\alpha_1}{\rho_1}\left[\frac{\partial\rho_1}{\partial t} + \vec{u}_1 \cdot \nabla\rho_1\right] \tag{3.18}$$

$$\frac{\partial\alpha_2}{\partial t} + \nabla \cdot (\alpha_2\vec{u}_2) = -\frac{S_1}{\rho_2} - \frac{\alpha_2}{\rho_2}\left[\frac{\partial\rho_2}{\partial t} + \vec{u}_2 \cdot \nabla\rho_2\right] \tag{3.19}$$

In the case of incompressible flow, the final term on the right-hand side vanishes. However, in cases with mass transfer this term could be important even if the density does not change significantly with temperature or pressure. The final form of the above equation relies on the summation of the phase equations to produce a term for the divergence of velocity, and subsequently the source for the pressure-momentum equation decomposition. Note that the equation relies on a volume-averaged velocity, due to the imposed transformations. Since the term on the left side of the rearranged phase fraction equation includes only the incompressible terms, it follows that adding equation 3.18 and 3.19 yields:

$$\frac{\partial(\alpha_1+\alpha_2)}{\partial t} + \nabla \cdot (\alpha_1\vec{u}_1 + \alpha_2\vec{u}_2) = \frac{S_1}{\rho_1} - \frac{S_1}{\rho_2} - \frac{\alpha_1}{\rho_1}\left[\frac{\partial\rho_1}{\partial t} + \vec{u}_1 \cdot \nabla\rho_1\right]$$
$$-\frac{\alpha_2}{\rho_2}\left[\frac{\partial\rho_2}{\partial t} + \vec{u}_2 \cdot \nabla\rho_2\right] \tag{3.20}$$

$$\nabla \cdot (\vec{u}) = S_1\left(\frac{1}{\rho_1} - \frac{1}{\rho_2}\right) - \frac{\alpha_1}{\rho_1}\left[\frac{\partial\rho_1}{\partial t} + \vec{u}_1 \cdot \nabla\rho_1\right] - \frac{\alpha_2}{\rho_2}\left[\frac{\partial\rho_2}{\partial t} + \vec{u}_2 \cdot \nabla\rho_2\right] \tag{3.21}$$

where $\vec{u} = \sum_i(\alpha_i\vec{u}_i)$ is the mixture velocity. This important result will be used later, in the PISO (Pressure Implicit with Split Operators) algorithm. Returning to equation 3.18 the phase velocity is difficult to deal with, as only the mixture velocity is tracked in the solver. However, it can be recast as:

$$\frac{\partial\alpha_1}{\partial t} + \nabla \cdot (\alpha_1\vec{u}_1) + \nabla \cdot (\alpha_1\vec{u}) - \nabla \cdot (\alpha_1\vec{u}) = \frac{S_1}{\rho_1} - \frac{\alpha_1}{\rho_1}\left[\frac{\partial\rho_1}{\partial t} + \vec{u}_1 \cdot \nabla\rho_1\right] \tag{3.22}$$

$$\frac{\partial\alpha_1}{\partial t} + \nabla \cdot (\alpha_1\vec{u}) + \nabla \cdot (\alpha_1\vec{u}_1) - \nabla \cdot (\alpha_1\vec{u}) = \frac{S_1}{\rho_1} - \frac{\alpha_1}{\rho_1}\left[\frac{\partial\rho_1}{\partial t} + \vec{u}_1 \cdot \nabla\rho_1\right] \tag{3.23}$$

$$\frac{\partial\alpha_1}{\partial t} + \nabla \cdot (\alpha_1\vec{u}) + \nabla \cdot (\alpha_1\vec{u}_1) - \nabla \cdot \left(\alpha_1(\alpha_1\vec{u}_1 + \alpha_2\vec{u}_2)\right) = \frac{S_1}{\rho_1}$$
$$-\frac{\alpha_1}{\rho_1}\left[\frac{\partial\rho_1}{\partial t} + \vec{u}_1 \cdot \nabla\rho_1\right] \tag{3.24}$$

$$\frac{\partial\alpha_1}{\partial t} + \nabla \cdot (\alpha_1\vec{u}) + \nabla \cdot (\alpha_1\alpha_2\vec{u}_R) = \frac{S_1}{\rho_1} - \frac{\alpha_1}{\rho_1}\left[\frac{\partial\rho_1}{\partial t} + \vec{u}_1 \cdot \nabla\rho_1\right] \tag{3.25}$$

38

where $\vec{u}_R = \vec{u}_1 - \vec{u}_2$ is the relative velocity between the phases. The third term on the left hand side of equation 3.25 represents a closure model, which will be discussed shortly before the momentum coupling implementation. Since only one phase continuity equation is solved, the effects of the compressibility of the second phase would be lost. However, a second rearrangement can be made:

$$\frac{\partial \alpha_1}{\partial t} + \nabla \cdot (\alpha_1 \vec{u}) + \nabla \cdot (\alpha_1 \alpha_2 \vec{u}_R) = \frac{S_1}{\rho_1} - \frac{\alpha_1}{\rho_1}\left[\frac{\partial \rho_1}{\partial t} + \vec{u}_1 \cdot \nabla \rho_1\right] + \alpha_1 \nabla \cdot \vec{u}$$
$$-\alpha_1 \nabla \cdot \vec{u} \quad (3.26)$$

Remembering the definition of the divergence from equation 3.21:

$$\frac{\partial \alpha_1}{\partial t} + \nabla \cdot (\alpha_1 \vec{u}) + \nabla \cdot (\alpha_1 \alpha_2 \vec{u}_R) = \frac{S_1}{\rho_1} - \frac{\alpha_1}{\rho_1}\left[\frac{\partial \rho_1}{\partial t} + \vec{u}_1 \cdot \nabla \rho_1\right] + \alpha_1 \nabla \cdot \vec{u}$$
$$-\alpha_1 \left(S_1 \left(\frac{1}{\rho_1} - \frac{1}{\rho_2}\right) - \frac{\alpha_1}{\rho_1}\left[\frac{\partial \rho_1}{\partial t} + \vec{u}_1 \cdot \nabla \rho_1\right] - \frac{\alpha_2}{\rho_2}\left[\frac{\partial \rho_2}{\partial t} + \vec{u}_2 \cdot \nabla \rho_2\right]\right) \quad (3.27)$$

$$\frac{\partial \alpha_1}{\partial t} + \nabla \cdot (\alpha_1 \vec{u}) + \nabla \cdot (\alpha_1 \alpha_2 \vec{u}_R) = S_1 \left(\frac{1}{\rho_1} - \alpha_1 \left(\frac{1}{\rho_1} - \frac{1}{\rho_2}\right)\right) - \frac{\alpha_1 \alpha_2}{\rho_1}\left[\frac{\partial \rho_1}{\partial t} + \vec{u}_1 \cdot \nabla \rho_1\right] +$$
$$\frac{\alpha_1 \alpha_2}{\rho_2}\left[\frac{\partial \rho_2}{\partial t} + \vec{u}_2 \cdot \nabla \rho_2\right] + \alpha_1 \nabla \cdot \vec{u} \quad (3.28)$$

Equation 3.28 is the form of the phase continuity equation used in OpenFOAM to ensure compatibility with the MULES solution procedure. The remaining divergence is calculated explicitly at each time step, using the current velocity field. The MULES algorithm solves the following discretized form of the phase continuity equation:

$$\frac{\alpha^{N+1} - \alpha^N}{\Delta t} + S_{IMP}\alpha^{N+1} = S_{EXP} + \Sigma_f(\vec{u}\alpha)_f \quad (3.29)$$

In which the notation N refers to the current time, S_{IMP} represents the implicit sources, and S_{EXP} represents explicit sources. The term on the end is the summation of the phase flux through each face, f. Given the above rearrangement, the phase density change must be compacted into the two source terms. It is worth noting that this change in the phase continuity equation translates into the governing equations. For total continuity:

$$\frac{\partial(\alpha_1 \rho_1 + \alpha_2 \rho_2)}{\partial t} + \nabla \cdot (\alpha_1 \rho_1 \vec{u} + \alpha_2 \rho_2 \vec{u}) + \nabla \cdot (\alpha_1 \alpha_2 \rho_1 \vec{u}_R - \alpha_1 \alpha_2 \rho_2 \vec{u}_R) = 0 \quad (3.30)$$

$$\frac{\partial(\rho)}{\partial t} + \nabla \cdot (\rho \vec{u}) + \nabla \cdot \left(\alpha_1 \alpha_2 \vec{u}_R (\rho_1 - \rho_2)\right) = 0 \quad (3.31)$$

In the OpenFOAM code, these terms are bundled together into a term called `rhoPhi`:

$$\{\rho \vec{u}\} = (\alpha_1 \rho_1 \vec{u} + \alpha_2 \rho_2 \vec{u}) + \left(\alpha_1 \alpha_2 \vec{u}_R (\rho_1 - \rho_2)\right) \tag{3.32}$$

At this point, it is necessary to define phi, which will be denoted by $\Phi = \vec{u} \cdot \vec{A}_f$ in which $\vec{A}_f$ represents the face area vectors. This is because the conservation of cell centered velocity is not guaranteed. Instead, the conservation of cell face fluxes is utilized. Although these terms should be based on the mass flux, this approach would be incompatible with the MULES definition, and so the volumetric flux is used instead (as in the incompressible case). The cell centered velocity is recovered when the divergence schemes are executed, causing the total flux to be summed across all faces and remapped back to the cell center velocity.

It is now possible to discuss the closure term for the relative velocity. The face flux is scaled:

$$\Phi_c = \left| \frac{\Phi}{|\vec{A}_f|} \right| = \left| \frac{\vec{u} \cdot \vec{A}_f}{|\vec{A}_f|} \right| \tag{3.33}$$

from which the scaled face flux is recast as the relative flux:

$$\Phi_R = \Phi_c \frac{(\nabla \alpha_1)_f}{|(\nabla \alpha_1)_f|} \cdot \vec{A}_f \tag{3.34}$$

Therefore, the face flux field becomes filtered to a face field of fluxes along the interfacial normal. Applying a specific scheme to the discretization of this term can then act to further compress the interface. For the purposes of the description in this chapter, the velocity and the face flux are used interchangeably. In practice, they are not the same concept, but the solver schemes act in a way to replace one with the other.

The actual mass continuity equation is:

$$\frac{\partial \rho}{\partial t} + \nabla \cdot \{\rho \Phi\} = 0 \tag{3.35}$$

where $\{\rho \Phi\}$ represents `rhoPhi`.

In solving the momentum equation, the primary difficulties are the nonlinear advection term and the lack of an explicit equation for pressure. One method of solving the problem is to utilize a split set of equations. As mentioned above, this is known as the PISO

algorithm. Using the current values of the velocity and pressure, the momentum equation can be constructed (from equation 3.3):

$$\frac{\partial(\rho\vec{u})}{\partial t} + \nabla \cdot (\{\rho\Phi\}\vec{u}) + \nabla \cdot \tau = \text{Forcing} \tag{3.36}$$

The use of `rhoPhi` eliminates the nonlinear portion of the advection term. The forcing function is comprised of the pressure, interfacial and body forces. Surface tension retains its definition from above (equation 3.4), but the volumetric gravity force and the gradient of pressure are slightly altered. Defining a modified pressure without the hydrostatic component gives:

$$p_{rgh} = P - \rho\vec{g} \cdot \vec{h} \tag{3.37}$$

where p_{rgh} is the pressure without the hydrostatic component, and $\vec{h}$ is the height vector. The forcing function can then be written as:

$$\text{Forcing} = \vec{F}_{ST} - \nabla p_{rgh} - (\vec{g} \cdot \vec{h})\nabla\rho \tag{3.38}$$

The density term is the remainder of the derivative (the density component) once p_{rgh} is substituted. The forcing function is calculated at the current time and the matrix of equations is assembled via equation 3.36 but not necessarily solved (depending on the user). The matrix assumes the linearized form:

$$[C][\vec{u}^*] = [b] \tag{3.39}$$

where $[C]$ is the coefficient matrix, and $[\vec{u}^*]$ is the predicted velocity that would be obtained if the equations were solved (equation 3.36 and 3.38). This represents the momentum equation, although using forcing functions based on the current time designates it a predictor. The matrix $[b]$ represents the source function (or forcing functions):

$$[b] = [r] + \left(-\nabla p_{rgh}^N\right) \tag{3.40}$$

where $[b]$ represents the explicit portions of the constructed equations (old time values in the derivatives, *etc*) and the forcing function evaluated at the current time. The left hand side encompasses:

$$[C][\vec{u}^*] = [A][\vec{u}^*] + [F][\vec{u}^*] \tag{3.41}$$

where the matrices $[A]$ and $[F]$ represent the diagonal component of the matrix and the off-diagonal or flux based component of the matrix, respectively. If the equation is rearranged:

$$[A][\vec{u}^*] + [F][\vec{u}^*] = [r] + \left(-\nabla p_{rgh}^N\right) \tag{3.42}$$

$$[A][\vec{u}^*] = [r] - [F][\vec{u}^*] + \left(-\nabla p_{rgh}^N\right) \tag{3.43}$$

The following matrix can be defined:

$$[H] = [r] - [F][\vec{u}^*] \tag{3.44}$$

Rearranging equation 3.43 gives:

$$[\vec{u}^{**}] = [A]^{-1}[H] - [A]^{-1}\left(\nabla p_{rgh}^N\right) \tag{3.45}$$

where if the equation is solved at this point, $[\vec{u}^{**}]$ represents the corrected velocity field when the solution includes updated values of the pressure and density (which relies on both pressure and temperature). The above equation represents the decoupled version of the equation, from which the pressure equation can be derived upon taking the divergence:

$$\nabla \cdot [\vec{u}^{**}] = \nabla \cdot \left([A]^{-1}[H] - [A]^{-1}\left(\nabla p_{rgh}^N\right)\right) \tag{3.46}$$

For an incompressible solver:

$$\nabla \cdot [\vec{u}^{**}] = \nabla \cdot \left([A]^{-1}[H] - [A]^{-1}\left(\nabla p_{rgh}^N\right)\right) = 0 \tag{3.47}$$

However, for a compressible solver the divergence was defined in equation 3.21. Therefore, the full equation is:

$$\nabla \cdot ([A]^{-1}[H]) - \nabla \cdot \left([A]^{-1}\left(\nabla p_{rgh}^{N+1}\right)\right) = S_1 \left(\frac{1}{\rho_1} - \frac{1}{\rho_2}\right)$$

$$- \frac{\alpha_1}{\rho_1}\left[\frac{\partial \rho_1}{\partial t} + \vec{u}_1 \cdot \nabla \rho_1\right] - \frac{\alpha_2}{\rho_2}\left[\frac{\partial \rho_2}{\partial t} + \vec{u}_2 \cdot \nabla \rho_2\right] \tag{3.49}$$

At this point in the implementation, the equations use the current values of the mixture velocity (phi) to calculate the terms on the right hand side. The equation is called the pressure equation because the sole variable to solve for is p_{rgh}^{N+1}. However, in this case the predicted velocity is used, and the corrected velocity is obtained after the pressure is solved from equation 3.49. This necessitates recalculating the velocity after the pressure is

obtained, until both equations converge simultaneously, and this behaviour defines the PISO loop.

Additionally, the right-hand side is calculated partially explicitly. A correction is applied to the change of density based on the time change of pressure, which is variable solved for in the overall equation. Each phase specific density becomes:

$$\rho_i = \Psi_i p_{rgh} \tag{3.50}$$

where Ψ_i is the compressibility. Note that the derivation necessitates that the mass transfer source for phase 1 be included in the pressure equation.

The algorithm for the new solver, called `compressibleInterFoamHTMT`, is shown in Figure 3.1.

compressibleInterFoamHTMT

Thermo Library

compressibleInterFoam

Additions

Initialize thermophysical models

T, P

Initialize *U, P, T*

Initialize interfacial area and source terms

Initialize mixture models, *Yi* and calculate properties

Link *Yi*

Begin Time Loop

Estimate Planar Area

PISO OUTER

Phase Continuity

Limit to 0.5 Phase Fraction Contour

Momentum Equation

Calculate Source Terms

Update Properties

Energy Equation

PISO INNER

Pressure Equation

Species Equations

End Time?

End

Figure 3.1 Overview of the algorithm used in compressibleInterFoamHTMT.

3.2.3 Utilities

As mentioned above, one of the main advantages of `compressibleInterFoam` is that it does not require interface reconstruction, which increases its computational efficiency. It would therefore seem counter-productive to add an interface reconstruction algorithm to this solver because it would inherently lead to longer solution times. However, as stated above, accurate knowledge of the local interfacial area is required to compute the rates of mass and energy transfer across the interface. Further, knowledge about the location of the interface can be used to define the mass fraction gradient at the interface. Therefore, in this study, the interface was constructed once per time step using a linear approximation (Tryggvason et al., 2011). This strikes a balance between efficiency and speed because it avoids the costly advection and correction steps when solving for the velocity and phase fraction fields, but still permits very accurate interfacial area prediction for energy and mass transfer calculations.

Figure 3.2 shows a generic linear interpretation (a flat plane in three-dimensional space) of a gas-liquid interface in a hexahedral cell. When this interface is parallel to the planes of an axis pair (Figure 3.2(i)), the calculation of the area is simply the cross-sectional area of the cell using the dimensions along those axes. For the case shown in Figure 3.2(ii), where the plane is effectively two-dimensional, the area calculation is simply the length of the line between the two points multiplied by the depth. A truly three-dimensional interface (as shown in Figure 3.2(iii)) requires special procedures.
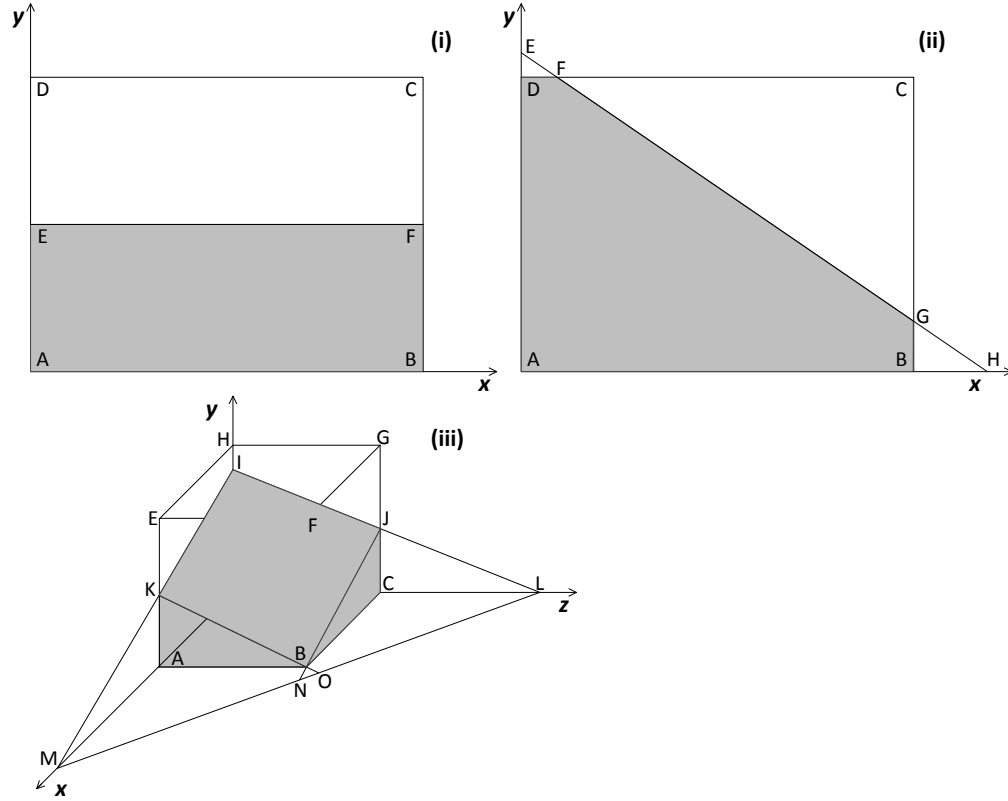
Figure 3.2 The three possible configurations for an area calculation: (i) a one-dimensional plane, (ii) a two-dimensional plane, and (iii) a three-dimensional plane.

In general, any plane can be defined in three dimensions by:

$$\frac{1}{|\nabla\alpha_1|}\left(\frac{\partial\alpha_1}{\partial x}x + \frac{\partial\alpha_1}{\partial y}y + \frac{\partial\alpha_1}{\partial z}z\right) = \zeta \tag{3.51}$$

where ζ is the plane constant. Knowing this equation, the phase fraction in the cells and the gradient of the phase fraction, α, the planar equation can be fixed. The generalized method is described in detail by Tryggvason, Scardovelli and Zaleski (2011). An actual implementation has already been done in the Gerris software (Popinet, 2013).

The above is true only if the cell is oriented such that $\frac{\partial\alpha_1}{\partial x} < \frac{\partial\alpha_1}{\partial y} < \frac{\partial\alpha_1}{\partial z}$, which can be enforced for any cell by considering rotations of the cell. This method is derived for the case of the unit cube, but the result of the area calculation formulations can be extended by using the true cell dimensions. Once known, this plane constant can be used in the

calculation of the interfacial area lying within the cell. The plane location can then also be used to determine the mass fraction gradient at the interface.

If the interface is aligned with a coordinate axis, the one-dimensional area is trivial to calculate. The plane constant corresponds to a perfectly flat plane parallel to one of the axes. In this case, the truncation of the cell is readily computed from knowledge of where the plane intersects the edges of the cell (which corresponds directly to the phase fraction).

The two-dimensional case is only slightly more complex. From Figure 2(ii), the interfacial area depends on the length of the hypotenuse of the triangle AHE, which is then multiplied by the depth. However, whether the entire length of the hypotenuse is used depends on if point E or point H fall outside the cell. Since the two-dimensional case is less complex than the three-dimensional case, it was separated into its own sub routine.

Regardless, the methodology employed in these cases is the same. The first step in the process is to normalize the gradient so it is consistent with the method outlined above. The algorithm then calculates the planar area that is confined to the positive portion of the local coordinate axes (for the 3D case, this corresponds to the area of the triangle ILM). The algorithm finishes by subtracting portions that remain outside the cell boundaries (using the known dimensions). This subtracts the triangles KOM and JLN, and potentially has to add the smaller triangle BNO, which was added twice.

The third step in the algorithm is to determine an accurate approximation of the mass fraction gradient at the interface. Figure 3.3 summarizes the method used to estimate the mass fraction gradient. Although the drawing shows a two-dimensional interface, the three-dimensional calculations follow the same general procedure. Following reconstruction, the location of the interface is known and it is possible to modify the gradient calculation using the known distances and estimated interfacial location constructed by the planar equation above. This method was used successfully by Schlottke and Weigand (2008), and also in several other studies. The gradient shown in Figure 3.3 would be given by:

$$\nabla Y = \langle \frac{Y_{i+1,j} - Y_{int}}{\Delta x + \Delta x_{corr}}, \frac{Y_{i,j+1} - Y_{int}}{\Delta y + \Delta y_{corr}}, 0 \rangle \qquad (3.52)$$

A similar relationship can be derived in the three-dimensional case.

47

Currently, the utilities are constructed for use with structured, hexahedral meshes. Further extensions would need to be made to allow for tetrahedral or polyhedral mesh types. However, the computations for these types of cells are not as straightforward. Therefore, since the primary purpose of this chapter was to test the mass and energy transfer portions of the algorithm, the methods were not extended to these types of cells.
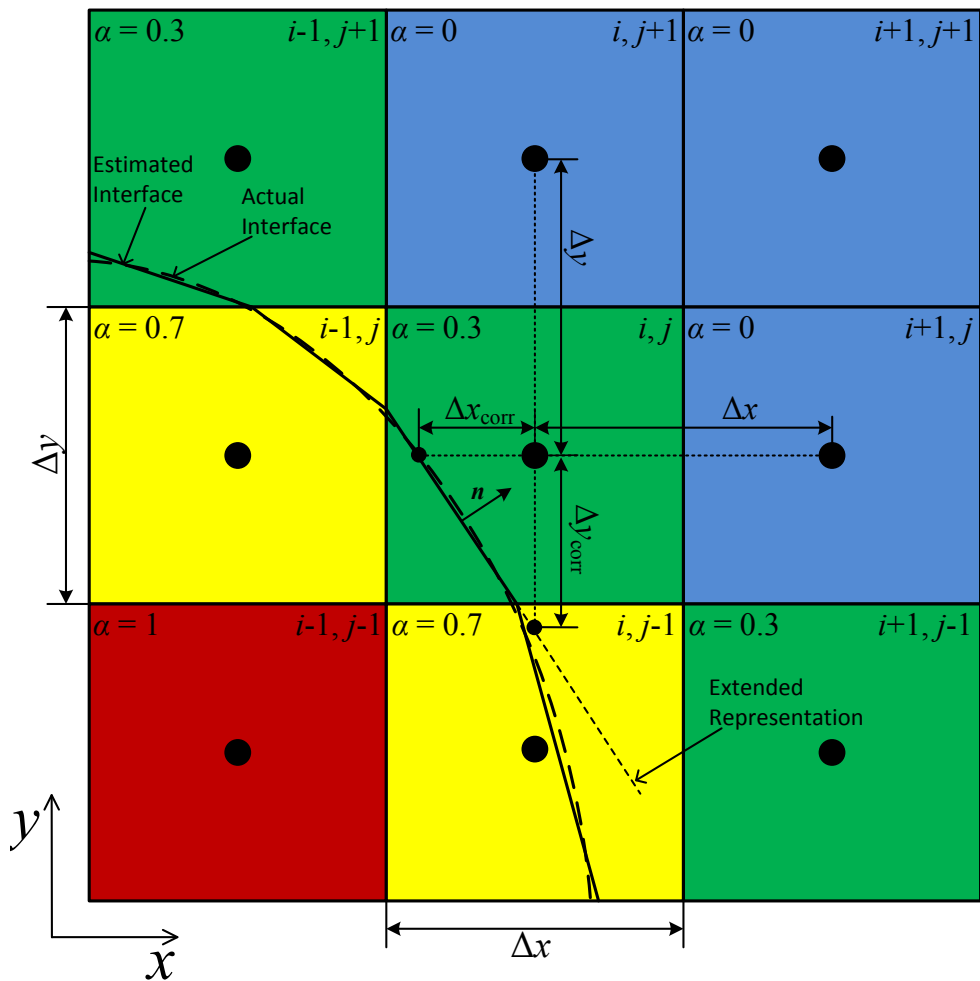
Figure 3.3 Conceptual diagram showing the piecewise linear construction of the interface and points used to approximate the mass fraction gradient.

3.3 Validation

Three test cases were used to validate the newly developed solver. The first validation case involved evaporation of a volatile liquid and diffusion in a Stefan tube. This case was convenient to ensure that coupling between the species and energy equations was appropriate, and that the interface jump conditions had been incorporated appropriately as source terms. The second validation case simulated the evaporation of a droplet suspended in microgravity. The main purpose of this case was to ensure that the interface reconstruction algorithm predicted the correct interfacial area to represent uniform mass transfer in three dimensions. The final validation case involved the simulation of a shrinking droplet. This test case is strongly linked to practical applications, such as droplet evaporation or bubble dissolution, and was convenient to validate total mass loss rate predictions.

The properties for the test were computed using OpenFOAM's built-in thermophysical library, and some of the properties were held constant at their average value. The density of liquid water was chosen to be constant, although this did not impact the first two validations as they were stationary. For the gas phase, the density was calculated from the ideal gas law, and it is therefore pressure, temperature and composition dependent. The properties are shown in tables 3.1 through 3.3.

Table 3.1 Properties of Liquid Water

Property	Value	Reference
Density, ρ (kg/m^3)	1000	-
Specific Heat Capacity, c_p (J/kg/K)	4200	Smith, Ness and Abbot, 2005
Dynamic Viscosity, μ (Pa s)	0.001	Yaws (2003)
Prandtl Number, Pr (-)	6.2	Yaws (2009)

Table 3.2 Properties of Air

Property	Value	Reference
Density, ρ (kg/m^3)	Ideal Gas Law	-
Specific Heat Capacity, c_p (J/kg/K)	1010	Smith, Ness and Abbot, 2005
Dynamic Viscosity, μ (Pa s)	1.5×10^{-5}	Yaws (2003)
Prandtl Number, Pr (-)	0.52	Yaws (2009)

Table 3.3 Properties of Water Vapour

Property	Value	Reference
Density, ρ (kg/m^3)	Ideal Gas Law	-
Specific Heat Capacity, c_p (J/kg/K)	1880	Smith, Ness and Abbot, 2005
Dynamic Viscosity, μ (Pa s)	1×10^{-5}	Yaws (2003)
Prandtl Number, Pr (-)	0.88	Yaws (2009)
Diffusion Coefficient, $D_{2,wM}$ (m^2/s)	$3.28 \times 10^{-5} \left(\dfrac{T}{350}\right)^{1.5}$	Incorpera, DeWitt, Berman and Lavine (2007)
Latent Heat of Vaporization, ΔH_{vap} (J/kg)	$5.2053 \times 10^7 \times 1/18 \times (1 - T_r)^{0.3199 - 0.212T + 0.25795T^2}$	Perry and Green (1997)
Saturation Pressure, P^{sat} (Pa)	$\exp\left(73.649 - \dfrac{7258.2}{T} - 7.3037\ln(T) + 4.1653 \times 10^{-6}T^2\right)$	Perry and Green (1997)

3.3.1 Stefan Tube

The geometry and boundary conditions are shown in Figure 3.4. The geometry measured 10 cm × 1 cm × 0.01 cm, and was assumed to be half full of water. The case was one-dimensional, and therefore the domain was divided into 150 uniformly sized cells in the vertical direction. The top and bottom boundaries were maintained at 350 K. The top boundary was assumed to be swept with air, and therefore the water vapour mass fraction was set to zero at this boundary.

Two key metrics were used to test the performance of the solver. First, the ability of the solver to predict the steady-state water vapour concentration profile in the tube was confirmed. Second, its ability to calculate the correct interfacial temperature at steady state was established. For the analytical solution, the temperature dependence of the properties over the temperature change 15 K were neglected. For steady-state conduction with constant boundary conditions and a known interface temperature, the energy balance and boundary conditions are:

$$\frac{d^2T}{dz^2} = 0, \ T|_{z=z_{int}} = T_{int}, \ T|_{z=z_{edge}} = T_{edge} \tag{3.53}$$

where T is the temperature and z is the spatial coordinate for the height. The subscript *edge* refers to the upper and lower boundaries, while *int* refers to the interface. Solving this equation with the boundary conditions yields the following equation for both sides of the interface:

$$T = \frac{T_{edge}-T_{int}}{z_{edge}-z_{int}}(z - z_{int}) + T_{int} \tag{3.54}$$

The species equation has a similar form to the energy equation. Therefore, the mass fraction profiles are given by:

$$Y = \frac{Y_{edge}-Y_{int}}{z_{edge}-z_{int}}(z - z_{int}) + Y_{int} \tag{3.55}$$

where in this case, Y refers to the mass fraction of water vapour in the gas. The remaining stipulation is that the interfacial temperature must provide a balance between heat transfer to the interface by conduction and the latent heat of vaporization. Thus,

$$-k_2 \left(\frac{dT}{dz}\right)_{z=z_{int}} = -k_1 \left(\frac{dT}{dz}\right)_{z=z_{int}} + S_E \tag{3.56}$$

where S_E is the energy source as prescribed in equation 3.13. To arrive at the final temperature, the value of the interfacial temperature was guessed, and the profiles were calculated from the above equations. The interfacial temperature was then varied until the expression in equation 3.56 was balanced.
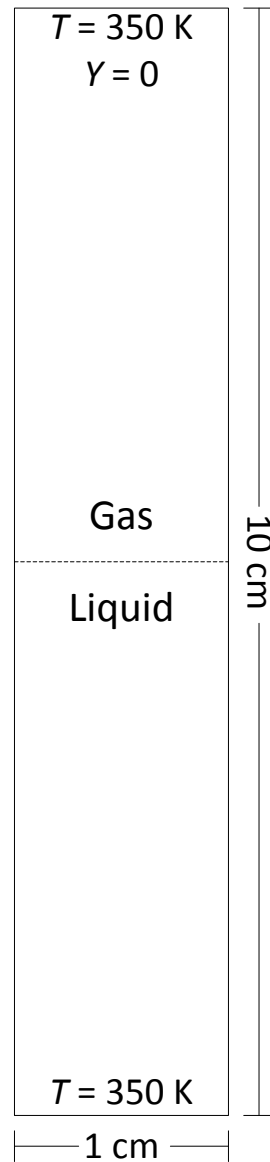
Figure 3.4 Case geometry for the Stefan tube, showing the boundary conditions adjacent to the appropriate boundaries.

The case was allowed to reach steady state over 25 000 s. The mass fraction contours as well as the temperature contours are shown in Figure 3.5. Given that the case is one dimensional, with fixed conditions at the boundaries, the only time dependent factors are the diffusion, conduction and the energy balance at the interface. The interfacial temperature is shown to be just below 334 K, and the interfacial water vapour mass fraction is approximately 0.137.

As expected, the water vapour mass fraction and temperature profiles are linear in each phase at steady state. Moreover, they compare well to the analytical solution despite using constant properties for the analytical solution. The impact of temperature and composition on density seem to be negligible for this case. The results indicate that the implementation of the immersed boundary conditions in the new solver are appropriate. Figures 3.6 and 3.7 show a comparison between the analytical an numerical predictions for the water vapour mass fraction and temperature profiles.
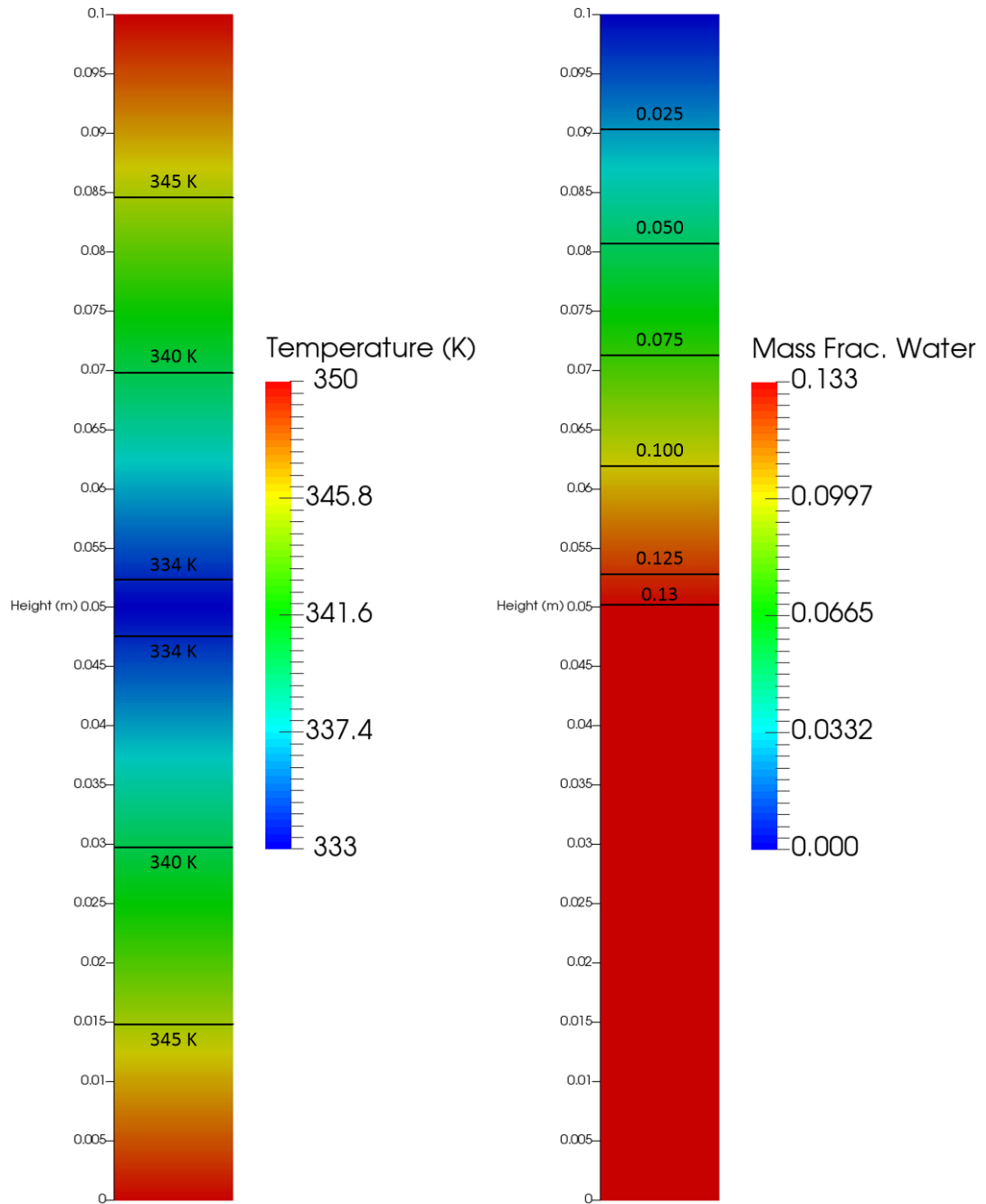
Figure 3.5 Temperature (left) and water vapour mass fraction (right) contours for the Stefan tube case using `compressibleInterFoamHTMT`.
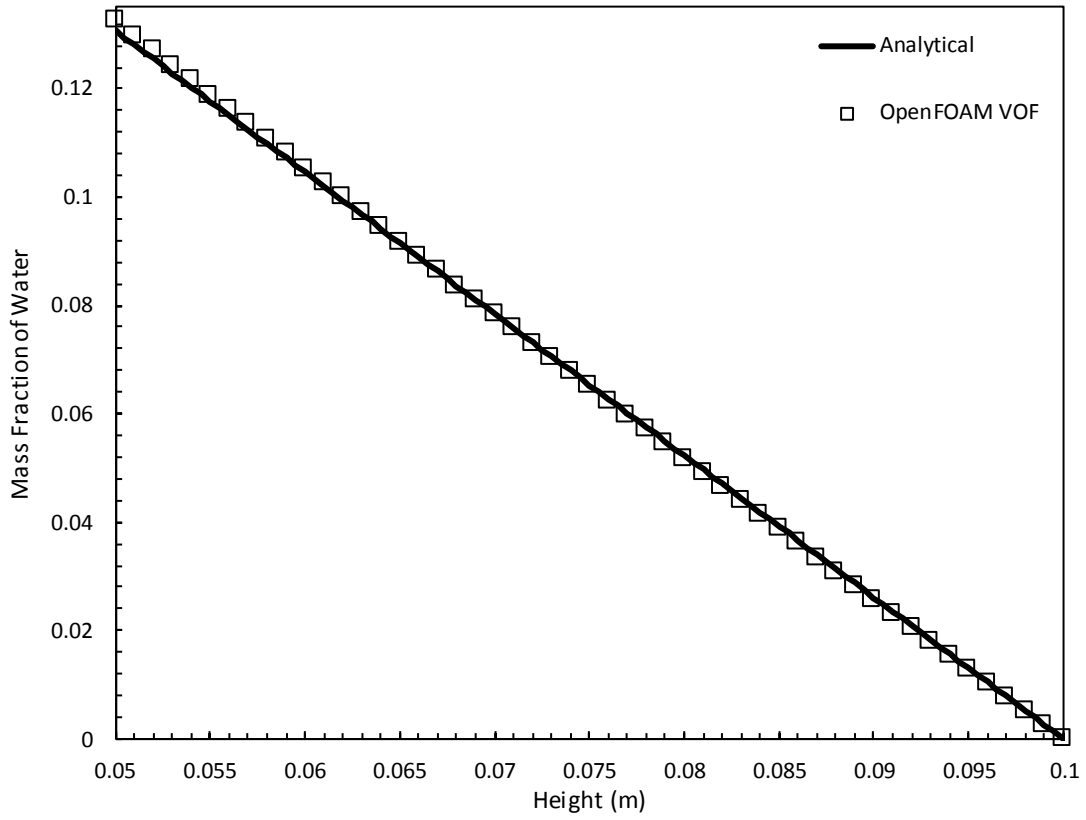
Figure 3.6 Steady-state water vapour mass fraction profile for the Stefan tube case, showing the comparison between the analytical solution and the results from `compressibleInterFoamHTMT`.
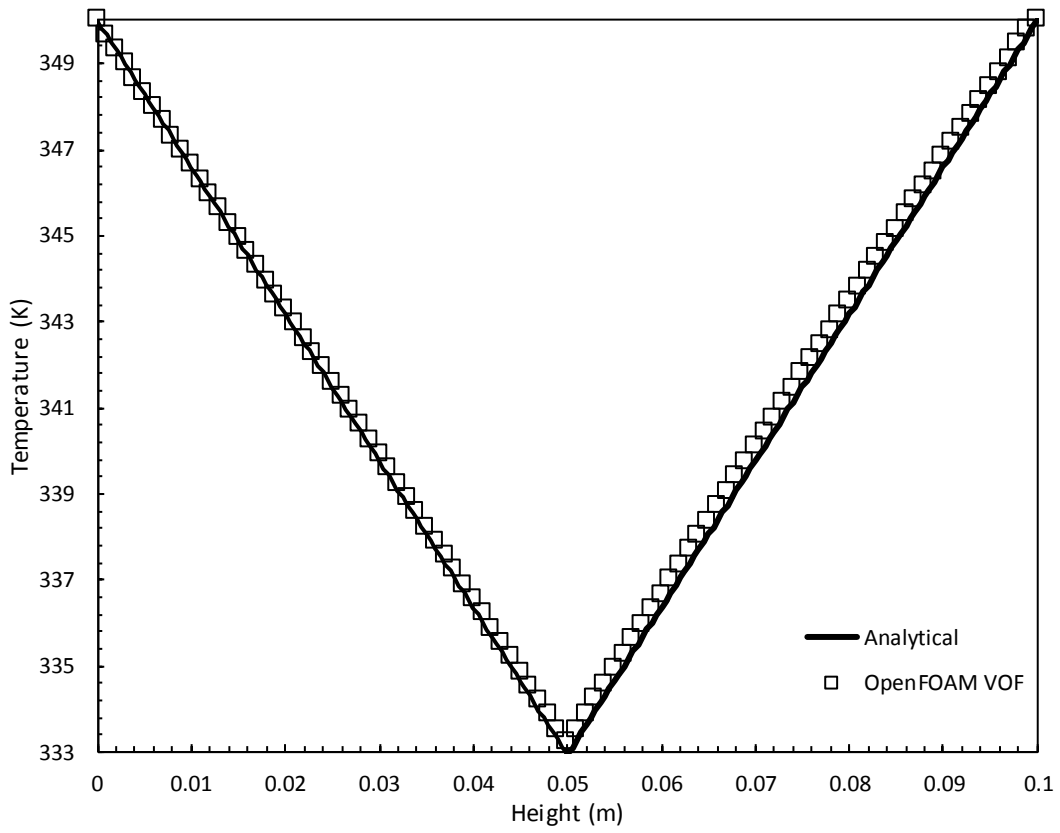
Figure 3.7 Steady-state temperature profile for the Stefan tube case, showing the comparison between the analytical solution and the results from `compressibleInterFoamHTMT`.

3.3.2 Droplet in Microgravity

The geometry and boundary conditions are shown in Figure 3.8. The water droplet was 2 mm in diameter and suspended in a dry air environment. The case was modeled using one eighth of the geometry due to symmetry, with a computational domain that measured 3 mm × 3 mm × 3 mm. The case was initialized by setting the liquid phase fraction to unity in cells within the sphere's radius. The simulation was then run without heat or mass transfer until the phase fraction stabilized. Finally, the resulting phase fraction field was used to for the simulations. Mesh independence was performed, and it was deemed that a mesh of size 57 × 57 × 57 cells was appropriate. The volumetric source in the phase continuity equation was turned off to generate a stable interfacial location and to prevent the droplet from shrinking (refer to the next section for the shrinking droplet simulation results).

The analytical solution was derived similarly to the Stefan tube problem. At steady-state, the energy equation reduces to:

$$\frac{1}{r^2}\frac{d}{dr}\left(r^2 K \frac{dT}{dr}\right) = 0, \; T|_{r=r_{int}} = T_{int} \, , \; T|_{r=r_{far}} = T_{far} \tag{3.57}$$

which yields a solution of the form:

$$T = T_{int} + \frac{T_{far}-T_{int}}{\frac{1}{r_{int}}-\frac{1}{r_{far}}}\left(\frac{1}{r_{int}} - \frac{1}{r}\right) \tag{3.58}$$

The species equation has an analogous form to the energy equation, giving the following mass fraction profile:

$$Y = Y_{int} + \frac{Y_{far}-Y_{int}}{\frac{1}{r_{int}}-\frac{1}{r_{far}}}\left(\frac{1}{r_{int}} - \frac{1}{r}\right) \tag{3.59}$$

The case reached steady state after approximately 150 s. The water vapour mass fraction contours as well as the temperature contours are shown in Figure 3.9 and Figure 3.10, respectively. Since no heat was supplied from within the droplet, the interfacial mass fraction decreased as the sphere cooled. For comparison, Figure 3.11 and Figure 3.12 show the steady state profiles for the water vapour mass fraction and the temperature, respectively. The final mass fraction and temperature profiles resulted in a sphere temperature of approximately 300 K, despite the ambient gas temperature at 350 K.

In this scenario, the liquid side is assumed to be at the interfacial temperature. For the energy balance, the liquid side does not contribute any additional, and so energy must be provided by the gas. As shown in the results in Figure 3.12, this causes a reduction of the temperature of the droplet to the low value of approximately 300 K.
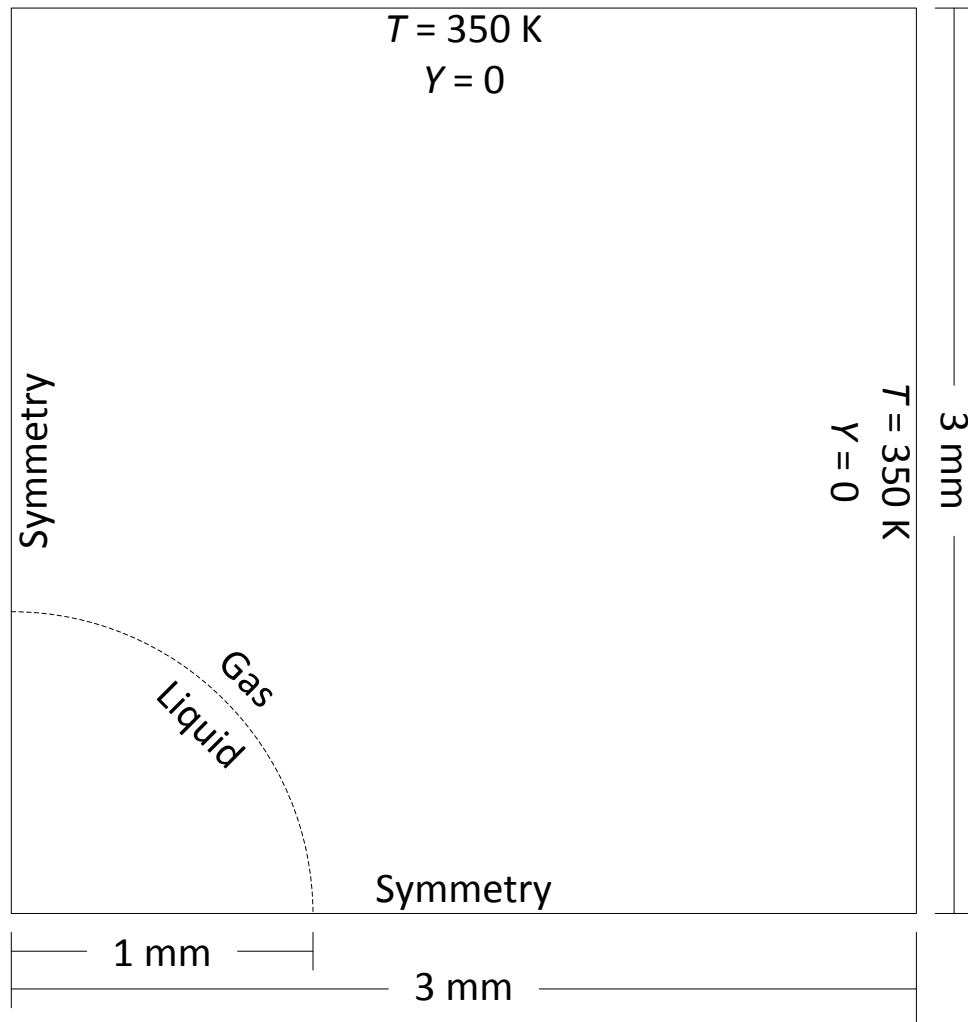
Figure 3.8 Geometry for the suspended evaporating droplet case, showing the boundary conditions adjacent to the appropriate boundaries.
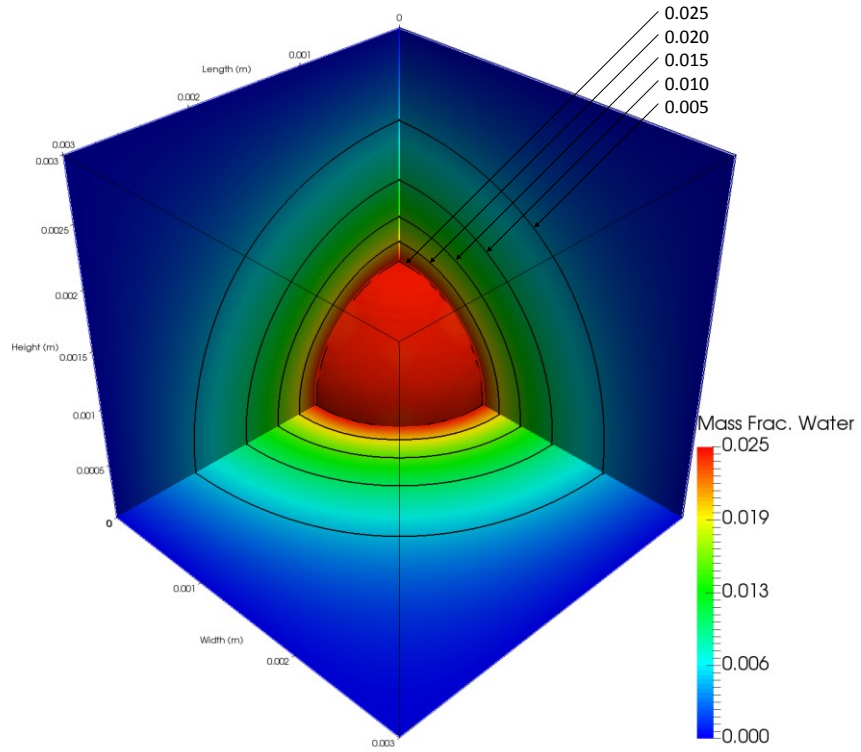
Figure 3.9 Steady-state water vapour mass fraction contour plot for the suspended evaporating droplet case.
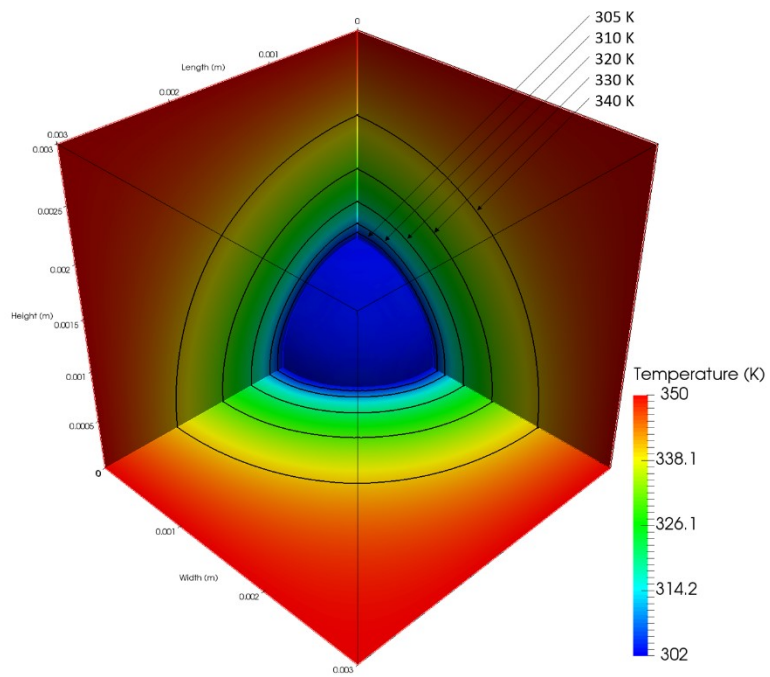
Figure 3.10 Steady-state temperature plot for the suspended evaporating droplet case.
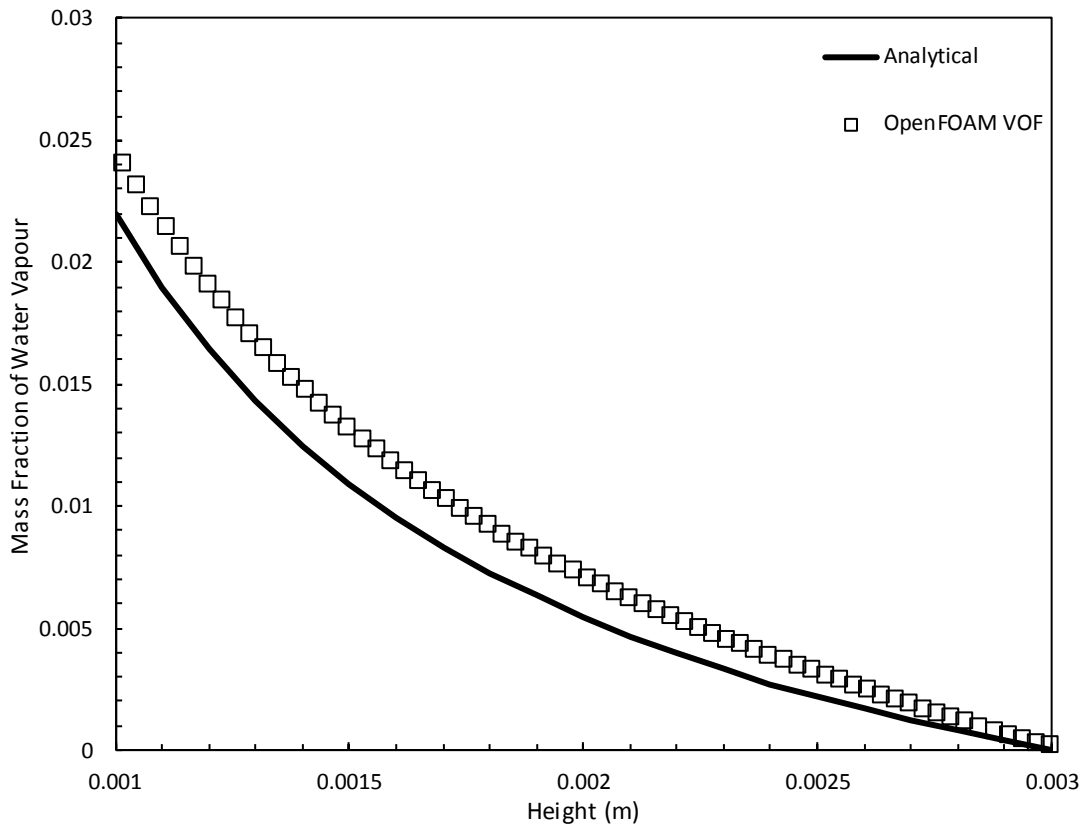
Figure 3.11 Steady-state water vapour mass fraction profile for the suspended droplet case showing a comparison to the analytical solution.
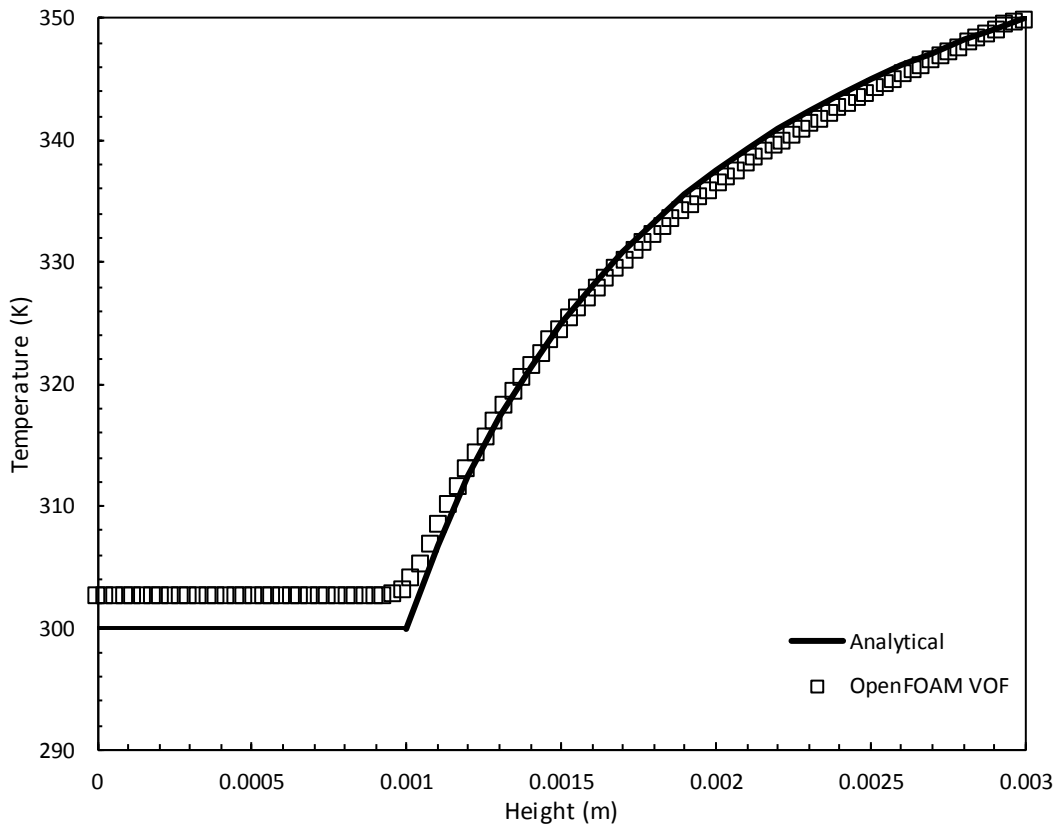
Figure 3.12 Steady-state temperature profile for the suspended droplet case showing a comparison to the analytical solution.

The profiles above have the correct and distinctive shape for spherical heat and mass transfer. Due to a lack of energy supplied from within the droplet, the mass transfer rate at steady state is quite low. Since the volumetric phase continuity source was turned off, the interface position did not change with time. The steady temperature reached in the simulation was approximately 2 degrees higher than in the analytical solution, the mass transfer profiles show a small difference. In the analytical case, the final temperature does not depend on averaged values. However, for the VOF solver, the averaged interfacial values provided a different set of immersed boundary conditions. In reality, the droplet should have shrunk long before reaching these steady state values.

Again, the fact that the properties were held constant in the analytical solution barely impacted the result. Additionally, the effects of variable density in the gas phase seemed negligible in the development of the water vapour mass fraction and temperature profiles.

Although the water vapour mass fraction and temperature profiles were taken along the edge of the domain, there was a negligible effect on the solution despite simulating the droplet in a box.

Further study must be done with a moving interface that results from interphase heat and mass transfer. In this case, the motion of the droplet interface will be governed in part by the balancing of the pressure both inside and outside the surface.

3.3.3 Shrinking Droplet

The geometry and boundary conditions for the final case are shown in Figure 3.8. The initial conditions for this case were identical to the suspended droplet. The key difference for this case was the removal of the energy balance, allowing for computational validation of the analytical solution of the shrinking sphere at a constant mass transfer rate. As shown in the analytical solutions above, the mass transfer flux is constant at a given temperature, regardless of radius. Therefore, the size of the droplet can be tracked analytically, and the corresponding mass fraction profile can be obtained from the application of the derived equation from the previous section. Due to the small geometry, the analytical solution from above can be used to develop the steady state profile at each time. The flux at the interface can then be used to calculate the shrinkage rate and therefore the new volume. From this new volume, the radius was calculated. Therefore, the solution procedure was equivalent to an analytical solution stepped forward in time by Euler's method. The governing equation for the water vapour mass fraction profile is given by equation 3.59.

Without a changing temperature, the water vapour mass fraction profile developed quickly relative to the interface shrinkage rate. Under these simplifying conditions, the derivative of the above equation 3.59 provides an approximation of the mass transfer rate at a given time:

$$\frac{dY}{dr} = \frac{Y_{far} - Y_{int}}{\frac{1}{r_{int}} - \frac{1}{r_{far}}} \left(\frac{1}{r^2}\right) \tag{3.60}$$

With this knowledge, the mass source, S_M, can be calculated as:

$$S_M = \rho_2 D_{2,wM} A_{int} \frac{dY}{dr} \tag{3.61}$$

where A_{int} is the current interfacial area of the droplet. The volumetric source, $\dot{V}_{int}$, can be calculated directly from:

$$\dot{V}_{int} = D_{2,wM} A_{int} \frac{dY}{dr} \tag{3.62}$$

The new volume of the droplet is calculated from Euler's method:

$$V_{new} = V_{old} + \dot{V}_{int} \Delta t \tag{3.63}$$

The new radius can then be calculated from the new volume. The case was run at 340 K, and the density of the liquid (dense) phase was arbitrarily set to 10 kg/m³ to speed up the solution. Although this change in density meant that the case no longer represented two real fluids, the change does not impact the validation procedure. Due to the shift in density, the time step had to be carefully controlled to prevent artificially high velocities at the interface due to the rapid velocity at which the interface shrank. The initial mass transfer forced the temperature to decrease to 322 K (from the original 340 K), before stabilizing and continuing. This effect ended approximately 0.3 s into the simulation, when the radius of the droplet was 0.85 mm. This condition was therefore used as the start of the figures that follow as well as the analytical solution. Figure 3.13 shows the movement of the outer boundary of the droplet over time, while Figure 3.14 shows the plot of radius against time when compared to the analytical solution.
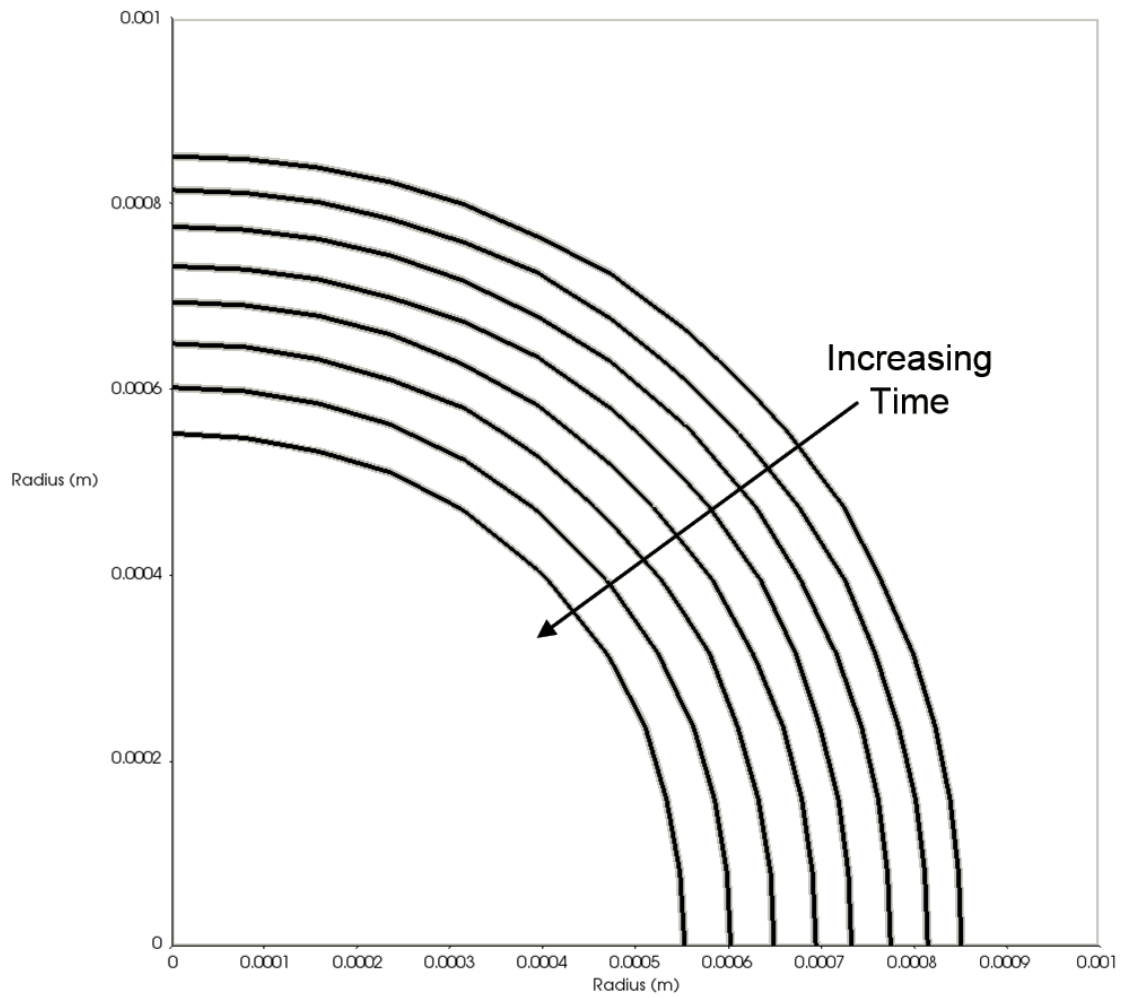
Figure 3.13 Radius of the shrinking droplet over time. The initial radius shown corresponds to where the simulation achieved a steady rate of droplet shrinkage.

64
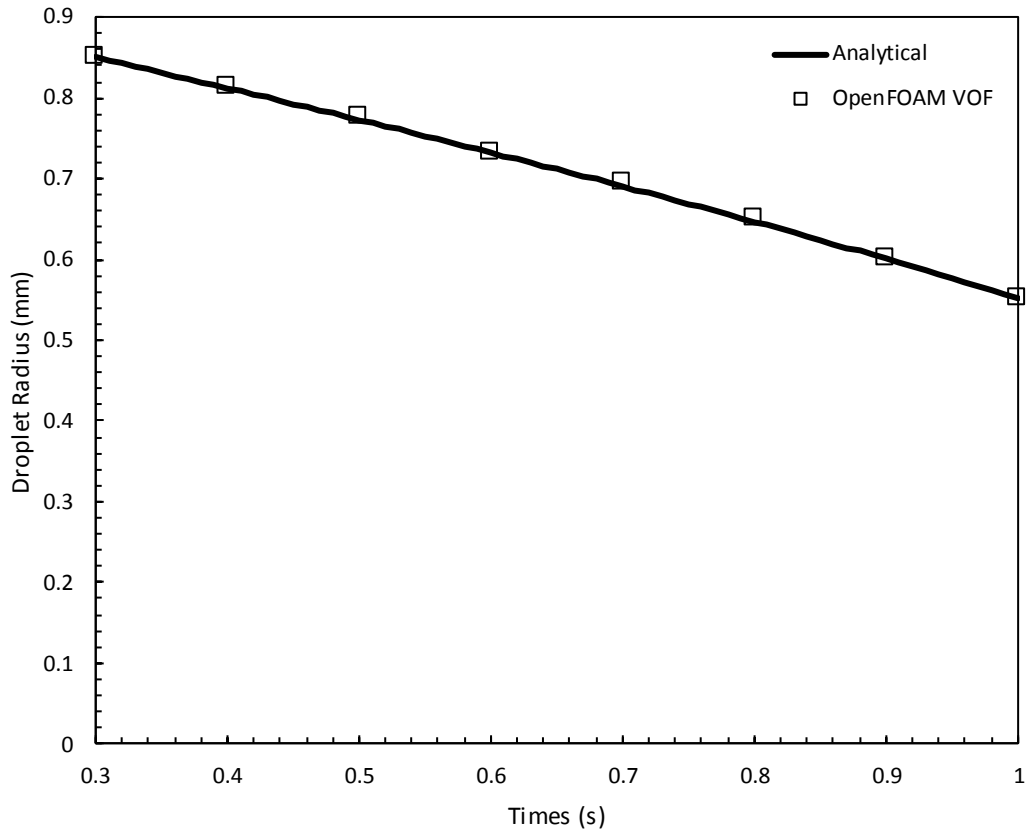
Figure 3.14 Variation of radius with time for the interval after the temperature stabilized to one second.

The droplet shrinkage rate was relatively constant. This was due to the short time over which the water vapour could diffuse. The size of the droplet and domain meant that the time to reach steady state was shorter than the time for the droplet to shrink appreciably. These conditions were chosen to satisfy the assumption upon which the analytical model was based.

3.4   Conclusions

A compressible VOF solver was developed to simulate interphase heat and mass transfer. Immersed boundary conditions for interphase heat and mass transfer were added through interfacial area approximation and estimation of mass fraction gradients.

Three validation cases were used to test the solver. The one-dimensional Stefan tube case provided insight into the ability of the new solver to handle interphase heat and mass

transfer under simplified condition. When compared to the analytical profiles of water vapour mass fraction and temperature, the new solver performed well and achieved similar results. Therefore, the underlying interfacial composition model, mass balance and energy balance were working.

The three-dimensional test of the solver using a droplet suspended in negligible gravity was used to test the capacity of the algorithm to determine the interfacial area. In this case, the interface was held stationary while the mass fraction and temperature profiles developed. The model predicted mass fraction and temperature profiles reasonably well when compared to analytical results. The density effects were again negligible.

The final and most crucial test was carried out on a droplet with a shrinking interface. The purpose of this test was to simulate the droplet shrinkage at a nearly constant temperature. The droplet used in the microgravity case was reused, but instead of maintaining a constant diameter (no phase fraction source), the temperaturewas held constant and the phase fraction was allowed to vary with the mass transfer rate. This simplification made the analytical solution easier to implement, as the water vapour mass fraction profile was quick to reach steady state. The overall prediction of diameter change over time compared well with the analytical solution, and the model accurately captured the uniform shrinkage of the droplet. The importance of this result is that the interface location can therefore be predicted and tracked as it deforms due to the interphase mass transfer.

Moving forward, the primary knowledge gained through this study was the ability to appropriately introduce the source terms due to interphase heat and mass transfer into a VOF framework. Regardless of how the mass transfer coefficients and interfacial area are calculated, the required structure of the solver will remain the same, providing a foundation upon which further modifications can be built. The novelty of this type of model will be in how it is attached to a dispersed phase model for the plume.

Chapter 4

Simulation of Compressible Underwater Gas Jets using an Interface Tracking Method

4.1 Introduction

Multiphase gas-liquid systems are commonly studied by scientists and engineers due to the large number of industrial and natural systems that involve these types of flows. In the process industries, the accurate prediction of two-phase fluid dynamics is of utmost importance in the design of multiphase reactors and separation systems. In many of these systems, it is not possible to make good predictions of their efficiency until the fluid dynamic behaviour is well characterized. The ability to study local flow phenomena through numerical simulation has rapidly increased with the rise of high performance computing. For this reason, multiphase computational fluid dynamics (CFD) is an area that is under rapid development. However, despite significant progress, much work remains to be done to expand the applicability of the available models to a wider range of complex situations.

Since multiphase flows can include a vast number of flow regimes, many different models have been used to simulate different types of phenomena. For highly dispersed flows, such as those in bubble columns (Laín et al., 2002; Li et al., 2009; Yang et al., 2011; Xiao et al., 2013; Li and Zhong, 2015; Bhusare et al., 2017), fluidized beds (Loha et al., 2013; Zhao et al., 2013; Adamczyk et al., 2014; Almohammed et al., 2014; Hou et al., 2017) and many others (Hamidipour et al., 2013; Dapelo et al., 2015; Messa et al., 2015), achieving sufficient mesh resolution to track the motion and deformation of individual particles is usually not possible in large systems. Two types of methods are commonly used in multiphase CFD to simulate dispersed flows: (i) the Euler-Euler (E-E) method, and (ii) Lagrangian particle tracking (LPT). In the E-E method, the conservation equations are phase or ensemble averaged and solved on an Eulerian grid. Effectively, this implies that the phases move independently until closure terms are added to couple their motion. In LPT, the conservation equations are solved on an Eulerian grid for the continuous phase,

while the motion of the dispersed phase(s) is resolved by solving Newton's second law of motion for individual particles or groups of particles. Again, coupling between the continuous and dispersed phases requires additional closure terms, which are usually based on empirical relationships. Both E-E and LPT facilitate the use of coarse meshes because the closure laws already model aspects of the flow that are smaller in scale than the mesh cells. However, one of the challenges in this approach is that it can be unclear how to balance the mesh resolution studies to maintain numerical accuracy with the limitation that the closure laws are normally only valid when the particles are actually dispersed in (i.e. smaller than) a cell (Badreddine et al., 2015). Another problem is that the closure relationships often change when there is a flow regime change because they were only derived for a limited range of conditions (Lahey et al., 2005). It would therefore be beneficial to develop closure laws and/or new multiscale methods that would permit the application of these models to problems where conventional closure relationships break down.

Closure relationships for interfacial forces in E-E and LPT models, such as drag, lift, turbulent dispersion, have been reviewed and tested for different cases by many authors (Pan et al., 2016; Fletcher et al., 2017). Many studies have demonstrated good predictions when applying E-E and LPT methods to a wide variety of cases. For example, Hamidipour et al. (2013) used an E-E framework to predict liquid holdup for a kerosene-air, cocurrently fed extraction column with glass bead internals. Li and Zhong (2015) used a three phase Eulerian multi-fluid model for three phase systems involving solids. Panneerselvam et al. (2008) also applied a three-fluid model, for the use of suspended gas and solid particles in an agitated reaction vessel for the study of impeller design. Different regimes, such as churn flow and annular flow, have been studied by Parsi et al. (2016). In gas-liquid flows, bubble columns are one particularly commonly studied system, and many authors have shown good correlation between experimental measurements and model predictions using E-E (Michta et al., 2012; Xiao et al., 2013; Li and Zhong, 2015; Rzehak and Krepper, 2016; Bhusare et al., 2017) and LPT methods (Laín et al., 2002; Dapelo et al., 2015). Another commonly studied system are so-called gas-stirred ladles or gas sparging into large tanks (and/or unconfined reservoirs). Several authors have demonstrated good agreement between experimental data and model predictions for such systems using both E-E (Dhotre

et al., 2007; Dhotre et al., 2009; Lou and Zhu, 2013) and LPT (Hu and Celik, 2008; Olsen and Skjetne, 2016). To make E-E and LPT methods more robust, population balance models (PBM) can be included, especially in large plumes where bubbles cannot be produced at uniform diameter.

Given some of the limitations associated with conventional use of E-E and LPT methods, there has recently been interest in methods for direct numerical simulation (DNS) and large-eddy simulation (LES). In practice, however, it is unlikely that DNS would be possible for the full domain except for very simple geometries and flow regimes (Pan et al., 2016). Therefore, multiscale methods, which use scalable closure laws and/or combine various modeling approaches, are necessary to overcome some of the current limitations. LPT models are most convenient for DNS and LES when particles are already present in a dispersed flow (Ström et al., 2016). For DNS of situations that involve the transition from segregated flow to dispersed flow (e.g., liquid jet atomization or gas jet breakup), interface tracking/capturing methods can be used to resolve particles down to the grid scale and LPT can be used below the grid scale (Jain et al., 2014; Grosshans et al., 2016; Ström et al., 2016). Of course, when models are combined into a multiscale approach, normally only some of the regions of the flow are directly resolved and others include sub-grid scale models. Common tools for resolving interface dynamics in multiphase flows include, but are not limited to, interface tracking methods such as front-tracking (FT), and interface capturing methods such as volume-of-fluid (VOF) and level-set (LS). These methods allow capturing of deforming interfaces and, with the appropriate algorithm, they can model the dynamic breakup and coalescence within multiphase flows. This study is focuses on investigating the mesh resolution limitations when VOF method is used to study gas jet motion and breakup. Therefore, the remainder of this introduction only provides a brief overview of some relevant applications of the VOF method.

Relative to other interface tracking/capturing approaches, the major strength of VOF is its mass conserving formulation and its capacity to naturally handle break-up and coalescence. De Schepper et al. (2008) applied the VOF method for stratified, wavy, plug, annular, bubbly and slug flow in horizontal tubes. As shown in their results, bubbly flow relies on the ability of the bubbles to be resolved on the grid scale, otherwise accurate interfacial

area estimations cannot be established. Saad et al. (2014) showed a similar case, but for different flow regimes in a heat exchanger. The ability of VOF methods to predict fluid interfaces at a variety of scales showcases its applicability to a wide set of practical applications. However, although the method can model flows with small particles such as bubbly flows, computational demand can be very high.

Du et al. (2017) used the VOF method to predict the hydrodynamics of packed reactor columns. Shi et al. (2013) applied VOF similarly but in rotating packed beds. Since various flow patterns can exist simultaneously, macroscale analysis may be insufficient, and this is a niche CFD can fill through case studies and numerical experimentation. However, this is true even for two-fluid domains.

For instance, as in the study by De Schepper et al. (2008), the transitions from wavy flow to bubbly flow might occur rapidly in the same simulation. The transition from slug flow to dispersed flow may also rapidly occur. In a sloshing tank, the interface will undergo several deformations, spanning multiple length scales. Although they used a 7 m tube with an 8 cm diameter, over 500,000 cells were used to model the domain. In practice, it may not be possible to uniformly resolve the domain and depending on the flow regime the same resolution may not always be adequate. He et al. (2017) have recently used VOF to track flow patterns in solid packing, as a continuation of the work by Du et al. (2017). In this case, the VOF method was used to model the interactions of the fluid at the level of the solid packing, this is particularly useful in predicting wetting characteristics in such reactors.

The VOF method can also be applied to a wider range of macroscopic applications, such as fluid jets. The work of Ménard et al. (2007) focuses on liquid sprays, and VOF is used to resolve the momentum length of liquid jets breaking up in gas. VOF was coupled to LS for better accuracy in predicting the surface curvature and hence the break-up mechanics, while the VOF algorithm provides lower resolution mass conservation. However, their model was only tested, not validated against experimental data. Xiao et al. (2016) performed a liquid jet atomization study with supersonic air crossflow. Kinzel et al. (2017) used VOF to predict the behaviour of cavitating flows during gas ventilation, using a

refined mesh in the wake to capture bulk fluid dynamics. In this situation, predicting the deformations of the resulting gas jet over time is important to cavity size and entrainment characteristics. In the nuclear sector, direct contact steam condensation is important for cooling and heating. Direct-contact condensation was explored by Li et al. (2015) as well as Yang et al. (2017) and Zhang et al. (2017) using a VOF methodology, where the jet shape depended on the liquid temperature and mass flux, as well as plume shape (oscillatory jet, steam chugging and oscillatory bubble). Prediction of the momentum length and breakup regions are important to the underlying mechanics (heat and mass transfer). The wide range of applications means that new solvers and models require validation for each use.

The primary objective of this chapter is to study mesh resolution limitations when a compressible volume-of-fluid methodology is used to simulate gas jet injection into a liquid. The goals are to identify the quality of macroscopic fluid dynamic predictions (e.g. jet length and trajectory), and how these relate to the loss of small-scale resolution (i.e. sub-grid parcels of gas). Ultimately, it is hoped that the study will provide more insight to further advance multiscale modeling approaches for gas jet breakup simulations. For this work, the compressible VOF solver available in the open source CFD toolbox, OpenFOAM (The OpenFOAM Foundation, 2018) was used. To test the solver within the general objective, simulations were performed for the injection of a horizontal air jet into water, and the results were compared to published experimental data. The emphasis was placed on the ability of the solver to predict the momentum length and the breakup mechanics of the jet. Within the context of this objective, it was important to examine the mesh resolution threshold at which the interface can be captured.

4.2 Methodology

The compressible VOF solver, `compressibleInterFoam`, available in OpenFOAM (The OpenFOAM Foundation, 2018) was used in this study. An overview of the algorithm used by this solver was already presented in Chapter 3. Therefore, only a brief summary of the main equations and algorithms will be presented here.

The continuity equation is:

$$\frac{\partial \rho}{\partial t} + \nabla \cdot (\rho \vec{u}) = 0 \tag{4.1}$$

where $\rho = \sum_i \alpha_i \rho_i$ is the mixture density, α_i is the phase fraction of phase i, and $\vec{u} = \sum_i \alpha_i \vec{u}_i$ is the velocity of the mixture. The phase continuity equation is rearranged to solve for one of the phase fractions:

$$\frac{\partial \alpha_1}{\partial t} + \nabla \cdot (\alpha_1 \vec{u}) + \nabla \cdot (\alpha_1 \alpha_2 \vec{u}_R) = -\frac{\alpha_1 \alpha_2}{\rho_1} \left[\frac{\partial \rho_1}{\partial t} + \vec{u}_1 \cdot \nabla \rho_1 \right] +$$
$$\frac{\alpha_1 \alpha_2}{\rho_2} \left[\frac{\partial \rho_2}{\partial t} + \vec{u}_2 \cdot \nabla \rho_2 \right] + \alpha_1 \nabla \cdot \vec{u} \tag{4.2}$$

where $\vec{u}_R = \vec{u}_1 - \vec{u}_2$ represents the relative velocity. The volume-averaged momentum equation is:

$$\frac{\partial (\rho \vec{u})}{\partial t} + \nabla \cdot (\rho \vec{u} \vec{u}) + \nabla \cdot \tau = -\nabla P + \rho \vec{g} + \vec{F}_{ST} \tag{4.3}$$

where τ is the viscous stress tensor, P is the pressure field, $\vec{g}$ is the gravity vector, and $\vec{F}_{ST}$ is the surface tension force which is calculated by the method of Brackbill et al. (1992):

$$\vec{F}_{ST} = \sigma \kappa \cdot \nabla_N \alpha_i \tag{4.4}$$

where σ is the surface tension coefficient, and κ is the surface curvature approximated from the gradient of the phase fraction. The subscript N refers to the normal portion of the gradient. Assuming a constant specific heat at constant volume, the energy equation is:

$$\frac{\partial (\rho c_v T)}{\partial t} + \nabla \cdot (\rho c_v T \vec{u}) + \frac{\partial (\rho E_k)}{\partial t} + \nabla \cdot (\rho E_k \vec{u}) + \nabla \cdot (\vec{u} P) = \nabla \cdot (K \nabla T) \tag{4.5}$$

where T is the temperature, E_k is the kinetic energy, K is the thermal conductivity, and c_v is the specific heat capacity at constant volume.

The general solution algorithm for `compressibleInterFoam` is shown in Figure 4.1. Since gas jets are typically at high velocity and it is generally infeasible to resolve turbulence scales directly, a turbulence model is required to adequately model the momentum and dissipation of kinetic energy through eddies. OpenFOAM can use either Reynolds-Averaged Navier-Stokes (RANS) or Large Eddy Simulation (LES) models. The RANS approach seeks to temporally and spatially average the governing equations and models the fluctuating terms in the transport equations by solving auxiliary transport equations. This method has been used with VOF solvers for various applciations,

particularly in cavitation modeling (Fard et al., 2012; Gong et al., 2016; Wu et al., 2016). However, the applicability of RANS in highly transient cases is questionable (Myrillas et al., 2013; Roohi et al., 2013).

LES divides the turbulent effects into resolved effects, equivalent to the assumption that eddies larger than the grid scale are accurately predicted by the solution of the governing equations. The other components are modeled, accounting for the turbulent eddies at or below the grid scale. Typically this is accomplished using effective viscosity models, which modify the total kinematic (or dynamic) viscosity to match the contributions from the sub-grid scale (SGS). The Smagorinsky-Lilly model, which includes one tuning parameter, is often used. In multiphase flows, this parameter often has values ranging from $0.1 - 0.2$ (Li et al., 2015). The use of LES models in literature is quite common. Xiao et al. (2016) have used it for their atomization of liquid jets. Roohi et al. (2013) obtained good comparisons for cavitation around a hydrofoil, although at the expense of using a fine mesh. For rapid deformation during liquid sloshing, Liu et al. (2016) found that LES, as well as their hybrid LES/RANS VLES model behaved in an optimal matter. Conversely RANS and laminar models overestimated the pressure peaks and failed to capture the turbulent dissipation. Smagorinsky-Lilly is one of the most common LES models (Myrillas et al., 2013; Khezzar et al., 2015; Li et al., 2015; Tian et al., 2015). However, other SGS models are also commonly used. For example, Rek et al. (2017) employed an implicit one equation model to model liquid jets in crossflow.
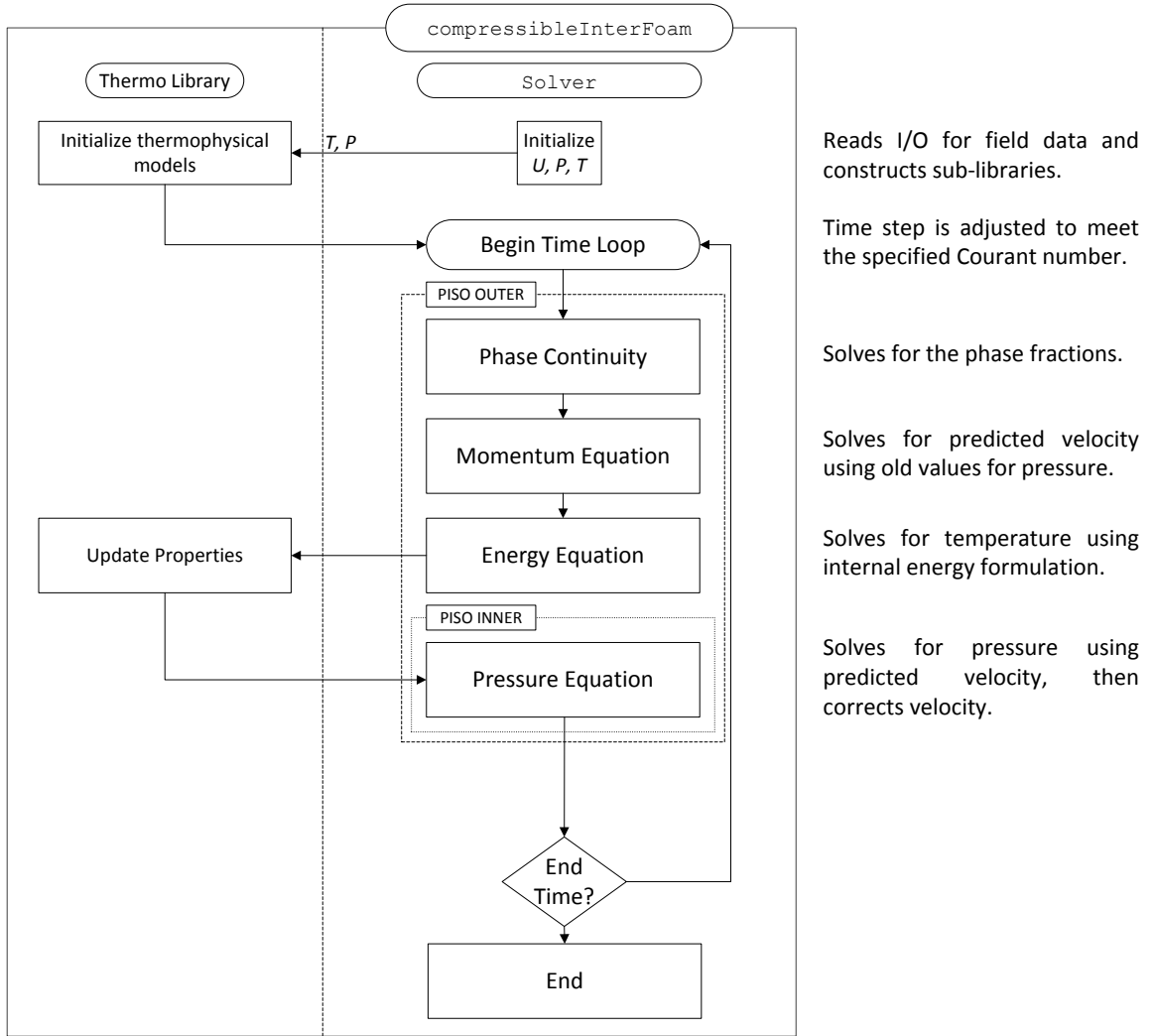
Figure 4.1 An outline of the solution procedure used in `compressibleInterFoam`.

In this study, the Smagorinksy-Lilly LES model was used to predict sub-grid scale turbulence. In the OpenFOAM implementation of this model, the turbulent dynamic viscosity is modeled as:

$$\mu_t = \rho C_s^2 V_{cell}^{2/3} |\bar{S}| \tag{4.6}$$

where μ_t is the turbulent dynamic viscosity, and C_s is a tuned parameter, which is filtered to the cube root of the cell volumes, V_{cell}. The value of the tuned parameter, C_s, typically ranges from 0.05 to 0.23 for single phase flows (Hu and Celik, 2008). Fewer validations are available in the literature for multiphase flows, but some recent studies have used a

value of 0.12 (Myrillas et al., 2013; Li et al., 2015). Therefore, this value was chosen in this study. $\bar{S}$ represents the sub-grid stress computed from:

$$|\bar{S}| = \frac{1}{2}\nabla \cdot \bar{\bar{u}} \tag{4.7}$$

where $\bar{\bar{u}} = \bar{u} - \bar{u}'$ is the resolved velocity, and $\bar{u}'$ is the unresolved velocity typically related to the sub-grid kinetic energy by $k_{SGS} = \frac{1}{2}(\bar{u}')^2$.

4.3 Validation

To test the hydrodynamic predictions of the `compressibleInterFoam` solver for gas jets, a test case was simulated. The test case involved a horizontal gas jet being injected into a quiescent liquid at atmospheric pressure to investigate the predictability of the jet breakup region. The use of a horizontal jet simplified the analysis somewhat because it provides a clearer indication of the transition between the near and far field due to the curving trajectory of the gas flow. Additionally, the tests provided useful feedback for the tuning of turbulence models, particularly for the boundary conditions in LES modelling. The validation case described below is based on the studies of Harby et al. (2014, 2017).

The ideal gas law was used for the prediction of air density. All other thermodynamic and transport properties were assumed to be constant for air and water. Since the tank was at atmospheric conditions and room temperature, and there are no drastic temperature or pressure changes, the constant property assumption is justifiable. Table 4.1 and Table 4.2 provide an overview of the property data.

Table 4.1 Properties of Liquid Water

Property	Value	Reference
Density, ρ (kg/m^3)	1000	-
Specific Heat Capacity, c_p (J/kg/K)	4182	Smith, Ness and Abbot, 2005
Dynamic Viscosity, μ (Pa s)	1×10^{-3}	Yaws (2003)
Prandtl Number, Pr (-)	6.22	Yaws (2009)

Table 4.2 Properties of Air

Property	Value	Reference
Density, ρ (kg/m^3)	Ideal Gas Law	-
Specific Heat Capacity, c_p (J/kg/K)	1007	Smith, Ness and Abbot, 2005
Dynamic Viscosity, μ (Pa s)	1.8×10^{-5}	Yaws (2003)
Prandtl Number, Pr (-)	0.7	Yaws (2009)

4.3.1 Case Setup

The case to be analyzed was based on the experiments performed by Harby et al. (2014, 2017) for horizontal air jet injection into a quiescent, atmospheric tank of water. The experimental setup was a rectangular tank, as shown in Figure 4.2. The tank measured 1 m long, 400 mm wide and 760 mm tall, although the water level was set to 600 mm. Harby et al. used nozzles of varying diameter, ranging from 2 mm to 5 mm, positioned 200 mm from the base of the tank to inject the air. The flow rates were also varied to achieve a range of Froude numbers. However, in this study, only the case using a 5 mm nozzle diameter and an injection velocity of 367 m/s was used for the simulation. The temperature at the nozzle exit was recorded in the original paper as 296 K (Harby et al., 2014). Further sensitivity studies were not performed for other nozzle diameters or inlet velocities due to the limitation of computational resources. The initial conditions used in the simulations are summarized in Table 4.3, while the boundary conditions are summarized in Table 4.4. As

mentioned above, the cases used LES to model turbulence, with the Smagorinksy-Lilly sub-grid scale model ($C_s = 0.12$).
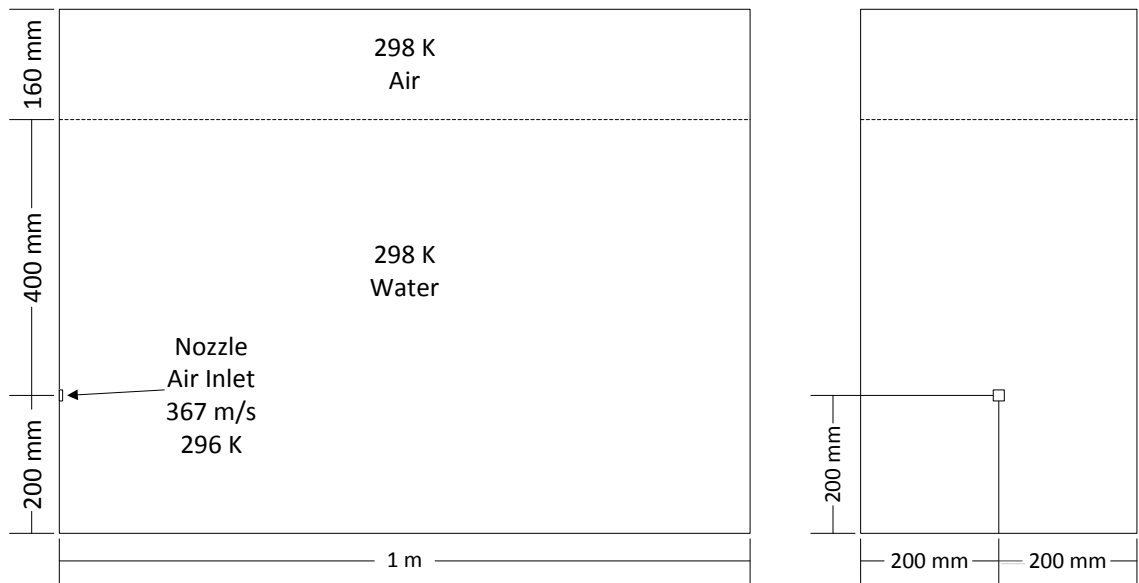
Figure 4.2 The case setup for the experiments of Harby et al. (2014, 2017).

Table 4.3 Initial conditions used to simulate the experiments of Harby et al. (2014, 2017).

Variable	Initial Condition
Gas Phase Fraction (-)	Filled to 600 mm
Temperature (K)	Uniform 298
Velocity (m/s)	Uniform 0
P_{rgh} (Pa)	Uniform 101325
Turbulent Kinematic Viscosity (m^2/s)	Uniform 1e-11

Table 4.4 Boundary conditions used to simulate the experiments of Harby et al. (2014, 2017).

Variable	Walls & Bottom	Inlet	Top
Gas Phase Fraction (-)	Zero gradient	1	Inlet-Outlet
Temperature (K)	Zero gradient	296	298
Velocity (m/s)	No slip	367	Inlet-Outlet
P_{rgh} (Pa)	Zero gradient	Zero gradient	101325
Turbulent Kinematic Viscosity (m^2/s)	Zero gradient	Zero gradient	Inlet-Outlet

4.3.2 Meshing

One main goal of this work was to investigate the effect of mesh resolution on the ability of the solver to resolve the gas jet breakup region. A mesh sensitivity study was therefore conducted. Three meshes were chosen based on computational resource availability and time constraints. The coarse, intermediate and fine resolution meshes are shown in Figure 4.3, Figure 4.4 and Figure 4.5, respectively.
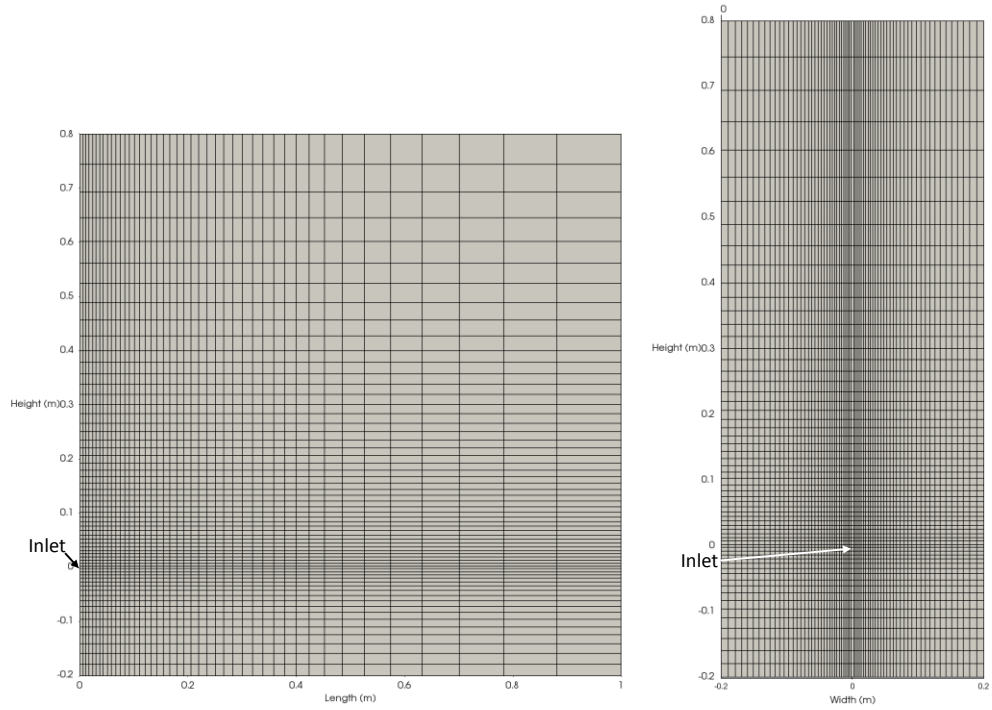
Figure 4.3 Coarse mesh, containing 188 232 computational cells.
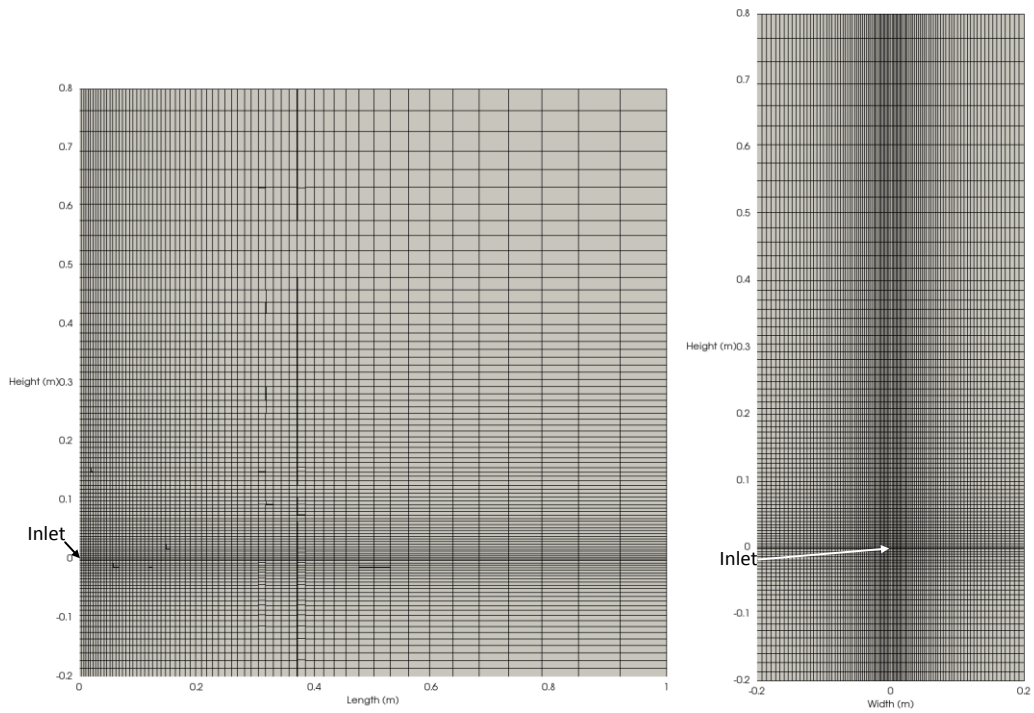
Figure 4.4 Intermediate mesh, containing 609 960 computational cells.
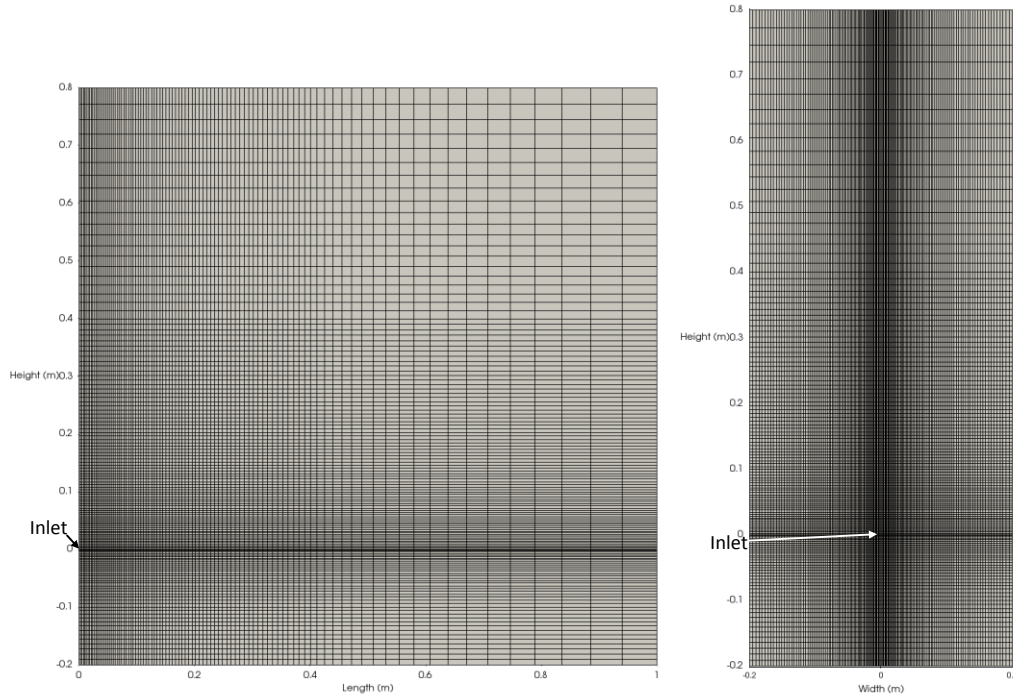
Figure 4.5 Fine mesh, containing 1 976 760 computational cells.

The coarse mesh was designed to have a single inlet cell and was the base case for the study Containing the fewest cells, it was expected that the simulation would capture the bulk hydrodynamics of the continuous gas phase, but poor resolution would be achieved in the buoyant region. The mesh was coarsened (with a first to last cell expansion factor of four) away from the inlet to allow better predictions near the release point. In reference to large-scale applications, the ability to capture complex flow in as few cells as possible is important. There will naturally be losses through the use of an unrefined mesh, but if the bulk hydrodynamics can be captured, other phenomena (such as heat and mass transfer) can still be approximated. Knowing where to apply and use refinement is necessary for the prediction of the gas jets. Given the experimental results, the tank size of 1 m is far greater than any of the jet and plume dimensions (Harby, 2014), and consequently less refinement was given to the end of the tank away from the inlet.

Due to geometrical constraints, the inlet nozzle was reshaped into a square. The area was maintained to match the original diameter, so that the mass flow rate and momentum were consistent with the done work by Harby et al. (2014, 2017). The nozzle diameter for the

chosen cases was 5 mm (the largest available in the experimental work), which resulted in a 4.43 mm × 4.43 mm square inlet. However, for the finer cases, refining the inlet was difficult while still trying to maintain a refined region around the jet. The scale up of the base mesh required slightly longer cells along the jet pathway to meet these requirements. However, this presented a way to test the effect of cell aspect ratio on the development of both the jet and plume.

Although a computer cluster was available for this study, computational resources were still a constraint because the simulations involved transient simulations with small time steps due to the high velocity. Therefore, the maximum number of cells in the fine mesh was limited to approximately 2 000 000. In a real gas release, the scale of the ocean or water column would be much larger than the nozzle itself and quantifying the limits of what could be captured is necessary to plan further models.

4.4 Results and Discussion

One primary goal of this study was to predict the momentum length of the jet region. In their work, Harby et al. (2014, 2017) used a high speed camera to capture the gas jets. Using their camera pixel conversions, as well as data in the 2017 paper, the momentum length for the case presented here was estimated to be approximately 150 mm. Figure 4.6 shows a comparison between the trajectory contours from Harby et al. (2017) and the simulation results from this work. Since the minimum phase fraction level in the experimental results is not specified, the simulation results are plotted using a low phase fraction contour of 0.05. The curves should therefore not be interpreted as a direct comparison. Instead, only the general shape and average jet length can be directly compared. All the cases started at 0 s. The contours from the simulation were taken from the averaged field over a period of 1 of 10 seconds for the coarse mesh, but only 1 to 4 seconds for the refined cases. Qualitatively and quantitatively the results are in good agreement with the figures produced in the work of Harby et al. (2017). In comparison to each other, the far-field gas fraction contours were also in agreement.

For the coarse mesh case, the far field region was poorly defined in the buoyant region. As will be shown later, this effect was due to the lack of resolution and the forces imposed in

the VOF solvers artificially keeping the gas region agglomerated together. This effect was reduced upon successive mesh refinements, but these cases required significantly more computational resources. For the jet region, the coarse mesh predicted the momentum length approximately as well as the refined cases. It is also possible that further time averaging of the coarse case would provide improvement of the far-field results. The difficulty with the coarse case is the loss of interfacial information at each time step, although the time-averaged contour eventually bounds the possible plume location.
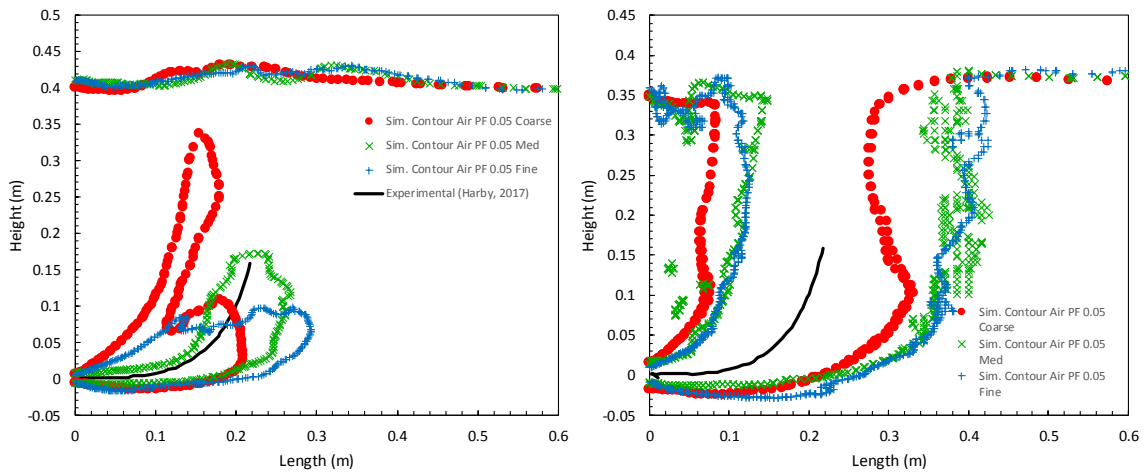
Figure 4.6 Contours showing a comparison between the experimental jet trajectory results from Harby et al. (2017) and numerical predictions for different mesh resolutions. On the left is the average phase fraction contour at 0.5, and on the right is the average phase fraction ontour at 0.05. The experimental trajectory is shown as a black line.

Although the momentum length was not perfectly predicted, the trends of the experimental results and the modeled results were in agreement. Due to the high computational demand of the simulations involving the finer meshes, it is difficult to obtain long time averages. It is therefore possible that the momentum length predictions shown in Figure 4.6 could be over-estimates because the jet length tends to decrease towards a pseudo steady-state. Further time averaging would provide more confidence in the results. However, given the results in Figure 4.6, the experimental results were predicted well for all three tests. Therefore, the momentum length was adequately captured by the model, even at low

refinement. This factor alone is already important to future work because it seems to indicate that the jet breakup length can be relatively well represented using a coarse mesh.

Within a VOF framework, the numerical approximation of the gas-liquid interface is normally defined by the 0.5 phase fraction contour. For methods involving the direct numerical simulation of interphase heat and mass transfer (such as those presented in Chapter 3), the accurate prediction of the actual interfacial area and its location is very important. For large-scale predictions, it is normally infeasible to directly resolve the total interfacial area due to the mesh resolution that would be required. Figure 4.7 shows both the instantaneous (4 second) and time-averaged phase fraction 0.5 contours. The instantaneous profile provides qualitative information about the interfacial area distribution and its resolution. Conversely, the time-averaged results indicate the region that is expected to have a continuous gas-liquid interface (i.e. jet before breakup).
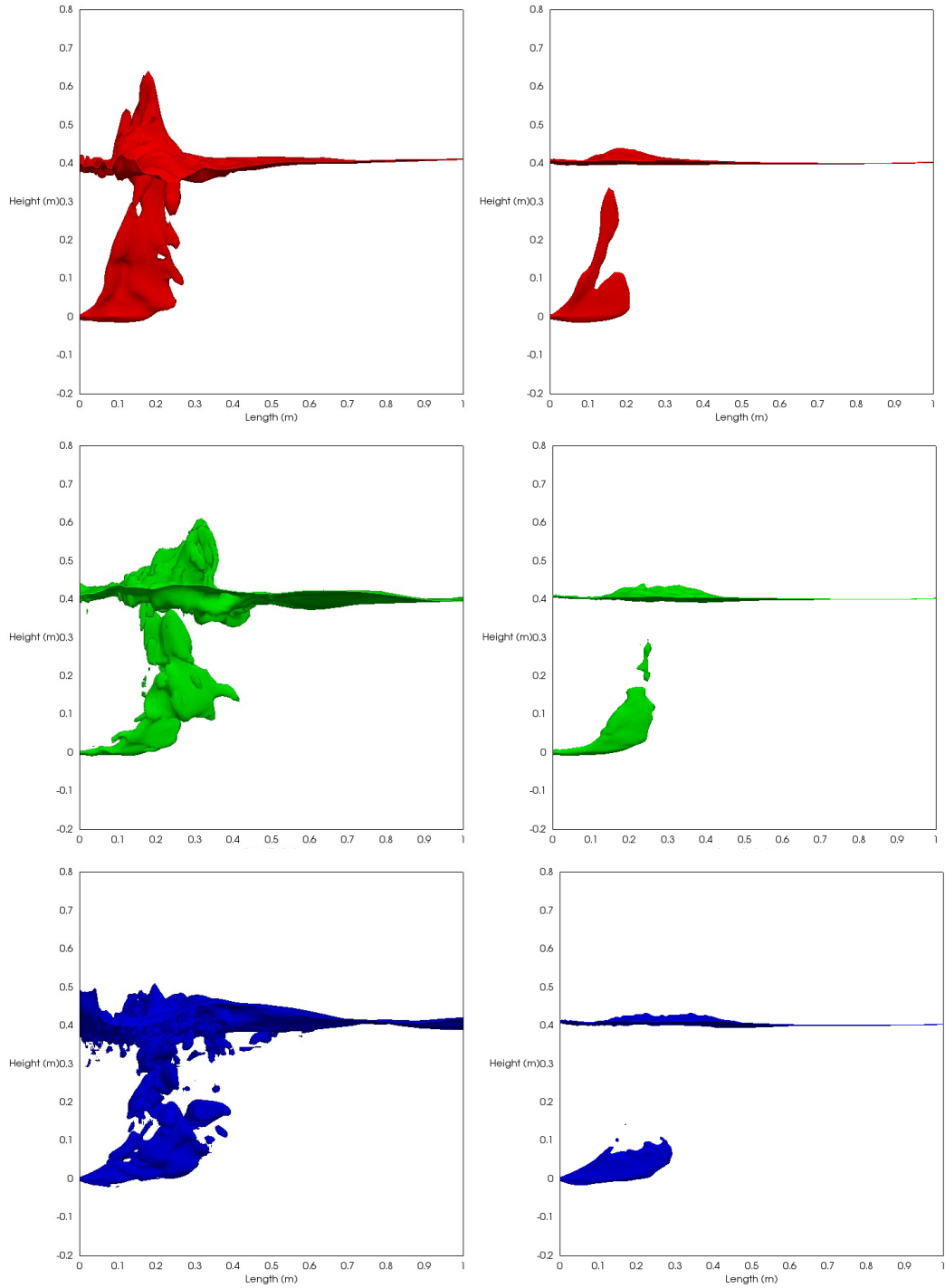
Figure 4.7 Results showing the 4 s (left) and average (right) gas phase fractions (0.5 phase fraction contour). Shown in red are the coarse case results, shown in green are the intermediate case results, and shown in blue are the finest case results.

In examining the results from the coarse and fine case, although the trajectory of the jet was similar, the ability to predict breakup behaviour was different. The buoyant plume region for the coarse mesh is largely of from the small-scale gas structures that would normally be present in this zone. Although the time-averaged solution predicts a region of low phase fraction, in truth the time step to time step appearance of large phase agglomerations persists, as shown in Figure 4.8. In the fine case, these regions of high gas holdup are more dispersed, but in reality a mesh refinement that could truly capture the interfacial area in the plume region would be prohibitively expensive. Therefore, it may be infeasible to predict the correct instantaneous phase fraction distribution using coarse meshes, but it may be possible to predict time-averaged results with reasonable accuracy.

The lack of convergence between refinements is troubling for the use of sophisticated and direct mass transfer simulation methods and applying them to large-scale problems. Dynamically tracking the interface, measuring the area, and then computing species gradients would be drastically different depending on which refinement was used. A large underprediction of mass transfer would be expected if coarse meshes were used in a large-scale system. Therefore, for cases such as these, direct prediction of mass will generally be infeasible within a VOF framework until much finer meshes can be simulated, which would require much more computational resources. However, the results indicate that the general location of the interface can be predicted with some accuracy, which provides a criterion to decide on the type of mass transfer modeling approach. Therefore, it would be possible to apply empirical closure models in the unresolved region and direct numerical prediction in the resolved regions. This is one option for the development of a multiscale approach for heat and mass transfer modeling within the VOF method, and it is the general approach taken in chapters 6 and 7.
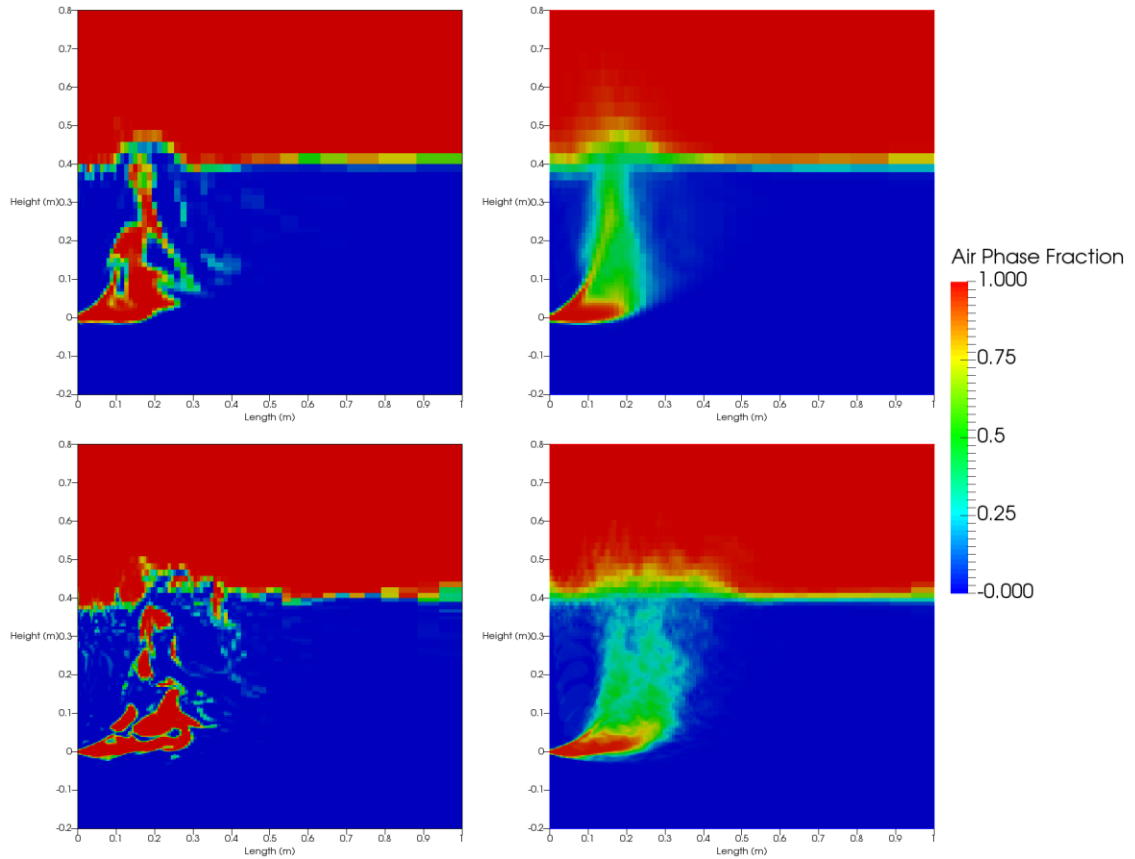
Figure 4.8 Instantaneous results showing the phase fraction contours for the coarse (top) and fine (bottom) meshes at times of 4 s (left) and the average (right).

The time-averaged turbulent kinematic viscosities are shown in Figure 4.9. For a time-averaged solution, the high values near the inlet are indicative of a lack of mesh scale resolution. If the turbulence was directly resolved, all three meshes would indicate similar results. The coarse mesh clearly provides the worst prediction, given the size of the cells in the region. Additional unresolved zones appeared at the interface, which were not present in the higher refinements. At the inlet, however, this was an expected result, given the high initial velocity of the gas.
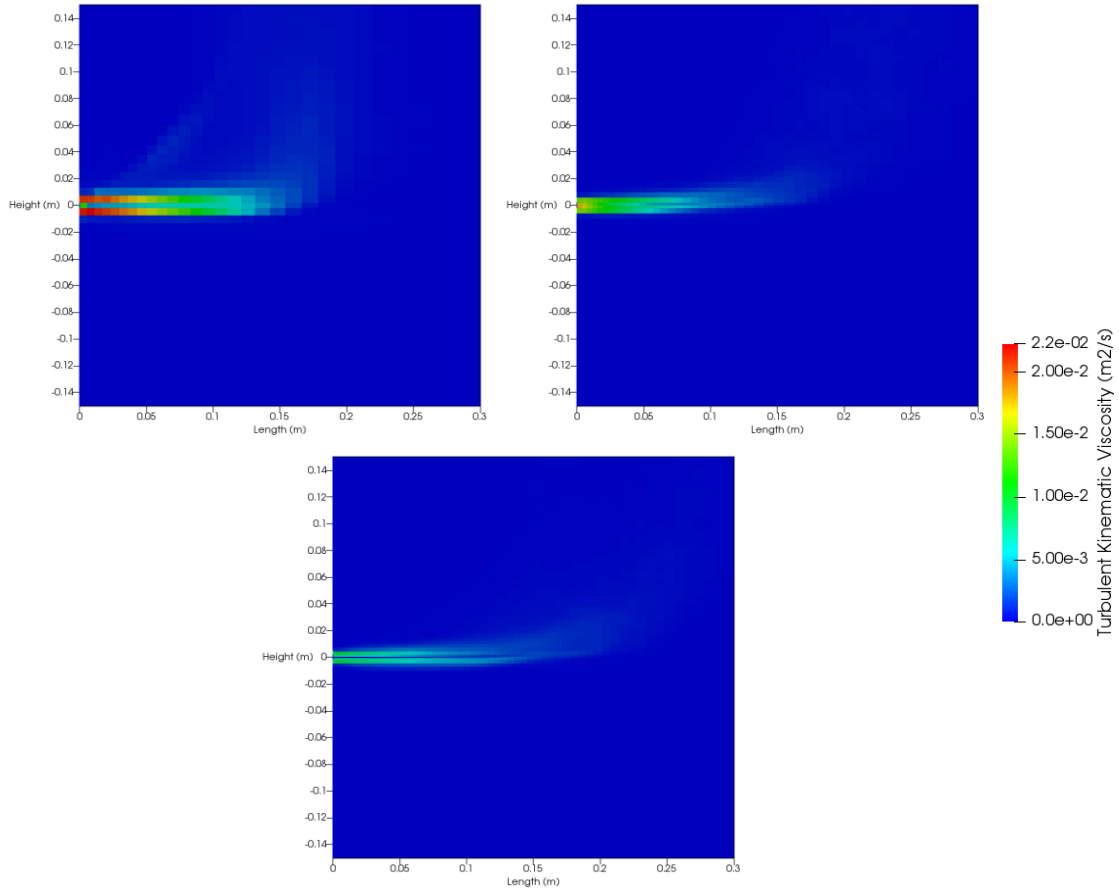
Figure 4.9 The time-averaged turbulent kinematic viscosity for three mesh refinements taken on a slice along the inlet pathway: coarse mesh (top left), intermediate mesh (top left), and fine mesh (bottom). The figure is zoomed in upon a 0.3 by 0.3 m box around the inlet.

4.5 Conclusions

In this study, the OpenFOAM solver `compressibleInterFoam` was used to model one of the experimental studies in Harby et al. (2014, 2017). The ability of the interface capturing approach to model both momentum and buoyancy-driven flows was tested. The case simulated was a high-speed jet with a relatively low mass flow rate due to the small nozzle diameter. Therefore, the penetration length could be captured within a small section of the tank where refinement could be made. Given the results, two questions remain to be answered. If many practical applications are potentially orders of magnitude greater in

scale, it is imperative to decide at what coarseness the mesh can be to maintain a balance between computational demand and accuracy.

Three meshes were used to simulate the system. Emphasis for the meshes was on the jet region, with less resolution at the far end of the tank and towards the surface. The coarsest mesh used one cell for the inlet, while the refined meshes employed four and nine. Given the size of the inlet relative to the domain, this introduced high aspect ratio cells into the system along the jet pathway. Although momentum lengths were predicted to be close to the experimental results, the aspect ratio of the mesh cells had an impact on the initial angle of the jet for the medium refinement case. Also, given that an LES model was used for the simulation, the difference in sub-grid scale model results for the coarse and fine cases mean that there was less direct resolution both near the inlet and at the free surface.

While the trajectory and thus the momentum length were reasonably well predicted, it was clear that there was a substantial loss of interfacial information for all mesh resolutions investigated. There was substantially more breakup for the finest mesh resolution, although the shape was similar to that of the coarsest case. However, even for the finest mesh, direct resolution of mass transfer via interface reconstruction would likely be infeasible. Therefore, large-scale predictions of mass transfer and more accurate predictions of plume fluid dynamics would require coupling to another methodology or the incorporation of appropriate sub-grid models.

SECTION II. NUMERICAL SIMULATION OF UNDERSEA SOUR GAS RELEASES

Chapter 5

Prediction of Undersea Sour Gas Releases: A Review of Applicable Modeling Techniques

5.1 Introduction

Although onshore reserves have yet to deplete, offshore oil and natural gas production are required to meet demand. Even exploring the well is substantially more difficult for offshore activities, as there is a barrier of seawater between the rig and the ocean floor. Even though the risk of a blowout or catastrophic release is low, a subsea release will behave differently than onshore counterparts and is generally more difficult to stop. Therefore, it is imperative that predictions can be made for worst case release scenarios to reduce the impact on society and the environment if such events occur.

When natural gas is first produced from the well, it often contains various acidic gases (e.g. CO_2, H_2S, etc.) and is therefore termed sour gas. The subsequent sweetening process separates the gas into a high purity hydrocarbon stream, and a stream containing the sour components, which is usually called acid gas. As an alternative to flaring these compounds, it is possible to use a depleted well to sequester them. This option has the added benefit of maintaining production well pressure. However, the acid gas stream creates an additional hazard due to the toxicity of the components. If a release of either sour gas or acid gas were to occur, the rapid release and expansion of pressurized gases would form a jet and plume, eventually reaching the surface and being transported to the atmosphere. Both the quantity of gas reaching the ocean surface and the location of the release to the atmosphere must be known to develop emergency response plans.

The objective of this chapter is to describe how numerical simulation can be applied to the modeling of release scenarios, with particular focus on computational fluid dynamics (CFD) methods. Although most models could be adapted for oil and/or gas releases, gas releases will be the primary focus of the discussion. A typical release would have three

major zones of flow, each with their own set of conditions and problems to consider. Closest to the release point, the pressure from inside the well forms a continuous release of momentum governed flow known as the jet region (or near field). The momentum from the well keeps the released phase together at a high phase fraction with a clearly defined interface. Depending on the pressure in the well, this could be a cold, liquid phase that would rapidly expand and evaporate to form a gas. As the released fluid travels further from the source, momentum dissipates, and the lighter fluid is carried up the water column by buoyant forces. This region is known as the plume region (or far field). This region is more disperse, and the bubbles aggregate or break up from the momentum core. As they continue to rise and disperse, they may also dissolve into the surrounding liquid, and are more vulnerable to influence by surrounding currents. Finally, any gas that reaches the surface will escape from the liquid phase and enter the atmosphere. This surface region is affected by the ocean-atmosphere interface and by detrainment of liquid from the gas plume.

Each region of a gas release is characterized by different length scales and physical processes, and therefore different modeling techniques may be required to capture their behaviour. Two general groups of numerical models are currently used to predict transport and fate of the released gas are mechanistic models (cone models and integral models) and computational fluid dynamics. Each modeling approach has associated advantages and disadvantages. In general, cone models assume a centerline pathway and develop the cone as a function of the distance along that path (Sridher, 2012). This means they are the simplest to implement and quickest to use. However, this also means that they rely heavily on empirical correlations and fitted values. Thus, when these models are applied to situations that are significantly different from the experiments that were used to fit parameters, expected accuracy is relatively low. The expected accuracy of cone models is also relatively low because gas dispersion is assumed to have no dependence on the gas release rate, gas jet dynamics, variation of bubble size, and other important characteristics. To improve accuracy, many measurements would be required at a variety of conditions to determine the cone angle. Furthermore, the cone angle is also known to be strongly influenced by interaction with the sea surface. Finally, the assumption of a single cone

angle under cross-flow conditions is not normally valid and therefore cone models become less useful under these conditions. Thus, cone models will not be the focus of this review.

Integral models instead assume a flow profile and are derived by applying mass and momentum balances to the plume (Sridher, 2012). Integral models can either be solved in an Eulerian or a Lagrangian reference frame (Yapa and Zheng, 1997a). Currently, three of the most developed models are DeepBlow (Johansen 2000, 2003), CDOG (Yapa and Zheng, 1997b; Zheng and Yapa, 1998, 2002; Chen and Yapa, 2001, 2002; Yapa et al., 2001; Zheng et al., 2002) and VDROP (Zhao et al., 2014a; Zhao et al., 2014b; Zhao et al., 2015; Zhao et al., 2016). The first two of these models have been significantly extended since their initial development, and both have been used in numerous case studies. Recent studies have focused on the addition of complex effects, such as hydrate formation and gas dissolution (Zheng et al., 2002), gas separation from mixed oil and gas plumes under cross-flow (Chen and Yapa, 2004), plume breakup dynamics (Dasanayaka and Yapa, 2009), and effects of dispersants (Yapa et al., 2012), as well as the incorporation of a population balance model (Zhao et al., 2014a). The primary limitation of integral models is that they rely on a number of empirical correlations. These empirical relationships must be obtained by fitting experimental data and it is not clear how accurately they can be extrapolated to different conditions. It is also necessary to make an assumption regarding the region in which the initial gas release undergoes breakup and where the buoyancy-driven plume will be formed. Currently, the near-field region is largely neglected in many integral approaches, and more emphasis is placed on the development of the plume. On the other hand, in addition to work being made to introduce complexity to integral models, they require considerably less computational resources when compared to CFD models.

The primary benefit of CFD models in comparison to cone and integral models, is that they rely on fewer empirical relationships. As discussed below, several different types of CFD models are applicable to simulate various parts of an underwater gas release. Near the release point, gas jet dynamics and gas jet breakup behaviour are very important, and therefore a CFD model may be able to provide more detailed information. Once a buoyancy-driven plume is established, the plume can be modeled using a dispersed flow model. Cloete et al. (2009) have previously applied a Lagrangian particle tracking (LPT)

algorithm to track bubble movement in an underwater gas plume. The primary problem associated with this method is that the computational cost becomes prohibitive when the number of bubbles that need to be tracked becomes too high. Further, one of the primary assumptions made in the method is that the particles do not occupy volume and this assumption is not applicable in regions where the gas fraction becomes too high (dense plumes). Clearly, this also means that this model will have limited applicability near the gas release point (i.e. the jet region) without special algorithm modifications. Cloete et al. (2009) also coupled the Lagrangian particle tracking algorithm with an interface tracking algorithm to resolve deformation of the ocean surface due to gas disengagement from the water.

In Eulerian multi-fluid dispersed flow models, the resulting governing equations are solved on a stationary grid. Each computational cell stores a phase fraction for all phases and uses them to phase average physical properties. The definition of the bubble sizes can be included by using a population balance model. Eulerian models are preferred to LPT in systems with high gas phase fractions or when the quantity of dispersed bubbles is very high. As for other dispersed flow models, empirical closure relationships must be used to couple the phase-averaged conservation equations. One limitation is that drag models are often limited to relatively low dispersed phase fractions. Drag models capable of predicting interaction at very high phase fractions are still being researched. Although the Eulerian approach has been used in CFD simulations of industrial systems for many years, there have been relatively few publications specifically aimed at modeling gas/oil blowouts. A recent exception is work done using the CFD code TransAT (Narayanan, 2011; Lakehal, 2013). In this study, an Eulerian mixture model (one-fluid formulation) was used with very large-eddy simulation (VLES) to account for turbulence. Further, the model included hydrate formation kinetics.

The purpose of this chapter is to provide background information about models that have been used for subsea gas release modeling and models that would be applicable for the simulation of gas releases. The primary focus is on CFD models, but an overview of integral approaches is also provided. A recent review by Olsen and Skjetne (2016a) also provides a comprehensive overview of modeling methodologies. They have commented

that the majority of literature is based around integral modeling, but conclude that CFD is a viable tool given the challenge of large-scale experimentation

5.2 Mechanistic Models

Software for jet and plume modeling has been heavily influenced by tools developed for the environmental assessment sector. This is to be expected, as environmental protection has become an important issue in the past century with the shift in paradigm towards sustainable development. Therefore, many earlier models, which can serve as a basis for the synthesis of more detailed blowout models, have previously been applied to various other types of releases.

Cone and integral models are formulated using macroscopic conservation laws and empirical closure relationships. Cone models were very popular in the past, but their limitations have reduced their use in recent years. Conversely, integral models are currently the most popular approach for subsea release modeling due to their relative speed, modifiability and accuracy. However, the main limitation of these models is that they do not resolve the small-scale interactions occurring at microscopic scales. These interactions are included through empirical closure models, but they are not directly resolved. This section reviews some available macroscopic models that are applicable to the modeling of underwater oil and gas releases.

Some of the earliest work on integral modeling of subsea releases is from Fanneløp and Sjøen in 1980, and Fanneløp and Bettelini (2007) extended and described this work more recently. Similar developments have also been made by Bhaumik (2005) as part of an extension of Socolofsky et al. (2002), and many others. Integral models are derived using the assumption of self-similarity, the entrainment hypothesis, and force and mass balance equations. The entrainment hypothesis relates the rate of entrainment at the edge of the plume to its upward velocity, which closes the force and material balance equations once appropriate property relationships are also specified. Property profiles within the plume must be assumed to have a specified shape (Hissong et al., 2014). They used a simple, top-hat profile mechanistic model in order to predict the rise of hydrocarbons through water.

It is worth mentioning that, although the abovementioned studies use an Eulerian formulation of the integral model, there are competing developments using Lagrangian approaches. Work proposed by Lee and Cheung in 1990, for their JETLAG model, relied on quantifying the momentum, volume and buoyant fluxes using small, non-interfering elements to represent the plume. These models accounted for horizontal entrainment based on the Froude number or a single velocity.

One of the most comprehensive and commonly cited integral models for underwater release modeling is the DeepBlow code (Johansen 2000, 2003). DeepBlow is a Lagrangian model in which the plume is represented by a series of non-interfering elements (Reed and Hetland, 2002). Each element is conceptualized by a cylinder or bent cone, characterized by its mass, location, radius, depth, average velocity, concentration, temperature and salinity. Similar to the CDOG model by Zheng et al. (2002), the plume can be considered as non-miscible fluids (oil and water, or gas and water). DeepBlow has the capacity to consider that bubbles may escape vertically out of a sloping plume. The code also allows for reductions in mass due to hydrate formation and dissolution into seawater. According to Johansen (2000), the DeepBlow solver is governed by a simple mass conservation equation where the volume is calculated using a constituent of mass within the cell that occupies a volume based on its density. The density is calculated using the basic compressibility equation of state.

Integral release models commonly include equations to account for hydrate formation, and this will shrink the volume accordingly based on the relative density. For the conservation of energy, DeepBlow tracks the contributions of each constituent. The total heat content of the Lagrangian volume elements is calculated as the summation of both sensible heat and latent heat effects. Dissolution of gas is modeled through the simple convective mass transfer equation:

$$\frac{dC_G}{dt} = -KA\left(C_{sol} - C_p\right) \tag{5.1}$$

Where $\frac{dC_G}{dt}$ is the gas dissolution rate, K is the mass transfer coefficient, A is the surface area, C_{sol} is the solubility of gas in sea water, and C_p is the far-field concentration of the dissolved gas in the water. If the far-field concentration in water tends towards zero and

that the bubble is spherical with a diameter of d_b, $A/V = 6/d_b$, and the gas dissolution rate is:

$$\frac{dC_G}{dt} = -\frac{6k}{d_b} C_{sol} \tag{5.2}$$

Johansen (2000) calculated the mass transfer coefficient using the empirical correlations provided by Hughmark (1967). The bubble slip velocity was calculated using a harmonic average between velocities calculated by using two empirical correlations for the drag coefficient.

Yapa et al. (Yapa and Zheng 1997a, b; Yapa et al., 2001) developed a model for deep water oil and gas releases primarily for use in the Gulf of Mexico. The original model, proposed in 1997, was primarily for vertical oil releases. However, this model was later expanded for deeper well releases also involving gases. Under ambient flow conditions, the plume forms a bent cone. The original model assumed that the bubbles are trapped at the core of the jet, or that the bubble disengagement from the jet was not possible. However, the model was later extended to account for gas separation from the oil plume.

The model uses a Lagrangian integral control volume approach to track the motion of the plume. In this approach, only the average properties and bubble sizes can be resolved for each control volume. This is one of the primary weaknesses of their model; however, as noted by Zheng et al. (2002), there is insufficient knowledge about the bubble size distribution in such plumes. It is noted by Johansen et al. (2001) that the bubble size tends to be in the range of 3 to 8 mm for deep sea releases of gas bubbles, and approximately the same for diesel droplets.

The model of Yapa et al. used a similar mass transfer model as Johansen (2000) (i.e., equation 5.2). However, a customized empirical mass transfer coefficient model was developed in Zheng and Yapa (2002). For greater accuracy, the equilibrium concentration of dissolved gas in the liquid was calculated by using a modification of Henry's law. The modification involved the incorporation of a fugacity term to account for high pressure and a term to account for salinity. The final form was,

$$C_{sol} = H^* f_G \exp\left(\frac{(1-P)\widehat{V}_L}{RT}\right) \tag{5.3}$$

where f_G is the fugacity of the gas, H^* is an alternate form of the Henry's law constant, and $\widehat{V}_L$ is the partial molar volume of gas in solution. Yapa et al. (2001) used a simple kinetic model, coupled with a simple spherical heat and mass transfer model, to determine the rate of hydrate formation.

More recently, a model known as GASOCEAN (Leite et al., 2014) was employed in Brazil to model subsurface gas releases. Using the linear momentum balance of gas, seawater and oil, it incorporates entrainment, dissolution, and bubble separation. It is based on prior work by Yapa and Zheng (1997) and Chen and Yapa (2004). It also uses Henry's law and a simple mass transfer rate expression to predict dissolution. Again, it also uses a Lagrangian control volume approach with a specific focus on the buoyant plume. As indicated by Bibilazu et al. (2010), not a lot of focus is placed on the initial expansion or hydrate formation. What remains to be studied is how much better the models would become if small-scale effects could be resolved using a more theoretical approach.

A more recent set of studies has been conducted using a model known as VDROP (Zhao et al., 2014a; Zhao et al., 2014b; Zhao et al., 2015; Zhao et al., 2016). These studies employ an integral model, but this approach has also been coupled to a population balance model (PBM) (Zhao et al., 2016). Unlike other integral models, the inclusion of PBM permits prediction of a particle size distribution and coalescence and breakup. The model has been applied to a few lab-scale experiments and full-scale case studies. The model has also been improved to incorporate an empirical jet model. So far, the model has been applied to both oil and gas releases.

Although many complex extensions have been proposed in recent years, the primary shortcomings of the currently available integral models are their inability to account for complex flow behaviour directly, as well as local variations in properties and mass transfer rates. Recent studies have also highlighted the need for jet modeling, and extensions have been proposed to incorporate some approaches into the available models. CFD models could help to overcome some of the limitations of these models because more features of the fluid dynamics can be directly resolved. However, the disadvantage is that CFD models

are still only starting to be applied to such systems, implying that they need further development and validation.

5.3 CFD Models

There are several categories of commonly used multiphase CFD models, and several combinations of different models that have been developed to overcome deficiencies for specific applications. The purpose of this section is to describe the most commonly used methods for large-scale multiphase flow simulations, with specific emphasis on their applicability for subsea gas release modeling.

5.3.1 Mixture Models

The mixture model is derived by volume averaging the conservation equations. In this case, the continuity, volume fraction equation for the dispersed phase, and momentum conservation equations are (ANSYS Inc., 2011, Ishii and Hibiki, 2010):

$$\frac{d\rho}{dt} + \nabla \cdot (\rho \vec{u}) = 0 \tag{5.4}$$

$$\frac{d(\alpha_b \rho_b)}{dt} + \nabla \cdot (\alpha_b \rho_b \vec{u}) = -\nabla\left(\alpha_b \rho_b \vec{u}_{drift,b}\right) + S_b \tag{5.5}$$

$$\frac{d(\rho \vec{u})}{dt} + \nabla \cdot (\rho \vec{u}\vec{u}) = -\nabla P + \nabla \cdot \mu(\nabla \vec{u} + (\nabla \vec{u})^T) + \rho \vec{g} + \vec{F}$$

$$+\nabla \cdot \left(\sum_{i=1}^{n} \alpha_i \rho_i \vec{u}_{drift,i}\vec{u}_{drift,i}\right) \tag{5.6}$$

where α_b is the volume fraction of the dispersed phase, $\rho = \sum_i \alpha_i \rho_i$ is the average density of the mixture, ρ_b is the density of the dispersed phase, $\vec{u}$ represents the mass-averaged velocity field, P is the pressure, $\rho \vec{g}$ is the gravitational force, $\mu = \sum_i \alpha_i \mu_i$ is the average viscosity of the mixture, $\vec{u}_{drift,i}$ is the drift velocity of the dispersed phase, $\vec{F}$ includes other volumetric body forces, and S_b accounts for sources/sinks for the dispersed phase. The mixture model is normally only applied to model dispersed flows when the bubbles are relatively well dispersed in the continuous phase and when bubble motion is not too different from the bulk motion of the continuous phase. One of the most common mixture models is the drift-flux model. The naming convention is related to the unresolved variable for which closure is needed. In equation 5.6, the drift velocity is strictly not known through the solution procedure. Instead, a force balance on the dispersed particle, or a well understood flow regime must be used to close the model.

Since the model has lower computational demands than many competing model types (particularly E-E and LPT models), it has seen use in many fields, such as aerosol and other deposition studies (Chen et al., 2006; Xi and Longest, 2008; Parker et al., 2010; Bové et al., 2016), and dispersion in indoor environments (Zhao et al., 2009). The model has also been applied to boiling flows (Hu et al., 2017). In addition, the model is considered simpler, while providing similar results to its contemporaries (Andreolli et al., 2017).

In terms of ocean environments, there have been only a select few studies carried out. Andreolli et al. (2017), have used the model to track the flow of crude oil through offshore pipelines, though no rupture studies were carried out. In general, the application of the drift-flux model to pipeline, steady flow is common due to the even distribution of the mixture (Talebi et al., 2012; Dong-hui et al., 2015; Teixeira et al., 2017). This allows for the closure terms to be written simply as distribution coefficients (Hu et al., 2017). Hu et al. (2017) applied this approach to model boiling flow in pipes.

Using simplified closure models requires a weakly coupled system (Teixeira et al., 2017), but the simplification leads to a large gain in computational efficiency. For oceanic environments, this is not true of the jet region, where momentum from the jet drives the gas, leading to a continuous phase in sharp contact with the surrounding seawater. However, once the buoyant driven plume develops, the dispersion of the gas may be modeled by a drift-flux model. The cost would be the loss of generality because a simplified closure model would be required to represent the flow regime. Alternatively, more complex closure models would have to be developed.

5.3.2 Euler-Euler Models

As mentioned above, Eulerian and Lagrangian models are commonly employed to model large-scale dispersed flows. Eulerian models may be derived either by averaging the conservation equations over the entire volume (referred to as one-fluid formulation, homogeneous model or mixture model), or by averaging the conservation equations over each phase (referred to as the multi-fluid formulation or inhomogeneous model). In either case, these models are based on the interpenetrating-continua assumption (Ishii and Hibiki, 2010), and therefore interface dynamics are not directly resolved. Instead, every grid cell

in the solution domain is occupied by different proportions of each phase and closure laws must be specified for interface momentum, energy and mass transfer. The accurate specification of these closure laws, which are usually empirical, is critical to the accuracy of these models.

In the Eulerian multi-fluid formulation, separate continuity and momentum conservation equations are solved for each phase. A complete derivation can be found in Ishii and Hibiki (2010). The equations can be written as:

$$\frac{d(\alpha_i \rho_i)}{dt} + \nabla \cdot (\alpha_i \rho_i \vec{u}_i) = S_i \tag{5.7}$$

$$\frac{d(\alpha_i \rho_i \vec{u}_i)}{dt} + \nabla \cdot (\alpha_i \rho_i \vec{u}_i \vec{u}_i) = -\alpha_i \nabla P - \nabla \cdot \tau_i + \alpha_i \rho_i \vec{g} + \vec{F}_{drag,i} + \vec{F}_{lift,i} + \vec{F}_{vm,i}$$

$$+\vec{F}_{other,i} \tag{5.8}$$

where α_i is the volume fraction of phase i, ρ_i is the density of phase i, S_i is the source of phase i, $\vec{u}$ is the velocity of phase i, P is the pressure, $\vec{g}$ is the gravitational acceleration, $\vec{F}_{drag,i}$ is the drag force, $\vec{F}_{lift,i}$ is the lift force, $\vec{F}_{vm,i}$ is the virtual mass force, $\vec{F}_{other,i}$ includes other volumetric body forces for phase i. Also,

$$\tau_i = -\alpha_i \mu_i (\nabla \vec{u}_i + (\nabla \vec{u}_i)^T) + \frac{2}{3} \alpha_i \mu_i \nabla \cdot \vec{u}_i \mathbf{I} \tag{5.9}$$

where $\mathbf{I}$ is the identity tensor and μ_i is the viscosity (sum of molecular and turbulent viscosities) of phase i.

Mass transfer effects can be incorporated into the multi-fluid model by solving conservation equations for N − 1 chemical species (where N is the number of chemical species). Additionally, energy transfer can be included by solving one energy conservation equation for each phase. The appropriate forms of the energy and species equations are:

$$\frac{d(\alpha_i \rho_i Y_{i,j})}{dt} + \nabla \cdot (\alpha_i \rho_i \vec{u}_i Y_{i,j}) = -\nabla \cdot (\alpha_i \vec{J}_{i,j}) + S_{M,i,j} \tag{5.10}$$

$$\frac{d(\alpha_i \rho_i h_i)}{dt} + \nabla \cdot (\alpha_i \rho_i \vec{u}_i h_i) = \alpha_i \frac{dP_i}{dt} + \tau_i : \nabla \vec{u}_i - \nabla \cdot (\alpha_i \vec{q}_i) + S_{E,i} \tag{5.11}$$

where $Y_{i,j}$ is the mass fraction of component j in phase i, $S_{M,i,j}$ is the source of species j in phase i due to interfacial mass transfer ($S_{M,b,j} = -S_{M,p,j}$), $\vec{J}_{i,j}$ is the diffusion flux of component j in phase i, P_i is the pressure in phase i, $\tau_i : \nabla \vec{u}_i$ accounts for viscous heating

and is usually neglected, $\vec{q}_i$ is the heat diffusion flux, and $S_{E,i}$ is the energy source in phase i ($S_{E,b} = -S_{E,p}$). In many cases, the diffusion flux can be estimated using Fick's law:

$$\vec{J}_{i,j} = -\rho_i D_{i,M,eff,j} \nabla Y_{i,j} \tag{5.12}$$

where $D_{i,M,eff,j} = D_{i,M,j} + D_{i.M.t,j}$ is the sum of the molecular ($D_{i,M,j}$) and turbulent ($D_{i.M.t,j}$) mass diffusivities in phase i. The heat diffusion flux (conduction) can often be estimated using Fourier's law:

$$\vec{q}_i = -\mathrm{K}_{eff,i} \nabla T \tag{5.13}$$

where $\mathrm{K}_{eff,i} = \mathrm{K}_i + \mathrm{K}_{t.i}$ is the sum of the molecular (K_i) and turbulent ($\mathrm{K}_{t,i}$) conductivities in phase i, and T is the temperature.

Euler-Euler models are commonly used to simulate bubbly flows, either in bubble columns (see for example: Li et al., 2009; Yang et al., 2011; Xiao et al., 2013; Pourtousi et al., 2014; Bhusare et al., 2017) or in tanks (see for example: Dhotre et al., 2007; Panneerselvam et al., 2008; Dhotre et al., 2009). Therefore, this method should be generally applicable to the plume region of a subsea gas release. However, many of the closure models were primarily developed and tested in confined geometries, and thus their applicability to open oceanic environments is difficult to judge. In this case, the problem is the scaleup of the closure models and more importantly the choice of turbulence models.

Although the majority of studies using Euler-Euler models focus on bubble columns, they have been used to model large-scale bubble plumes (e.g., Buscaglia et al., 2002). In Buscaglia et al. (2002), and E-E model was applied to dilute bubble plumes and obtained reasonable agreement with an integral model for dissolution of oxygen for the purposes of aeration.

5.3.3 Lagrangian Particle Tracking Models

The Euler-Lagrange approach (also called Lagrangian particle tracking) is also commonly used to model dispersed multiphase flows. In the Euler-Lagrange approach the flow field for the continuous (water) phase is obtained by solving the momentum conservation equations and the continuity equation on a fixed grid. The Eulerian conservation equations

are analogous to equations 5.7 and 5.8. Particles are tracked in a Lagrangian reference frame, and coupling between the continuous phase, dispersed phase and within the dispersed phase may be one-way, two-way or four-way (Fraga et al., 2016). Since particles can be tracked through a relatively coarse flow field, relatively coarse meshes can be used. Therefore, this approach is nearly as efficient as Euler-Euler methods for dilute systems but becomes more computationally expensive when a large number of particles must be tracked.

LPT methods for gas-liquid flows are commonly used to model bubble columns (Delnoij et al., 1999; Laín et al., 2002; Hu and Celik, 2008; Gruber et al., 2013) or bubbly pipe flow (Peña-Monferrer et al., 2014; Dapelo et al., 2015). For highly dispersed bubbly flows, LPT methods are advantageous because population balance models are relatively straightforward to include. However, due to the number of particles in a large-scale flow, tracking broad data for each particle may become unfeasible. Additionally, the scale up to other bubble size classes is a concern, as the sizes found in industrial applications are often small to promote interphase heat and mass transfer. Since many closure models for coalescence and breakup are based on case specific data (Delnoij et al., 1997; Gruber et al., 2013), accurate prediction of the coalescence time must be treated similarly to other closure terms.

A comprehensive overview of the E-L method is provided in Prosperetti and Tryggvason (2007). Additionally, Cloete et al. (2009) have previously used a version of this method to simulate the dispersion of an undersea plume of gas bubbles, and the simulation of small scale plumes has been carried out by Fraga et al. (2016). However, heat and mass transfer effects were not included, and only a very simple method was employed to account for changes in bubble size. Additionally, the continuous phase was assumed to be unaffected by the motion of the dispersed phase. In the E-L method, the motion of each bubble is tracked by solving the force balance:

$$m_b \frac{d\vec{u}_b}{dt} = \vec{F}_{drag,b} + \vec{g}(\rho_b - \rho_p) + \vec{F}_{other} \qquad (5.14)$$

where the subscript b refers to the dispersed phase, the subscript p refers to the continuous phase, m_b is the mass of the bubble, $\vec{F}_{drag,b}$ is the drag force, and $\vec{F}_{other}$ includes additional

forces (virtual mass, lift, etc.), but can be included in the same way as for Euler-Euler models above (Darmana et al., 2005).

In the LPT method, extra momentum forces are added to the momentum of the particle, but otherwise carry the same form as in E-E models, as seen as early as Delnoij et al. (1997, 1999), Gruber et al. (2013) and Peña-Monferrer et al. (2014). However, it is necessary to account for bubble breakup and coalescence using a probability based model. Similar to the available force balance closure models, these probability based collision models are empirical, and it is not clear which one will yield the most suitable results. Further, the movement of bubbles is influenced by turbulent velocity fluctuations. The turbulent dispersion of bubbles can be related directly to the turbulence model predictions. However, this implies that an appropriate choice of turbulence model is critical, since this choice will have a strong impact on the simulation results.

If heat and mass transfer effects are to be included in the model, it is necessary to solve the species and energy conservation equations (see 5.10 and 5.11) for the continuous phase. Interphase heat and mass transfer effects can be included in the LPT model by solving species and energy conservation equations in the Lagrangian reference frame. For example, if only one chemical species changes phase, it is sufficient to solve the energy conservation equation and the one species balance:

$$\frac{dT_b}{dt} = \frac{h_c A_b}{m_b c_{p,b}} \left(T_b - T_p \right) \qquad (5.15)$$

$$\frac{dY_b}{dt} = \frac{\rho_p K_p a_b}{\rho_b} \left(Y_{sol} - Y_p \right) \qquad (5.16)$$

Where a_b is the surface area density of the bubble, Y_b is the mass fraction in the dispersed phase, and the convective heat (h_c) and mass transfer coefficients (K_p) are described in subsequent sections. Specification of the most appropriate empirical models for the convective transfer coefficients is critical for the accurate implementation of these relationships. It is important to note that the bubble diameter would need to be recalculated at each time step using the newly calculated bubble mass and density. Darmana et al. (2005), Gong et al. (2009), and Olsen and Skjetne (2016b) have used LPT methods with gas dissolution from underwater plumes using the method described above.

The LPT method can become very computationally expensive for very large numbers of particles. Further, this method suffers from some of the same problems that limit the accuracy of the E-E methods. Specifically, the LPT method still relies on correlations for coupling interphase energy, mass and momentum transport, and these correlations have a strong impact on the accuracy of the simulation. Further, no generally accepted turbulence model exists, and the choice of turbulence model is expected to have a strong impact on the simulation of bubble plumes. Currently, LPT methods have been used to model large-scale releases in the work of Cloete et al. (2009), Fraga et al. (2016), Olsen and Skjetne (2016b), and Olsen et al. (2017).

5.3.4 Interface Tracking/Capturing Models

Relevant interface tracking/capturing methods have been discussed in chapters 2, 3 and 4. For the purposes of this work, the volume-of-fluid method will be the primary model discussed. Wörner (2012), and Tryggvason et al. (2011) provide a comprehensive summary of the relative advantages and disadvantages of different interface tracking techniques. The literature discussed in Chapter 2 primarily focused on ways in which VOF could be used to augment studies of gas jet/plume releases.

A summary of the equations has already been presented in Chapter 3. They will be shown again in brevity. The VOF method is based on the one-fluid formulation, which is derived by averaging the conservation equations over the entire computational domain. In this case, the continuity, volume fraction, and momentum conservation equations are:

$$\frac{\partial \rho}{\partial t} + \nabla \cdot (\rho \vec{u}) = 0 \tag{5.17}$$

$$\frac{\partial \alpha_1}{\partial t} + \nabla \cdot (\alpha_1 \vec{u}) + \nabla \cdot (\alpha_1 \alpha_2 \vec{u}_R) = S_1 \left(\frac{1}{\rho_1} - \alpha_1 \left(\frac{1}{\rho_1} - \frac{1}{\rho_2} \right) \right) - \frac{\alpha_1 \alpha_2}{\rho_1} \left[\frac{\partial \rho_1}{\partial t} + \vec{u}_1 \cdot \nabla \rho_1 \right] +$$

$$\frac{\alpha_1 \alpha_2}{\rho_2} \left[\frac{\partial \rho_2}{\partial t} + \vec{u}_2 \cdot \nabla \rho_2 \right] + \alpha_1 \nabla \cdot \vec{u} \tag{5.18}$$

$$\frac{\partial (\rho \vec{u})}{\partial t} + \nabla \cdot (\rho \vec{u} \vec{u}) + \nabla \cdot \tau = -\nabla P + \rho \vec{g} + \vec{F}_{ST} \tag{5.19}$$

where α_1 is the volume fraction of the liquid phase, S_1 is any mass source for the liquid phase, ρ is the average density of the mixture ($\rho = \sum_i \alpha_i \rho_i$), $\vec{u}$ represents the mass-averaged velocity field, P is the pressure, $\vec{g}$ is the gravitational force, μ is the average

viscosity of the mixture ($\mu = \sum_i \alpha_i \mu_i$). Normally, the only other important body force is due to surface tension. Most VOF methods use the continuum surface force (CSF) of Brackbill et al. (1992). In this case,

$$\vec{F}_{ST} = \sigma \kappa \cdot \nabla_N \alpha_i \qquad (5.20)$$

where κ refers to the surface curvature and σ to the surface tension coefficient. If heat and mass transfer effects are important, species and energy conservation equations must be included. The one-fluid form of the energy balance can be written as:

$$\frac{\partial(\rho c_v T)}{\partial t} + \nabla \cdot (\rho c_v T \vec{u}) + \frac{\partial(\rho E_k)}{\partial t} + \nabla \cdot (\rho E_k \vec{u}) + \nabla \cdot (\vec{u} P) = \nabla \cdot (K \nabla T)$$
$$- \nabla \cdot \left(\sum_j e_j \vec{j}_j \right) + S_E \qquad (5.21)$$

where c_v is the phase-averaged specific heat capacity at constant volume, E_k is the kinetic energy, K is the thermal conductivity ($K = \sum_i \alpha_i K_i$), e is the internal energy, $\vec{j}$ is the mass flux term, and S_E is the energy source term. The species equations are usually phase averaged because the concentration profile across the interface is usually discontinuous. Thus,

$$\frac{\partial(\alpha_i \rho_i Y_{i,j})}{\partial t} + \nabla \cdot \left(\alpha_i \rho_i Y_{i,j} \vec{u} \right) = -\nabla \cdot \vec{j}_j + S_{M,j} \qquad (5.22)$$

which is the same as equation 5.10.

Although interface capturing/tracking methods are convenient for simulating the breakup of bubbles, droplets or jets, a sufficiently fine grid is required to accurately resolve the interface. As a result, it would be impractical to apply these methods directly to model the large-scale behaviour of an underwater gas plume. The results of Chapter 4 reaffirm that the mesh requirements for direct simulation of heat and mass transfer are impractical, and that only the bulk jet characteristics will be reasonably predicted.

Recently, a trend towards coupled models has appeared in the literature. In many industrial applications, while dispersed phases exist, there is also the presence of a continuous phase that is not handled well by the dispersed phase model. For E-E, application of the model to free surfaces poses a difficult closure modeling challenge. Jain et al. (2014) have explored coupled interface tracking in bubble columns modeled by LPT methods for resolving

airspace above the free surface, and Wardle and Weller (2013) employed a hybrid E-E VOF model for liquid-liquid column simulation. Coupled methods are also commercially available through the ANSYS E-E model (ANSYS, 2011).

Although interface capturing/tracking methods are convenient for simulating the breakup of bubbles, droplets or jets, a sufficiently fine grid is required to accurately resolve the interface. As a result, it would be impractical to apply these methods directly to model the large-scale behaviour of an underwater gas plume. However, it should be possible to use a VOF method to simulate gas jet breakup in the vicinity of the release point.

5.4 Interphase Force Models

As mentioned above, dispersed flow models such as mixture models, Euler-Euler models and LPT models require appropriate closure models to complete the equations. For the momentum equations, these relationships can be divided into a few key categories, with the most important being the drag, lift, and virtual mass force models, and the turbulent dispersion model. The interphase force models are empirically derived from experimental data and have limitations on their range of applicability. It is therefore necessary to choose the models carefully to ensure validity for the application of interest.

5.4.1 The Drag Force and Slip Velocity

The drag force acts in the force balance as a resistance imposed by the contact of two fluids. In general, for a spherical bubble, the drag force can be calculated by,

$$\vec{F}_{drag,b} = \frac{3}{4} \frac{\alpha_p \alpha_b \rho_p}{d_b} C_D |\vec{u}_b - \vec{u}_p| (\vec{u}_p - \vec{u}_b) \qquad (5.23)$$

where the subscript b refers to the dispersed phase, the subscript p refers to the primary phase, d_b is the bubble diameter, C_D is the drag coefficient, and $\vec{F}_{drag,b} = -\vec{F}_{drag,p}$. The drag coefficient must be determined using an empirical correlation because no purely theoretical model with a very broad range of applicability exists. Since the drag coefficient has a large impact on the momentum coupling between the phases, its accurate specification is very important. It is not clear which drag model will be most appropriate to the simulation of an undersea gas plume.

Cloete et al. (2009) calculated the drag coefficient using:

$$C_D = \frac{2}{3}\left(\frac{E_0}{3}\right)^{0.5}$$
(5.24)

Many of the models have been developed from systems involving bubbly flow in other geometries, particularly bubble columns (Yang et al., 2011; Xiao et al., 2013; Bhusare et al., 2017). The exact form of the drag force is subject to change for different flow regimes. A constant drag coefficient model was employed by Bhusare et al. (2017), Dhotre et al. (2007) and Dhotre et al. (2009). The argument for a constant coefficient makes sense when the relative velocity is high and therefore drag becomes practically independent of the Reynolds number. For non-constant modeling, the Schiller-Naumann model is a common choice (Yang et al., 2011; Xiao et al., 2013):

$$C_D = \begin{cases} \frac{24}{Re}(1 + 0.15Re^{0.687}), & Re < 1000 \\ 0.44, & Re \geq 1000 \end{cases}$$
(5.25)

In this case, the Reynolds number is based on the bubble diameter and the relative velocity between phases. Yang et al. (2011) compared data fitted from a bubble column experiment and the results obtained from using Schiller-Naumann, Tomiyama modified Schiller-Naumann and the model of White. The results had mixed agreement over applicable ranges and bubble sizes. Therefore, the applicability of these models is questionable for flow in an unbounded ambient, particularly for various bubble size ranges and shapes. Another problem with the Schiller-Naumann formulation is the lack of consideration for bubble shape or swarms. The model of Ishii and Zuber, taken from Li et al. (2009) and Yan et al. (2017), accounts for some of these variations:

$$C_D = f(x) = \begin{cases} \frac{24}{Re}(1 + 0.15Re^{0.687}), & \text{Spherical} \\ \frac{2}{3}\sqrt{Eo}E, & \text{Elliptical} \\ \frac{8}{3}E', & Cap \end{cases}$$
(5.26)

where Eo is the Eötvös number, a dimensionless quantity meant to represent the shape of the bubble. It can be calculated from:

$$Eo = \frac{g(\rho_p - \rho_b)d_b^2}{\sigma}$$
(5.27)

where σ is the surface tension. It is not clear which correlation will be the most appropriate without performing some preliminary validation studies. The functions E and E' are corrective terms that account for the shape of the bubble. This model has also been used by Rzehak and Krepper (2016) to simulate drag in bubble columns. The importance of bubble shape is that the Schiller-Naumann model predicts well for spherical particles, which cannot be assumed as the diameter increases, especially for bubbles. However, many columns and injectors produce a fine bubble swarm, so it is a widely applicable with correction.

Another popular model is that of Tomiyama et al. (1998) for contaminated systems:

$$C_D = \max\left(\frac{24}{Re}(1 + 0.15Re^{0.687}), \frac{8}{3}\left(\frac{Eo}{Eo+4}\right)\right) \tag{5.28}$$

The function should be automatically filtered, depending on the range of the Reynolds and Eötvös number. As mentioned in Yan et al. (2017), this model predicts well over a large range of Reynolds numbers, whereas Schiller-Naumann both overpredicts for low Reynolds number and underpredicts for high Reynolds number. The Ishii and Zuber model predicts well for high Reynolds numbers but overpredicts for low Reynolds numbers. In these studies, the bubble diameter was varied for a single bubble rising.

The difficulty for translation to a large-scale subsea release case is that there will be zones of high gas hold up. In these regions, momentum layers will overlap, and the bubble swarm will behave differently from the single bubble experiments (Buffo et al., 2016). Swarm corrected drag coefficients typically have the following form:

$$C_D = f(\alpha_b)C_{D,0}(Re) \tag{5.29}$$

where $f(\alpha_b)$ represents a function to account for swarm effects while $C_{D,0}(Re)$ represents the drag for a single bubble (such as the Tomiyama model, above). Therefore, swarm corrections are modifiers to the single bubble drag models, accounting for the wakes of other bubbles. For example, the work of Buffo et al. (2016) used,

$$f(\alpha_b) = \begin{cases} 1 - \alpha_b, & \alpha_b < 0.8 \\ 1, & \alpha_b \geq 0.8 \end{cases} \tag{5.30}$$

with Tomiyama as the basic drag model. Some other examples include the work of Roghair et al. (2011; 2012; 2013), who modeled bi-disperse flows.

The choice of drag model is important, because it contributes to estimation of the relative or slip velocity for a dispersed phase model. Given that the oceanic environment is contaminated, a model such as Tomiyama would be the best choice of those presented. Although there are newer ways to formulate models, such as those presented by Buffo et al. (2016), the Tomiyama model is very commonly used. Furthermore, the Tomiyama model has been tested repeatedly with adequate results across a large range of Reynolds numbers. Also, since the exact bubble size in the plume region of a release is not known, the error introduced by the drag model is likely to be relatively small compared to the assumption of a diameter or size distribution. A swarm correction could be used to improve drag force predictions, but the best choice for a large-scale release is currently not known.

5.4.2 The Lift Force

If bubbles are assumed to be much smaller than the interparticle spacing, but the particles are not too small, the shear induced lift force acting on the dispersed phase can be calculated from,

$$\vec{F}_{lift,b} = -C_l\rho_b\alpha_b(\vec{u}_p - \vec{u}_b) \times (\nabla \times \vec{u}_p) \tag{5.31}$$

where C_l is the lift coefficient (which is often assumed to have a value of between 0 and 0.5, as stated by Díaz et al., 2009, Gruber et al., 2013, and Pourtousi et al., 2014), and $\vec{F}_{lift,b} = -\vec{F}_{lift,p}$. In practice, lateral dispersion is governed primarily by lift and turbulent dispersion. Díaz et al. (2009) comment that the above formulation of the lift is incomplete, in part since a constant lift coefficient implies that lift can only act in one direction for a given flow. An alternative formulation is the model of Tomiyama et al. (2002):

$$C_l = -0.004Eo + 0.48 \tag{5.32}$$

where the Eötvös number accounts for the bubble shape and allows the sign to vary with the bubble distribution. This model gives negative lift forces for bubble sizes greater than 9 mm in an air-water system. Díaz et al. (2009) also mention more complex models, but this only highlights the uncertainty of the field. Their own experiments utilized three

representative values for the coefficient (-1,0,0.5) across various gas flow rates. Their conclusions were that the lift force had a significant effect on lateral dispersion depending on the gas velocity, across bubbles sized 1 to 10 mm. For smaller gas flow rates, including positive lift helped prediction of lateral dispersion, but for higher velocity it weakened predictions.

For applications to large-scale gas releases, bubbles will often be greater than 9 mm in diameter. For high velocities, correlated functions tend to weaken predictions. Therefore, it seems the best practice is to assume a constant value given other uncertainties.

5.4.3 The Virtual Mass Force

The virtual mass force accounts for the inertia added to the primary phase due to the motion of the secondary phase. The virtual mass force is often approximated using

$$\vec{F}_{vm,b} = C_{vm}\alpha_b\rho_b\left[\left(\frac{\partial \vec{u}_p}{\partial t} + (\vec{u}_p \cdot \nabla)\vec{u}_p\right) - \left(\frac{\partial \vec{u}_b}{\partial t} + (\vec{u}_b \cdot \nabla)\vec{u}_b\right)\right] \qquad (5.33)$$

where the subscript b refers to the dispersed phase, the subscript p refers to the primary phase, and $\vec{F}_{vm,b} = -\vec{F}_{vm,p}$. C_{vm} is the virtual mass coefficient, which is usually approximated using a constant coefficient. Often a value of 0.5 is used (Dhotre et al., 2013; Messa et al., 2015; Rzehak and Krepper, 2016) or it can be incorporated into the drag coefficient (Panneerselvam et al., 2008; Roghair et al., 2011). For bubble columns, Pourtousi et al. (2014) have observed little impact unless population balance modeling is included.

5.4.4 The Turbulent Dispersion Force

As a consequence of turbulence modeling, there are a number of extra closures to be made to the momentum equation in a multi-fluid model. Turbulence is expected to have a profound effect on the dispersion of the gas phase, and so the balance of forces can be supplemented by a turbulent dispersion force of the form (Burns et al., 2004, Fletcher et al., 2017):

$$\vec{F}_{TD} = C_{TD}\frac{v_t}{Sc_t}\left(\frac{1}{\alpha_p} - \frac{1}{\alpha_b}\right)\nabla\alpha_b \qquad (5.34)$$

110

This model relates the turbulent dispersion force to a constant parameter, C_{TD} as well as the turbulent mass diffusivity represented as the turbulent kinematic viscosity, ν_t, and the turbulent Schmidt number, Sc_t. The turbulent dispersion force represents the lateral dispersion induced by the fluctuating velocity terms not included in the drag force model. This is the form of Burns et al. (2004) for the special case of two fluids. It acts as a diffusion term on the dispersed phase (or continuous phase, depending on the formulation) and has been used in recent works for bubble columns (Li et al., 2010; Fletcher et al., 2017).

Additionally, for high gas hold-up, the bubbles are expected to influence the viscosity of the liquid phase through bubble induced turbulence. This effect is added to the liquid phase viscosity (Joshi et al., 2017):

$$\mu_{eff} = \mu_{molecular} + \mu_t + \mu_{BIT} \tag{5.35}$$

$$\mu_{BIT} = C_{BIT}\alpha_b\rho_p d_b|\vec{u}_R| \tag{5.36}$$

Again, the model relies on a parameter, C_{BIT}, which requires tuning. Typical values have been reported as 0.6 (Dhotre et al., 2007; Dhotre et al., 2009).

Since subsea releases will be turbulent, inclusion of these models will be important to facilitate realistic predictions. Since these parameters will affect the tendency for the plume to dissipate, like with the drag and lift models, they will also affect interphase heat and mass transfer.

5.5   Turbulence Modeling

In multiphase systems, turbulence is usually modeled by extending available single-phase models. Turbulence modeling is known to be challenging in both single-phase and multiphase flow modeling because no known generalized model can be applied to all situations. This problem is further exacerbated in multiphase flow modeling because it is difficult to validate the available models. Some more effort will be required to identify the most appropriate turbulence model for the description of an undersea gas plume. Two turbulence modeling approaches are commonly used: large eddy simulation (LES) and Reynolds-Averaged Navier Stokes (RANS).

Among RANS models, the $k - \epsilon$ model is the most widely used (Argyropoulos et al., 2015). Turbulence is modeling through the inclusion of two additional transport equations for the turbulent kinetic energy (k) and its dissipation rate (ε). The equations take the form (Bohle et al., 2008):

$$\frac{\partial\left(\alpha_p\rho_p k\right)}{\partial t} + \nabla\cdot\left(\alpha_p\rho_p\vec{u}_p k\right) = \nabla\cdot\left[\alpha_p\left(\mu_p + \frac{\mu_{t,p}}{\sigma_k}\right)\nabla k\right]$$

$$+\mu_{t,p}\nabla\vec{u}_p\cdot\left(\nabla\vec{u}_p + \left(\nabla\vec{u}_p\right)^T\right) - \frac{2}{3}\alpha_p\rho_p k\nabla\cdot\vec{u}_p\alpha_p\rho_p \qquad (5.37)$$

$$\frac{\partial\left(\alpha_p\rho_p\epsilon\right)}{\partial t} + \nabla\cdot\left(\alpha_p\rho_p\vec{u}_p\epsilon\right) = \nabla\cdot\left[\alpha_p\left(\mu_p + \frac{\mu_{t,p}}{\sigma_k}\right)\nabla\epsilon\right]$$

$$+\alpha_p\frac{\epsilon}{k}\left[C_1\mu_{t,p}\nabla\vec{u}_p\cdot\left(\nabla\vec{u}_p + \left(\nabla\vec{u}_p\right)^T\right) - C_2\rho_p\epsilon\right] - \left(\frac{2}{3}C_1 + C_3\right)\alpha_p\rho_p\epsilon\nabla\cdot\vec{u}_p \qquad (5.38)$$

where k is the turbulent kinetic energy and ε is the kinetic energy dissipation rate. The constants for the standard $k - \epsilon$ model are: C_1 = 1.44, C_2 = 1.92, C_3 = -0.33, C_μ = 0.09, σ_k = 1.0 (Renze et al., 2014), and σ_ε = 1.3. Additional source terms are sometimes added in multiphase applications. The turbulent viscosity is calculated from,

$$\mu_{t,p} = \rho_p C_\mu \frac{k^2}{\epsilon} \qquad (5.39)$$

The other branch of turbulence modeling is known as LES. In this methodology, the grid scale turbulent effects are assumed to be modeled directly. However, for turbulent effects at or below the mesh resolution, a sub-grid scale model is employed. The reasoning behind the development of these methods is to compensate for deficiencies in transient predictions when using RANS models. Additionally, as mentioned by Fraga et al. (2016), RANS models assume isotropic turbulence, which is inherently untrue in bubbly systems even at small liquid velocities. The most common of these models is known as the Smagorinksy or Smagorinsky-Lilly model. From Niceno et al. (2008), the model employs an average velocity:

$$\bar{\bar{u}} = \bar{u} - \bar{u}' \qquad (5.40)$$

Physically, this means that the velocity can be represented as a resolved part, $\bar{\bar{u}}$, and a sub-grid part, $\bar{u}'$. This is similar to the RANS method, which temporally splits the field into a steady and fluctuating portion. However, LES models are filter averaged (Renze et al.,

2014). The basic Smagorinksy model is an eddy viscosity model that simply relates the turbulent viscosity to the sub-grid scale strain rate tensor:

$$\mu_{SGS} = \mu_t = \rho_p (C_S \Delta)^2 |\bar{S}| \tag{5.41}$$

where C_S is a constant (between 0.05 and 0.23 for single phase flows, Hu and Celik, 2008), Δ is the filter width (typically the cube root of the cell volume), and $|\bar{S}|$ is the strain rate tensor. One equation models, like that employed in Renze et al. (2014) are of the form,

$$\frac{\partial k_{SGS}}{\partial t} + \nabla \cdot (k_{SGS} \vec{u}_p) - \nabla \cdot \left(\frac{\mu_{eff}}{\rho_p} \nabla k_{SGS} \right) = 2 \nu_{SGS,p} |S|^2 - \frac{C_\epsilon k_{SGS}^{3/2}}{\Delta} \tag{5.42}$$

where k_{SGS} is the sub-grid scale kinetic energy, and C_ϵ is a constant (typically 1.048). The turbulent viscosity is

$$\mu_t = \rho_p C_k (k_{SGS})^{0.5} \Delta \tag{5.43}$$

where C_k is another constant (0.094) and the turbulent dissipation is

$$\epsilon = \frac{(\mu_{eff,p})^3}{\rho_p^3 (C_S \Delta)^4} \tag{5.44}$$

where C_S is the final constant with a value of 0.16. In the formulation of Renze et al. (2014) the turbulent dissipation played an important role in determining coalescence and breakup in their population balance model.

A summary of how recent work has employed these models is shown in Table 5.1. The $k - \epsilon$ models (RANS) are widely used in bubble column simulations as well as bubbly flow simulations. In Buffo et al. (2016), they determined LES models provided slightly better results for many applications, but RANS models are sufficient for most practical industrial problems.

RANS are the predominant models used in simulations, but many of these systems involve confined flows (bubble columns, fluidized beds, aeration tanks). In this sense, LES is lacking due to the reliance on directly resolving the interactions near the wall. However, in the large-scale gas releases, often the only wall present will be the ocean bed itself. Even for the case of bubble columns, LES models have been employed with greater accuracy than in RANS models (Darmana et al., 2015; Dhotre et al., 2009; Pourtousi et al., 2014),

and are deemed more accurate (Argyropoulos et al., 2015). Argyropoulos et al. (2015) also mention that the major factor against LES models was computational power, a gap that is rapidly diminishing. Hu and Celik (2008) also mention that, for complex flows where the resolved scale needs to be unperturbed, LES models are preferable for preserving these complex phenomena. In this way, LES models can be seen as less intrusive because the resolved portion of the mesh does not require treatment. Additionally, LES models generally provide superior transient predictions.

Ultimately, both models have been used successfully in a variety of cases. The large body of work for RANS models may be attributed to the computational cost being less than that of LES models. However, this is an important point, since runtime is an issue for large-scale cases. Still, the benefits of RANS models reduce for cases without confined geometries, and both models will still require tuning. The act of tuning is the most time-consuming component, and perhaps the most difficult challenge to be faced when resolving turbulence in a simulation.

Table 5.1 Overview of turbulence model usage in recent studies.

Study	Simulation Type	Simulated System	Turbulence Model
Adamczyk et al. (2014)	LPT	Fluidized Bed	RANS
Almohammed et al. (2014)	LPT	Fluidized Bed	RANS
Bhole et al. (2008)	E-E with PBM	Gas Sparger/ Bubble Column	RANS
Buffo et al. (2016)	E-E with PBM	Bubble Column	RANS
Buscaglia et al. (2002)	E-E	Bubble Plume	RANS
Darmana et al. (2005)	LPT	Bubble Column	LES
Dhanasekharan et al. (2005)	E-E	Airlift Reactor	RANS
Dhotre et al. (2007)	E-E	Bubble Plume	RANS
Dhotre et al. (2009)	E-E	Bubble Plume	LES
Diaz et al. (2009)	E-E	Bubble Column	RANS
Fayolle et al. (2007)	E-E	Aeration Tank	RANS
Fletcher et al. (2017)	E-E	Bubble Column	RANS
Fraga et al. (2016)	LPT	Bubble Plumes	LES
Gimbun et al. (2009)	E-E with PBM	Aeration Tank	RANS
Gruber et al. (2013)	LPT with PBM	Bubbly Flow	LES
Hu and Celik (2008)	LPT	Aeration Tank	LES
Khan et al. (2017)	E-E	Bubble Column	LES/RANS/RSM
Lain et al. (2014)	LPT	Bubble Column	RANS
Olsen and Skjetne (2016)	LPT	Bubble Plume	RANS
Renze et al. (2014)	E-E with PBM	Bubble Column	LES
Wang and Wang (2007)	E-E	Bubble Column	RANS

5.6 Bubble Size Distributions

For many practical release scenarios, bubbles formed will not be uniform in size. Instead, clusters of bubbles will form, coalesce and breakup. Even in cases of controlled distribution, such as in bubble columns, there is no guarantee that the bubbles will not break up or coalesce. Therefore, the bubble size is rarely constant. In the case of an ocean release, the bubble size distribution is expected to change with time and location. To account for variations in the bubble size distribution it is necessary to solve a population balance equation (PBE). The mathematical formulations for the solution of the PBE are quite complex, and several solution techniques have been proposed. A good overview of the application of the PBEs to particulate systems is provided in Ramkrishna (2000).

One method for tracking bubble size distribution is to classify bubble sizes based on a method of bins (Zhao et al., 2014a; Zhao et al., 2014b), in which breakup or coalescence simply move groups from one bin to another. In this methodology, more bins effectively means greater ability to approximate the real distribution, but at the cost of computational time. Another efficient algorithm for solving these types of problems currently available is the quadrature method of moments (QMOM) and its extensions. A good summary of the pertinent numerical techniques is provided in Marchisio and Fox (2013). Renze et al. (2014), as well as Buffo et al. (2016), have implemented the QMOM in OpenFOAM.

No matter which method is chosen, the PBE requires the specification of breakup and coalescence models. These models govern the probability of the bubble or droplets to collide and interact. Gruber et al. (2013) utilized an LPT method with a PBE to compare two common breakup and coalescence models for bubble columns. The study found that if the Sauter mean bubble diameter is known a priori, it can be used with similar gains for gas holdup prediction, although with losses of interfacial area estimation. While these models have been implemented on a small scale (Gimbun et al., 2009; Gruber et al., 2013; Renze et al., 2014; Gruber et al., 2015; Buffo et al., 2016), their predictive capacity for large-scale releases is unknown. Although the work of Zhao et al. (2014a; 2014b; 2015; 2016) have applied PBE based solution procedures to real release data from oil rigs, the method used was an integral model.

5.7 Mass and Energy Transfer Modeling

This section outlines common methods for heat and mass transfer modeling for large-scale problems. Although an overview of the problem has been summarized in Chapter 3, models applicable to large-scale releases in general will be discussed here.

Similar to the momentum equations, the species and energy equations in each phase must be coupled to the other phase by incorporating appropriate source terms. These coupling terms are the only way to account for interphase heat and mass transfer in multi-fluid models. Unfortunately, there no generalized heat and mass transfer closure relations that can be applied to all systems. Therefore, this section is divided into two parts. The first part summarizes the problems associated with energy transfer modeling, while the second part focuses on mass transfer.

5.7.1 Energy Transfer Correlations

The rate of heat transfer between phases can often be modeled using a simple convective heat transfer relationship:

$$S_{E,b} = h_c a (T_b - T_P) \tag{5.45}$$

$$h_c a = \alpha_p \frac{K_p N u_b}{d_b} \frac{6 \alpha_b}{d_b} \tag{5.46}$$

where a is the surface area per volume (for spherical bubbles $a = 6\alpha_b/d_b$), K_p is the thermal conductivity of phase p, Nu_b is the Nusselt number of phase b. The Nusselt number, and thereby the convective heat transfer coefficient, must be obtained from an empirical correlation. Although it was initially derived based on data from very simple droplet evaporation experiments, the correlation of Ranz and Marshall (1952 a,b) remains one of the most commonly used relationships. This correlation is,

$$Nu_b = 2 + 0.6 Re_b^{1/2} Pr_p^{1/3} \tag{5.47}$$

where

$$Re_b = \rho_p |\vec{u}_R| d_b / \mu_p \tag{5.48}$$

$$Pr_p = c_{p,p} \mu_p / K_p \tag{5.49}$$

Other commonly used models are similar in form to equation 5.47 but have different constants. Many of these models were originally developed for spherical droplets, but since this remains a common assumption for dispersed phases, these types of correlations are often used. For subsea gas releases, the dissolution of the gas is not expected to produce a significant heat transfer term, although the application of a dispersed phase model such as E-E or LPT will require it for general heat transfer from phase to phase. The application of the mixture model is similar to the treatment of an interface tracking model, where the energy is volume averaged and therefore interphase heat transfer is approximated directly through the averaging of the properties.

5.7.2   Mass Transfer Correlations

Interphase mass transfer is often modeled using a simple convective mass transfer relationship:

$$S_{M,b,j} = \rho_p K_p a \left(Y_{sol,j} - Y_{p,j} \right) \tag{5.50}$$

$$k_p a = \alpha_p \frac{D_{M,p,j} Sh_{b,j}}{d_b} \frac{6\alpha_b}{d_b} \tag{5.51}$$

where $Sh_{b,j}$ is the Sherwood number in phase b of compound j, Y_{sol} is the mass fraction in equilibrium with the bulk dispersed phase (solubility limit). Note that the overall mass transfer coefficient is replaced with the primary phase mass transfer coefficient since the gas side is assumed to be negligible. Otherwise, K_p represents the overall liquid side mass transfer coefficient. Correlations for the Sherwood number are generally of the form:

$$Sh_{b,j} = 2 + C_M Re_b^n Sc_{p,j}^{1/3} \tag{5.52}$$

where:

$$Sc_{p,j} = \mu_p / \left(\rho_p D_{M,p,j} \right) \tag{5.53}$$

The coefficient C_M and n are model parameters. Such mass transfer correlations have been employed in many studies (Gruber et al., 2015; Rzehak and Krepper, 2016; Fletcher et al., 2017).

The mass transfer coefficient is also often calculated from models based on Higbie's penetration theory (Fayolle et al., 2007; Talvy et al., 2007; Wang and Wang, 2007; Gimbun et al., 2009; Huang et al., 2010). For a rising bubble

$$K_p = 2\sqrt{\frac{D_{M,i,j}\bar{u}_R}{\pi d_b}} \qquad (5.54)$$

This mass transfer correlation is also known as the slip penetration model and is employed for mobile (clean) interfaces. These models are closely related to surface renewal models, where the fluid is assumed to have a specified contact time with the interface. This model has been shown to provide a good prediction of experimental data in bubble columns (Alves et al., 2006; Wang and Wang, 2007).

Another commonly used relationship is the eddy-cell model, which relates the surface renewal to the turbulent dissipation in the cell. This model has been used by Gimbun et al. (2009), Wang and Wang (2007) and Dhanasekharan et al. (2005)

$$K_p = \frac{2}{\sqrt{\pi}}\sqrt{D_{M,i,j}}\left(\frac{\epsilon_p \rho_p}{\mu_p}\right)^{0.25} \qquad (5.55)$$

In this model, which is based on the Higbie model, it is the turbulent dissipation that governs the timescales for the surface to renew. As mentioned by Wang and Wang (2007), the mechanism is not well understood since there are two models (Higbie and eddy-cell), that rely on fundamentally different assumptions that can yield similar results. As found in their work on bubble columns, the authors saw that both models could predict the transfer of oxygen.

For immobile (contaminated) interfaces, the Frössling model has been shown to provide good estimates (Alves et al., 2006). It is given by

$$K_p = 0.6\sqrt{\frac{\bar{u}_R}{d_b}}D_{M,i,j}^{2/3}v_p^{-1/6} \qquad (5.56)$$

It is not clear which heat and mass transfer correlations will be most appropriate for the simulation of an undersea gas plume. However, the Higbie model has been employed in previous literature. It is known that the interface in an ocean envrionment is likely to be

immobile due to the presence of surfactants. Therefore, the Frössling model may be the most likely option, due to its relative simplicity and applicability.

5.8 Thermodynamic and Transport Property Models

Modeling the thermodynamic properties of acid gas mixtures is important to be able to predict their behaviour during a release. The vapour-liquid equilibrium (VLE) strongly affects both the rate of absorption of sour gases (carbon dioxide, hydrogen sulfide, etc.) into solution and the final equilibrium concentration. Therefore, accurate VLE models, accounting for interactions between the gas and surrounding seawater are critical. For the case of the release of a high-pressure gas, accurate prediction of the compressibility is also important.

5.8.1 Compressibility

The compressibility of the released gas must be known to accurately calculate density changes on expansion. These density changes directly affect the velocity of the gas through the momentum conservation equations and continuity equation. Gas compressibility effects at high pressures are normally modeled using one of the available equations of state (EOS), and it is likely that the commonly used models would be able to accurately describe the compressibility. The Soave-Redlich-Kwong (SRK-EOS) and Peng-Robinson (PR-EOS) equations of state are two of the most commonly used models. Both of these equations have been used to calculate compressibility for similar systems (Bigalke et al., 2009; Rehder et al., 2009; Carroll and Mather, 1995; Battistelli and Marcolini, 2009), and therefore it is expected that either model would be capable of modeling the compressibility.

For shallow water releases, the ideal gas model is used in DeepBlow (Johansen, 2000). This model can be used with very little error for depths to 50 m. This model is also used in many LPT methods, such as the one employed by Olsen and Skjetne (2016b). It is, of course, not recommended to use this model for exceedingly high pressures, such as those found in ultra deep water rigs (up to 3000 m). However, when applicable, the ideal gas model can be used to simplify computations.

5.8.2 Phase Equilibria

Much work has been done by Carroll and Mather (1995) to describe the thermodynamic interactions of hydrogen sulfide-paraffin mixtures using the Peng-Robinson equation of state (PR-EOS). They have also studied the vapor-liquid equilibrium of such systems and presented some data, but this data cannot be used to model a gas plume in seawater.

Battistelli and Marcolini (2009) proposed a model known as TMGAS, which is an equation of state that models multicomponent mixtures of arbitrary sour gases, hydrocarbons and water. It is also capable of simulating aqueous salt solutions. For non-aqueous phase calculations, TMGAS uses a compressibility factor calculated from the Peng-Robinson EOS. The detailed treatment of the aqueous phase is provided in Battistelli et al. (1997). This is a comprehensive model that is capable of providing accurate predictions of the solubility of acid gases in both hydrocarbon and aqueous phases. However, the complexity of the model may make it very difficult to implement inside a CFD code, due to the added computational cost. Therefore, it may be necessary to develop a simplified version of the model for use in the CFD code.

In CFD models, simplified techniques are most commonly used to facilitate phase equilibrium predictions. The models employed by Rzehak and Krepper (2016), Fletcher et al. (2017), and many others (Darmana et al., 2005; Talvy et al., 2007; Wang and Wang, 2007; Gong et al., 2010; Gruber et al., 2015) employed a Henry's law relationship to determine the interfacial mass fraction. This is also common in the integral models described earlier. For simplifying the code and improving runtime, especially when local resolution cannot be attained, this method can be employed. Therefore, this approach is likely to be most applicable to undersea gas release modeling with CFD.

The other phenomenon that must be considered in a gas release is the possible formation of gas hydrates or ice. Hydrate formation is governed by heat transfer, mass transfer and phase equilibrium, and it would be necessary to account for this this phenomenon by incorporating appropriate thermodynamic relationships into the CFD model. If hydrate or ice formation are expected to occur, it would likely be necessary to incorporate empirical models into the code. For shallow water releases, such as those considered in Chapter 7,

hydrates are not expected to form. Despite a high well pressure, the ambient pressure would not be in the range to maintain formed hydrates further toward the surface. Therefore, while they may form, they will not persist, and will not have a chance to impact the gas release itself.

5.9 Conclusions

The importance of predicting the fate of underwater blowouts cannot be understated. Even if the risk is low, a worst-case scenario must be assumed, and an environmental protection zone must be defined to develop emergency response plans. The depressurization of a well can contain immiscible liquids and gas and be released at low temperatures. Since experiments at such scales are very difficult, modeling can provide an alternative with which to assess the problem. However, the difficulty is to construct and validate an adequate model. Currently, integral models are preferred for such studies, but they do not capture the microscopic interactions or transient behaviour of the release. On the other hand, CFD has the potential to investigate small-scale interactions of the fluids in a realizable way. However, CFD models for such complex situations and large scales are still actively being developed, and therefore no single approach is the obvious choice.

LPT models track the movement of individual bubbles or particles as they move through the continuous fluid. Particle motion is described by a balance of forces, with coupling to the continuous phase. The advantage of these methods is their conceptual simplicity, but computational time increases with the resolution and number of particles, and numerical algorithms can be relatively complex. However, since the particles are on a background grid, the continuous phase can often be modeled on a relatively coarse Eulerian mesh.

Eulerian multi-fluid models are also commonly used for dispersed multiphase flow modeling. By ensemble averaging, the governing equations are split and are allowed to interpenetrate each other. Like LPT methods, the coupling of phases is handled through a balance of forces on the dispersed particles. These forces often cannot be resolved and must be treated by closure models. The main disadvantage of these models is that the validity of the closure laws has only been evaluated for some systems, and therefore the error introduced by scaleup is unknown.

Interface tracking methods directly resolve the phase boundary within the mesh. The cost of these methods is the required mesh resolution to limit interface smearing. Although such models are useful for the direct prediction of complex phenomena such as breakup and coalescence, their computational cost is typically too high for large-scale systems with complex interfaces. On the scales of an undersea gas release, interface tracking may therefore not be the best option to model the entire domain. However, these methods may be useful for modeling the gas jet and plume development in the near-field region.

In practice, a release is not simply a plume. Depending on the pressure in the well, and the exit velocity at the wellhead, the momentum imparted will define a significant jet region. For shallow waters, this jet region may not be a negligible portion of the release pathway. Integral models, Lagrangian particle tracking models and multi-fluid models usually neglect this region, due to a lack of techniques to model them. However, continuous phases, traveling with the momentum imparted from the well, can be modeled by interface tracking. Depending on the depth of the well, the jet region will provide better initial conditions for the plume region in terms of bubble size and gas fraction profiles. In this way, multiscale modeling could compensate for the weaknesses in different types of models. For interface tracking methods, limiting application to the jet region means that refinement only needs to be concentrated in a specific zone, and the amount of refinement is less due to the continuous nature of the flow. In the far field, when dispersion of the phases prevents interface tracking, another type of model could be used on a coarser grid predict plume behaviour.

In summary, there are many CFD techniques that could be used for subsea gas release modeling. Interface tracking methods are promising for the prediction of jet behaviour in the near-field region. LPT, E-L and mixture models could all be used to model phenomena in the plume region. However, an area that is underdeveloped is jet modeling as it applies to the dissolution rate. A multiscale model that couples an interface tracking model with one of these dispersed flow models may be a good method for predicting the behaviour of the gas phase. Therefore, the development and application of one such model, coupling VOF interface capturing with a mixture model, is the focus of the remainder of this thesis.

Chapter 6

The Development of a Multiscale Model for

Underwater Gas Releases

6.1 Introduction

Gas streams may be inadvertently released into the ocean from undersea transportation pipelines and wells at offshore gas processing facilities. When a pressurized gas enters the water column it depressurizes rapidly, and three zones are formed: a jet region, a plume region and a surface region. The jet region is characterized by a continuous flow of gas due to the momentum resulting from the high pressure at the injection point. The jet region eventually transitions to the plume region as the momentum dissipates into the surrounding liquid and small bubbles are formed. This transition is not sharp and can occur over a significant distance. Heat and mass transfer can occur in all regions. The jet region typically contains low interfacial area, but mixing rates are generally high due to the high velocity. The plume region contains high interfacial area, but local mixing rates are reduced. Therefore, both regions can contribute significantly to the overall transfer rates. The surface region may also contribute significantly to interphase transfer, but its contribution is more difficult to characterize because it is often influenced by external conditions. The focus of this study is on developing a multiscale model for the jet and plume regions.

The contributions of the jet region on the plume region's initial conditions are often overlooked. The jet region is assumed to be negligible, even though the continuous region can have an impact on how the breakup will occur, as well as contribute to the mass transfer in the entire system. With modern computing, multiscale modeling is a possible solution. The length scales resolved in the jet region are larger than those in the dispersed region, as the jet itself will be a continuous phase. Therefore, the coupling of a suitable IT in the near-field region will help to eliminate the assumption that the entire release may be treated as a bubbly plume. In the dispersed region, using a dispersed phase model (Euler-Euler, Lagrangian particle tracking, or mixture model) reduces computational requirements.

124

Most of the information about suitable modeling approaches is already provided in Chapter 6. However, there are several options for model coupling. A general overview will be given below, starting with the coupling of IT and E-E dispersed phase model, followed by the coupling IT and LPT models, and finally discussing the novel linkage between the volume-of-fluid (VOF) and the mixture models.

Wardle and Weller (2013) have used a (VOF) method combined with a multi-fluid approach to simulate segregated and dispersed liquid-liquid systems. The method employed by the authors utilizes primarily an E-E approach, using phase-averaged equations to solve for the fluid motion. For situations involving segregated flows the VOF compressive interface method (see Chapter 4) is used in place of the relative velocity closure term. The choice of when to switch between the models is determined by blending the phase fraction into regions where for certain values the flow is treated as VOF and for others it is treated as E-E. This addition enables the model to resolve free surface flows. Such models are becoming more common and are even included in commercial E-E CFD codes (ANSYS, 2011). As noted by Wardle and Weller (2013), the downside of the compressive closure term is the production of parasitic currents at the interface.

IT methods have also been utilized to predict free surface and segregated flows for LPT models. In this methodology, the continuous fluid is modeled directly on an Eulerian grid, while the small-scale particles are resolved using discrete trackers in the domain. The advantage of this method is the capacity to utilize less resolution for the Eulerian grid, at the cost of coupling terms which are typically solely from continuous to dispersed. However, the computational cost in general is increased when compared to E-E based methods due to the need to track a large number of particle clusters (Fraga et al., 2016). This model has been used to simulate bubbly flows in the literature (Sungkorn et al., 2011; Fraga et al., 2016; Wutz et al., 2016), although typically the multiscale aspect refers to the size of the bubble distribution against the surrounding domain. A more unique use has been employed by Municchi and Radl (2017) in order to utilize immersed boundary solvers (such as VOF) to accelerate interfacial force convergence on packed particles. Although primarily for suspended particles, this model approaches the concept of linking multiple regimes in the same solution domain.

The effect of the continuous phase on the particles is always included in model implementations (Sungkorn et al., 2011; Fraga et al., 2016; Wutz et al., 2016). The continuous phase acts as a background field for the particle conservation equation, for which the particles can be moved by bulk advection of the continuous phase. The reverse coupling for the momentum terms is more problematic. For heat and mass transfer applications, correlations provided in Chapter 5 are viable.

Other multiscale models have also been employed. For cavitating flows, Ma et al. (2017) have proposed the use of a level-set (LS) method to resolve the liquid phase in continuous segments, while a discrete singularity model (DSM) was used to model the dispersed bubbles with a Lagrangian tracking method. LS methods are within the family of Eulerian interface capturing models, which are comparable to VOF but with the interface is embedded as a function set to be zero at the interface itself. The primary benefit is the sharp interface resolution. The downside is computational time expended to ensure that the zero level set actually corresponds to the interfacial location.

The objective of this chapter is to develop another type of multiscale modeling approach that combines the volume-of-fluid method for direct simulation of interface dynamics in high mesh resolution zones with a drift-flux method for dispersed flow modeling in zones with poor mesh resolution. The model is intended to be scalable, such that the transition between VOF and drift-flux modeling is automatically controlled based on mesh resolution and phase fraction. For gas injection into liquids, this will usually mean that some of the jet region will be resolved by VOF, while the plume region will be modeled using the drift-flux model. However, for high resolution meshes, portions of the plume region would also be resolved using VOF.

The convenience of combining VOF with the drift-flux approach is that both models apply the one-fluid methodology, though the nuances are distinct. For VOF, the interfacial forces are resolved directly if the interface can be resolved and confined to a small number of cells. However, the number of cells required to attain this accuracy can be immense for a fully-resolved bubble, and thus the model is of little practical use in regions where there is no clear segregation between the phases (i.e. dispersed flow). By comparison, the drift-flux

model employs mixture-averaged properties with additional closure relationships to model the slip and drift velocities of the gas phase through a balance of forces. The caveat is a theoretical limit on the applicability of the empirical models that are used to determine the slip and drift velocities, as well as the assumptions about the bubble size distribution.

The presented model also uses two distinct modeling approaches to resolve interphase mass transfer. In the regions governed by the VOF method, the local contacting time is combined with penetration theory to develop a mass transfer coefficient model. Conversely, empirical mass transfer correlations are combined with the bubble slip velocity in regions where the drift-flux model is applied. A mixture-averaged formulation is used for the energy equation, and therefore interphase energy transfer is included through a volumetric source term. In this study, the drift-flux modeling approach was first validated through comparison to a published dataset involving the rise and dispersion of a bubble plume in a cylindrical tank. The combined fluid dynamics model and mass transfer modeling approach were then tested through comparison with an published dataset for aeration in a rectangular tank by horizontal gas injection.

6.2 Methodology

The model was implemented using OpenFOAM, an open source CFD toolbox (The OpenFOAM Foundation, 2018). The standard solver library in OpenFOAM includes a solver for incompressible drift-flux modeling, `driftFluxFoam`, and a solver that employs a compressible formulation of the volume-of-fluid method, `compressibleInterFoam`. These two solvers formed the basis of the developed code, but extensive reformulation was necessary to couple the two methods and include interphase mass transfer.

6.2.1 Volume-of-Fluid Method

The compressible VOF model is formulated based on the phase continuity equation:

$$\frac{\partial(\alpha_i \rho_i)}{\partial t} + \nabla \cdot (\alpha_i \rho_i \vec{u}) = S_i \tag{6.1}$$

where α_i, ρ_i, and $\vec{u}_i$ are the phase fraction, density and velocity of phase i. The mass source term, S_i, can either be positive or negative depending on the direction of mass transfer. For

the discussion presented below, the gas phase was assumed to be the primary phase (phase 1), while the liquid phase was specified to be secondary (phase 2). A mass source leaving the liquid phase and transferring to the gas phase is arbitrarily set to be positive. Although this choice does not affect the overall formulation of the model, since it would only change the sign in the phase continuity equation, it facilitates the description of the model. Further, although the present study is restricted to two-phase flow, a similar approach could be applied for more phases.

The summation of any number of phase continuity equations produces the overall continuity equation:

$$\frac{\partial \rho}{\partial t} + \nabla \cdot (\rho \vec{u}_m) = 0 \tag{6.2}$$

in which the mixture density is defined by

$$\rho = \sum_i \alpha_i \rho_i \tag{6.3}$$

and the velocity is mass averaged

$$\vec{u}_m = \frac{1}{\rho} \sum_i (\alpha_i \rho_i \vec{u}_i) \tag{6.4}$$

In the OpenFOAM implementation of the VOF method, the phase continuity equation is rearranged to split the compressible terms and the incompressible terms. For phase 1, the continuity equation is

$$\frac{\partial \alpha_1}{\partial t} + \nabla \cdot (\alpha_1 \vec{u}_1) = \frac{S_1}{\rho_1} - \frac{\alpha_1}{\rho_1} \left[\frac{\partial \rho_1}{\partial t} + \vec{u}_1 \cdot \nabla \rho_1 \right] \tag{6.5}$$

where the source term assumes transfer is specified to be positive from phase 2 to phase 1, and the compressible terms are included as the last set of terms on the right side.

The volume-averaged velocity is defined as:

$$\vec{u} = \sum_i (\alpha_i \vec{u}_i) \tag{6.6}$$

Using the inter-gamma scheme (Gopala and Wachem, 2008) leads to the following substitution on the left side of the equation:

$$\frac{\partial \alpha_1}{\partial t} + \nabla \cdot (\alpha_1 \vec{u}_1) + \nabla \cdot (\alpha_1 \vec{u}) - \nabla \cdot (\alpha_1 \vec{u}) = \frac{S_1}{\rho_1} - \frac{\alpha_1}{\rho_1} \left[\frac{\partial \rho_1}{\partial t} + \vec{u}_1 \cdot \nabla \rho_1 \right] \tag{6.7}$$

This equation can be rearranged into the following form using the definition of the relative velocity for the VOF method $\left(\vec{u}_{R,VOF} = \vec{u}_1 - \vec{u}_2\right)$:

$$\frac{\partial \alpha_1}{\partial t} + \nabla \cdot (\alpha_1 \vec{u}) + \nabla \cdot \left(\alpha_1 \alpha_2 \vec{u}_{R,VOF}\right) = \frac{S_1}{\rho_1} - \frac{\alpha_1}{\rho_1}\left[\frac{\partial \rho_1}{\partial t} + \vec{u}_1 \cdot \nabla \rho_1\right] \qquad (6.8)$$

The relative velocity term cannot be evaluated directly and is instead based on a constitutive relationship, which will be explained later. Since the summation of the phase continuity equation defines the divergence of the velocity, an integral component of pressure-velocity coupling in the PISO algorithm is strong coupling between the phase fraction and the velocity and pressure fields. To facilitate this coupling, the following substitutions are made on the right side:

$$\frac{\partial \alpha_1}{\partial t} + \nabla \cdot (\alpha_1 \vec{u}) + \nabla \cdot \left(\alpha_1 \alpha_2 \vec{u}_{R,VOF}\right) = \frac{S_1}{\rho_1} - \frac{\alpha_1}{\rho_1}\left[\frac{\partial \rho_1}{\partial t} + \vec{u}_1 \cdot \nabla \rho_1\right] + \alpha_1 \nabla \cdot \vec{u}$$

$$-\alpha_1 \nabla \cdot \vec{u} \qquad (6.9)$$

One of the added terms can be expanded in order to account for the compressibility effects of the second phase:

$$\frac{\partial \alpha_1}{\partial t} + \nabla \cdot (\alpha_1 \vec{u}) + \nabla \cdot \left(\alpha_1 \alpha_2 \vec{u}_{R,VOF}\right) = S_1\left(\frac{1}{\rho_1} - \alpha_1\left(\frac{1}{\rho_1} - \frac{1}{\rho_2}\right)\right) - \frac{\alpha_1 \alpha_2}{\rho_1}\left[\frac{\partial \rho_1}{\partial t} + \vec{u}_1 \cdot \nabla \rho_1\right] +$$

$$\frac{\alpha_1 \alpha_2}{\rho_2}\left[\frac{\partial \rho_2}{\partial t} + \vec{u}_2 \cdot \nabla \rho_2\right] + \alpha_1 \nabla \cdot \vec{u} \qquad (6.10)$$

which is the form of the equation used in the compressible VOF family of solvers in OpenFOAM and described in detail in Chapter 3. This form is used to stabilize the equation since the divergence in the solution for the pressure will rely on the contributions from both phases. The remaining divergence is included explicitly and will tend toward the expanded terms through iteration.

Since the use of cell centered velocities and pressures can lead to decoupling of these fields, OpenFOAM uses divergence free face fluxes. The volumetric face flux, Φ, is defined as

$$\Phi = \vec{u}_f \cdot \vec{A}_f \qquad (6.11)$$

where the velocity field is interpolated to the cell faces ($\vec{u}_f$) and then multiplied by the face areas, $\vec{A}_f$, to obtain volumetric flowrate leaving the cell at each face. The velocity face field, Φ_c, is obtained by dividing the volumetric flow by the magnitude of the area:

$$\Phi_c = \frac{\Phi}{|\vec{A}_f|} \tag{6.12}$$

In the VOF method in OpenFOAM, the relative flux (Φ_R) with respect to the interface is

$$\Phi_R = \Phi_c \cdot \hat{n}_f \tag{6.13}$$

where,

$$\hat{n}_f = \frac{(\nabla \alpha_1)_f}{|(\nabla \alpha_1)_f|} \cdot \vec{A}_f \tag{6.14}$$

which represents the unit interfacial normal. This is a numerical constitutive term, added to stabilize the flow near the interface. This term can be discretized independently of the motion due to volume-averaged velocity and can be corrected through a compressive term (defaulted to unity).

6.2.2 Drift-Flux Method

In the drift-flux method, the phase continuity equation is still given by equation 6.1 (Ishii and Hibiki, 2010). Again, splitting the compressible and incompressible terms gives equation 6.5. The velocity of phase i can then be written in terms of the average velocity and the drift velocity as (Ishii and Hibiki, 2010; Manninen et al., 1996):

$$\vec{u}_i = \vec{u} + \vec{u}_{ik} \tag{6.15}$$

where $\vec{u}_{ik}$ is the drift velocity of phase i relative to phase center of volume denoted as k. Introducing this term for phase 1 yields

$$\frac{\partial \alpha_1}{\partial t} + \nabla \cdot (\alpha_1 \vec{u}_1) + \nabla \cdot (\alpha_1 \vec{u}_{1k}) = \frac{S_1}{\rho_1} - \frac{\alpha_1}{\rho_1}\left[\frac{\partial \rho_1}{\partial t} + \vec{u}_1 \cdot \nabla \rho_1\right] \tag{6.16}$$

If phase 1 is the dispersed phase, the drift velocity is related to the relative velocity for the DF method by a factor of the continuous phase fraction $(\vec{u}_{1k} = \alpha_2 \vec{u}_{R,DF})$. Therefore,

$$\frac{\partial \alpha_1}{\partial t} + \nabla \cdot (\alpha_1 \vec{u}_1) + \nabla \cdot (\alpha_1 \alpha_2 \vec{u}_{R,DF}) = \frac{S_1}{\rho_1} - \frac{\alpha_1}{\rho_1}\left[\frac{\partial \rho_1}{\partial t} + \vec{u}_1 \cdot \nabla \rho_1\right] \tag{6.17}$$

130

Equation 6.17 has the same form as for the VOF method (equation 6.8). The equations are identical except that the closure model for the relative velocity is formulated differently.

In the drift-flux model, the closure term for the relative velocity is related to the balance of forces acting on a particle of known diameter (Manninen et al., 1996). The force balance on the particle can be complicated, but the general form is a balance of interfacial forces and buoyancy:

$$\sum \vec{F}_{int} = V_b \frac{(\rho_1 - \rho)}{\rho} \nabla P - \vec{F}_t \tag{6.18}$$

where V_b is the volume of the bubble, and $\vec{F}_t$ comprises the turbulent forces acting on the bubble. The left side is a summation of interfacial forces similar to those employed in multi-fluid models. On the right side, the gradient of pressure can be replaced by rearranging the momentum equation (Manninen et al., 1996), and $\vec{F}_t$ is the turbulent dispersion force. Thus,

$$\sum \vec{F}_{int} = V_b \frac{(\rho_1 - \rho)}{\rho} \rho \left(\vec{g} - \frac{d\vec{u}}{dt} - \nabla \cdot (\vec{u}\vec{u}) \right) - \vec{F}_t \tag{6.19}$$

where $\vec{g}$ is the gravity vector. In this study, only drag and lift are considered in the force balance. The drag and lift force can be written as (see, for example, Dhotre et al. (2007, 2009)),

$$\frac{\vec{F}_{drag}}{V_b} = \frac{3\alpha_1 \rho_2 C_D}{4 d_b} |\vec{u}_{R,DF}| \vec{u}_{R,DF} \tag{6.20}$$

$$\frac{\vec{F}_{lift}}{V_b} = \alpha_1 \rho_2 C_l \vec{u}_{R,DF} \times (\nabla \times \vec{u}) \tag{6.21}$$

where $\vec{F}_{drag}$ is the force due to drag, C_D is the drag coefficient, d_b is the bubble diameter, and C_l is the lift coefficient. The resulting force balance yields

$$\vec{u}_{R,DF} = \frac{4 d_b (\rho_1 - \rho)}{3 \rho_2 C_D |\vec{u}_{R,DF}|} \left(\vec{g} - \frac{d\vec{u}}{dt} - \nabla \cdot (\vec{u}\vec{u}) \right) - \frac{4 d_b C_l}{3 C_D |\vec{u}_{R,DF}|} \vec{u}_{R,DF} \times (\nabla \times \vec{u})$$
$$- \vec{u}_{t,DF} \tag{6.22}$$

where $\vec{u}_{t,DF}$ is the turbulent dispersion velocity. The turbulent dispersion velocity can be written as:

$$\vec{u}_{t,DF} = \frac{D_{M1}}{\alpha_1} \nabla \alpha_1 \tag{6.23}$$

131

where D_{M1} is a turbulent dispersion/diffusion coefficient. Determination of the most suitable correlation for D_{M1} is not straightforward. Generally, it should be interpreted as a tuned parameter. One form is provided by Burns et al. (2004), and was also used by Li et al. (2010) and Fletcher et al. (2017). In this case,

$$D_{M1} = \alpha_1 C_{TD} C_D \frac{v_{2,t}}{Sc_t} \left(\frac{\nabla \alpha_1}{a_1} - \frac{\nabla \alpha_2}{\alpha_2} \right) \tag{6.24}$$

where C_{TD} is a tuning parameter, Sc_t represents a turbulent Schmidt number in the continuous phase, and $v_{2,t}$ is the turbulent kinematic viscosity in the continuous phase. In this study, turbulent Schmidt number was assumed to be unity and C_{TD} was determined by fitting to experimental data for plume dispersion.

Since the turbulent dispersion velocity does not depend on the relative velocity, it can be included in the phase continuity equation as a separate term. Therefore, the phase continuity equation is solved as

$$\frac{\partial \alpha_1}{\partial t} + \nabla \cdot (\alpha_1 \vec{u}) + \nabla \cdot (\alpha_1 \alpha_2 \vec{u}_{R,DF}) = S_1 \left(\frac{1}{\rho_1} - \alpha_1 \left(\frac{1}{\rho_1} - \frac{1}{\rho_2} \right) \right) - \frac{\alpha_1 \alpha_2}{\rho_1} \left[\frac{\partial \rho_1}{\partial t} + \vec{u}_1 \cdot \nabla \rho_1 \right] +$$

$$\frac{\alpha_1 \alpha_2}{\rho_2} \left[\frac{\partial \rho_2}{\partial t} + \vec{u}_2 \cdot \nabla \rho_2 \right] + \alpha_1 \nabla \cdot \vec{u} + \nabla \cdot (D_{M1} \nabla \alpha_1) \tag{6.25}$$

The relative velocity must be determined from equation 6.22, without the turbulent dispersion term:

$$\vec{u}_{R,DF} = \frac{4 d_b (\rho_1 - \rho)}{3 \rho_2 C_D |\vec{u}_{R,DF}|} \left(\vec{g} - \frac{d\vec{u}}{dt} - \nabla \cdot (\vec{u}\vec{u}) \right) - \frac{4 d_b C_l}{3 C_D |\vec{u}_{R,DF}|} \vec{u}_{R,DF} \times (\nabla \times \vec{u}) \tag{6.26}$$

This expression requires iterative solution for the relative velocity. In this study, fixed-point iteration was used to solve for the relative velocity during solution because it was the simplest and most stable iterator. However, this iteration can approach unstable values during the solution without careful control of the time step when the velocity and pressure fields are highly dynamic.

6.2.3 Combined VOF and DF Method

As shown above, the VOF and drift-flux formulation have nearly identical expressions for the phase continuity equation (equations 6.10 and 6.25). Therefore, a blending scheme can be employed to combine the two methods. The two formulations can be filtered using a

fraction that can depend on the local phase fraction, spatial location, and any other terms that might affect transitions between the suitability of the methods. The filter, χ, can be introduced into the combined phase continuity equation to give

$$\frac{\partial \alpha_1}{\partial t} + \nabla \cdot (\alpha_1 \vec{u}) + \nabla \cdot \left(\alpha_1 \alpha_2 [\chi \vec{u}_{R,VOF} + (1 - \chi) \vec{u}_{R,VOF}]\right) = S_1 \left(\frac{1}{\rho_1} - \alpha_1 \left(\frac{1}{\rho_1} - \frac{1}{\rho_2}\right)\right) -$$

$$\frac{\alpha_1 \alpha_2}{\rho_1} \left[\frac{\partial \rho_1}{\partial t} + \vec{u}_1 \cdot \nabla \rho_1\right] + \frac{\alpha_1 \alpha_2}{\rho_2} \left[\frac{\partial \rho_2}{\partial t} + \vec{u}_2 \cdot \nabla \rho_2\right] + \alpha_1 \nabla \cdot \vec{u} + \nabla \cdot \left((1 - \chi) D_{M1} \nabla \alpha_1\right) \qquad (6.27)$$

In this study, the filter fraction was assigned a value of 0 or 1 based on the local gas phase fraction. Based on experience with VOF simulations and fitting, the criteria used in this study were $\chi = 1$ for $\alpha_1 < 0.3$ and $\chi = 0$ for $\alpha_1 > 0.3$. If the interface exists at fractions nearing 0.5, using the drift flux up to that limit will destabilize the compressive interface terms in the VOF equation. This would immediately smear the interface. However, the phase fraction should be allowed to disperse if the interface becomes diffuse on its own. This is analogous to shear effects acting in proximity with the interface.

6.2.4 Solution of the Velocity and Pressure Equations

The momentum equation solved is as follows,

$$\frac{\partial (\rho \vec{u})}{\partial t} + \nabla \cdot (\rho \vec{u} \vec{u}) + \nabla \cdot (\tau + (1 - \chi) \tau_{DF}) = -\nabla P + \rho \vec{g} + \vec{F}_{ST} \qquad (6.28)$$

where P is the pressure field, assumed to be shared between the phases, and $\vec{F}_{ST}$ is the surface tension force. The exact decomposition of this equation into the form that is compatible with the PISO (Pressure Implicit with Split Operators) method is detailed in Chapter 3. Finally, τ is the viscous stress tensor, which is valid in both phases with the addition of an extra stress term in the drift-flux model to compensate for the diffusion velocity ($\vec{u}_{iM}$). Ishii and Hibiki (2010) have written this as

$$\vec{u}_{1M} = -\frac{\alpha_2 \rho_2}{\rho} \vec{u}_{R,DF} \qquad (6.29)$$

The source term is defined as

$$\tau_{DF} = \sum_i \alpha_i \rho_i \vec{u}_{iM} \vec{u}_{iM} \qquad (6.30)$$

However, since the velocity is volume averaged instead of mass averaged, the drift velocity is used instead (Manninen et al., 1996):

$$\tau_{DF} = -\sum_i \alpha_i \rho_i \vec{u}_{ik} \vec{u}_{ik} \tag{6.31}$$

$$\vec{u}_{1k} = \alpha_2 \vec{u}_{R,DF} \tag{6.32}$$

$$\vec{u}_{2k} = -\frac{\alpha_1}{\alpha_2} \vec{u}_{1k} \tag{6.33}$$

Additionally, the viscous stress tensor can be written as

$$\tau = -\mu_{eff}(\nabla \vec{u} + (\nabla \vec{u})^T) \tag{6.34}$$

where μ_{eff} is the effective dynamic viscosity, which will be shown later.

6.2.5 Interphase Heat and Mass Transfer

The treatment of heat and mass transfer must be tailored to be consistent with the hybrid VOF-DF method described above. A volume-averaged energy equation will be used, and therefore no closure terms are required for interphase heat transfer aside from an energy source due to interphase mass transfer. Phase-averaged species equations are solved, with interphase mass transfer closure models selected to reflect the hybrid VOF-DF approach. The energy equation solved is

$$\frac{\partial(\rho c_v T)}{\partial t} + \nabla \cdot (\rho c_v T \vec{u}) + \frac{\partial(\rho E_k)}{\partial t} + \nabla \cdot (\rho E_k \vec{u}) + \nabla \cdot (\vec{u}P) = \nabla \cdot (K_{eff} \nabla T)$$

$$+ S_E \tag{6.35}$$

where c_v represents the specific heat capacity at constant volume, T is the temperature, $E_K = \frac{1}{2}\vec{u}^2$ is the kinetic energy, K_{eff} is the thermal conductivity, and S_E is the source term due to interphase mass transfer, which is set equal to

$$S_E = \sum_j S_{M,j}(\Delta H_{sol} - RT) \tag{6.36}$$

where $S_{M,j}$ is the mass source for species j, ΔH_{sol} is the heat of dissolution, modified by the ideal gas law to make it consistent with the formulation of the energy equation. The internal energy (e) is derived from

$$\tag{6.37}$$

$$e = \int_{T_{ref}}^{T} c_v dT$$

134

The reference temperature may be taken as 0 K and that the value of the heat capacity is constant for a given time step, reducing the expression to $e = c_v T$ where $c_v = \sum_i \alpha_i c_{v,i}$. The conduction term, expanded using Fourier's law, is based on the combination of the thermal conductivities of both phases and a turbulent contribution:

$$K_{eff} = \sum_i \alpha_i \left[K_i + \frac{\mu_{t,i}}{c_{p,i}} \frac{1}{Pr_{t,i}} \right] \tag{6.38}$$

where K_i is to the thermal conductivity in phase i, and the second term is the turbulent contribution to the thermal conductivity based upon the turbulent dynamic viscosity ($\mu_{t,i}$), the heat capacity at constant pressure ($c_{p,i}$), and $Pr_{t,i}$ is the turbulent Prandtl number. The species equations for each phase are:

$$\frac{\partial(\alpha_i \rho_i Y_{i,j})}{\partial t} + \nabla \cdot (\alpha_i \rho_i Y_{i,j} \vec{u}) - \nabla \cdot (\alpha_i \rho_i D_{i,M,jEff} \nabla Y_{i,j}) = S_{M,j} \tag{6.39}$$

where $Y_{i,j}$ represents the mass fraction of component j in phase i. $D_{i,M,jEff}$ is the total diffusion coefficient, which is based on the combination of molecular and turbulent mass diffusivities:

$$D_{i,M,jEff} = D_{i,M,j} + D_{t,i} \tag{6.40}$$

$$D_{t,i} = \frac{v_{t,i}}{Sc_{t,i}} \tag{6.41}$$

The turbulent mass diffusivity is based on the turbulent kinematic viscosity and the specification of a turbulent Schmidt number, $Sc_{t,i}$. In cases of high turbulence, the Schmidt number is assumed to have a value of one.

The mass source, and consequently the energy source, were derived to be consistently formulated to streamline implementation. The assumption for this study is that the gas side has a negligible mass transfer resistance compared to the liquid side. In jet flows and plume flows, as discussed in Chapter 5, the form of the mass transfer coefficient that lends itself to both continuous and dispersed regions would be a penetration or surface renewal model. In general, the species source at the interface is

$$S_{M,j} = -\alpha_2 \rho_2 K_2 a \left(Y_{2,j}^* - Y_{2,j} \right) \tag{6.42}$$

where $Y_{2,j}^*$ is the liquid-side mass fraction of species j in equilibrium with the gas phase. The term $K_2 a$ is the overall mass transfer coefficient. The interfacial area density, a, can be written as

$$a = \begin{cases} V^{1/3} & \chi = 1 \text{ (VOF)} \\ \frac{6\alpha_1}{d_b} & \chi = 0 \text{ (DF)} \end{cases} \tag{6.43}$$

For the simulations presented in this work, there are two available mass transfer coefficient correlations (K_2). The first, which represents the Higbie model, is shown below:

$$K_2 = 2\sqrt{\frac{D_{i,M,j}}{\pi\lambda}} \tag{6.44}$$

This model is useful for clean interfaces. However, the model of Frössling has been shown to be more suitable for contaminated interfaces (Alves et al., 2005):

$$K_2 = 0.6\sqrt{\frac{1}{\lambda}}\left(D_{i,M,j}\right)^{2/3}(\nu_2)^{-1/6} \tag{6.45}$$

where ν_2 is the kinematic viscosity is that of the liquid. This form is more reasonable for contaminated (immobile) interfaces. The term λ represents the renewal or penetration time and varies depending on χ. For the DF model ($\chi = 1$),, the method of Higbie is used (Alves et al., 2006; Wang and Wang, 2007):

$$\lambda = \frac{d_b}{\bar{u}_R} \tag{6.46}$$

For the VOF model ($\chi = 0$), an alternative approach is used:

$$\lambda = \frac{\Delta t}{Co_{local}} \tag{6.47}$$

which relates the time step, Δt, to the actual fractional time spent in the cell at a given velocity, or the Courant Number (Co_{local}). This term is similar to that of Higbie. However, since the interface is captured when the VOF model is active, the source term is further limited to cells containing the 0.5 contour (similar to the work in Chapter 3).

6.2.6 Turbulence Model

As discussed in Chapter 4, turbulence modeling is important for many practical engineering applications. Due to the closure terms in the above model, the turbulence model must also act in tandem with the interfacial forces. The calculation of the turbulent mass diffusivity and thermal conductivity also rely on the choice of turbulence model.

As mentioned in Chapter 4, LES models are a common choice in recent studies. Indeed, Dhotre et al. (2009) have also validated their work with a LES model, and compared predictions to results from a RANS model (Dhotre et al., 2007). They found reasonable agreement between the two models.

The Smagorinsky model was employed in this study:

$$\mu_t = \rho C_s^2 V^{2/3} |\bar{S}| \tag{6.48}$$

$$|\bar{S}| = \frac{1}{2} \nabla \cdot \bar{\bar{u}} \tag{6.49}$$

where C_s is a tuned parameter, often referred to as the Smagorinksy coefficient. The term $|\bar{S}|$ refers to the subgrid stress calculated from the filtered velocity, $\bar{\bar{u}}$. The turbulent kinematic viscosity is important in defining the turbulent dispersion, as well as the turbulent mass and energy transfer. In addition, the viscosity is further modified to include bubble induced turbulence (BIT) by (from Chapter 5)

$$\mu_{eff} = \mu + \mu_t + \mu_{BIT} \tag{6.50}$$

$$\mu_{BIT} = C_{BIT} \alpha_1 \rho_2 d_b |\vec{u}_R| \tag{6.51}$$

where the coefficient C_{BIT} is a tuned parameter set equal to 0.6 in the current study based on the work of Dhotre et al. (2007; 2009).

6.2.7 Numerical Solution Algorithm

The algorithm used to solve the model is shown in Figure 6.1. The solver, now called `compressibleDriftInterFoamHTMT`, first reads key variables (T, P_{rgh}, $\bar{u}$, Y_{ij}, α) and then constructs two libraries. The first library handles phase mixture calculations and stores the thermodynamic models for each phase (correlations for K, c_v, c_p). The second

library stores routines associated with the relative velocity. This library begins by gathering the necessary components (d_b, C_D, C_l) and predicting the relative velocity. This is accomplished by iterating over equation 6.26 to solve for the drift velocity and the relative velocity. The relative velocity is then passed to the solver to start the timeloop.

In the time loop, the phase continuity, with a substep to solve for the turbulent dispersion (since the MULES algorithm, as detailed in Chapter 4, does not provide an effective way to do so), is solved using equation 6.27. The volume-averaged properties are updated (density, *etc*), and the filter value is set based on the current phase fractions. The momentum equation (equation 6.28) is constructed (or solved), and then the energy equation (equation 6.35) is solved. At this point, the temperature and pressure dependencies of the properties are updated. Finally, the inner PISO correction takes the constructed velocity equation and solves pressure to enforce continuity.

To complete the time step, the mass transfer rates are calculated in each cell for each component j (equation 6.42). The species equations are then solved (equation 6.39). This step takes place outside of the PISO loop for stability, since subtle perturbations due to the composition shifts can cause numerical instability in the property calculations based on temperature and pressure.

Once the species equations are solved, the bubble induced turbulence is updated. At the end of the time step, any necessary print variables are stored before the cycle begins anew. Time stepping continues until the specified end time is reached.
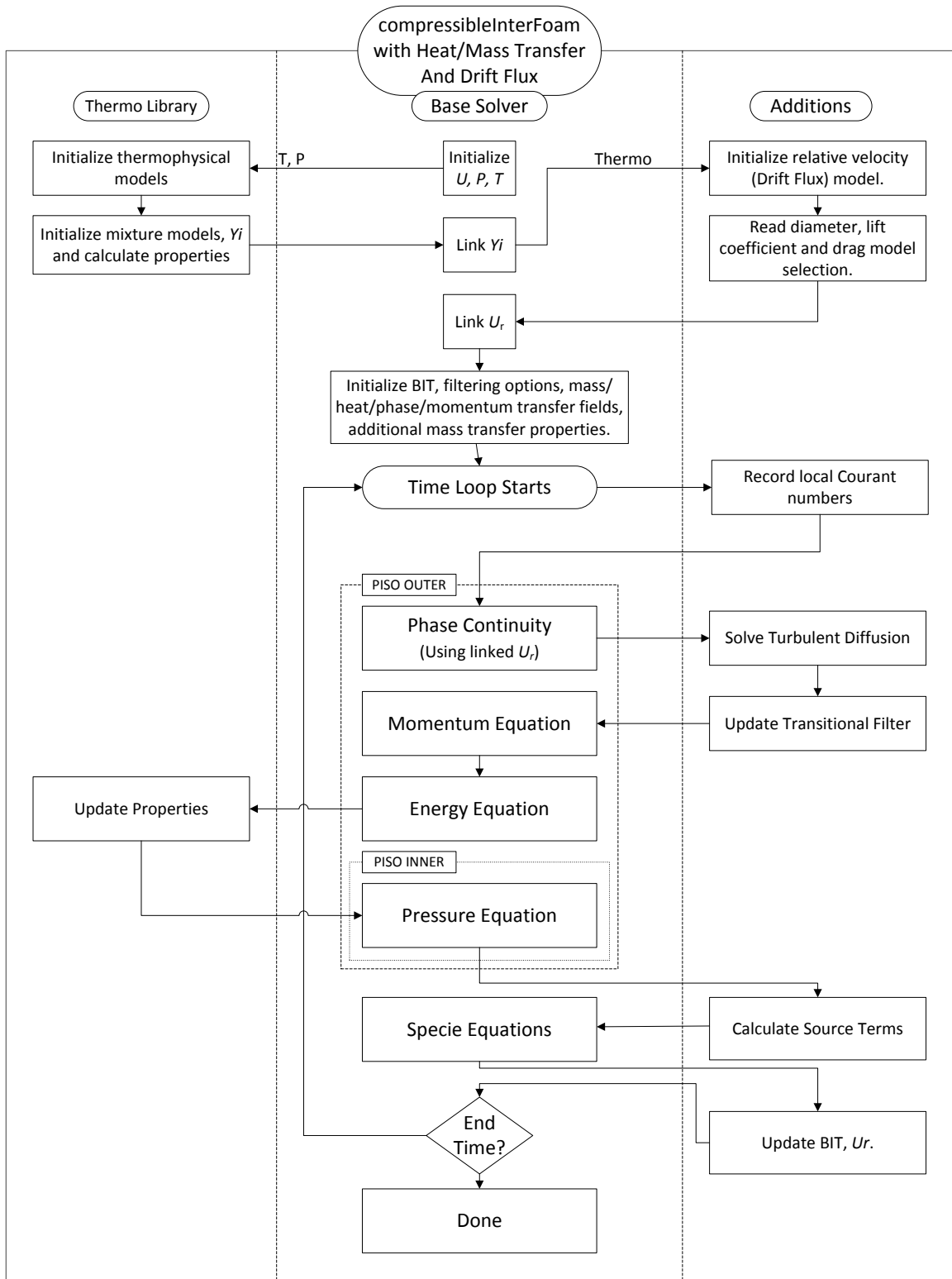
Figure 6.1 Algorithm for the VOF-DF coupled model.

6.3 Validation

Two simulation cases were used to demonstrate the validity of the new modeling approach, and to investigate sensitivity to the tuned parameters. The first case was a comparison to the simulation studies in Dhotre et al. (2007, 2009), which used the data from Simiano et al. (2005). This case involved a vertical plume of bubbles released into a large cylindrical tank with a free surface. The primary objective of this study was to tune the turbulent dispersion coefficient (C_{TD}), for use in subsequent case studies. The second case was focused on the validation of the mass transfer modeling approach using the data from Park and Yang (2017). This case involved the horizontal co-injection of a premixed gas/liquid jet into a tank initially containing deoxygenated water. The published study included values of the volumetric mass transfer coefficient at different conditions. A sensitivity study was performed to investigate the impact of the mesh resolution, drift-flux mass transfer model, and bubble diameter on the predicted volumetric mass transfer coefficient. The following sections present the cases, describe the simulation conditions, and provide an overview of the results.

6.3.1 Dhotre/Simiano Case

The cases simulated in the studies by Dhotre et al. (2007, 2009) are recreations of an orginal experiment by Simiano et al. (2005). The objective of this work was to tune the parameters used in the drift-flux model. Therefore, the case was chosen to be entirely within the drift-flux zone and solved solely with the drift-flux framework.

6.3.1.1 Case Description

In the work of Simiano (2005), the original experiment involved the injection of air into quiescent water through 350 needles, having a 1 mm inner diameter spread across a 15 cm distributor plate at the bottom of the 2 m tall, 2 m diameter vessel. The liquid level was set at 1.5 m, and the injection flow rate was varied. Although data for multiple flow rates is provided in Simiano (2005), only the 7.5 normal L/min flow rate was considered in the current work. The experiment was carried out at atmospheric pressure and room temperature. However, since the normal volumetric flow rate was reported, the inlet was adjusted for both depth and temperature. The case setup is shown in Figure 6.2.
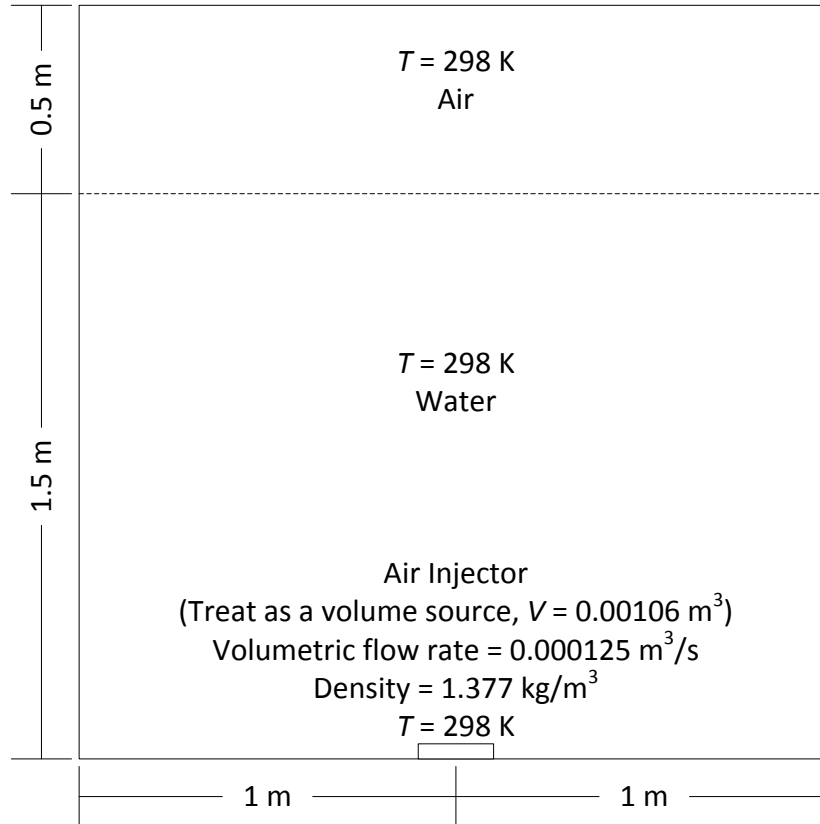
Figure 6.2 Setup for the Dhotre/Simiano case.

This case was selected for comparison in this study because it had previously been studied in the literature, and because it provides a case where only the drift-flux model is applicable (i.e. completely dispersed flow). Since only the drift-flux model is applicable, the case was used to tune the turbulent dispersion and lift forces. The maximum phase fraction at the inlet was 6% gas by volume, accounting for all 350 injectors spread across the 15 cm diameter plate. The tank was open to air at the top, and the remaining boundaries acted as walls. For the calculation of the inlet parameters, summarized in Table 6.1, it was assumed that the air above the tank was at ambient conditions. Table 6.2 shows a summary of the initial conditions, while Table 6.3 and Table 6.4 describe the assumed fluid properties for both phases.

Table 6.1 Boundary Conditions used to simulate the experiment of Simiano (2005).

Variable	Walls & Bottom Value	Inlet Value	Top Value
Gas Phase Fraction (-)	Zero gradient	0.06	Inlet-Outlet
Temperature (K)	Zero gradient	298	298
Velocity (m/s)	No slip	0.45472	Inlet-Outlet
P_{rgh} (Pa)	Zero gradient	Zero gradient (effectively)	101325
Turbulent Kinematic Viscosity (m^2/s)	Zero gradient	Zero gradient (effectively)	Inlet-Outlet

Table 6.2 Initial Conditions used to simulate the experiment of Simiano (2005).

Variable	Value
Gas Phase Fraction (-)	0 up to 1.5 m, 1 above 1.5 m
Temperature (K)	298
Velocity (m/s)	0
P_{rgh} (Pa)	101325
Turbulent Kinematic Viscosity (m^2/s)	1×10^{-11}

Table 6.3 Properties of Liquid Water

Property	Model	Reference
Density, ρ (kg/m^3)	1000	-
Specific Heat Capacity, c_p (J/kg/K)	4182	Smith, Ness and Abbot, 2005
Dynamic Viscosity, μ (Pa s)	1×10^{-3}	Yaws (2003)
Prandtl Number, Pr (-)	6.2	Yaws (2009)

Table 6.4 Properties of Air

Property	Value	Reference
Density, ρ (kg/m^3)	Ideal Gas Law	-
Specific Heat Capacity, c_p (J/kg/K)	1007	Smith, Ness and Abbot, 2005
Dynamic Viscosity, μ (Pa s)	1.8×10^{-5}	Yaws (2003)
Prandtl Number, Pr (-)	0.7	Yaws (2009)

In the one-fluid model, only the volume-averaged velocity and phase fraction can typically be specified at the boundary because a special boundary condition was not implemented to incorporate a relative velocity directly at the boundary. Therefore, specification of a consistent inlet boundary condition for a case where only one phase enters the domain is challenging. Instead of specifying an inlet boundary condition, the inlet flow of gas was specified through an appropriate set of source terms in the transport equations for total mass, phase fraction and momentum. The correct definition of the momentum was added through a source term using OpenFOAM's `fvOptions` library. The phase equation source was set to a volumetric flow rate equivalent to the value in Table 6.1. The total momentum of the gas phase was calculated and added to the cells just above the inlet distributor. The volume was set according to the distributor radius (7.5 cm). and the height of one mesh cell (6 cm), for a total volume of 1.06×10^{-3} m^3. Within this volume, a source of 0.000125 m^3/s was added (corresponding to 7.5 L/min). An additional source was applied to the momentum equation using the gas density at the bottom of the tank. The tank contained 1.5 m of water, leading to an air density of 1.377 kg/m^3. To derive the actual velocity, the total area available for gas flow (A_{gas}) had to be calculated:

$$A_{gas} = (350 \text{ holes})\left[\left(\tfrac{\pi}{4}\right)(0.001 \text{ m})^2\right]\left[\tfrac{\text{m}^2}{\text{hole}}\right] = 2.75 \times 10^{-4}\text{m}^2 \qquad (6.52)$$

Therefore, the velocity of the gas was calculated through the volumetric flow rate and the area, and is presented in Table 6.1. From the density and the velocity, the momentum source term was set to 0.626 kg/m^2/s. Overall, the use of volumetric injection sources instead of a boundary condition is not expected to affect the results significantly. Dhotre et

al. (2007) used an inlet condition averaged over the entire distributor area and tested the sensitivity to the specified phase fraction without noticing a significant impact.

Two meshes were used for the cases described above, as shown in Figure 6.3 and Figure 6.4. The meshes were selected to maintain a reasonable computational time and to study the impact of mesh on the solution. A full mesh independence study was not performed because of the computational time that would be involved and because it is unclear if the mesh independence could be achieved within a model that uses an implicitly filtered LES model within a multiphase CFD model. Instead the goal was to investigate the impact of the turbulent dispersion coefficient on the solution, and whether its optimized value would be affected by mesh resolution.
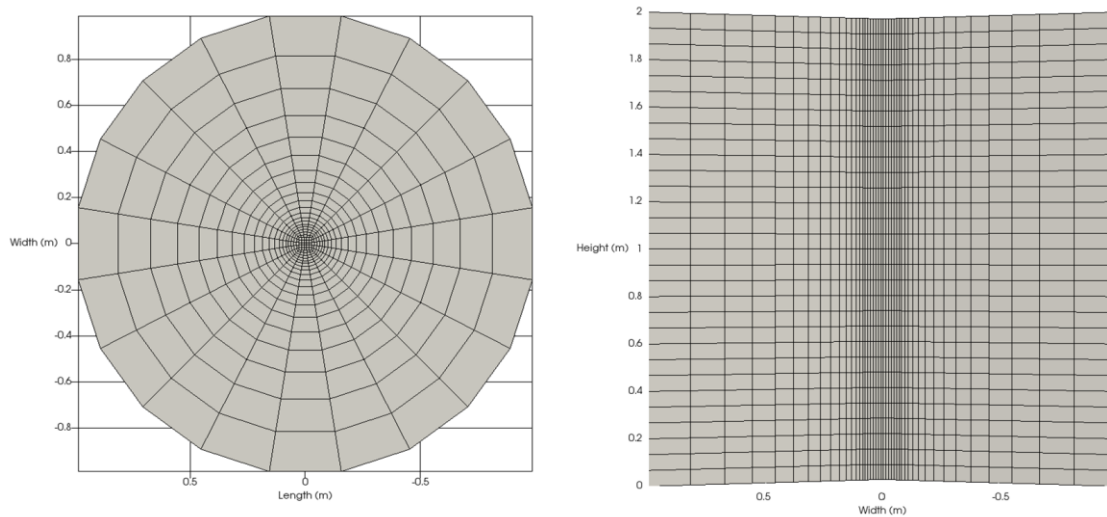
Figure 6.3 Coarse mesh for the Dhotre/Simiano case.
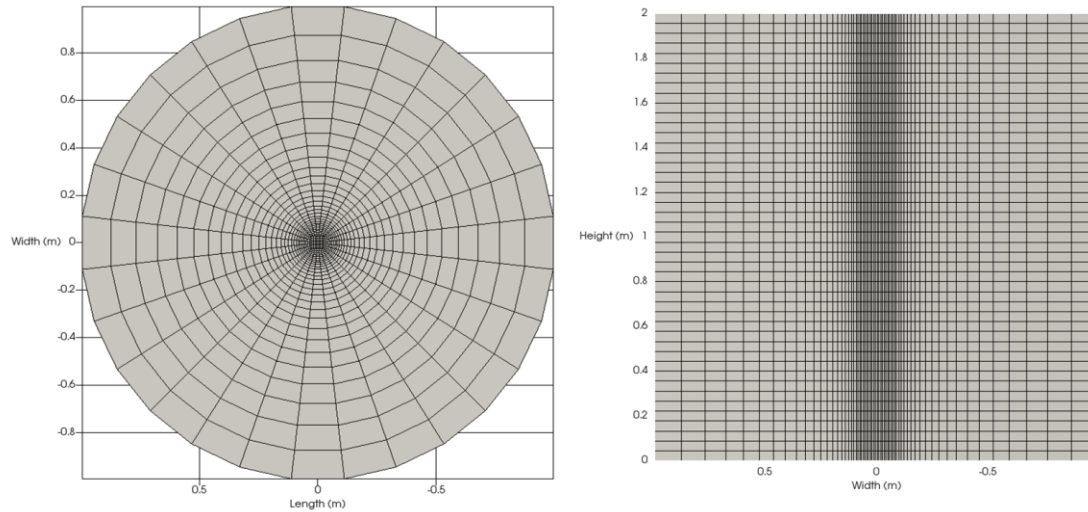
Figure 6.4 Fine mesh for the Dhotre/Simiano case.

The studies by Dhotre et al. (2007, 2009) used a constant drag coefficient of 0.44, which is equivalent to use of the Schiller-Naumann correlation at high Reynolds numbers. Therefore, this drag coefficient was used for comparison to the published results for this case in this study. The same lift coefficient of 0.1 was also employed. Therefore, only the turbulent dispersion coefficient was adjusted in this case. Simulations were performed using values of 40 and 50 for C_{TD} for both meshes. For the turbulence model, a value of 0.12 for the Smagorinksy coefficient was used. The turbulent dispersion coefficient from the Dhotre et al. (2007, 2009) papers could not be used directly because the formulation in the drift-flux model is not directly equivalent to the formulation in the Euler-Euler model.

6.3.1.2 Results and Discussion

The time-averaged, pseudo steady-state results for the phase fraction contours are shown for all four cases in Figure 6.5. The results show that there is some sensitivity to both the turbulent dispersion coefficient and the mesh. As expected, the coarsest mesh and the highest dispersion coefficient yield the most spreading of the phase fraction. The general behaviour appears to be similar between the four cases, with the primary difference occurring near the free surface. A portion of this difference is likely due to the low resolution near the free surface for the coarse mesh, which would lead to poor resolution

145

of the radial velocity at the top of the plume and may cause artificial entrainment of the gas phase. Therefore, the mesh did have an effect on the results, as can be seen near the surface with the lack of smoothness in the profile. However, a further quantitative comparison is required to compare the differences between these cases in more detail.

Figure 6.6 shows a comparison between the predicted gas phase fraction profiles, the model predictions of Dhotre et al. (2007), and the experimental results of Simiano (2005). Closer to the gas distributor, the model predictions all provide good predictions of the experimental results and agree with the model predictions of Dhotre et al. (2007). Closer to the free surface, the phase fraction prediction is higher than the experimental result, with the centreline value being overpredicted more than the values at the outer edge of the plume. Compared to the results from Dhotre et al. (2007), the predictions are worse along the centreline, but slightly better on the edge of the plume.

Overall, the predictions are relatively good considering the sensitivity of various model parameters. One thing to note is that it may appear as though the mass flow rate of gas does not match between the simulation results and the experimental data. However, it is important to remember that the gas phase velocities, shown in Figure 6.7, are different between the various datasets.
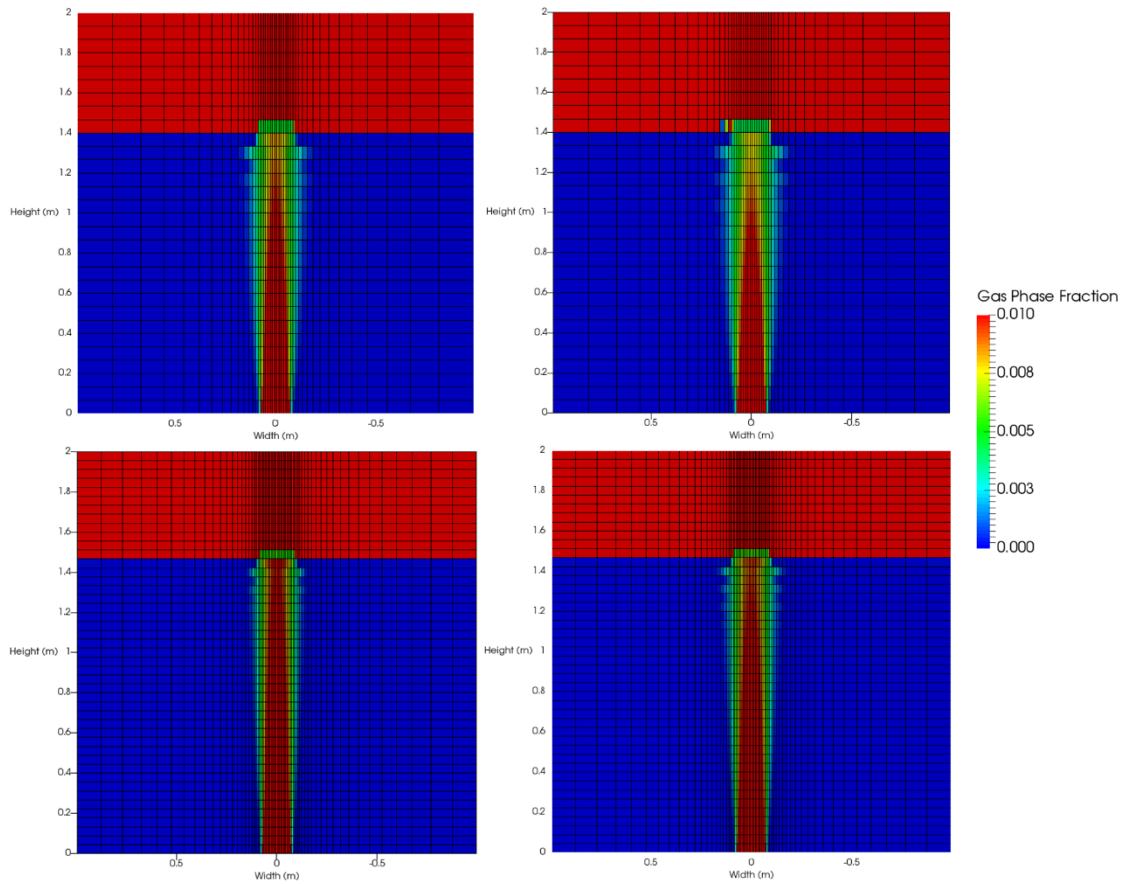
Figure 6.5 Predicted phase fraction contours for the four combinations of mesh resolution and turbulent dispersion coefficient used to replicate the Dhotre/Siminao case. Top Left: $C_{TD} = 40$, Coarse; Top Right: $C_{TD} = 50$, Coarse; Bottom Left: $C_{TD} = 40$, Refined; Bottom Right: $C_{TD} = 50$, Refined.

There are several possible reasons for the differences between the model predictions in this study, the experimental data and simulation results from Dhotre et al. The first possible reason is due to the surface effects. Mesh refinement is concentrated towards the centerline. Therefore, resolution at the interface was lacking in the simulations and could contribute to differences towards the top of the vessel. Another possible reason is that momentum and mass are added to the system as source terms at the bottom of the vessel instead of directly at the boundary. This may have led to liquid and gas axial velocities that are slightly greater towards the centerline because mass and momentum were injected uniformly in the overall volume. Another possible reason is that the turbulence modeling approach applied in this

study, and especially the turbulence at the wall, was different than in the Dhotre at al. simulations. All these factors, as well as the general differences between the modeling approaches and codes used, could have contributed to the differences.
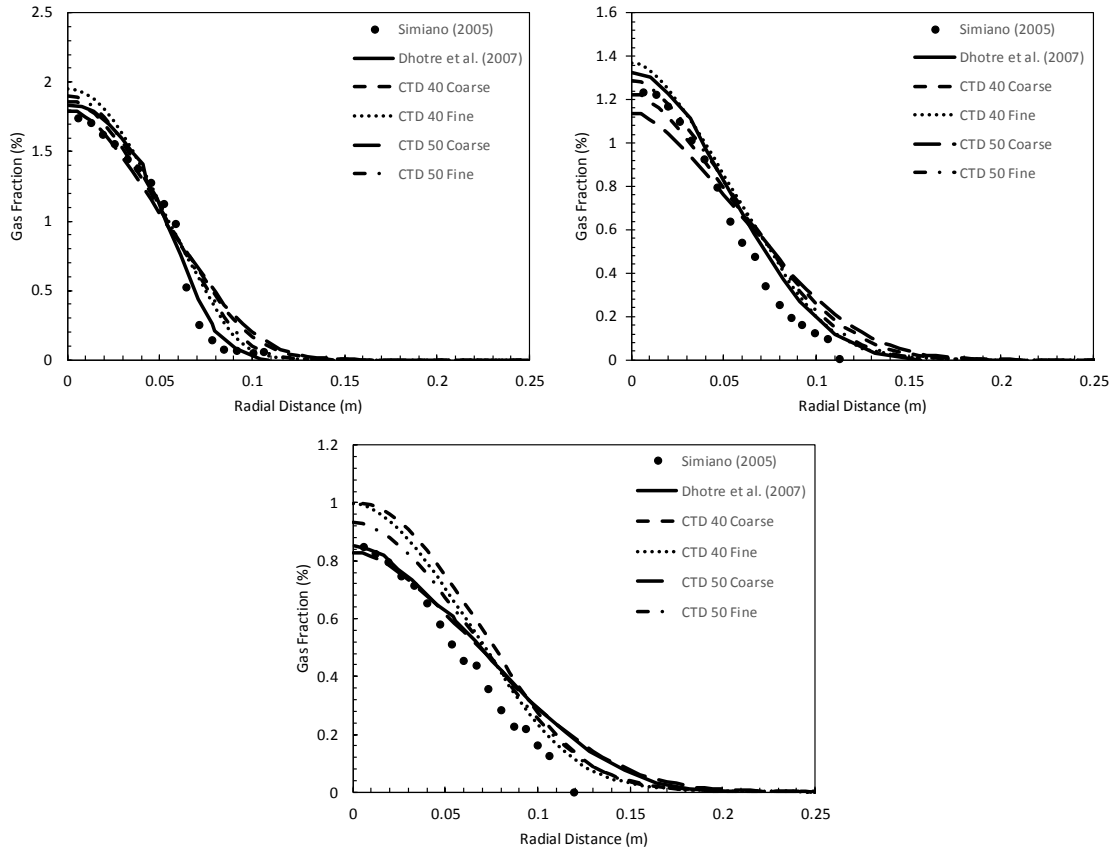
Figure 6.6 Gas phase fraction profiles at different elevations from the base of the vessel. Top left: 0.35 m; Top right: 0.75 m; Bottom: 1.1 m.

The gas phase fraction profiles generally provide a reasonable fit to the experimental data. Although there is a difference between the predictions for the various meshes and C_{TD} values, the trends are relatively similar. It is likely that the turbulent dispersion coefficient and/or other parameters (e.g. the lift coefficient) could be further tuned to provide and even better fit to the experimental data.

The axial gas velocity profiles are shown in Figure 6.7. Clearly, there is an overprediction of the centerline velocity relative to the predictions of Dhotre et al. (2007), especially at

higher elevations. This difference appears to be primarily due to the difference in gas phase fraction dispersion predictions. From the axial liquid velocity profile shown in Figure 6.8, it is clear that the higher spreading predictions for the gas phase fraction in the Dhotre et al. model result in less entrainment of liquid along the centerline and more entrainment on the outer edge of the plume. Since the gas velocity is relative to the liquid velocity, this difference in entrainment results in an over-prediction of the velocities along the centerline in the current model. However, relative to the results from Dhotre et al., the experimental liquid velocity data on the edge of the plume is predicted more closely by the current model.
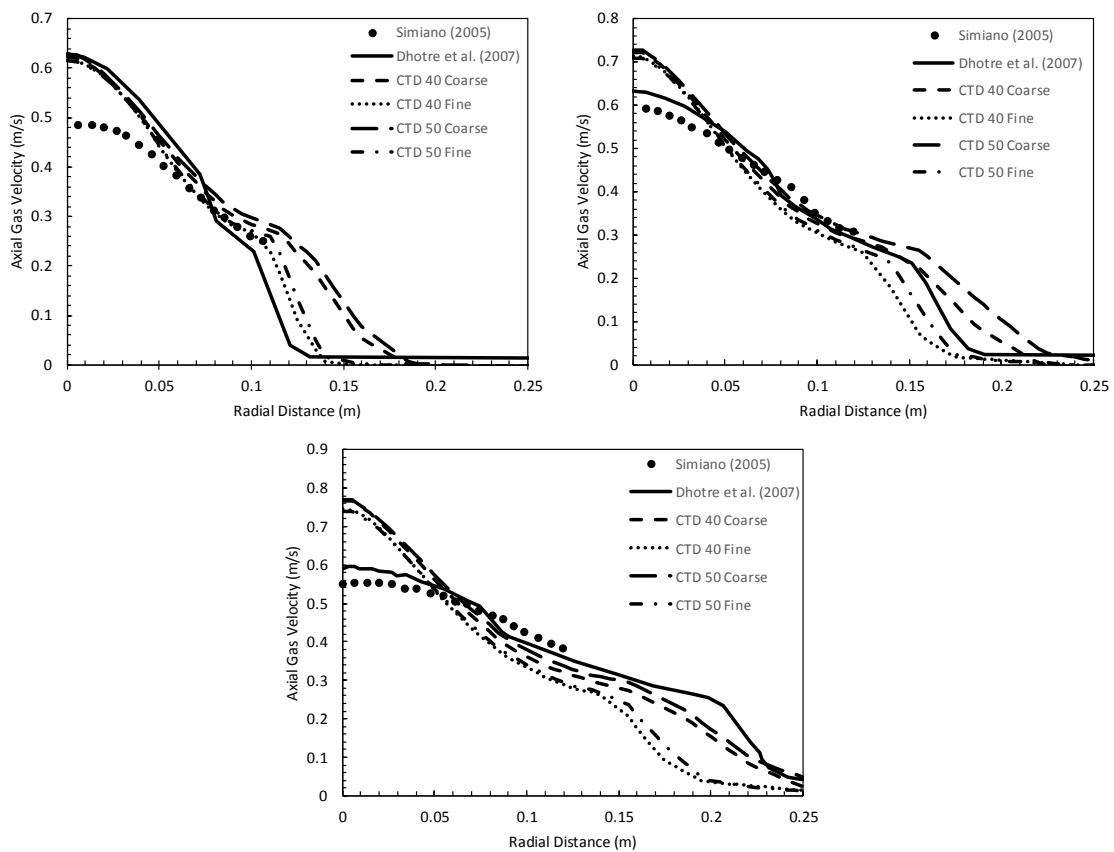
Figure 6.7 Gas axial velocity profiles at different elevations from the base of the vessel. Top left: 0.35 m; Top right: 0.75 m; Bottom: 1.1 m.
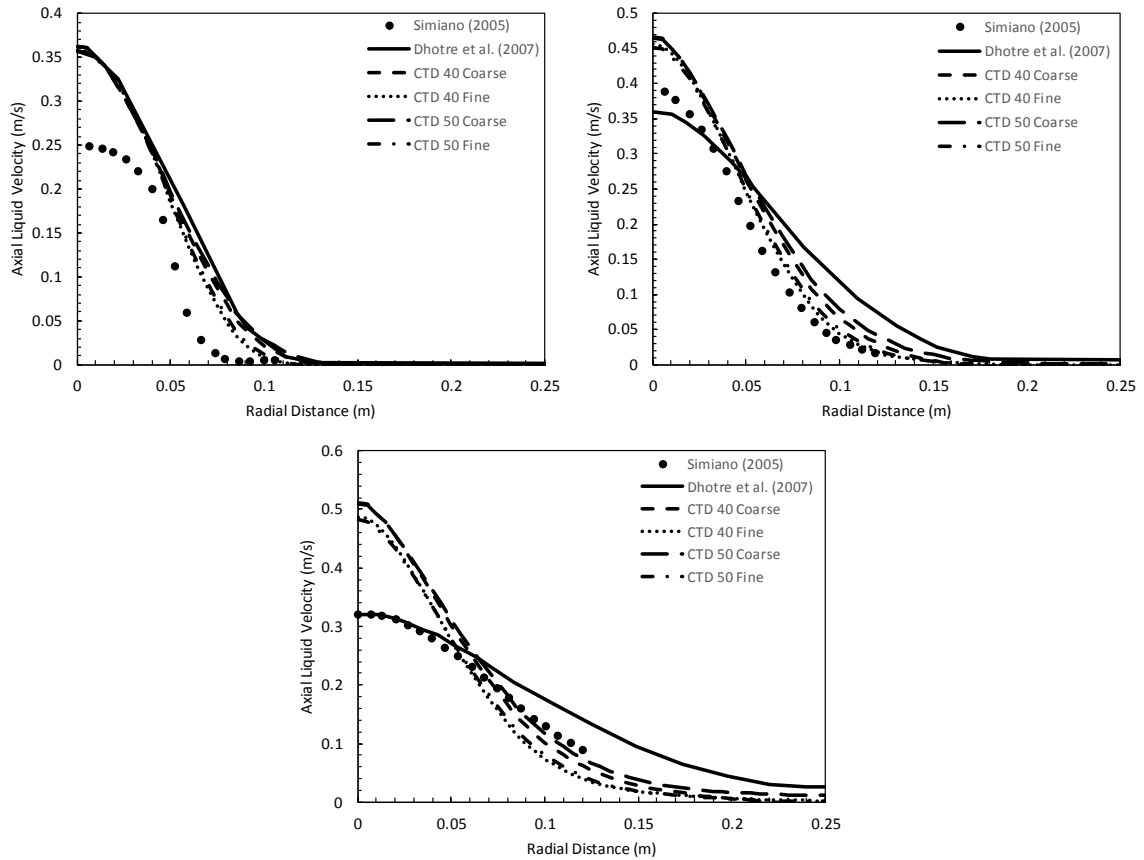
Figure 6.8 Liquid axial velocity at different elevations from the base of the vessel. Top left: 0.35 m; Top right: 0.75 m; Bottom: 1.1 m.

Since the data is plotted radially, differences near the center contribute less to local flowrate prediction errors because cross-sectional area increases radially. Therefore, although the axial velocities appear worse at the center, the prediction may be better overall given the reduction in error and shape further from the centerline when compared to Dhotre et al. (2007), particularly for the axial liquid velocity.

Overall, the presented simulations provide a good fit to the experimental data and match reasonably well to the results from an Euler-Euler simulation by Dhotre et al. (2007, 2009). As expected, the simulation results showed some sensitivity to mesh resolution and the chosen value of the turbulent dispersion coefficient. However, in the range investigated, the turbulent dispersion coefficient only had a small impact on the results, and therefore a

value between 40 and 50 appears to provide a reasonable fit to the data. Extrapolation of this result to other systems should still only be done with some care because of the coupling between the turbulent dispersion coefficient and various other parameters, including the lift and drag coefficients.

6.3.2 Park and Yang Case

The second validation case focused on the application of the combined VOF-DF model. The case is based on the experiments of Park and Yang (2017), who studied the aeration of water through injection of a premixed air/water jet horizontally into a rectangular tank full of water.

6.3.2.1 Case Description

As shown in Figure 6.9, the tank is 1.8 m long, 0.9 m wide and 0.9 m tall. The nozzle is placed 0.2 m above the bottom, and the liquid level is approximately set to 0.55 m. Although numerous experiments were carried out by Park and Yang (2017), this validation was done on the B25Q1 dataset. As stated in their paper, this case involved a 1/5 valve opening, a primary nozzle ratio of 0.327 (opening ratio in the gas-liquid mixing device), and a Reynolds number of 1.02×10^5. This corresponded to inlet phase fractions of 0.55 air and 0.45 water.
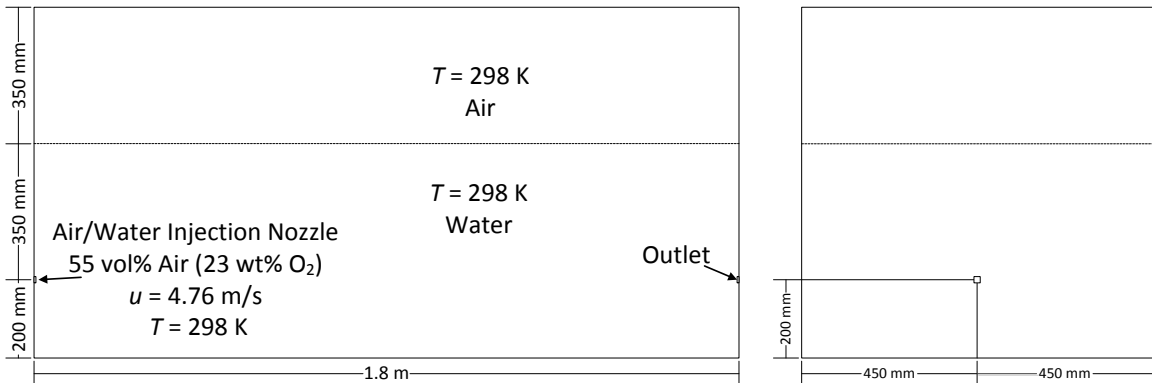
Figure 6.9 Setup for the Park and Yang (2017) validation case.

A summary of the initial and boundary conditions is provided in Table 6.5 and Table 6.6. Unlike the Simiano case, the inlet contains both air and water. In their experimental setup,

151

the system had a recirculation line. In this study, the recirculation line was modeled by an outlet in the simulation to maintain a constant water level. The properties used for this study are provided in Table 6.7, Table 6.8 and Table 6.9. In order to facilitate mass transfer, air is represented by separate oxygen and nitrogen. The properties are therefore given for these components, which are then mass averaged in the actual simulation.

Table 6.5 Boundary Conditions used to simulate the experiment of Park and Yang (2017).

Variable	Walls & Bottom Value	Inlet Value	Outlet Value	Top Value
Gas Phase Fraction (-)	Zero gradient	0.55	Zero gradient	Inlet-Outlet
Temperature (K)	Zero gradient	298	Zero gradient	298
Velocity (m/s)	No slip	4.76	2.16	Inlet-Outlet
P_{rgh} (Pa)	Zero gradient	Zero gradient	Zero gradient	101325
Turbulent Kinematic Viscosity (m^2/s)	Zero gradient	Zero gradient	Zero gradient	Inlet-Outlet
O_2 (Gas) Mass Fraction (-)	Zero gradient	0.233	Zero gradient	Inlet-Outlet
O_2 (Liquid) Mass Fraction (-)	Zero gradient	0	Zero gradient	Inlet-Outlet
H_2O Mass Fraction (-)	Zero gradient	1	Zero gradient	Inlet-Outlet
N_2 Mass Fraction (-)	Zero gradient	0.767	Zero gradient	Inlet-Outlet

Table 6.6 Initial Conditions used to simulate the experiment of Park and Yang (2017)

Variable	Initial Condition
Gas Phase Fraction (-)	0 up to 550 mm, 1 above 550 mm
Temperature (K)	298
Velocity (m/s)	0
P_{rgh} (Pa)	101325
Turbulent Kinematic Viscosity (m^2/s)	1×10^{-11}
O_2 (Gas) Mass Fraction (-)	0.233
O_2 (Liquid) Mass Fraction (-)	0
H_2O Mass Fraction (-)	1
N_2 Mass Fraction (-)	0.767

Table 6.7 Properties of Liquid Water

Property	Value	Reference
Density, ρ (kg/m^3)	1000	-
Specific Heat Capacity, c_p (J/kg/K)	4182	Smith, Ness and Abbot, 2005
Dynamic Viscosity, μ (Pa s)	1×10^{-3}	Yaws (2003)
Prandtl Number, Pr (-)	6.2	Yaws (2009)

Table 6.8 Properties of Nitrogen

Property	Model	Reference
Density, ρ (kg/m^3)	Ideal Gas Law	-
Specific Heat Capacity, c_p (J/kg/K)	1041	Smith, Ness and Abbot, 2005
Dynamic Viscosity, μ (Pa s)	1.78×10^{-5}	Yaws (2003)
Prandtl Number, Pr (-)	0.7	Yaws (2009)

Table 6.9 Properties of Oxygen

Property	Model	Reference
Density, ρ (kg/m^3)	Ideal Gas Law	-
Specific Heat Capacity, c_p (J/kg/K)	920	Smith, Ness and Abbot, 2005
Dynamic Viscosity, μ (Pa s)	2.07×10^{-5}	Yaws (2003)
Prandtl Number, Pr (-)	0.7	Yaws (2009)
Diffusion Coefficient, D_{2,M,O_2}	2.4×10^{-9}	Yaws (2003)
Henry's Law Coefficient, H (-)	0.02973	Sander (2015)

The three computational meshes used for this case are shown in Figure 6.10, Figure 6.11 and Figure 6.12. As for the previous test case, it is unlikely that a truly mesh independent result could be achieved given the use of the LES model and the many interacting parameters in the multiphase models. However, the model presented in this study is intended to provide scalable prediction, and therefore it is important to investigate the sensitivity of the predictions on the mesh resolution. In theory, the volume-of-fluid solver should provide predictions in a larger fraction of the domain for higher refinement. However, if the drift-flux predictions are properly tuned, it should provide very similar predictions in the same zones when the mesh is coarsened, assuming that the empirical modeling assumptions in the drift-flux model represent the physical situation appropriately.
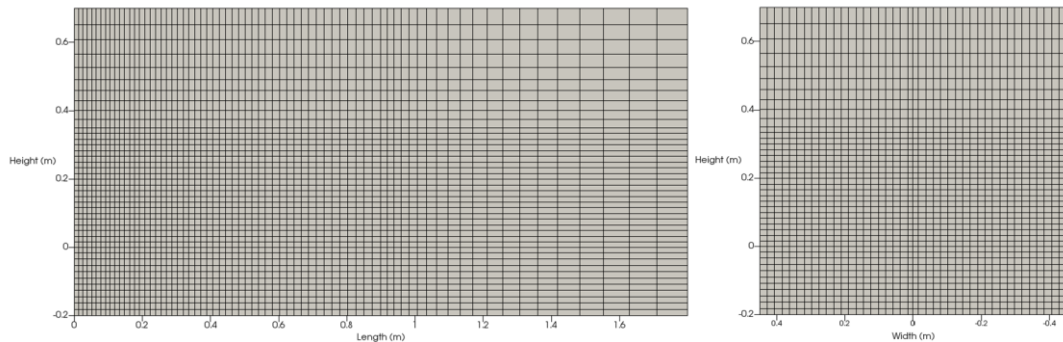
Figure 6.10 Coarse mesh for the Park and Yang (2017) validation case.
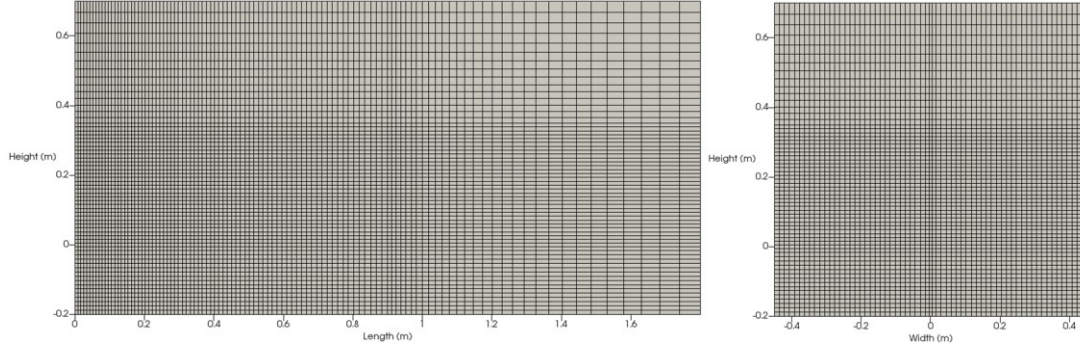
Figure 6.11 Intermediate mesh for the Park and Yang (2017) validation case.
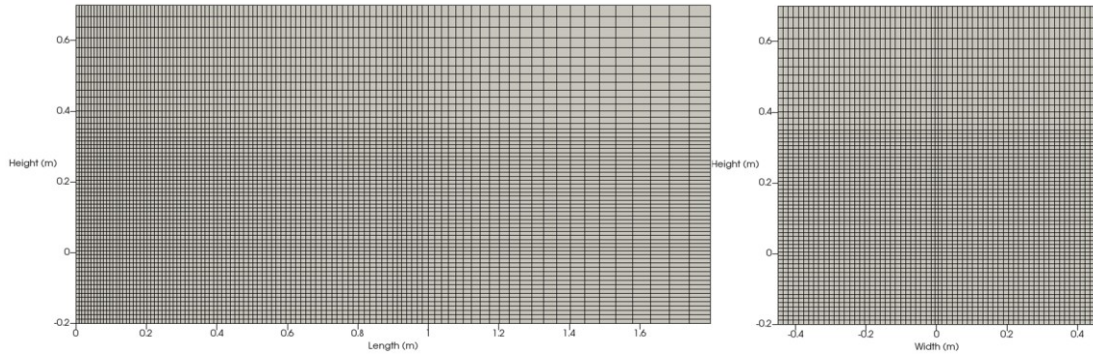
Figure 6.12 Fine mesh for the Park and Yang (2017) validation case.

In their work, Park and Yang (2017) initially removed all oxygen from the water. This was a useful initial condition for the cases. In their paper, Park and Yang (2017) calculated the mass transfer coefficient from

$$K_2 a \left[\frac{1}{s}\right] = \frac{\ln\left(\frac{C_{st}-C_0}{C_{st}-C}\right)}{t} \tag{6.53}$$

where C_{st} is the saturation concentration approximately equal to 8.48 mg/L (8.35 mg/L using the Henry's Law Coefficient from Sander, 2015), C_0 is the initial oxygen concentration (set to zero), and C is the concentration at time t. For the case simulated in this study, the value of the overall mass transfer coefficient was 1.85×10^{-3} s^{-1}.

Similar to the previous case used above, the Smagorinsky coefficient was 0.12. The drag coefficient was calculated by the Tomiyama model (Chapter 5). The lift coefficient was set to a constant value of 0.1, and the turbulent dispersion coefficient was set to 40, after analyzing the Simiano (2005) case.

6.3.2.2 Results and Discussion

The effect of mesh resolution on the predicted gas phase fraction contours is shown in Figure 6.13. The phase fraction at the inlet was close to the 0.5 contour, and as a consequence only a very small portion of the jet was predicted by the VOF solver. The light green regions represent the area in which the gas fraction was above 0.5. The results show that the penetration length fell below the prediction of 0.6 m as detailed in Park and Yang (2017). However, as the mesh was refined, the VOF region predicted a longer momentum length. A further refinement could have been done if the computational resources had been available, but it is unclear how much refinement would be required to match experimental results. The black contour line represents the phase fraction 0.01 contour, which shows the dispersion of the plume because of the DF model. Even though the jet momentum was underpredicted, the spreading of the plume at least seemed consistent between the three refinement studies. This also corresponds to the zone where most of mass transfer occurred.

The inaccurate prediction of the momentum length shows one of the weaknesses of the model. The VOF solver should be able to predict the dynamics of the gas-liquid interface in resolved regions, and the DF solver should be able to predict the fluid dynamics in unresolved regions. However, if it is not possible to provide sufficient mesh refinement to resolve jet breakup fully using VOF, breakup predictions would have to be made within the DF framework. Since the DF model does not currently implement a population balance equation (PBE) to track changes in the bubble size distribution due to breakup and coalescence, it cannot simulate these processes adequately. Therefore, it is important to ensure enough mesh resolution is used for VOF to make these predictions or, alternatively, to include a PBE in the DF model. This latter extension will be the focus of future work.
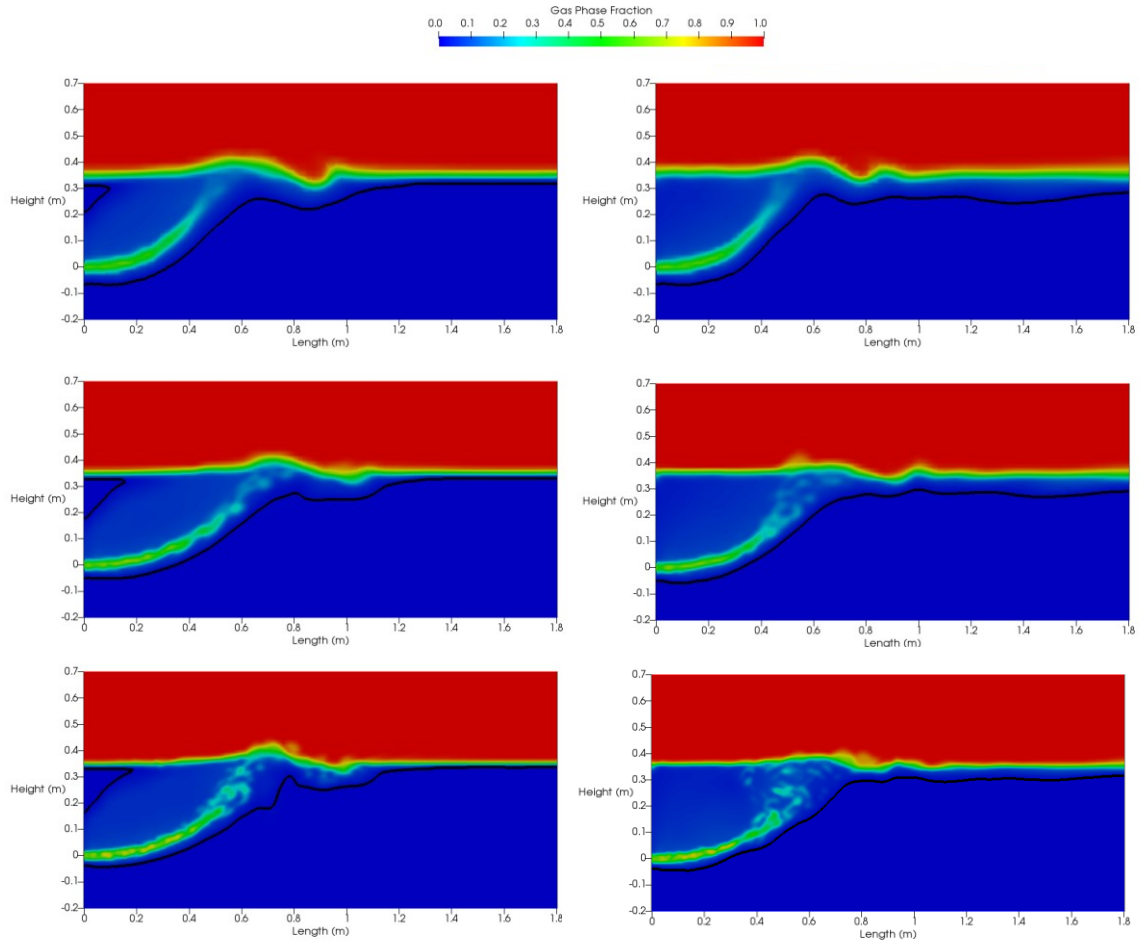
Figure 6.13 The mesh refinement test for the Park and Yang (2017) case using the Frössling model. Featured are the average gas phase fraction fields at times 1.4 s (left) and 3.0 s (right). The cases featured are the coarse mesh (top), intermediate mesh (middle) and fine mesh (bottom). The black line represents the phase fraction 0.01 contour.

As is shown in Figure 6.14, the predicted value of the mass transfer coefficient varied with mesh refinement. Given the differences in the phase fraction distribution shown in Figure 6.13, where the jet penetration length increases with each successive refinement, this result is to be expected. Since the inlet was a gas-liquid mixture, the gas was already diffuse, and without sufficient resolution DF is used in most of the domain. Theoretically, the DF model could describe the jet region of the injection, but this would require closure terms that are properly tuned for jet modeling. Since such closures were not incorporated into the model in this case, sufficient mesh resolution is required to permit the VOF model to resolve the jet region. Despite the lack of resolution for the coarse mesh, the results for the overall

mass transfer coefficient are reasonable, and the variation between the predictions is relatively small. The slope of the lines in Figure 6.14 represents the value of the overall mass transfer coefficient. In Park and Yang (2017), a value of 1.85×10^{-3} s^{-1} was obtained. The values for the three refinements are close in value to each other, with the coarsest refinement being the furthest from the experimental value. The predicted overall mass transfer coefficients for the two finer meshes are more similar to each other. From Figure 6.13, it is clear that this is because the two simulations produced much more similar hydrodynamic predictions. Although the 1 mm Frössling predictions are not the same as the experimental results, they are on the same order of magnitude. The main reason for the difference between predicted and experimental values is that the average bubble size was unknown. Therefore, the mass transfer predictions were redone using different bubble diameters.
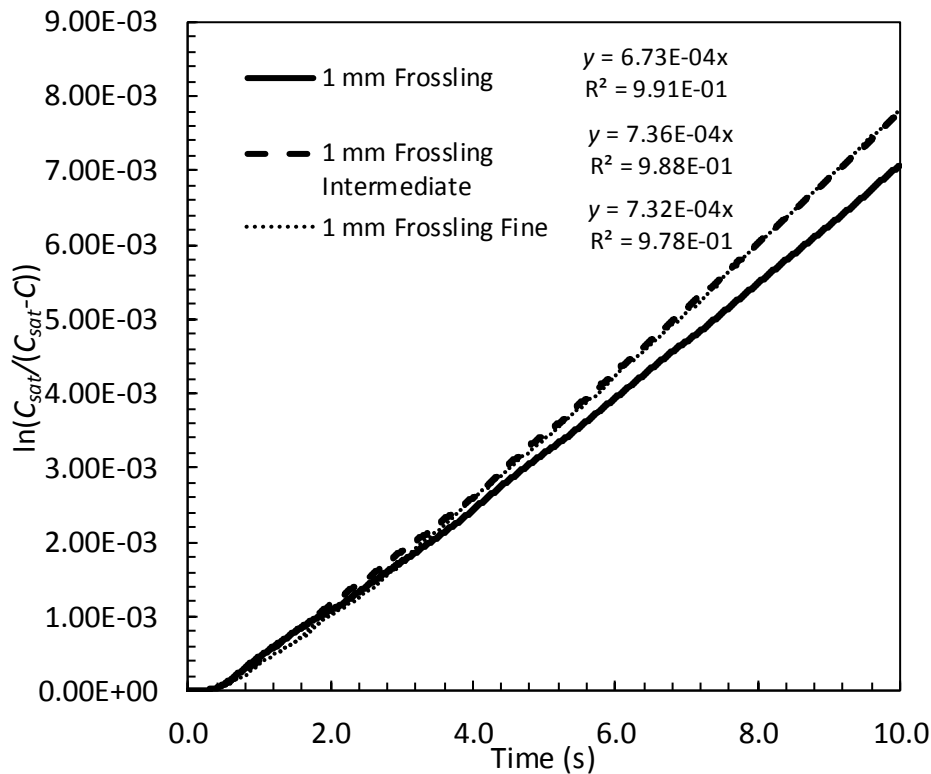
Figure 6.14 Quantitative results for the three meshes, showing the total mass transfer coefficient as calculated by the three cases in the same order as the legend.

Figure 6.15 shows the phase fraction contours for four different assumed bubble sizes in the drift-flux region. In reality, a bubble size distribution would exist. However, the incorporation of a population balance model within the drift-flux framework was outside of the scope of this project. As shown in Figure 6.15, the momentum length remains consistently underpredicted for all bubble sizes. The only exception is the 0.25 mm bubble diameter simulation, where the mass transfer rate was significantly higher than for the other three diameters used. In the 0.25 mm case, as shown by the 0.01 phase fraction contour, the gas phase dispersed too much through the liquid. However, compared to the results of Park and Yang (2017), the total momentum length of the jet is lower for the coarse cases, as was discussed previously. Figure 6.15 shows that the momentum length of the jet was relatively unaffected by the assumed bubble diameter.

As mentioned in the methodology, the two plume-region mass transfer models (Higbie and Frössling) were compared. These represent the upper and lower bounds for local mass transfer coefficients. From Figure 6.16, the 1 mm and 2 mm bubble size predictions bound the experimental mass transfer coefficient for the Higbie model. However, for the Frössling model, the 0.5 mm bubble size provides a very close approximation of the result obtained by Park and Yang (2017). As expected, the values of the predicted overall mass transfer coefficient are higher for the Higbie model, and for bubbles of smaller diameter. In general, the steady-state mass transfer values were predicted on the correct order of magnitude, despite the hydrodynamics of the jet underpredicting the momentum length. In the case of the hydrodynamics, the detrainment of gas from the jet core likely occurred too early, but most of the mass transfer occurs in the plume region. Predictions with a representative bubble size distribution and a finer mesh would likely be required to match experimental values for both the momentum length and mass transfer coefficient.
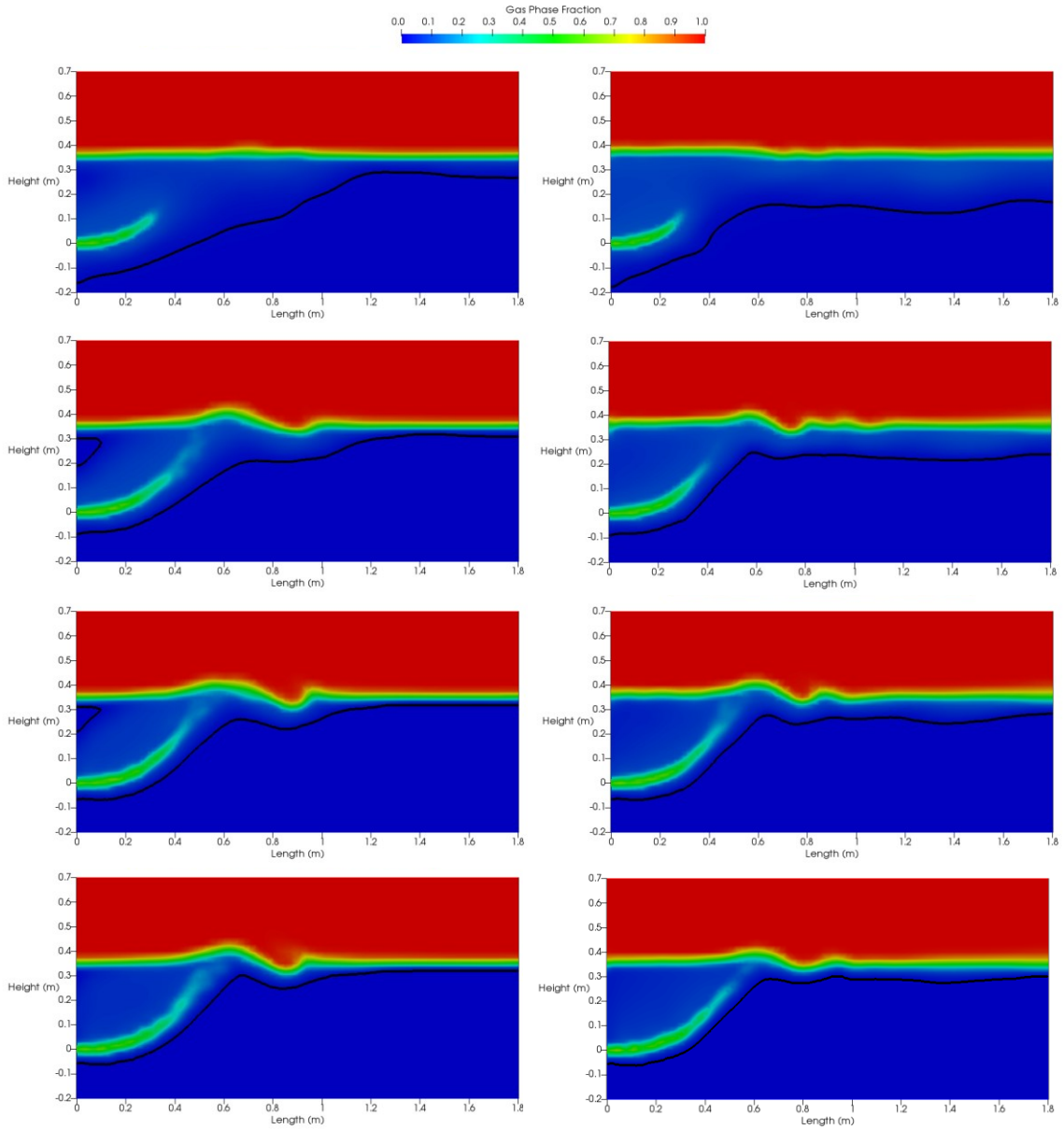
Figure 6.15 The diameter test for the Park and Yang (2017) case using the Frössling model. Featured are the average gas phase fraction fields at times 1.4 s (left) and 3.0 s (right). The cases featured are the 0.25 mm d_b, 0.5 mm d_b, 1 mm d_b, and 2 mm d_b in descending order. The black line represents the phase fraction 0.01 contour.
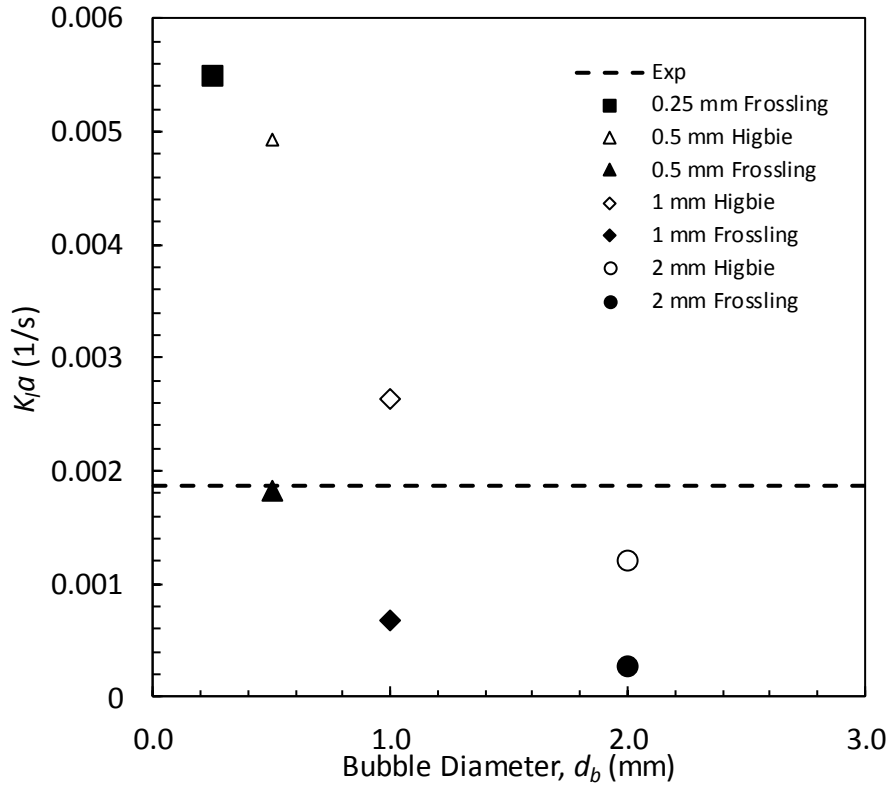
Figure 6.16 Overall mass transfer coefficients calculated for both clean and contaminated bubbles at 0.25 mm, 0.5 mm, 1 mm and 2 mm in size. They are plotted as a single point after taking the fitted slope.

It should be mentioned that the cases used, even at their finest refinement, are still far above the ability to capture the bubbles using the VOF solver. Similar to issues noticed in Chapter 5, it becomes evident that the ability to resolve bulk jet dynamics can be overwhelmed by the diffusive nature of the drift-flux model. As shown above, the increase in refinement directly correlates to a better jet momentum prediction, which was equally valid in Chapter 5. However, it is important to note that the variability in mass transfer predictions could be related to the incorrect prediction of the momentum length because, as the jet is carried further, the plume covers a larger volume as a result. Of course, the effect on mass transfer will scale with the size of the jet, and subsequent studies should consider the variability in jet lengths as part of the discussion.

It is not clear whether the Higbie or Frössling model is more applicable to the investigated system. However, since real systems normally contain surfactants, the Frössling model is more likely to be valid. The mass transfer predictions seem to indicate an average bubble diameter of approximately 0.5 mm. However, the fluid dynamics show that this diameter is insufficient to fully match momentum length predictions for both mass transfer and hydrodynamics. Even though there are some differences between the predicted and experimental values, the fact that mass transfer coefficients are on the right order of magnitude is reassuring for future large-scale modeling projects.

6.4 Conclusions

A hybrid volume-of-fluid and drift-flux model was developed to allow for mass transfer to be estimated in areas of high gas holdup, while maintaining low mesh resolution requirements to capture interfacial transport phenomena in regions of low gas holdup. The model was constructed using OpenFOAM's compressive interface capturing approach, the drift-flux model and appropriate auxiliary equations. The pairing of VOF and DF models is natural because both models treat the two-phase medium as a single continuum, although with different closure terms and constitutive laws.

To validate the model, in preparation for the simulation of large-scale releases, it was applied to two cases. The first case was a replication of experimental work by Simiano (2005) and the modeling work done by Dhotre et al. (2007, 2009). Due to the differences in the modeling of the interfacial forces and the calculation of the relative velocity, the sole parameter left to be fitted was the turbulent dispersion coefficient. To analyze this parameter, the case was simulated at several values, with the best solution falling between 40 and 50. Compared to the results of Dhotre et al. (2007), the phase fraction profiles for the gas was overpredicted at the centerline, as well as underpredicted towards the tailing edges. However, the overall peak was close to the experimental results. This trend was carried through the axial gas and liquid profiles, with the worst match being near the free surface. Given the coarseness of the cases, the effects of interfacial wobble were a contributing factor. Furthermore, the mixture model may have retained more momentum near the center due to the averaging of properties by the VOF method.

The current work employed the same drag, lift and bubble induced turbulence models as Dhotre et al. (2007), but there are perhaps better combinations of models that might have yielded the exact experimental results. Additionally, solely the drag and lift forces were used to generate the relative velocity through the interfacial force balance. More sophisticated two-phase models might employ other modifications, but these two forces were deemed necessary for predicting the drift velocity as well as the lateral dispersion. In this case, model fit could likely be improved but the parameters were chosen to permit comparison with the previously published results.

To test the transition model, as well as the mass transfer predictions, one case of Park and Yang (2017) was modeled. A horizontal air jet was mixed with liquid to form a two-phase jet that was injected into a large tank containing water. Liquid was removed from the back end of the tank to maintain the liquid level. In the published experiment, the overall mass transfer coefficient was measured using an average concentration of oxygen at the back end of the tank. Since no information was available on bubble size distribution, a sensitivity analysis was performed using three representative bubble sizes. The predictions from these bubble sizes highlighted that the transition model did work, reducing the mass transfer in the jet core by only applying at the 0.5 contour, while the dispersed region was modeled as bubbly flow.

The exact hydrodynamics were not predicted as well as the mass transfer coefficients. The mass transfer coefficients were of the same order of magnitude as the experimental result. However, the real case would have been a bubble size distribution and therefore the exact hydrodynamics were impossible to predict correctly. Future work would be to extend the model with a population balance model in order to directly track the bubble size distribution. Alternatively, much finer meshes could have been used to allow the VOF model to resolve more of the jet.

The model functioned well in the prediction of vertical gas dispersion, which is the expected worst-case scenario in an underwater release. Additionally. the prediction of the mass transfer coefficient was bounded by sensitivity on the bubble diameter. These cases provided the necessary tuning of closure parameters in order to obtain reasonable results

on coarse meshes. Additionally, they proved that the mass transfer rate can be bounded, and therefore a worst-case scenario could be predicted in larger gas releases.

Chapter 7

Simulation of a Large-Scale Underwater Acid Gas Reinjection Well Blowout

7.1 Introduction

In offshore gas production, natural gas is often contaminated with significant concentrations of sour components such as carbon dioxide and hydrogen sulfide. The sour gas is normally treated (sweetened) directly on the platform to remove these compounds. Once removed, the toxic components must be further treated before release to the atmosphere or sequestered.

One option is to inject the mixture of carbon dioxide and hydrogen sulfide, typically called acid gas, into a depleted part of the reservoir. This acid gas reinjection process not only sequesters the toxic gas, but also helps to maintain pressure in the production well. However, acid gas transportation and reinjection of the toxic gas mixture is associated with its own safety challenges because of the possibility that containment might be lost. Therefore, appropriate emergency response plans must be developed to mitigate the risks posed by such a release. Analysis of the risks posed by underwater gas releases is typically performed using numerical models. Traditionally, most models are based on the integral plume modeling approach, with appropriate modifications to incorporate heat and mass transfer predictions (Johansen, 2000; Yapa et al., 2001; Zheng et al.; 2002; Zhao et al., 2014b). Recently, models based on computational fluid dynamics (CFD) have become more prevalent (Cloete et al., 2009; Olsen and Skjetne, 2016; Olsen and Skjetne, 2017). However, application of such models to the analysis of acid gas releases from shallow wells is rare.

Underwater releases differ from atmospheric releases because gases first travel through the water column before reaching the atmosphere. This provides time for some of the chemical species to dissolve in the seawater, and to disperse and decelerate before reaching the free surface. The fraction of the gases that dissolve in the water column primarily depends on

mixing and dispersion, the residence time of the gas in the water, the solubilities of the gases in seawater, and the release rate. The release rate would be predetermined by the reservoir pressure and the size of the orifice from which the gas is released. The mixing and dispersion of the gas in the water is primarily controlled by the depth of the release point, the release rate, and the release trajectory. In the case of an acid gas release, the components have a relatively high solubility in water compared to the hydrocarbon fraction in produced gas. Therefore, a significant amount of acid gas would dissolve even in shallow water gas releases.

Conceptually, the release of acid gas from a shallow well can be split into three regions, as shown in Figure 7.1. The gas release would be driven into the water column by the pressure from inside the well. Driven by momentum and expansion, the gas would initially form a continuous jet. Further away from the release point, as momentum dissipates into the surrounding liquid, the jet would slow and begin to breakup. With a loss of momentum, buoyancy forces would become dominant. In the buoyancy-driven plume region, the gas would continue to disperse and travel in a wider path as lateral forces drive it away from the centerline. The rise velocity would continue to decrease on the outer edge of the plume, approaching terminal velocity. The plume region would persist to a level just below the free surface, where simultaneous detrainment of the undissolved gas and entrainment of gas from the waves governs the flow regime. From a modeling perspective, the three regions are governed by different physical processes and length scales. Therefore, multiscale modeling approaches are likely necessary to provide adequate predictions.

During the gas expansion, the momentum-driven jet would form a continuous interface. Hydrodynamically, the bulk motion of the gas phase in the jet region would be compact, and this would result in a lower dissolution rates because the gas at the core has little chance to interact with the surrounding liquid. During breakup and the development of the plume region, the gas would disperse and mass transfer would increase as bubble clusters form. With greater surface area, the bubbles would experience drag and lateral dispersion forces. However, the method of modeling bubbles by tracking the interface would require a computationally expensive (and perhaps impossible) number of cells. This only further necessitates a multiscale modeling approach.
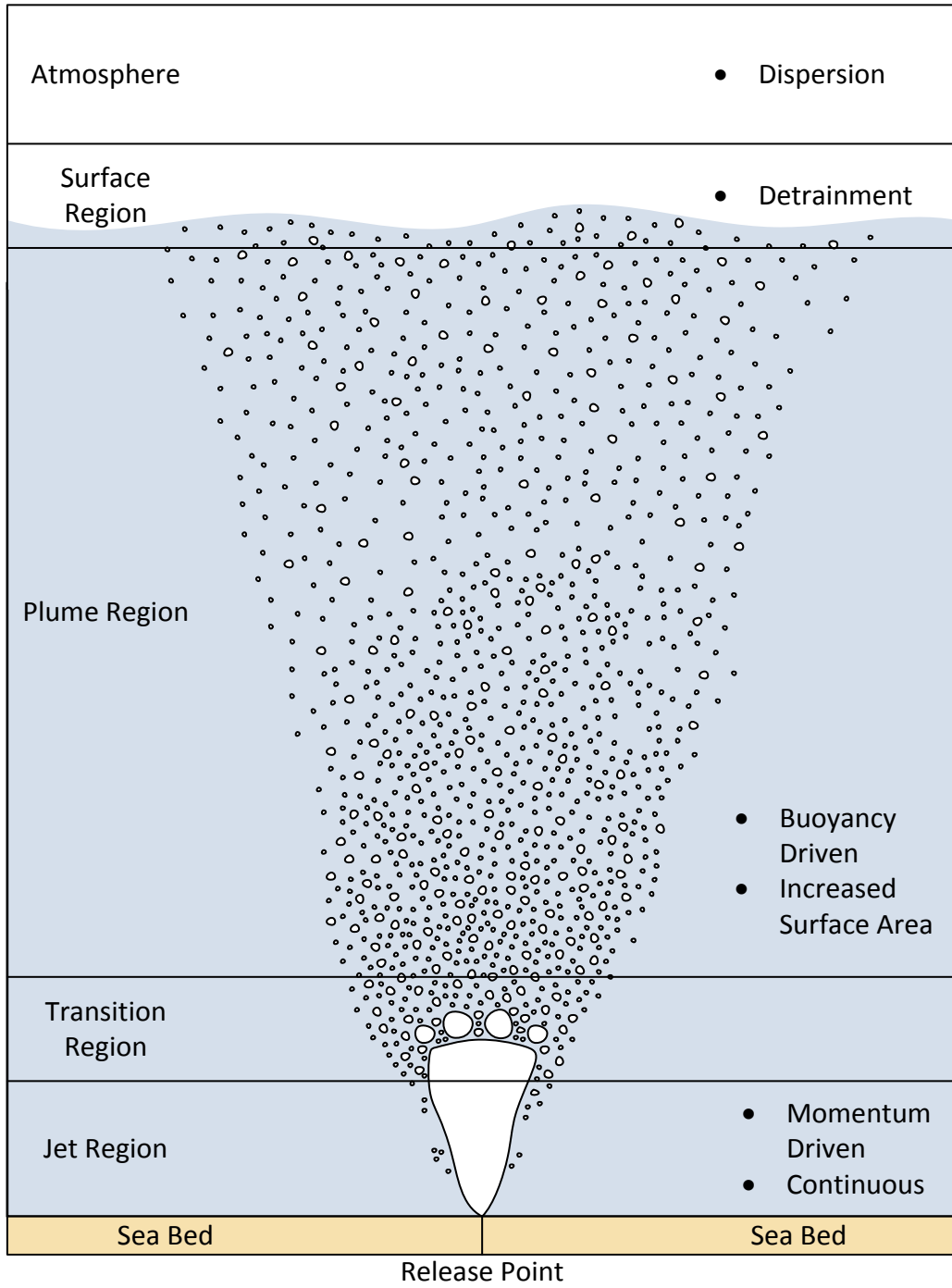
Figure 7.1 An overview of a subsea gas release, divided into three major regions.

The objective of this work was to apply the previously developed multiphase, multiscale CFD model (Chapter 6) to simulate a shallow well acid gas release scenario and predict the subsequent emission rate to the atmosphere. The CFD model used a coupled volume of fluid (VOF) and drift-flux (DF) model. The benefits and challenges with this type of model have been discussed in Chapter 6 but will be expanded for the release scenario. To illustrate some of the challenges, the path used to develop the model will be briefly discussed to provide perspective on the modeling choices. The adopted model and the case for the release scenario will be described. Finally, the results from case studies used in this work will be discussed, followed by a description of the primary conclusions.

7.2 Methodology

A full description of the algorithm was provided in Chapter 6. This section therefore only provides an overview of the main equations and a summary of important modifications. The model was developed using OpenFOAM, an open source CFD toolbox (The OpenFOAM Foundation, 2018). It employs the volume-of-fluid method to facilitate interface tracking in regions with high mesh resolution and the drift-flux model in regions with low mesh resolution. A blending factor is applied to permit a smooth transition between the models. The species and energy conservation equations are solved with appropriate source terms to facilitate heat and mass transfer predictions.

Following the derivation presented in Chapter 6, the blended phase continuity equation can be written as

$$\frac{\partial \alpha_1}{\partial t} + \nabla \cdot (\alpha_1 \vec{u}) + \nabla \cdot \left(\alpha_1 \alpha_2 \left[\chi \vec{u}_{R,VOF} + (1-\chi)\vec{u}_{R,VOF}\right]\right) = S_1 \left(\frac{1}{\rho_1} - \alpha_1 \left(\frac{1}{\rho_1} - \frac{1}{\rho_2}\right)\right) -$$

$$\frac{\alpha_1 \alpha_2}{\rho_1} \left[\frac{\partial \rho_1}{\partial t} + \vec{u}_1 \cdot \nabla \rho_1\right] + \frac{\alpha_1 \alpha_2}{\rho_2} \left[\frac{\partial \rho_2}{\partial t} + \vec{u}_2 \cdot \nabla \rho_2\right] + \alpha_1 \nabla \cdot \vec{u} + \nabla \cdot \left((1-\chi)D_{M1}\nabla \alpha_1\right) \qquad (7.1)$$

where α_i is the phase fraction of phase i, $\vec{u}$ is the velocity vector, χ is the filter fraction (or blending factor between VOF and DF), S_i is the total mass source into phase 1, ρ is the density, and D_{M1} is the turbulent diffusivity for the phase fraction. The subscript R refers to the relative velocity, for which there is a different definition if the cell is dominated by the VOF or the DF methodologies. The turbulent dispersion force is calculated from:

$$D_{M1} = \alpha_1 C_{TD} C_D \frac{v_{2,t}}{Sc_t} \left(\frac{\nabla \alpha_1}{a_1} - \frac{\nabla \alpha_2}{a_2} \right) \tag{7.2}$$

In which C_{TD} is the turbulent dispersion coefficient and is equal to 40 (from the results of Chapter 6). The drag coefficient, C_D, was calculated from the Tomiyama correlation (Tomiyama et al., 1998):

$$C_D = \max \left(\frac{24}{Re} (1 + 0.15 Re^{0.687}), \frac{8}{3} \left(\frac{Eo}{Eo+4} \right) \right) \tag{7.3}$$

where Re is the Reynolds number based on the relative velocity, and Eo is the Eötvös number. which is for contaminated bubbles. For the VOF solver, the relative velocity may be calculated from:

$$\vec{u}_{R,VOF} = \vec{u} \cdot \hat{n}_f \tag{7.4}$$

$$\hat{n}_f = \frac{(\nabla \alpha_1)_f}{|(\nabla \alpha_1)_f|} \cdot \vec{A}_f \tag{7.5}$$

where $\hat{n}_f$ is the interfacial normal vector, approximated by the unit normal gradient of the phase fraction dotted with the face area vector, $\vec{A}_f$. This operation produces a flux, although the divergence scheme in OpenFOAM automatically performs a surface integral on the cell to transform this quantity back to a velocity. For the DF model

$$\vec{u}_{R,DF} = \frac{4 d_b (\rho_1 - \rho)}{3 \rho_2 C_D |\vec{u}_{R,DF}|} \left(\vec{g} - \frac{d\vec{u}}{dt} - \nabla \cdot (\vec{u}\vec{u}) \right) - \frac{4 d_b C_l}{3 C_D |\vec{u}_{R,DF}|} \vec{u}_{R,DF} \times (\nabla \times \vec{u}) \tag{7.6}$$

where d_b is the bubble diameter, the subscript 1 refers to the gas phase, the subscript 2 refers to the liquid phase, and $\vec{g}$ is the gravity vector. The relative velocity, $\vec{u}_{R,DF}$, is determined by solving equation 7.6 using fixed point iteration. C_l is the lift coefficient, which is set at a constant 0.1 (Dhotre et al., 2007).

Momentum is governed by the Navier-Stokes equation:

$$\frac{\partial (\rho \vec{u})}{\partial t} + \nabla \cdot (\rho \vec{u}\vec{u}) + \nabla \cdot (\tau + (1 - \chi)\tau_{DF}) = -\nabla_N P_{rgh} + \rho \vec{g} + \vec{F}_{ST} \tag{7.7}$$

$$\tau_{DF} = -\sum_i \alpha_i \rho_i \vec{u}_{ik} \vec{u}_{ik} \tag{7.8}$$

where τ is the stress tensor, τ_{DF} is the additional stress for the drift flux model based on the drift velocities ($\vec{u}_{ik}$), P_{rgh} is the pressure excluding the hydrostatic pressure taken at

the normal gradient defined by N, and $\vec{F}_{ST}$ are any additional body forces (e.g. surface tension).

The momentum equation (7.7), when implemented in OpenFOAM, is solved using the PISO (Pressure Implicit with Split Operators) algorithm. Following this method, the velocity is first predicted using the discretized momentum equation and the current values of the pressure and the density (which depends on both pressure and temperature). The equation is then decomposed to derive an expression for the divergence of the velocity field. This divergence is used to derive a pressure equation.

Turbulence was modeled using LES method with the Smagorinksy sub-grid scale model. In this operation, the velocity is split into two parts:

$$\bar{\bar{u}} = \vec{u} - \vec{u}' \tag{7.9}$$

where $\bar{\bar{u}}$ is the resolved velocity and $\vec{u}'$ is the unresolved velocity below the grid size. The unresolved part must be calculated according to the sub-grid model, which produces an effective change in viscosity:

$$\mu_t = \rho C_s^2 V^{2/3} |\bar{S}| \tag{7.10}$$

where μ_t is the turbulent dynamic viscosity. The term, C_S, refers to the Smagorinsky coefficient, which was set to 0.12 (Dhotre et al., 2009). The total viscosity can then be defined as

$$\mu_{eff} = \mu + \mu_t + \mu_{BIT} \tag{7.11}$$

where the subscript *eff* refers to the effective dynamic viscosity, which is a combination of the molecular dynamic viscosity, turbulent dynamic viscosity and the effects of bubble induced turbulence:

$$\mu_{BIT} = C_{BIT} \alpha_1 \rho_2 d_b |\vec{u}_R| \tag{7.12}$$

where μ_{BIT} is the change in effective viscosity by bubble induced turbulent, and C_{BIT} is the coefficient for the bubble induced turbulence set equal to 0.6 (Dhotre et al., 2007).

Phase-averaged species conservation equations were solved for each dissolving gas species in each phase, but not for the solvents (i.e. air and water). The species equations were formulated as

$$\frac{\partial(\alpha_i\rho_i Y_{i,j})}{\partial t} + \nabla \cdot \left(\alpha_i\rho_i Y_{i,j}\vec{u}\right) - \nabla \cdot \left(\alpha_i\rho_i D_{i,M,jEff}\nabla Y_{i,j}\right) = S_{M,j} \tag{7.13}$$

where $Y_{i,j}$ is the mass fraction of species j in phase i and $S_{M,j}$ refers to the mass source for species j. This source term must have different signs depending on the phase $\left((S_{M,j})_1 = -(S_{M,j})_2\right)$. $D_{i,M,jEff}$ is the effective diffusivity, including both molecular and turbulent diffusion processes, and is defined by

$$D_{i,M,jEff} = D_{i,M,j} + D_{t,i} \tag{7.14}$$

$$D_t = \frac{v_{t,i}}{Sc_{t,i}} \tag{7.15}$$

where $D_{i,M,j}$ is the diffusivity of species j in phase i with respect to the mixture, $D_{t,i}$ is the turbulent diffusivity calculated from the ratio of turbulent kinematic viscosity ($v_{t,i}$), and the turbulent Schmidt number ($Sc_{t,i}$, assumed to be 1). In this study, the species mass transfer source terms were calculated using the liquid phase overall mass transfer coefficient and the liquid side concentration driving force. Thus,

$$(S_{M,j})_2 = \alpha_2\rho_2 K_2 a\left(Y_{2,j}^* - Y_{2,j}\right) \tag{7.16}$$

where the source was written for phase 2 (liquid). The species mass transfer source in the gas phase has the same magnitude as the liquid phase source, but the opposite sign. The value of $K_2 a$ represents the overall mass transfer coefficient. In this case, Y is the mass fraction of species j, where $Y_{2,j}^*$ represents the mass fraction in equilibrium with the gas phase.

In the presented simulations, two models were used to calculate the overall mass transfer coefficient. The method of Higbie is often cited to be applicable for clean interfaces:

$$K_2 = 2\sqrt{\frac{D_{i,M,j}}{\pi\lambda}} \tag{7.17}$$

171

where λ represents the renewal or penetration time. For contaminated interfaces, the method of Frössling is often used:

$$K_2 = 0.6\sqrt{\frac{1}{\lambda}}\left(D_{i,M,j}\right)^{2/3}(v_2)^{-1/6} \tag{7.18}$$

The renewal times were calculated differently depending on the method used,

$$\lambda = \begin{cases} \dfrac{\Delta t}{Co_{local}}, & \chi = 1 \text{ (VOF)} \\ \dfrac{d_b}{\vec{u}_R}, & \chi = 0 \text{ (DF)} \end{cases} \tag{7.19}$$

where Co_{local} is the local Courant number. The local interfacial area density was calculated as

$$a = \begin{cases} V^{-1/3}, & \chi = 1 \text{ (VOF)} \\ \dfrac{6\alpha_1}{d_b}, & \chi = 0 \text{ (DF)} \end{cases} \tag{7.20}$$

For the VOF model, the area density is on the same order as the inverse of the cell length, while for the DF model the area density is based on the size of the bubbles inside the cell. One volume-averaged energy equation was solved:

$$\frac{\partial(\rho c_v T)}{\partial t} + \nabla \cdot (\rho c_v T \vec{u}) + \frac{\partial(\rho E_k)}{\partial t} + \nabla \cdot (\rho E_k \vec{u}) + \nabla \cdot (\vec{u}P) = \nabla \cdot \left(K_{eff}\nabla T\right)$$
$$+ S_E \tag{7.21}$$

where $e = c_v T$ represents the internal energy, T as the temperature, E_k as the kinetic energy, K_{eff} as the thermal conductivity, and S_E as the source term, which is set equal to:

$$S_E = \sum_j S_{M,j}(\Delta H_{sol} - RT) \tag{7.22}$$

where ΔH_{sol} is the heat of dissolution. The term RT enforces consistency with the form of the energy equation. The heats of dissolution are equivalent to the slope of the Henry's law coefficient as a function of temperature, which will be seen in the case setup.

The numerical algorithm used to solve the model in OpenFOAM is described in detail in Chapter 6.

7.3 Case Setup

As shown in Figure 7.2, the simulated geometry spans 25 m square, with a height of 55 m. The depth was set at 45 m. This size was chosen to allow for enough space for the plume to develop. The original wellhead diameter was approximately 5 inches. At steady state, the mass flow rate should be 37 kg/s, comprised of 86.5% carbon dioxide and 13.5% hydrogen sulfide by mass. The outlet temperature at steady state was 220 K. Holding the mass flow rate constant, the inlet was resized using the inlet velocity and the gas density at 45 m of water depth. The criteria for mass conservation is:

$$\dot{m}_{Adjusted} = \dot{m}_{actual} = \rho_1 \vec{u}_{actual} A_{Adjusted} \qquad (7.22)$$

for which the adjusted area, $A_{Adjusted}$, was calculated from the actual velocity and the actual mass flow rate. The density of the gas was calculated at 550 kPa and 220 K. This produced a 0.36 m square inlet patch and a velocity of approximately 22 m/s. To maintain the actual inlet diameter, the velocity would have been scaled to 1400 m/s, which would have drastically increased computational requirements through the Courant number. The second benefit of scaling up the inlet size was to relax the mesh requirements in the jet region.
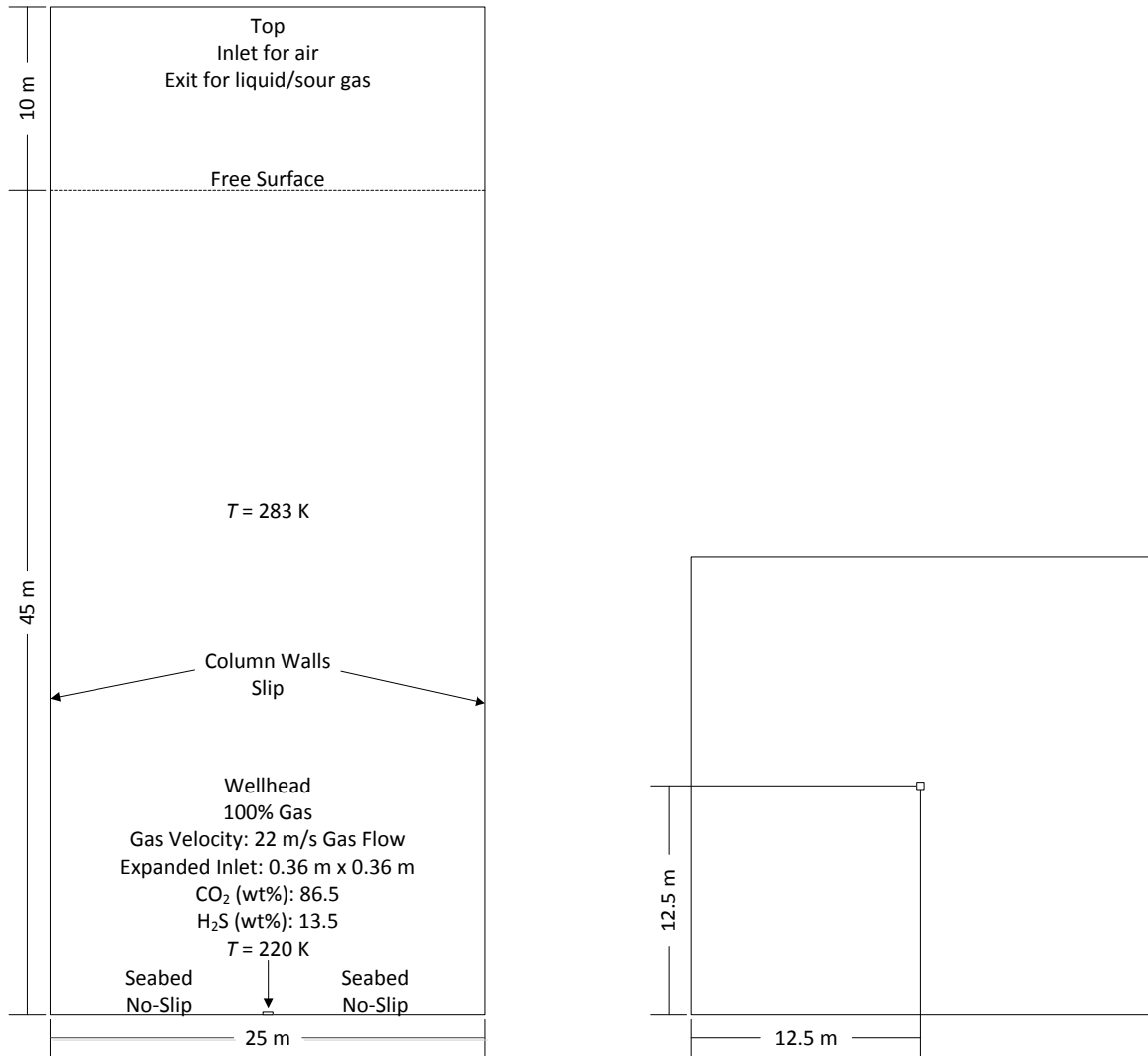
Figure 7.2 Case setup for the full-scale release.

OpenFOAM's built-in thermophysical libraries were used to model the temperature and pressure dependence of the physical properties. The ambient temperature was assumed to be a typical North Atlantic Ocean temperature of 283 K. Thus, properties were assumed to be constant at this ambient temperature. This decision was made from experience in initial simulations, where the gas quickly rose from the inlet temperature of 220 K to the ambient water temperature of 283 K. For the liquid phase, the properties were considered to be approximately equivalent to seawater, except for the mass diffusivities with were obtained from the literature. The gas phase diffusivities were estimated based on correlation. For the

obtained solution, the interphase mass transfer depended primarily on the mass diffusivities in the liquid. For the species equations, the diffusivities also depended on the turbulent. A summary of the liquid properties is provided in Table 7.1.

The ideal gas law was used to estimate the density of the gas phase. Henry's law coefficients for carbon dioxide and hydrogen sulfide were obtained from Sander (2015). The values of other physical properties in the gas phase are listed in Table 7.2. Based on the work of Douabul and Riley, (1979), the solubility of hydrogen sulfide does not change much with salinity. From the work of Weiss (1974), the carbon dioxide solubility does change with salinity, although for the salinities of up to 10%, the change is minimal. Therefore, the salinity effect was neglected in the current study.

Table 7.1 Properties of Liquid Water

Property	Value	Reference
Density, ρ (kg/m^3)	1027	-
Specific Heat Capacity, c_p, (J/kg/K)	4000	National Physical Laboratory (2017)
Dynamic Viscosity, μ (Pa s)	0.0012	National Physical Laboratory (2017)
Prandtl Number, Pr (-)	10	National Physical Laboratory (2017)
Diffusivity of CO_2, $D_{2,M,CO2}$ (m^2/s)	1.91×10^{-9}	Yaws (2003)
Diffusivity of H_2S, $D_{2,M,H2S}$ (m^2/s)	1.41×10^{-9}	Yaws (2003)

Table 7.2 Properties of the Gases

Property	CO₂ Value	H₂S Value	Air Value	Reference
Density, ρ (kg/m³)		Ideal Gas Law		-
Molar Mass, MW (g/mol)	44.01	34.08	28.9	-
Specific Heat Capacity, c_p (J/kg/K)	828	996	1000	Yaws (2009)
Dynamic Viscosity, μ (Pa s)	1.442×10^{-5}	1.503×10^{-5}	1.762×10^{-5}	Yaws (2009)
Prandtl Number, Pr (-)	0.75	0.57	0.71	Yaws (2009)
Diffusivity*, $D_{l,M,j}$ (m²/s)	7.73×10^{-5}	7.73×10^{-5}	—	Coulson et al. (1999)
Solubility**, H (-)	$H_{283K} = 1.32$ $m = 2100$	$H_{283K} = 3.10$ $m = 2400$	-	Rolf Sander (2015)

* The diffusivity is calculated from: $D = D_{298K} \left(\frac{T}{298}\right)^{1.5} \left(\frac{101325}{P}\right)$

** The Solubility is calculated from: $H = H_{283K} \left(m \left(\frac{1}{T} - \frac{1}{283}\right) \right)$

Three computational meshes were used in the presented study, as shown in Figure 7.3, Figure 7.4 and Figure 7.5. Despite scaling up the inlet, generating the mesh was still a challenge. Cells were concentrated in the centerline region with a cell expansion ratio of 10 from the center (first cell) to the walls (last cell). Two million cells was the upper limit for mesh refinement due to computational resource limitations. The boundary and initial conditions are summarized in Table 7.3 and Table 7.4, respectively.
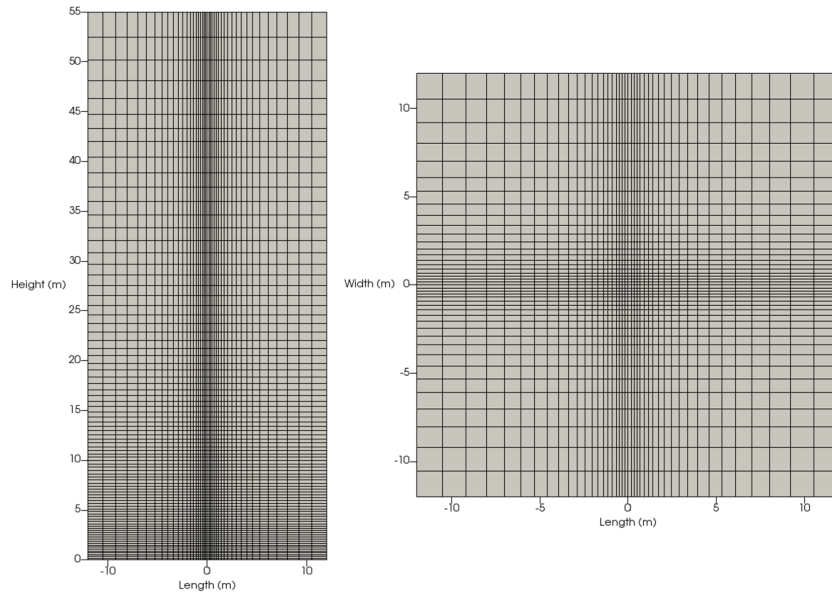
Figure 7.3 Coarse mesh used for the full-scale release scenario (number of cells = 153 468; smallest mesh dimension = 0.18 m; largest mesh dimension = 1.8 m; maximum aspect ratio = 17.3).
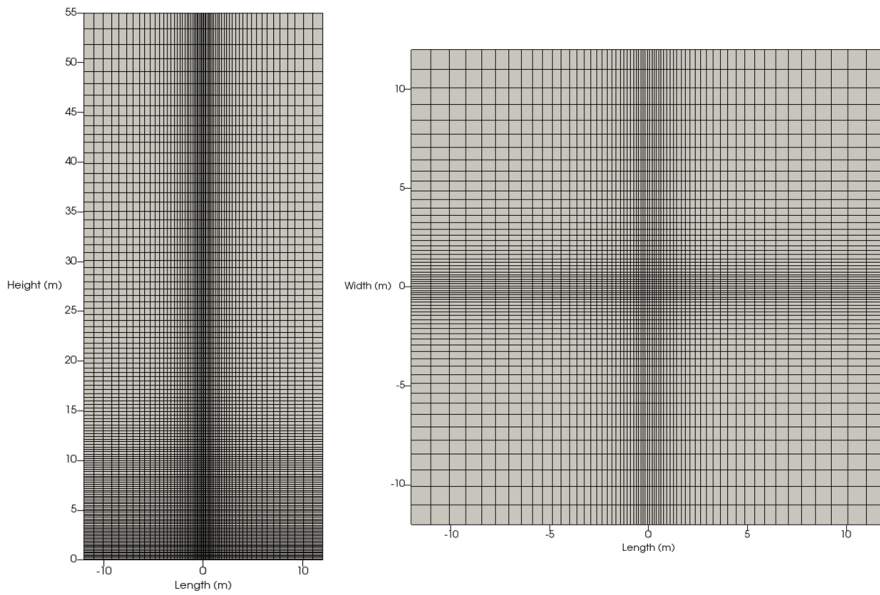
Figure 7.4 Intermediate mesh used for the full-scale release scenario (number of cells = 519 939; smallest mesh dimension = 0.12 m; largest mesh dimension = 1.2 m; maximum aspect ratio = 16.4).
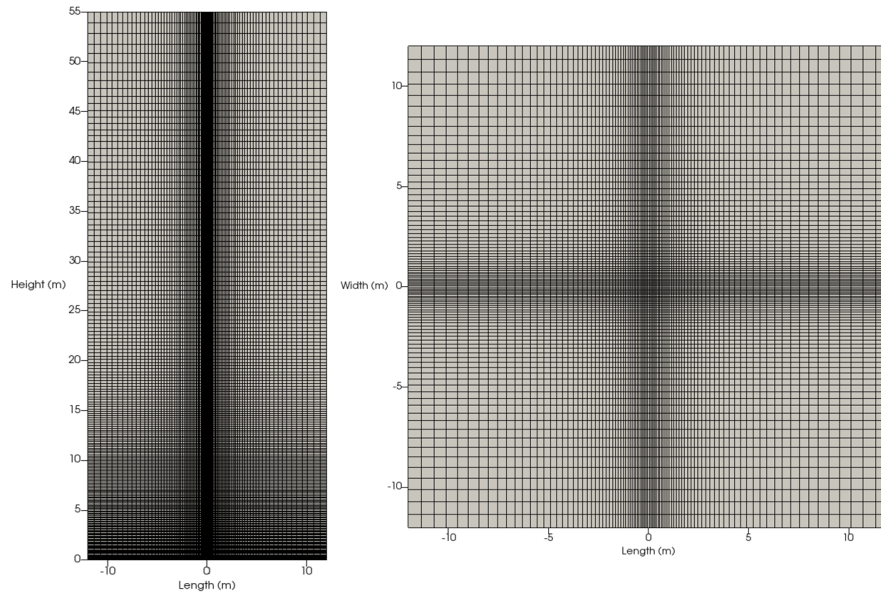
Figure 7.5 Fine mesh used for the full-scale release scenario (number of cells = 1 768 900; smallest mesh dimension = 0.072 m; largest mesh dimension = 0.79 m; maximum aspect ratio = 16.4).

As mentioned above, the closure terms necessary to model the system were chosen to be the Tomiyama drag, constant lift and Smagorinksy turbulence model. From the Simiano experiments (2005), and the work in Chapter 6, the lift coefficient was fixed at 0.1 and the turbulent dispersion was fixed at 40. Since there are more tuning parameters than can be experimentally fixed at the large scale due to a lack of experimental data, these two parameters were held constant. The Tomiyama model was selected for its overall predictive capacity and its applicability for contaminated systems. For the transition between the two models, a phase fraction filter of 0.3 was applied.

Table 7.3 Boundary Conditions used in the large-scale gas release scenario.

Variable	Walls	Inlet	Bottom	Top
Gas Phase Fraction	Zero gradient	1	Zero gradient	Inlet-Outlet
Temperature (K)	Zero gradient	220	Zero gradient	283
Velocity (m/s)	Slip	22	No slip	Inlet-Outlet
P_{rgh} (Pa)	Zero gradient	Zero gradient	Zero gradient	101325
Turbulent Kinematic Viscosity (m^2/s)	Zero gradient	Zero gradient	Zero gradient	Inlet-Outlet
H_2S (Liquid) Mass Fraction	Zero gradient	Zero-gradient	Zero gradient	Inlet-Outlet
H_2S (Gas) Mass Fraction	Zero gradient	0.135	Zero gradient	Inlet-Outlet
CO_2 (Liquid) Mass Fraction	Zero gradient	Zero gradient	Zero gradient	Inlet-Outlet
CO_2 (Gas) Mass Fraction	Zero gradient	0.865	Zero gradient	Inlet-Outlet
H_2O (Liquid) Mass Fraction	Zero gradient	Zero gradient	Zero gradient	Inlet-Outlet
Air (Gas) Mass Fraction	Zero gradient	0	Zero gradient	Inlet-Outlet

Table 7.4 Initial Conditions used in the large-scale gas release scenario.

Variable	Initial Condition
Gas Phase Fraction	0 up to 45 m, 1 above 45 m
Temperature (K)	283
Velocity (m/s)	0
P_{rgh} (Pa)	101325
Turbulent Kinematic Viscosity (m^2/s)	1×10^{-11}
H_2S (Liquid) Mass Fraction	0
H_2S (Gas) Mass Fraction	0
CO_2 (Liquid) Mass Fraction	0
CO_2 (Gas) Mass Fraction	0
H_2O (Liquid) Mass Fraction	1
Air (Gas) Mass Fraction	1

7.4   Results and Discussion

7.4.1 Mass Transfer Model Comparison and Preliminary Analysis of Mesh Dependence

Two mass transfer models were compared to try to determine the maximum and minimum expected dissolution rates. The Higbie model has been shown in the literature (Alves et al., 2005; Alves et al., 2006; Wang and Wang, 2007) to provide good predictions of mass transfer rates for bubbles with clean (mobile) interfaces. Conversely, the Frössling model has been shown in the literature (Alves et al., 2005) to provide good predictions of mass transfer rates for bubbles with contaminated (immobile) interfaces. Therefore, the Higbie model provides higher mass transfer rate predictions than the Frössling model. Although

an acid gas release in the ocean is more likely to lead to bubbles with contaminated interfaces (i.e. applicability of the Frössling model), the two models were used to investigate the bounds of the dissolution predictions.

Choice of the most appropriate bubble diameter to use in the DF model for the plume region of the release was not trivial. Since the actual diameter is unknown, a sensitivity study was performed (presented in the next section) to investigate the effect of bubble size on the dissolution rate predictions. The range of the studied bubble sizes was chosen based on Sellami et al. (2015), who studied the rise of carbon dioxide bubbles in an ocean environment. Although the mass flow rate was not the same as the current work, Sellami et al. (2015) provided a range of stable bubble sizes for carbon dioxide between 4 mm and 11 mm, with the majority between 6.5 mm and 9 mm. Therefore, 7.75 mm was selected as the likely mean bubble size, 4 mm was selected as the lower bound, 11 mm was selected as the likely upper bound, and two larger sizes of 13.75 mm and 16.5 mm were selected to investigate sensitivity.

To investigate mesh dependence, the first set of simulations employed the Higbie model with an assumed plume region bubble diameter of 7.75 mm. This case was chosen because the combination of the likely mean bubble diameter with the higher mass transfer predictions of the Higbie model would result in high dissolution rate predictions. Therefore, the results should provide an estimate of the highest likely dissolution rates. The dissolution rate predictions from this set of simulations are shown in Figure 7.6. For the three mesh refinements shown, the dissolution predictions remained mostly the same. This similarity between the results for the three meshes indicates that the prediction of the mass transfer rate is largely mesh independent.

Figure 7.6 shows a relatively low dissolution rate as the gas jet develops into a plume. However, once the plume begins to develop, the dissolution rate rapidly increases, and predictions stabilize to a nearly constant value soon after the plume reaches the top of the water column. It is important to note that the plume takes approximately 10 to 12 s to reach the surface for this set of simulations. The predictions in this case indicate that nearly all of the hydrogen sulfide and more than 80% of the carbon dioxide would dissolve in the

water column. However, as mentioned above, this is expected to be relatively large over-prediction of physical reality.
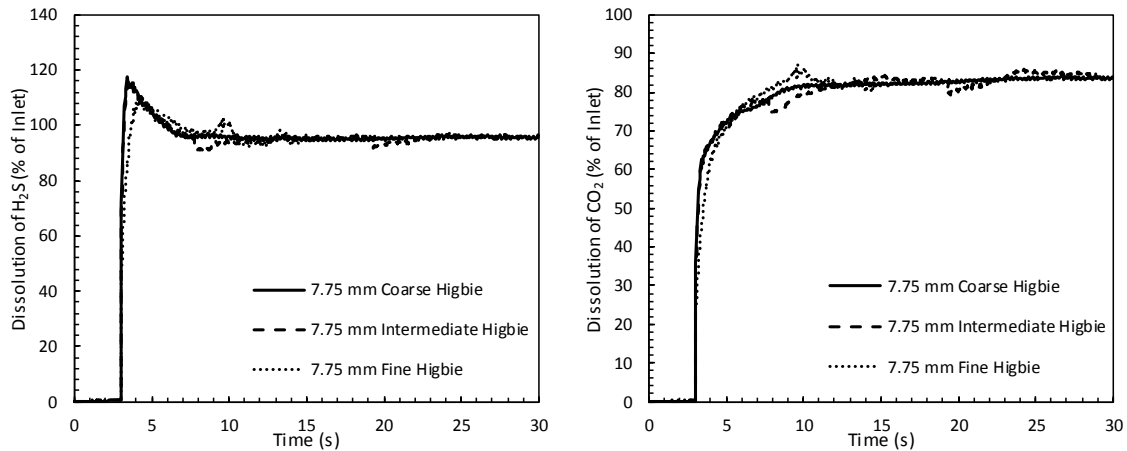
Figure 7.6 Comparison of dissolution rate predictions for an assumed plume region bubble diameter of 7.75 mm and the Higbie mass transfer model, showing the results for three mesh refinements.

To investigate mesh dependence of the dissolution predictions further, the second set of simulations employed the Frössling model with an assumed plume region bubble diameter of 11 mm. This case was chosen because the combination of the highest likely bubble diameter with the lower mass transfer predictions of the Frössling model would result in the lowest expected dissolution rate predictions. Therefore, the results should provide an estimate of the worst-case scenario. The dissolution rate predictions from this set of simulations are shown in Figure 7.7. For the three mesh refinements shown, the dissolution predictions remained very similar. This similarity between the results from the three meshes indicates that the effect of mesh resolution is small in the range investigated.

As in the previous set of simulations, the predicted dissolution rates are initially very low and then rapidly increase as the plume region develops. In this set of simulations, the plume takes approximately 12 s to reach the surface, soon after which the dissolution rate predictions stabilize. The stabilized dissolution rate predictions hovered around 29% of the total inlet mass for carbon dioxide and 48% for hydrogen sulfide. Although hydrogen sulfide is approximately 2.3 times more soluble in the water than carbon dioxide, dissolution rates do not differ by this factor because of the higher mass transfer driving force that exists for carbon dioxide due to its higher concentration in the gas phase.

182
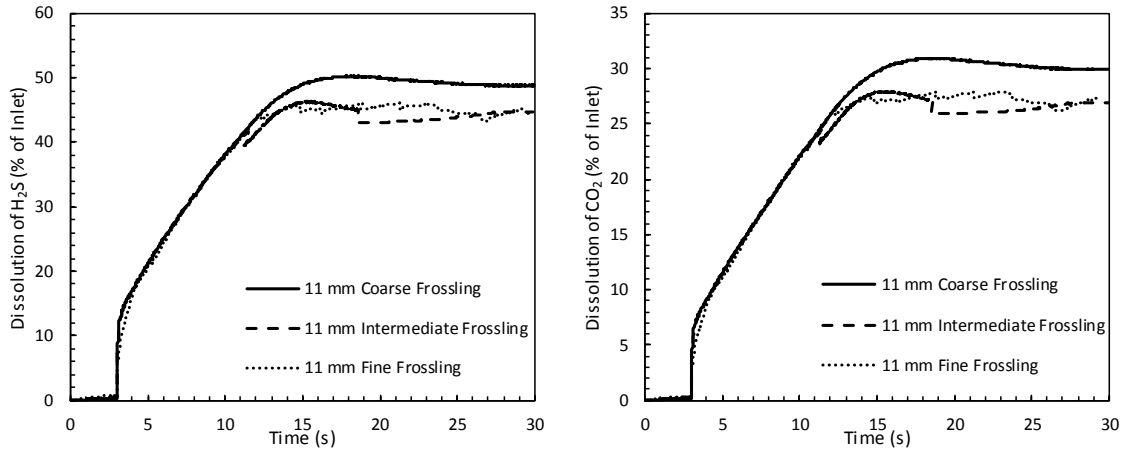
Figure 7.7 Comparison of dissolution rate predictions for an assumed plume region bubble diameter of 11 mm and the Frössling mass transfer model, showing the results for three mesh refinements.

The small discontinuities in the above figures occurred when cases had to be restarted during the simulations and are due to an initial condition set into the solver. After several iterations, the mass transfer rate was shown to return to the values prior to the restart. The cases were run over a long enough time that these small variations do not seem to affect the steady value.

7.4.2   Detailed Analysis of Mesh Dependence

In the simulations presented in this study, the solver was set to transition from VOF to the drift-flux method when the gas phase fraction dropped below 0.3. The average phase fraction profiles are shown in Figure 7.8 for the three mesh refinements. The 0.5 gas phase fraction contour surface, or interfacial contour, is also shown on the diagram. It is clearly shown that, as mesh refinement increases, the jet region is further resolved. Even though the interfacial phase fraction contour is approximately the same size in the three figures, the transition between the jet region (governed by VOF) and the plume region (governed by DF) is much smoother for the refined mesh. For the coarse mesh, both the jet region and surface region were unrefined, losing sharpness in the transition between the VOF and DF models. However, for the plume region, the results were nearly identical. From this it can be deduced that the drift-flux model provides reasonably stable predictions for relatively coarse meshes. The dissolution rate predictions were consistent between the three cases primarily because the DF model provides stable predictions for the plume region and this

183

is where most mass transfer occurs. Although the phase fraction predictions in the jet region changed between the three refinement cases, these predictions did not impact the dissolution rate predictions in Figure 7.6 and Figure 7.7 significantly.

With increased mesh refinement, the free surface appeared to form a flatter interface. Although the predictions appear to be more reasonable for the higher mesh resolution case, these differences in surface fluid dynamics predictions did not significantly impact mass transfer rate predictions. No validation studies were performed to investigate the accuracy of the surface region predictions. Further studies would have to be completed to evaluate the validity of surface region predictions for different model parameter values and mesh resolutions.
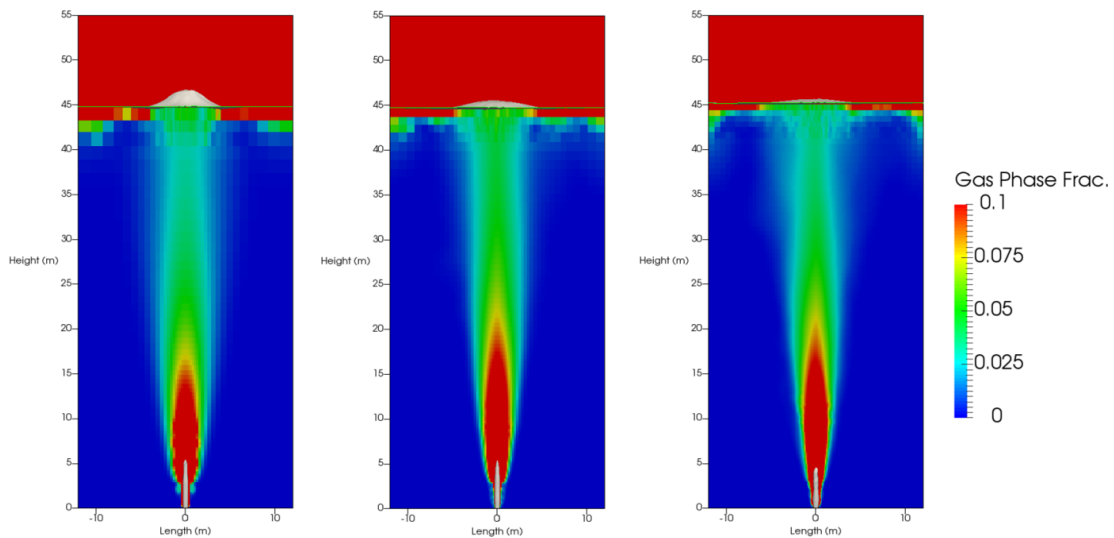
Figure 7.8 Phase fraction contours and interfacial contours for the 11 mm Frössling case, with the coarse case on the left, the intermediate case in the middle and the fine case on the right.

The volumetric mass transfer sources are compared in Figure 7.9 and Figure 7.10. In general, the highest mass transfer source was found immediately following the transition between the jet and plume (VOF and DF models). Although the jet penetrated a few meters into the transition region, the breakup of the jet and the formation of bubbles drastically increased the potential mass transfer. Mass transfer rates in the jet region were very low compared to the plume. Much of the dissolution occurred in the bottom half of the water

column, which lead to the reduced gas phase flow rate near the top of the water column, as shown above in Figure 7.8. Although there are small differences in the mass source predictions for the mesh refinement cases, Figure 7.9 and Figure 7.10 show that the difference is relatively small. One difference in the dissolution predictions that is shown in Figure 7.9 and Figure 7.10 was that the fine mesh predicted more variation and fine-scale structures in the jet and transition regions. However, the level of refinement is still relatively low for direct simulation of jet dynamics. It is expected that there would be a much smoother transition in the predictions between the jet and the plume region upon much further mesh refinement.

The use of 0.3 gas fraction as the transition region criterion did not have a significant impact the mass transfer predictions. Since the dissolution occurred primarily in the plume region, and the dissolution rapidly decreased toward the surface, triggering the transition at approximately the same location was sufficient to provide stable predictions. There is not much flexibility in the transition criterion because VOF is intended to be valid near 0.5 phase fractions. However, very coarse meshes can lead to errors because the interface may artificially stay stable over a larger surface in a coarse mesh. Therefore, the scalability of the model could be improved by triggering interface instability earlier in unresolved meshes.

Figure 7.9 CO_2 mass source densities and interfacial contours for the 11 mm Frössling case, with the coarse case on the left, the intermediate case in the middle and the fine case on the right.
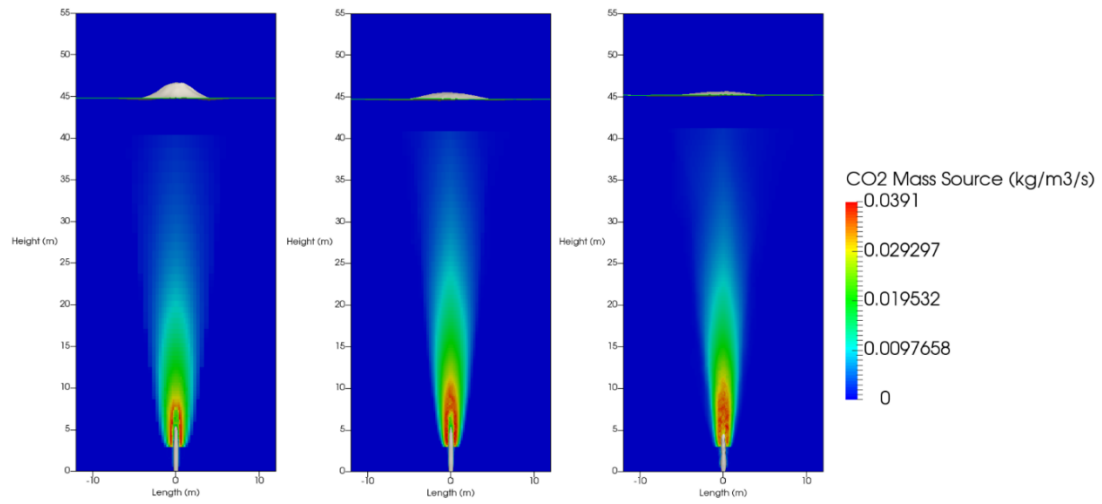

Figure 7.10 H_2S mass source densities and interfacial contours for the 11 mm Frössling case, with the coarse case on the left, the intermediate case in the middle and the fine case on the right.
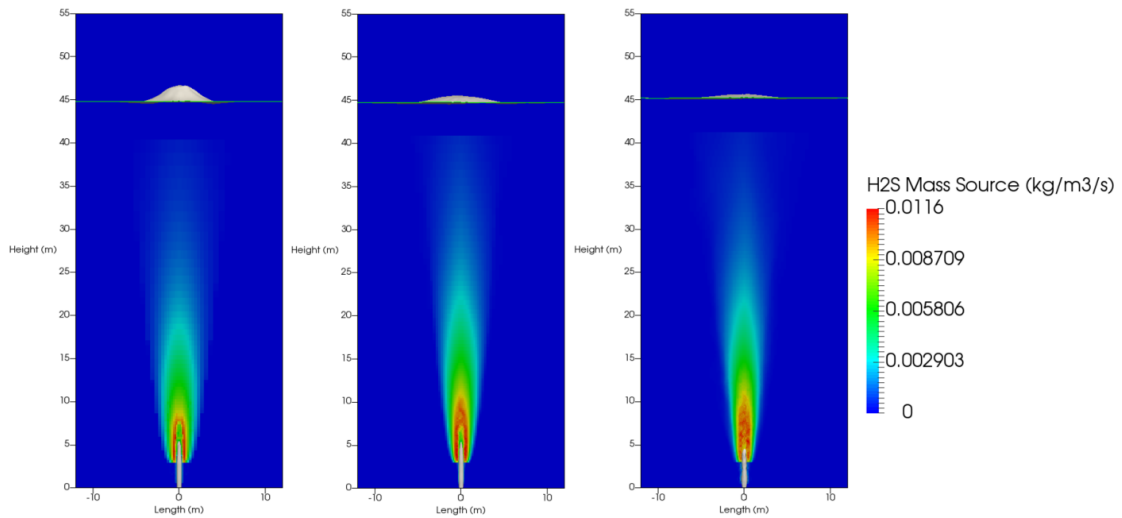
The liquid phase concentration contours for carbon dioxide and hydrogen sulfide are shown in Figure 7.11 and Figure 7.12, respectively. Overall, the concentration contours show similar behaviour. However, due to the lower resolution along the centerline, predictions resulted in higher velocities that carried more of the dissolved gases toward the surface in the coarse case. This resulted in a narrower profile prediction but did not affect the global dissolution rate very much.

As shown in the right most images in Figure 7.11 and Figure 7.12, the dissolved gas dispersed by the time it reached the surface, although it was far from saturating the medium. This agrees with the results from Figure 7.6 and Figure 7.7, which showed that the total dissolution rate rapidly approaches a constant value after the plume reaches the top of the water column. Had the domain become saturated, the case would have had to be run on a larger domain. The width limitation of the domain therefore only affected the fluid near the surface, which had only a relatively small impact on the total dissolution rate predictions. Given the transition back to VOF near the free surface, the detrainment rate would have been low.

Figure 7.11 CO₂ concentrations and interfacial contours for the 11 mm Frössling case, with the coarse case on the left, the intermediate case in the middle and the fine case on the right.
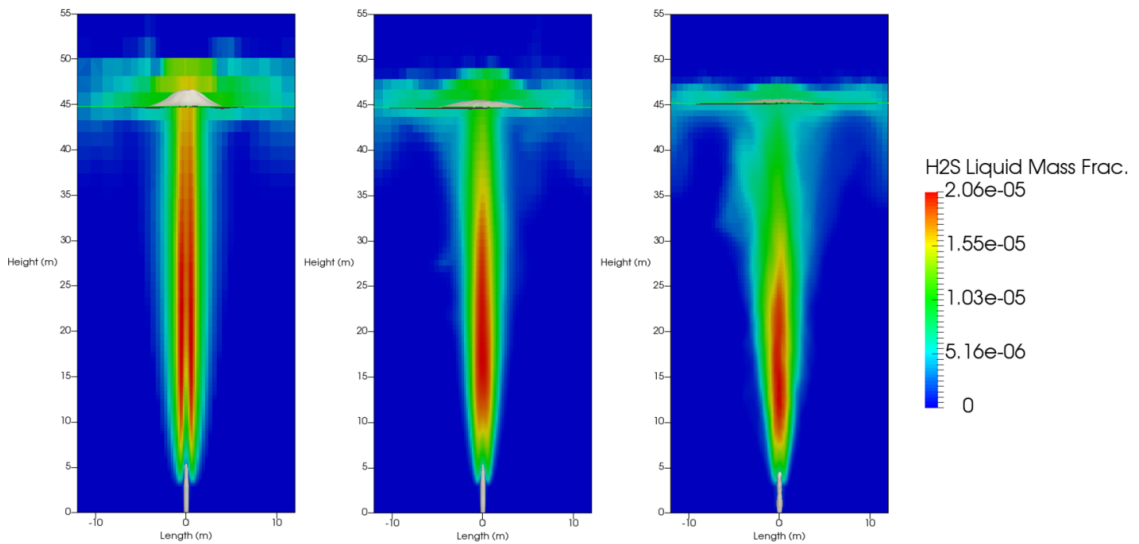
Figure 7.12 H₂S concentrations and interfacial contours for the 11 mm Frössling case, with the coarse case on the left, the intermediate case in the middle and the fine case on the right.

For the refinement study, the last examined metric was the average vertical velocity. Figure 7.13 shows that the velocity predictions in the field were impacted by mesh resolution. The contours shown in Figure 7.13 match the behaviour shown in the previous concentration contours, and are the likely cause for the predicted differences. Since the gas inlet was small compared to the surrounding domain, most of the refinement was focused on the centerline. The main difference in the velocity predictions seems to be due to differences in the prediction in the jet region. Upon refinement, predictions of the jet region become more accurate, including more fine-scale dynamic aspects of the flow and breakup/dispersion behaviour. These fine-scale processes contribute significantly to the decrease of the momentum after the gas phase leaves the jet region. Therefore, the velocity in the plume region becomes lower and the gas phase becomes more dispersed.
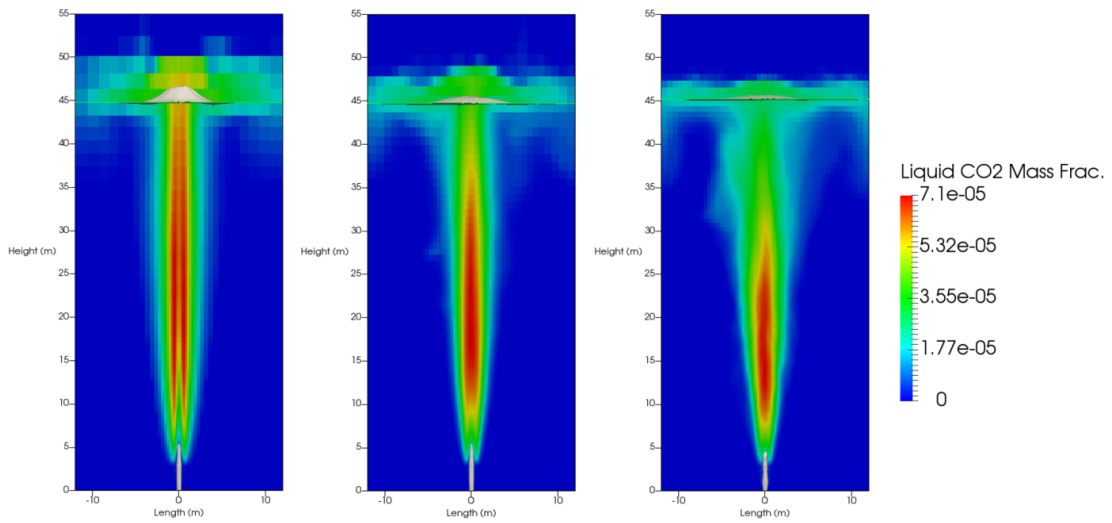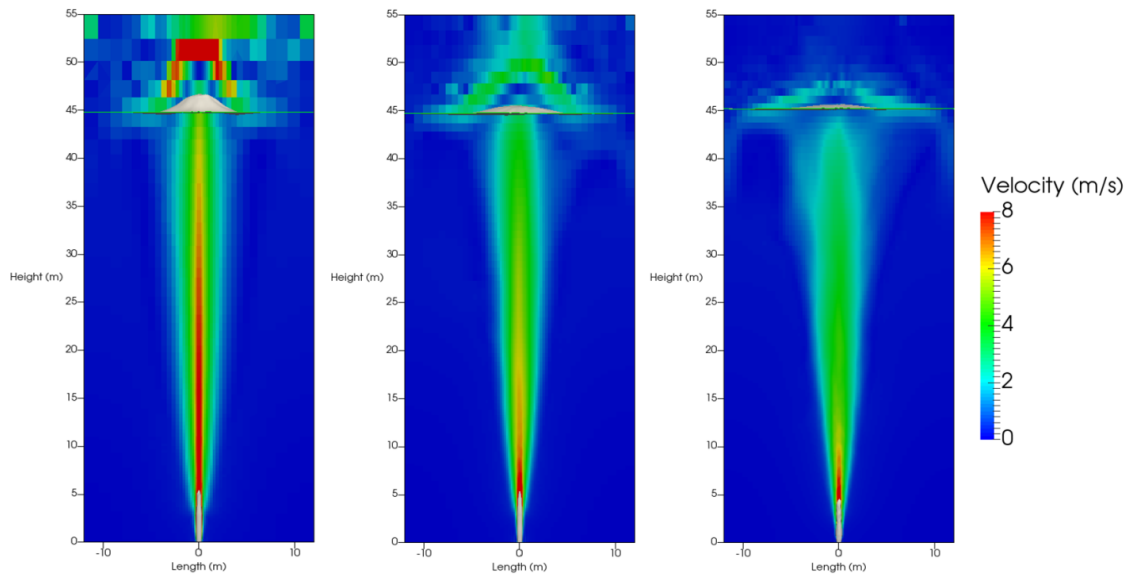

Figure 7.13 Average velocity and interfacial contours for the 11 mm rigid case, with the coarse case on the left, the intermediate case in the middle and the fine case on the right.

Mesh resolution clearly has an impact on the solution. The velocity and mass fraction profiles indicated a wobbling effect in both the jet and plume region as the mesh was refined. If averaged over a longer time, these wobbles would turn into a larger dispersed

189

region. Additionally, higher mesh resolution would provide more realistic predictions for the transition between the jet and plume, as shown in the right most part of Figure 7.8. The high aspect ratio of the cells along the centerline could also have impacted the results. To overcome this problem, the mesh could have been generated with a refinement region near to the jet instead. It was decided to use a symmetric mesh with hexahedral cells to avoid the chance of numerical error forcing transition between VOF and DF. It was clear from the results that, with refinement, the physically unrealistic effects disappeared as seen in Figure 7.13. However, obtaining physically realistic predictions in all regions would require a relatively fine mesh, which would increase computational requirements.

Despite the differences in the velocity and concentration contours, the coarse mesh provided similar predictions as the finer meshes for the total dissolution rate. The coarse mesh was therefore chosen to represent the system for further sensitivity analyses due to the lower computational requirements. However, as was shown above, the velocity at the surface differs significantly between mesh refinements. Therefore, reliable surface effect predictions would require cases to be run at a higher level of refinement.

7.4.3 Effect of Assumed Plume Region Bubble Size

Since the mass transfer solution remained relatively mesh independent between the Higbie and Frössling test cases, the coarse mesh was used for the sensitivity analysis. Since seawater contains a significant quantity of surface active compounds that could migrate to the gas-liquid interface, it was decided to continue using the contaminated interface approximation (i.e, Frössling model) for the sensitivity analysis. As mentioned above, the work of Sellami et al. (2015) indicated a likely bubble diameter value in the range of 4 mm to 11 mm. Therefore, simulations were performed using assumed plume region bubble diameters of 4 mm, 7.75 mm and 11 mm. To investigate sensitivity to even larger diameters, two additional diameters of 13.75 mm and 16.5 mm were also used in the sensitivity studies.

The predicted dissolution rates for different bubble diameters over time are shown in Figure 7.14. The steady dissolution rates are plotted as a function of bubble diameter in Figure 7.15.
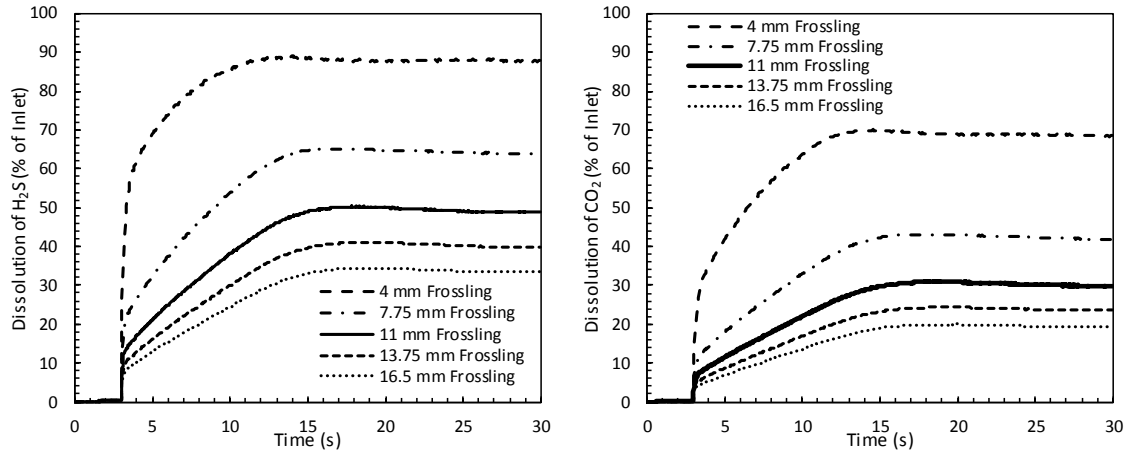
Figure 7.14 Dissolution rates for both H_2S (left) and CO_2 (right) for the Frössling mass transfer cases at various bubble diameteters. The total dissolution rate is plotted as a percentage of the inlet mass flow rate.
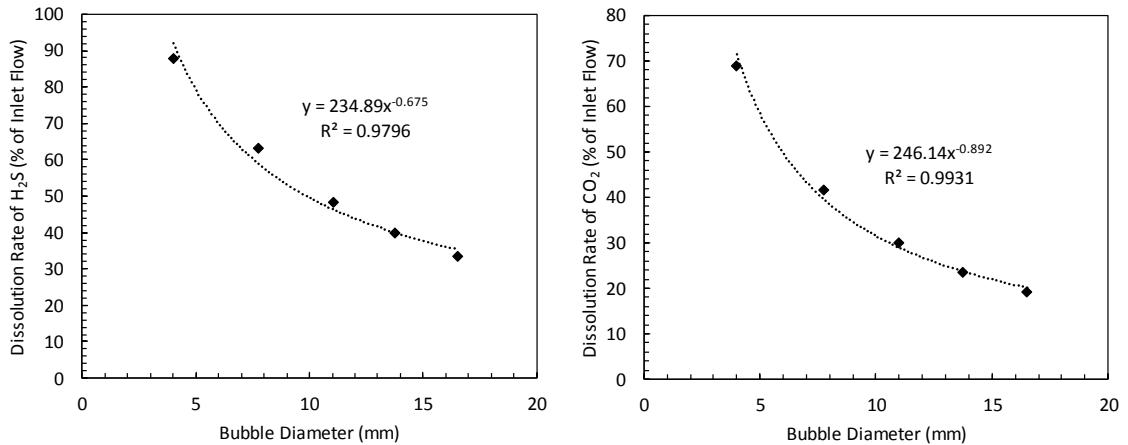
Figure 7.15 Variation of steady total dissolution rates as a function of bubble diameter for mass transfer predictions based on the Frössling model with the coarse mesh.

As expected, smaller bubble sizes produced significantly higher dissolution rate predictions. The dissolution rates for 4 mm bubbles correspond to approximately 68.9% dissolution of CO_2 and 87.8% dissolution of H_2S entering the system. Conversely, the 11 mm bubbles predicted only 30% CO_2 dissolution and 48.3% H_2S dissolution. As mentioned above, these two diameters represent the bounds of likely bubble diameters that would be found in a fully-dispersed plume. Therefore, they represent the most likely low bound and high bound estimates of the dissolution rates. In reality, a plume would likely be composed of a range of bubble sizes, but the average predictions would probably still lie in this range. In order to test the sensitivity of the analysis further, simulations were repeated at 13.75

mm and 16.5 mm, corresponding to a 25% and 50% increase from the worst case scenario, respectively. As shown on Figure 7.9, there is a rapid decrease in the differences between dissolution rate predictions for increased bubble sizes. As a result, the 16.5 mm shows a 19.3% dissolution of CO_2 and a 33.4% dissolution of H_2S.

There are two reasons for the higher dissolution rates for the smaller bubble diameters. First, given the small bubble diameter, the drag forces result in a lower rise velocity. Second, the interface area density, which is inversely proportional to the bubble diameter, increases rapidly for smaller bubble diameters. Since the interfacial area density is directly proportional to the mass transfer rate, this increase results in increased mass transfer rates for smaller bubbles. As shown in Figure 7.10, the relationship between the dissolution rates of carbon dioxide and hydrogen sulfide and the bubble diameter follows an inversely proportional trend but is not directly inversely proportional. This seems to indicate that the increased interfacial area density is the primary effect impacting dissolution rate predictions, but the velocity of the gas and its lateral spreading rate are also important.

Additionally, for the assumed bubble size there was no prediction of the rate of change of the bubble diameter due to decompression through the water column. The bubble diameter would change as a function of depth. However, making accurate predictions for bubble size change would necessitate an additional model, similar to a PBM, since the size reduction is a function of reducing external pressure, the phase loss due to mass transfer, and breakup and coalescence processes. The incorporation of a PBM into the model was outside the scope of this project, but the loss of transfer area due to the mass transfer itself was directly implemented through the change in the phase fraction. Under these conditions, it was assumed that bubbles disappeared as mass was lost but maintained the same average diameter.

7.4.4 Atmospheric Emissions

The last objective of this work was to summarize release predictions to the atmosphere. The 11 mm Frössling case was deemed to be the most likely worst-case scenario. Table 7.5 summarizes the release conditions and atmospheric predictions for the case. The velocity was taken as that of the gas phase just below the free surface, where there was

simultaneously more resolution as well as no effects due to splashing. These results are the final product that could be used as the input to an atmospheric dispersion model focused on the defined point source.

Table 7.5 Release scenario for the 11 mm case using the Frössling model.

	Units	Release Scenario
	MMSCFD	65
Total release rate	m^3 (STP)/s	21.3
	kg/s	38
Composition at sea floor	CO_2 Mass Fraction	0.865
	H_2S Mass Fraction	0.135
Mass flow rate at ocean surface	kg/s	25.63
Composition at ocean surface	CO_2 Mass Fraction	0.898
	H_2S Mass Fraction	0.102
Decrease in CO_2	-	30%
Decrease in H_2S	-	49%
Effective diameter of plume at ocean surface	m^2	14
Gas velocity at ocean surface	m/s	1.23

7.4.5 General Discussion

The results shown above demonstrated the application of the combined VOF-DF modeling methodology to the simulation of a shallow water acid gas release. The mesh refinement studies indicated that the predicted dissolution rates were relatively independent of mesh resolution. The main reason for this is that most of the mass transfer occurred in the plume region, which was controlled primarily by DF predictions. The mesh dependence studies also indicated that the jet region predictions were more sensitive to mesh resolution, and that higher resolutions are required to improve the smoothness of the transition between the models. Finding an appropriate mesh resolution would likely become much more important in scenarios with even higher release rates because such cases would have a larger jet region.

As shown in Figure 7.6 and Figure 7.7, the dissolution rate predictions showed a time lag before increasing to a steady value. This delay was caused by the formation and subsequent transition of the gas jet to a plume. To avoid immediate transition to a plume for very coarse mesh resolutions, the transition model was set to activate at least 3 m above the gas release point. This was done to prevent instabilities near the inlet from affecting the establishment of the initial plume. This constraint had a negligible impact on the results since the transition did not occur until about 5 m above the release point. Although this helped to stabilize the simulations and did not impact the dissolution rate predictions significantly, it did lead to some discontinuity in the transition from the jet to the plume in the coarse mesh cases. However, the results for finer mesh resolutions indicated that this transition becomes smoother, which supports the validity of the modeling approach.

The results shown in Figure 7.8 demonstrate that the jet core persists to a height of approximately 5 meters, or one ninth of the water column. For shallow water release scenarios, this result indicates that the initial jet region can be important. The assumption that the entirety of the jet region can be neglected (i.e. that there is a rapid transition to a plume) should therefore be used with caution. The jet region has a lower rate of mass transfer, and it therefore inhibits the dissolution rate of the gas. It would therefore be desirable to perform further fine mesh simulations to try to further resolve the detailed behaviour of the jet region. This would allow better input to coarse grid plume models and better definition of the transition criterion used in the model in this study.

It should be noted that the cases investigated in this study were based on a steady release rate. In reality, if gas were released from a ruptured pipeline or wellhead, there would normally be an initial release with a much higher flow rate than the steady value. Although results were only shown for a steady release rate in this study, one of the advantages of the developed model is its applicability to the modeling of highly transient releases with effectively no modifications. A transient release scenario would simply result in changing jet dynamics and transition over time.

One major simplification that was made in this study was the assumption that the acid gas release consisted of only a gas phase. In many cases, the release would realistically have

been a mixture of gas and liquid. However, this decision was made to simplify the modeling to a point where it would be tractable. Future modifications of the model could be made to add extensions for the three or four phases that would result if another liquid were released into the water column. Despite this simplification, the predictions made with the Higbie and Frössling mass transfer models and a range of bubble sizes appear to provide a good estimate of the likely bounding predictions for the dissolution rate. Since the bubbles rising through the water column in the ocean would likely have contaminated interfaces, the results from the Frössling model are more trustworthy. Additionally, based on published data in the literature, the fully established plume region bubble diameter would likely be in the range of 4 to 11 mm. A reasonable estimate of the likely dissolution rate could therefore be based on the predictions using the Frössling model with an 11 mm bubble diameter because this adds a margin of error to the unknown bubble diameter. For the studied conditions, this resulted in predictions of 30% CO_2 dissolution and 48.3% H_2S dissolution relative to the release rate.

This data was summarized for input to atmospheric release models in Table 7.5, with the intent of utilizing this model to further define an immediate protection zone in the case of catastrophic failure.

7.5 Conclusions

The simulation of a shallow water acid gas reinjection well blowout is a complicated scenario. The scale of the ocean environment, limitations of currently available modeling approaches and limitations of available computational resources provide a hurdle in the development of an adequate model. The complexities of the fluid dynamics make the use of a single, unified approach challenging. Within a computational fluid dynamics framework, a multiscale modeling approach is one way to manage the challenges posed by this scenario. An alternate approach would be to apply different modeling approaches to each region and then use the outputs from one model as the input to others. Multiscale modeling approaches could be based on a variety of frameworks. For example, the Eulerian multi-fluid modeling methodology could be applied with various closure models that are applicable to the various regions in the release. Alternatively, a methodology based on the

Lagrangian particle tracking approach could be developed with various closure models to represent each region in the release.

In this study, a multiscale modeling approach based on the combination of the volume-of-fluid and drift-flux models were developed and applied. The VOF model was chosen because it can provide direct prediction of gas jet dynamics. The drift-flux model was chosen primarily because of its capacity to make accurate far-field predictions, while also having a structure that allowed the direct integration of the two methods. Relative to other multiscale modeling approaches, the benefits of this methodology were minimizing the number of closure models that needed to be incorporated into the model because the gas jet could potentially be directly resolved by the VOF model. Relative to multi-model approaches, the primary benefit is computational requirements because only one sets of conservation models needed to be solved for all regions in the release. The primary disadvantage of the adopted modeling approach is the need to choose an appropriate mesh resolution that ensures a smooth transition between the VOF and DF models. However, this disadvantage is also commonly encountered when the VOF methodology is coupled to either LPT or EE models.

The simulations presented in this study focused on a full-scale release scenario of acid gas from an offshore shallow well blowout. The conditions were chosen to be as realistic as possible, with a reasonable release rate. Studies were performed to investigate the effects of mesh resolution and chosen far-field mass transfer model on the predicted gas dissolution rate because this directly impacts the release rate to the atmosphere. Sensitivity studies were then performed to analyze the impact of assumed plume region bubble diameter on the dissolution rate. The results indicated that the predicted gas dissolution rate is relatively insensitive to the chosen mesh resolution. This result was attributed to the applicability of the drift-flux model at low resolutions, and the fact that most mass transfer occurred in the plume region. The results also indicated that, as expected, the chosen mass transfer model has a strong impact on the dissolution rate predictions. The Frössling model, which predicts lower mass transfer rates than the Higbie model was suggested as an appropriate mass transfer model because of its applicability for predicting mass transfer from bubbles with contaminated interfaces. The results from bubble diameter sensitivity

studies indicated a strong link between the dissolution rate predictions and bubble diameter. This link appeared to be primarily due to the increased bubble surface area density at smaller diameters but can also be partially attributed to bubble rise velocity and plume spreading. A plume region bubble diameter of 11 mm was suggested to be the likely maximum. Based on this diameter and the Frössling model the likely dissolution rates for the release scenario were determined to be 30% of the inlet flow rate for CO_2 and 48.3% of the inlet flow rate for H_2S. The predicted composition and flow rate of the gas entering the atmosphere were summarized to provide input conditions for atmospheric dispersion models.

Chapter 8

Conclusions

Developing a model to predict gas dissolution in a subsea environment, and the consequent emission rate to the atmosphere following an acid gas release is challenging. The model must be able to predict transition between multiple flow regimes having different relevant length scales and governing processes. The initial jet will be largely continuous, but transition to a plume of dispersed gas bubbles that will drift towards the surface where the gas will detrain into the atmosphere. The modeling of such releases is important to predict emergency protection zones to mitigate effects of an accidental release. A worst-case scenario is likely to be the most appropriate basis on which to formulate these plans.

In this work, a hybrid volume-of-fluid (VOF) and drift-flux (DF) model was developed to predict fluid dynamics and gas dissolution rates within the entire water column following an acid gas well blowout. The model was developed to be scalable so that it could be used to provide reasonable predictions on coarse computational meshes and more detailed insight on finer meshes. To develop the model, literature was reviewed to select appropriate modeling approaches for the gas jet and plume regions of a release. A method was explored to facilitate direct prediction of gas-liquid mass transfer rates, but this method was shown to be computationally too expensive for full-scale predictions. The final model was designed to take advantage of the benefits of VOF for prediction of the gas jet and DF for the prediction of the plume dynamics. This hybrid approach was validated through comparison to published data in two case studies, and then used to make full-scale predictions for a realistic acid gas release scenario,

8.1 Major Contributions

This section provides a brief summary of the major contributions included in each of the chapters presented in this dissertation.

8.1.1 Chapter 2

Development of the model began with the consideration of the jet region itself. In preparation for the development of a model for the jet region, a review of multiphase modeling techniques was compiled. The notable conclusions from this study were:

- Interface tracking/capturing methods (IT) are the most applicable to continuous phase regions.
- IT methods have high computational requirements, even if applied without mass transfer.
- The algebraic VOF methodology is preferred due to global conservation of mass, a simplified advection step, and the information required to construct estimate mass transfer.

8.1.2 Chapter 3

A compressible VOF solver was developed to enable direct prediction of interphase mass transfer, potentially in gas-liquid system. The developed model was tested using three validation cases. The following conclusions were reached:

- Mass fraction and temperature profiles compared well with theoretical results.
- Use of a compressible solver improved the capacity of the model to predict interface shrinkage due to mass gain or loss.

8.1.3 Chapter 4

The ability of the compressible VOF solver to predict gas jet dynamics on relatively coarse meshes was tested. In a test of the VOF solver on a horizontal gas jet/plume, it was shown that:

- The trajectory of the jet could be predicted well for relatively coarse mesh resolution.
- Mesh independence was difficult to obtain because the grid resolution increases resolution of fine-scale bubbles.

- It would not be possible to simulate the true interfacial area by the approximation method employed in Chapter 3 for a full-scale ocean release using available computational resources.

8.1.4 Chapter 5

Most modeling of subsea releases has been accomplished using integral models. A literature review was conducted to highlight the recent literature on large-scale release models. A summary of the most important conclusions is:

- Integral models are fairly accurate and quick tools that can model plume trajectory and dissolution. However, they are not able to resolve small-scale physical processes in multiple dimensions and time.
- The prevailing methods used for bubble plume studies are Lagrangian particle tracking (LPT) and Eulerian-Eulerian multi-fluid models (E-E). Although these models can provide predictions for the plume region, applicability to the jet region is questionable.
- The jet region is usually ignored and therefore there is a gap in the literature that can be addressed using multiscale models.

8.1.5 Chapter 6

A hybrid model was developed to allow VOF-based prediction of the gas jet dynamics and DF predictions in the plume region. The model was validated using two test cases. The first case was a vertical bubble plume, for which parameters were tuned to replicate the experimental results.

- After appropriate tuning, the drift-flux model provided good agreement with published numerical studies and experimental data.
- The dynamics of vertical bubble plumes were well predicted by the DF model, even at coarse mesh resolutions.

The second validation was for the mass transfer algorithm, which was tested on a horizontal plume of oxygen aerating a tank. The conclusions were:

- Jet penetration length was not very well predicted using a bubble diameter that provided good mass transfer predictions. This could have been related to the mixed inlet condition.

- Although the model assumed an average bubble size, predicted values of the mass transfer coefficient were close to experimental results. The mass transfer coefficient predictions were relatively insensitive to mesh refinement.

- Using a sensitivity study on the bubble size and mass transfer model, it was shown that the results could effectively bound the experimental value.

8.1.6 Chapter 7

An actual subsea acid gas injection well blowout scenario was simulated using the multiscale model. A summary of conclusions from this chapter are:

- Convergence on the dissolution rate was possible using relatively coarse meshes.

- Although a large portion of the gas dissolves, a significant portion still reaches the surface. The amount dissolved depends on the release rate, release composition and assumed bubble size in the plume. Since the bubble size is not definitively known, it is only possible to define a likely range of dissolution rates.

8.2 Future Work

Although the model was used to predict the behaviour of a subsea acid gas well blowout, there are a number of lingering points to discuss and improve on:

- In an actual release, bubbles in the plume region will not have a uniform size. Further development should be made towards implementing a population balance equation.

- Dynamic mesh refinement should be investigated as a method to further smooth transition between the jet and plume models.

- The choice of mass transfer models should be further studied, in order to develop a better bounding of the actual solution.

- The model should be extended to three phase releases, for which the jet region would be larger.

References

Aboulhasanzadeh, B., Thomas, S., Taeibi-Rahni, M., Tryggvason, G., 2012. Multiscale computations of mass transfer from buoyant bubbles. Chemical Engineering Science, 75. 456-467.

Abu-Al-Saud, M., Riaz, A., Tchelepi, H., 2017. Multiscale level-set method for accurate modeling of immiscible two-phase flow with deposited thin films on solid surfaces. Journal of Computational Physics, 333. 297-320.

Adamczyk, W., Klimanek, A., Białecki, R., Węcel, G., 2014. Comparison of the standard euler-euler and hybrid euler-lagrange approaches for modeling particle transport in a pilot scale circulating fluidized bed. Particuology, 15. 129-137.

Albadawi, A., Donoghue, D.B., Robinson, A.J., Murray, A.B., Delauré, Y.M.C., 2013. Influence of surface tension implementation in volume of fluid and coupled volume of fluid with level set methods for bubble growth and detachment. International Journal of Multiphase Flow, 53. 11-28.

Almohammed, N., Alobaid, F., Breuer, M., Epple, B., 2014. A comparative study on the influence of the gas flow rate on the hydrodynamics of a gas-solid spouted fluidized bed using Euler-Euler and Euler-Lagrange/DEM models. Powder Technology, 264. 343-364.

Alves, S., Orvalho, S., Vasconcelos, J., 2005. Effect of bubble contamination on rise velocity and mass transfer. Chemical Engineering Science, 60. 1-9.

Alves, S., Vasconcelos, J., Orvalho, S., 2006. Mass transfer to clean bubbles at low turbulent energy dissipation. Chemical Engineering Science, 61. 1334-1337.

Andreolli, I., Zortea, M., Baliño, J., 2017. Modeling offshore steady flow field data using drift-flux and black-oil models. Journal of Petroleum Science and Engineering, 157. 14-26.

ANSYS Inc. (2011), ANSYS FLUENT Theory Guide, Canonsburg, PA.

Argyropoulos, C., Markatos, N., 2015. Recent advances on the numerical modelling of turbulent flows. Applied Mathematical Modelling, 39. 693-732.

Banerjee, R., 2007. A numerical study of combined heat and mass transfer in an inclined channel using the VOF multiphase model. Numerical Heat Transfer, Part A: Applications. An International Journal of Computation and Methodology, 52. 163-183.

Banerjee, R., 2013. Numerical investigation of evaporation of a single ethanol/iso-octane droplet. Fuel, 107. 724-739.

Baltussen, M.W., Kuipers, J.A.M., Deen, N.G., 2014. A critical comparison of surface tension models for the volume of fluid method. Chemical Engineering Science, 109. 65-74.

Badreddine, H., Sato, Y., Niceno, B., Prasser, H., 2015. Finite size Lagrangian particle tracking approach to simulate dispersed bubbly flows. Chemical Engineering Science, 122. 321-335.

Benson, D.J., 2002. Volume of fluid interface reconstruction methods for multi-material problems. Applied Mech Review, 55 (2). 151-165.

Battistelli, A., Marcolini, M., 2009. TMGAS: A new TOUGH2 EOS module for the numerical simulation of gas mixtures injection in geological structures. International Journal of Greenhouse Gas Control, 3. 481-493.

Bhaumik, T., 2005. Numerical modeling of multiphase plumes: A comparative study between two-fluid and multi-fluid integral models. Doctorial Thesis at Texas A&M University, USA.

Bhole, M.R., Joshi, J.B., Ramkrishna, D., 2008. CFD simulation of bubble columns incorporating population balance modeling. Chemical Engineering Science, 63. 2267-2282.

Bhusare, V., Dhiman, M., Kalaga, D., Roy, S., Joshi, J., 2017. CFD simulations of a bubble column with and without internals by OpenFOAM. Chemical Engineering Journal, 317. 157-174.

Bibilazu, A., Andrawus, J., Adom, E., Steel, J., Brikinns, T., 2010. Numerical modelling of subsea multiphase plumes: An Eulerian integral approach. Proceedings of the World Congress on Engineering, London, U.K.

Bigalke, N.K., Rehder, G., Gust, G., 2009. Methane hydrate dissolution rates in undersaturated seawater under controlled hydrodynamic forcing. Marine Chemistry, 115. 226-234.

Bonometti, T., Magnaudet, J., 2007. An interface-capturing method for incompressible two-phase flows. Validation and application to bubble dynamics. International Journal of Multiphase Flow, 33. 109-133.

Bothe, D., Fleckenstein, S., 2013. A volume-of-fluid-based method for mass transfer processes at fluid particles. Chemical Engineering Science, 101. 283-302.

Bové, J., Strlič, M., Mazzei, L., 2016. Applicability of a drift-flux model of aerosol deposition in a test tunnel and an indoor heritage environment. Building and Environment, 106. 78-90.

Brackbill, J.U., Kothe, D.B., Zemach, C., 1992. A continuum method for modeling surface tension. Journal of Computational Physics, 100. 335-354.

Buffo, A., Vanni, M., Renze, P., Marchiso, D., 2016. Empirical drag closure for polydisperse gas-liquid systems in bubbly flow regime: Bubble swarm and micro-scale turbulence. Chemical Engineering Research and Design, 113. 284-303.

Burghoff, S., Kenig, Y., 2005. CFD modelling of mass transfer and interfacial phenomena on single droplets. Proceedings of the European Symposium on Computer Aided Process Engineering, L. Puigjaner and A. Espuna (Editors). 103-108.

Burns, A., Frank, T., Hamill, I., Shi, J., 2004. The Favre averaged drag model for turbulent dispersion in Eulerian multi-phase flows. 5th Internation Conference on Multiphase Flow, Yokohama, Japan.

Buscaglia, G., Bombardelli, F., García, M., 2002. Numerical modeling of large-scale bubble plumes accounting for mass transfer effects. International Journal of Multiphase Flow, 28. 1763-1785.

Buwa, V., Deo, D., Ranade, V., 2006. Eulerian-Lagrangian simulations of unsteady gas-liquid flows in bubble columns. International Journal of Multiphase Flow, 32. 864-885.

Canadian Association of Petroleum Engineers, 2017. The World Needs Energy. Retrieved from http://www.capp.ca/canadian-oil-and-natural-gas/the-world-needs-energy

Carroll, J.J., Mather, A.E., 1995a. A generalized correlation for the Peng-Robinson interaction coefficients for paraffin-hydrogen sulfide bunary systems. Fluid Phase Equilibria, 105. 221-228.

Carroll, J.J., Mather, A.E., 1995b. The correlation of the vapour-liquid equilibrium in hydrogen sulfide-paraffin hydrocarbons using the Peng-Robinson equation. Fluid Phase Equilibria, 112. 167-168.

Carroll, J., 2009. Acid gas injection: Past, present and future. International Acid Gas Symposium 2009, Canada.

Charin, A.H.L.M., Tuković, Ž., Jasak, H., Silva, L.F.L.R., Lage, P.L.C., 2017. A moving mesh interface tracking method for simulation of liquid-liquid systems. Journal of Computational Physics, 334. 419-441.

Chen, F., Yapa, P.D., 2001. Estimating hydrate formation and decomposition of gases released in a deepwater ocean plume. Journal of Marine Systems, 30. 21-32.

Chen, F., Yapa, P.D., 2002. A model for simulating deepwater oil and gas blowouts – Part II: Comparison of numerical simulations with "Deepspill" field experiments. Journal of Hydraulic Research, 41. 353-365.

Chen, F., Yapa, P.D., 2004. Modeling gas separation from a bent deepwater oil and gas jet/plume. Journal of Marine Systems, 45. 189-203.

Chen, F., Yu, S., Lai, A., 2006. Modeling particle distribution and deposition in indoor environments with a new drift-flux model. Atmospheric Environment 40. 357-367.

Cloete, S., Olsen, J.E., Skjetne, P., CFD modeling of plume and free surface behavior resulting from a sub-sea gas release. Applied Ocean Research 31 (2009) 220-225.

Coulson, J.M., Richardson, J.F., Backhurst, J.R., Harker, J.H., 1999. Coulson and Richardson's chemical engineering volume 1 – Fluid flow, heat transfer and mass transfer, 6th Edition. Published by Elsevier.

Cui, X., Li, X., Sui, H., Li, H., 2012. Computational fluid dynamics simulations of direct contact heat and mass transfer of a multicomponent two-phase film flow in an inclined channel at sub-atmospheric pressure. International Journal of Heat and Mass Transfer, 55. 5808-5818.

Daily GPI, 2001.Gas rig blowout in offshore gulf, one missing. Retrieved from http://www.naturalgasintel.com/articles/56881-gas-rig-blowout-in-offshore-gulf-one-missing

Dapelo, D., Alberini, F., Bridgeman, J., 2015. Euler-Lagrange CFD modelling of unconfined gas mixing in anaerobic digestion. Water Research, 85. 497-511.

Darmana, D., Deen, N., Kuipers, J., 2005. Detailed modeling of hydrodynamics, mass transfer and chemical reactions in a bubble column using discrete bubble model. Chemical Engineering Science, 60. 3383-3404.

Dasanayaka, L.K., Yapa, P.D., 2009. Role of plume dynamics phase in a deepwater oil and gas release model. Journal of Hydro-environmental Research, 2. 243-253.

Deen, N., Solberg, T., Hjertager, B., 2000. Numerical simulation of the gas-liquid flow in a square cross-sectioned bubble column. CHISA 14th International Congress of Chemical and Process Engineering, Praha, Czech Republic.

Deen, N.G., Kuipers, J.A.M., 2013. Direct numerical simulation of wall-to liquid heat transfer in dispersed gas-liquid two-phase flow using a volume of fluid approach. Chemical Engineering Science, 102. 268-282.

Delnoij, E., Lammers, F., Kuipers, J., van Swaaij, S., 1997. Dynamic simulation of dispersed gas-liquid two-phase flow using discrete bubble model. Chemical Engineering Science, 52 (9). 1429-1458.

Delnoij, E., Kuipers, J., van Swaaij, S., 1999. A three-dimensional model for gas-liquid bubble columns. Chemical Engineering Science, 54. 2217-2221.

De Schepper, S., Heynderickx, G., Marin, G., 2008. CFD modeling of all gas-liquid and vapor-liquid flow regimes predicted by the Baker Chart. Chemical Engineering Journal, 138. 349-357.

Deshpande, K.B., Zimmerman, W.B., 2006. Simulation of interfacial mass transfer by droplet dynamics using the level set method. Chemical Engineering Science, 61. 6486-6498.

Deshpande, S.S., Anumolu, L., Trujillo, M., 2012. Evaluating the performance of the two-phase flow solver interFoam. Computational Science & Discovery, 5.

Dietzel, M., Ernst, M., Sommerfeld, M., 2016. Application of the Lattice-Boltzmann method for particle-laden flows: Point-particles and fully resolved particles. Flow Turbulence Combust, 97. 539-570.

Dinsenmeyer, R., Fourmigué, J., Caney, N., Marty, P., 2017. Volume of fluid approach of boiling flows in concentrated solar panels. International Journal of Heat and Fluid Flow, 65. 177-191.

Diwarkar, S.V., Das, S.K., Sundararajan, T., 2009. A quadratic spline based interface (QUASI) reconstruction algorithm for accurate tracking of two phase flows. Journal of Computational Physics, 228. 9107-9130.

Du., W., Zhang, J., Lu, P., Xu, J., Wei, W., He, G., Zhang, L., 2017. Advanced understanding of local wetting behaviour in gas-liquid-solid packed beds using CFD with a volume of fluid (VOF) method. Chemical Engineering Science, 170. 378-392.

Dhanasekharan, K., Sanyal, J., Jain, A., Haidari, A., 2005. A generalized approach to model oxygen transfer in bioreactors using population balances and computational fluid dynamics. Chemical Engineering Science, 60. 213-218.

Dhotre, M., Smith, B., 2007. CFD simulation of large-scale bubble plumes: Comparisons against experiments. Chemical Engineering Science, 62. 6615-6630.

Dhotre, M., Niceno, B., Smith, B., Simiano, M., 2009. Large-eddy simulation (LES) of the large scale bubble plume. Chemical Engineering Science, 64. 2692-2704.

Dhotre, M., Deen, N., Niceno, B., Khan, Z., Joshi, J., 2013. Large eddy simulation for dispersed bubbly flows: a review. International Journal of Chemical Engineering, 2013.

Díaz, M., Montes, F., Galán, M., 2009. Influence of the lift force closures on the numerical simulation of bubble plumes in a rectangular bubble column. Chemical Engineering Science, 64. 930-944.

Dong-hui, L., Jing-yu, X., 2015. Measurement of oil-water flow via the correlation of turbine flow meter, gamma ray densitometry and drift-flux model. Journal of Hydrodynamics, 27(4). 548-555.

Douabul, A., Riley, J., 1979. The solubility of gases in distilled water and seawater − V. hydrogen sulphide. Deep-Sea Research, 26A. 259-268.

Faghri, A., Zhang, Y., Transport Phenomena in Multiphase Systems. Elsevier, Burlington, MA, USA, 2006.

Fan, E.S.-C., Bussmann, M., 2013. Piecewise linear volume tracking in spherical coordinates. Applied Mathematical Modelling, 37. 3077-3092.

Fanneløp, T.K., Sjøen, K., 1980. Hydrodynamics of underwater blowouts. 18th Aerospace Sciences Meeting, Pasadena, USA.

Fanneløp, T.K., Bettelini, M., 2007. Very large deep-set bubble plumes from broken gas pipes. Report for Petroleumstilsynet.

Fard, M., Nikseresht, A., 2012. Numerical simulation of unsteady 3D cavitating flows over axisymmetric cavitators. Scientia Iranica B, 19 (5). 1258-1264.

Fayolle, Y., Cockx, A., Gillot, S., Roustan, M., Héduit, A., 2007. Oxygen transfer prediction in aeration tanks using CFD. Chemical Engineering Science, 62. 7163-7171.

Fleckenstein, S., Bothe, D., 2015. A Volume-of-Fluid-based numerical method for multi-component mass transfer with local volume changes. Journal of Computational Physics, 301. 35-58.

Fletcher, D., McClure, D., Kavanagh, J., Barton, G., 2017. CFD simulation of industrial bubble columns: Numerical challenges and model validation successes. Applied Mathematical Modelling, 44. 25-42.

Fraga, B., Stoesser, T., Lai, C., Socolofsky, S., 2016. A LES-based Eulerian-Lagrangian approach to predict the dynamics of bubble plumes. Ocean Modelling, 97. 27-36.

Frick, F., 2004. Visual Plumes mixing zone modeling software. Environmental Modelling & Software, 19. 645-654.

Ganguli, A.A., Kenig, E.Y., 2011. A CFD-based approach to the interfacial mass transfer at free gas-liquid interfaces. Chemical Engineering Science, 66. 3301-3308.

Gerlach, D., Alleborn, N., Buwa, V., Durst, F., 2007. Numerical simulation of periodic bubble formation at a submerged orifice with constant gas flow rate. Chemical Engineering Science, 62. 2109-2125.

Gimbun, J., Rielly, C., Nagy, Z., 2009. Modelling of mass transfer in gas-liquid stirred tanks agitated by Rushton turbine and CD-6 impeller: a scale up study. Chemical Engineering Research and Design, 87. 437-451.

Gjennestad, M. Aa., Munkejord, S.T., 2015. Modelling of heat transport in two-phase flow and of mass transfer between phases using the level-set method. Energy Procedia, 64. 53 – 62.

Gopala, V.R., Wachem, B.G.M., 2008. Volume of fluid methods for immiscible-fluid and free-surface flows. Chemical Engineering Journal, 141. 204-221.

Gong, X., Takagi, S., Matsumoto, Y., 2009. The effect of bubble-induced liquid flow on mass transfer in bubble plumes. International Journal of Multiphase Flow, 35. 155-162.

Gong, Y., Zhan, J., Li, T., 2016. Numerical investigation of the effect of rotation on cavitating flows over axisymmetric cavitators. Journal of Hydrodynamics, 28 (3). 431-441.

Grosshans, H., Movaghar, A., Cao, L., Oevermann, M., Szász, R., Fuchs, L., 2016. Sensitivity of VOF simulations of the liquid jet breakup to physical and numerical parameters. Computers and Fluids, 136. 312-323.

Gruber, M., Radl, S., Khinast, J., 2013. Coalescence and break-up in bubble columns: Euler-Lagrange simulations using a stochastic approach. Chemie Ingenieur Technik, 85 (7). 1118-1130.

Gruber, M., Radl, S., Khinast, J., 2015. Rigorous modeling of CO2 absorption and chemisorption: The influence of bubble coalescence and breakage. Chemical Engineering Science, 137.188-204.

Gruber, N., Radl, S., Kinast, J., 2016. Effect of bubble-particle interaction models on flow predictions in three-phase bubble columns. Chemical Engineering Science, 146. 226-243.

Gründing, D., Fleckenstein, S., Bothe, D., 2016. A subgrid-scale model for reactive concentration boundary layers for 3D mass transfer simulations with deformable fluid interfaces. International Journal of Heat and Mass Transfer, 101. 476-487.

Gueyffier, D., Li, J., Nadim, A., Scardovelli, R., Zaleski, S., 1999. Volume-of-fluid interface tracking with smoothed surface stress methods for three-dimensional flows. Journal of Computational Physics, 152. 423-456.

Gumulya, M., Utikar, R., Pareek, V., Mead-Hunter, R., Mitra, S., Evans, G., 2015. Evaporation of a droplet on a heated spherical particle. Chemical Engineering Journal, 278. 308-319.

Günther, C., Meinke, M., Schröder, W., 2014. A flexible level-set approach for tracking multiple interfaces in embedded boundary methods. Computers & Fluids, 102. 182-202.

Haelssig, J.B., Tremblay, A.Y., Thibault, J., Etemad, S.Gh., 2010a. Direct Numerical Simulation of Interphase Heat and Mass Transfer in Multicomponent Vapour-Liquid Flows. Int. J. Heat Mass Transfer, 53. 3947-3960.

Haelssig, J.B., Tremblay, A.Y., Thibault, J., Etemad, S.Gh., 2010b. Interface tracking and direct numerical simulation of interphase heat and mass transfer in multicomponent vapour-liquid flows. 60th CSChE Conference, Saskatoon, Canada.

Hamidipour, M., Chen, J., Larachi, F., 2013. CFD study and experimental validation of trickle bed hydrodynamics under gas, liquid and gas/liquid alternating cyclic operations. Chemical Engineering Science, 89. 158-170.

Harby, K., Chiva, S., Muñoz-Cobo, J., 2014. An experimental investigation on the characteristics of submerged horizontal gas jets in liquid ambient. Experimental Thermal and Fluid Science, 53. 26-39.

Harby, K., Chiva, S., Muñoz-Cobo, J., 2014. Modelling and experimental investigation of horizontal buoyant gas jets injected into stagnant uniform ambient liquid. International Journal of Multiphase Flow, 93. 33-47.

Haroun, Y., Legendre, D., Raynal, L., 2010. Direct numerical simulation of reactive absorption in gas-liquid flow on structured packing using interface capturing method. Chemical Engineering Science, 65. 351-356.

Haroun, Y., Legendre, D., Raynal, L., 2010. Volume of fluid method for interfacial reactive mass transfer: application to stable liquid film. Chemical Engineering Science, 65. 2896-2909.

Haroun, Y., Raynal, L., Legendre, D., 2012. Mass transfer and liquid hold-up determination in structured packing by CFD. Chemical Engineering Science, 75. 342-348.

Hassanvand, A., Hashemabadi, S.H., 2011. Direct numerical simulation of interphase heat and mass transfer in gas-liquid multiphase systems. International Communications in Heat and Mass Transfer, 38. 943-950.

Hänsch, S., Walker, S., Narayanan, C., (in press). Mechanistic studies of single bubble growth using interface-tracking methods. Nuclear Engineering and Design.

Harlow, F.H., Welch, J.E., 1965. Numerical calculation of time-dependent viscous incompressible flow of fluid with free surface. The Physics of Fluids, Vol. 8, 12. 2182-2189.

Hartmann, D., Meinke, M., Schröder, W., 2008. Differential equation based constrained reinitialization for level set methods. Journal of Computational Physics, 227. 6821-6845.

He, Z., Zhang, L., Saha, K., Som, S., Duan, L., Wang, Q., 2017. Investigations of effect of phase change mass transfer rate on cavitation process with homogenous relaxation model. International Communications in Heat and Mass Transfer, 89. 98-107.

Hendershot, D., 2013. Process safety: Remembering Piper Alpha. Journal of Chemical Health and Safety. 58-59.

Hirt, C.W., Amsden, A.A., Cook, J.L., 1972. An arbitrary lagrangian-eulerian computing method for al flow speeds. Journal of Computational Physics, 135. 203-216.

Hirt, C.W., Nichols, B.D., 1981. Volume of fluid (VOF) method for dynamics of free boundaries. Journal of Computational Physics, 39. 201-225.

Hissong, D., Pomeroy, J., Norris, H., 2014. A mechanistic model for hydrocarbon plumes rising through water. Journal of Loss Prevention in the Process Industries, 30. 236-242.

Hou, B., Wang, X., Zhang, T., Li, H., 2017. A model for improving the Euler-Euler two-phase flow theory to predict chemical reactions in circulating fluidized beds. Powder Technology, 321. 13-30.

Hu, G., Celik, I., 2008. Eulerian-Lagrangian based large-eddy simulation of a partially aerated flat bubble column. Chemical Engineering Science, 63. 253-271.

Hu, L., Chen, D., Huang, Y., Li, X., Yuan, D., Wang, Y., 2017. JFNK method with a physics-based preconditioner for the fully implicit solution of one-dimensional drift-flux model in boiling two-phase flow. Applied Thermal Engineering, 116. 610-622.

Huang, Q., Yang, C., Yu, G., Mao, Z., 2010. CFD simulation of hydrodynamics and mass transfer in an internal airlift loop reactor using a steady two-fluid model. Chemical Engineering Science, 65. 5527-5536.

Hughmark, G.A., 1967. Liquid-liquid spray column drop size, holdup, and continuous phase mass transfer. Industrial and Engineering Chemistry Fundamentals, 6. 408-413.

Incropera, F., DeWitt, D., Bergman, T., Lavine, A., 2007. Fundamentals of heat and mass transfer, 6th Edition. Wiley, Hoboken, NJ.

International Energy Agency, 2016. World Energy Outlook 2016. Retrieved from http://www.iea.org/Textbase/npsum/WEO2016SUM.pdf

Irfan, M., Muradoglu, M., 2017. A front tracking method for direct numerical simulation of evaporation process in a multiphase system. Journal of Computational Physics, 337. 132-153.

Ishii, M., Hibiki, T., 2010. Thermo-Fluid Dynamics of Two-Phase Flow. Springer, New York.

Jain, D., Kuipers, J., Deen, N., 2014. Numerical study of coalescence and breakup in a bubble column using a hybrid volume of fluid and discrete bubble model approach. Chemical Engineering Science, 119. 134-146.

Jirka, G.H., Doneker, R.L., Hinton, S.W., 1996. User's Manual for CORMIX: A Hydrodynamic Mixing Zone Model and Decision Support System for Pollutant Discharges into Surface Waters. US EPA.

Johansen, Ø., 2000. DeepBlow – a Lagrangian plume model for deep water blowouts. Spill Science & Technology Bulletin, 6. 103-111.

Johansen, Ø., Rye, H., Melbye, A.G., Jensen, H.V., Serigstad, B, Knutsen, T., 2001. Deep Spill JIP – Experimental Discharges of Gas and Oil at Helland Hansen – June 2000, Technical Report. SINTEF Technical Report: STF66 F01082.

Johansen, Ø., 2003. Development and verification of deep-water blowout models. Marine Pollution Bulleting, 47. 360-368.

Joshi, J., Nandakumar, K., Evans, G., Pareek, V., Gumulya, M., Sathe, M., Khanwale, M., 2017. Bubble generated turbulence and direct numerical simulations. Chemical Engineering Science, 157. 26-75.

Kadivar, E., Kadivar, E., Javadi, K., Javadpour, S., 2017. The investigation of natural super-cavitation flow behind three-dimensional cavitators: Full cavitation model. Applied Mathematical Modelling, 45. 165-178.

Kenig, E.Y., Ganguli, A.A., Atmakidis, A.A., Chasanis, P., 2011. A novel method to capture mass transfer phenomena at free fluid-fluid interfaces. Chemical Engineering and Processing, 50. 68-76.

Khan, Z., Bhusare, V., Joshi, J., 2017. Comparison of turbulence models for bubble column reactors. Chemical Engineering Science, 164. 34-52.

Khezzar, L., Kharoua, N., Kiger, K., 2015. Large eddy simulation of rough and smooth liquid plunging jet processes. Progress in Nuclear Energy, 85. 140-155.

Kim, J., Lee, J., 2015. Numerical study of cloud cavitation effects of hydrophobic hydrofoils. International Journal of Heat and Mass Transfer, 83. 591-603.

Kinzel, M., Krane, M., Kirschner, I., Moeny, M., 2017. A numerical assessment of the interaction of a supercavitating flow with a gas jet. Ocean Engineering, 136. 304-313.

Labois, M., Narayanan, C., 2017. Non-conservative pressure-based compressible formulation for multiphase flows with heat and mass transfer. International Journal of Multiphase Flow, 96. 24-33.

Lahey, R., 2005. The simulation of multidimensional multiphase flows. Nuclear Engineering and Design, 235. 1043-1060.

Laín, S., Bröder, D., Sommerfeld, M., Göz, M., 2002. Modelling hydrodynamics and turbulence in a bubble column using the Euler-Lagrange procedure. International Journal of Multiphase Flow, 28. 1381-1407.

Lakehal, D., Meier, M., Fulgosi, M., 2002. Interface tracking towards the direct simulation of heat and mass transfer in multiphase flows. International Journal of Heat and Fluid Flow, 23. 242-257.

Lakehal, D., Labois, M., 2011. A new modelling strategy for phase-change heat transfer in turbulent interfacial two-phase flow. International Journal of Multiphase Flow, 37. 627-639.

Lakehal, D., 2013. Computational Multiphase Flow in the Oil & Gas Industry. Presentation by ASCOMP GmbH.

Lee, J.H.W, Cheung, V., 1990. Generalized Lagrangian model for buoyant jets in current. Journal of Environmental Engineering, ASCE, 116(6). 1085-1105.

Lee, J., Son, G., 2017. A sharp-interface level-set method for compressible bubble growth with phase change. International Communications in Heat and Mass Transfer, 86. 1-11.

Leite, F., Silva, M., Araujo, M., Silva, R., Droguett, E., 2014. Modeling subsurface gas release in tropical and shallow waters: Comparison to field experiments off Brazil's northeast coast. Human and Ecological Risk Assessment, 20. 150-173.

Li, C., Cheung, S., Yeoh, G., Tu, J., 2009. Influence of drag forces on a swarm of bubbles in isothermal bubbly flow conditions. Seventh International Conference on CFD in Minerals and Process Industries. Held in Melbourne Australia.

Li, G., Yang, X., Dai, G., 2009. CFD simulation of effects of the configuration of gas distributors on gas-liquid flow and mixing in a bubble column. Chemical Engineering Science, 64. 5104-5116.

Li, C., Yeoh, H., Cheung, S., Tu J., 2010. Modelling horizontal gas-liquid flow using averaged bubble number density approach. Journal of Computational Multiphase Flows, 2 (2). 89-99.

Li, S., Wang, P., Lu, T., 2015. Numerical simulation of direct contact condensation of subsonic steam injected in a water pool using VOF method and LES turbulence model. Progress in Nuclear Energy, 78. 201-215.

Li, W., Zhong, W., 2015. CFD simulation of hydrodynamics of gas-liquid-solid three-phase bubble column. Powder Technology, 286. 766-788.

Lima Neto, I., Zhu, D., Rajaratnam, N., 2008. Horizontal Injection of gas-liquid mixtures in a water tank. Journal of Hydraulic Engineering, 134 (12). 1722-1731.

Liu, A.B., Mather, D., Reitz, R.D., 1993. Modeling the effects of drop drag and breakup on fuel sprays. SAE Technical Paper Series.

Liu, D., Tang, W., Wang, J., Xue, H., Wang, K., 2016. Comparison of laminar, RANS, LES and VLES for simulation of liquid sloshing. Applied Ocean Research, 59. 638-649.

Liu, Y., Yu, X., 2016. A coupled phase-field and volume-of-fluid method for accurate representation of limiting wave deformation. Journal of Computational Physics, 321. 459 − 475.

Loha, C., Chattopadhyay, H., Chatterjee, P., 2013. Euler-Euler CFD modeling of fluidized bed: Influence of specularity coefficient on hydrodynamic behavior. Particuology, 11. 673-680.

Lou, W., Zhu, M., 2013. Numerical simulation of gas and liquid two-phase flow in gas-stirred systems based on Euler-Euler approach. Metallurgical and Materials Transactions B, 44. 1251-1263.

Ma, J., Hsiao, C., Chahine, G., 2017. A physics based multiscale modeling of cavitating flows. Computers and Fluids, 145. 68-84.

Manninen, M., Taivassalo, V., Kallio, S., Akademi, A., 1996. On the mixture model for multiphase flow. VTT Publications, 288.

Marchisio, D.L., Fox, R.O., 2013. Computational Models for Polydisperse Particulate and Multiphase Systems. Cambridge University Press, United Kingdom.

Marschall, H., Hinterberger, K., Shüler, C., Habla, F., Hinrichsen, O., 2012. Numerical Simulation of species transfer across fluid interfaces in free-surface flows using OpenFOAM. Chemical Engineering Science, 78. 111-127.

Ménard, T., Tanguy, S., Berlemont, A., 2007. Coupling level set/VOF/ghost fluid methods: Validation and application to 3D simulation of the primary break-up of a liquid jet. International Journal of Multiphase Flow, 33. 510-524.

Mencinger, J., Žun, I., 2011. A PLIC-VOF method suited for adaptive moving grids. Journal of Computational Physics, 230. 644-663.

Meng, Q., 2016. The spatiotemporal characteristics of environmental hazards causes by offshore oil and gas operations in the Gulf of Mexico. Science of the Total Environment, 565. 663-671.

Messa, G., Ferrarese, G., Malavasi, S., 2015. A mixed Euler-Euler/Euler-Lagrange approach to erosion prediction. Wear, 342-343. 138-153.

Michta, E., Fu, K., Anglart, H., Angele, K., 2012. Numerical predictions of bubbly two-phase flow with OpenFOAM. Journal of Computational Multiphase Flows, 4 (2). 351-362.

Morsi, S.A., Alexander, A.J., 1972. An investigation of particle trajectories in two-phase flow systems. Journal of Fluid Mechanics, 55. 192-208.

Municchi, F., Radl, S., 2017. Consistent closures for Euler-Lagrange models of bi-dispersed gas-particle suspensions derived from particle-resolved direct numerical simulations. International Journal of Heat and Mass Transfer, 111. 171-190.

Muradoglu, M., Tryggvason, G., 2008. A front-tracking method for computation of interfacial flows with soluble surfactant. Journal of Computational Physics, 227. 2238-2262.

Myrillas, K., Rambaud, P., Mataigne, J., Gardin, P., Vincent, S., Buchlin, J., 2013. Numerical modeling of gas-jet wiping process. Chemical Engineering and Processing, 68. 26-31.

Narayanan, C., 2011. TransAT for Oil & Gas: On the Simulation of Deep-water Oil Spill. ASCOMP GmbH Technical Report: TRS-A/01-2011.

National Physics Laboratory, 2017. Physical Properties of Sea Water. Retrieved from:

http://www.kayelaby.npl.co.uk/general_physics/2_7/2_7_9.html

Natural Resources Canada, 2016. Additional Statistics on Energy. Retrieved from http://www.nrcan.gc.ca/publications/statistics-facts/1239

Natural Resources Canada, 2017. Energy Fact Book 2016-2017. Retrieved from https://www.nrcan.gc.ca/sites/www.nrcan.gc.ca/files/energy/pdf/EnergyFactBook_2016_17_En.pdf

Ngo, L., Choi, H., 2017. Efficient direct re-initialization approach of a level set method for unstructured meshes. Computers and Fluids, 154. 167-183.

Ningegowda, B.M., Premachandran, B., 2014. A coupled level set and volume of fluid method with multi-directional advection algorithms for two phase flows with and without phase change. International Journal of Heat and Mass Transfer, 79. 532 – 550.

Noh, W.F., Woodward, P., 1978. SLIC (simple line interface calculation), in A. I. van Dooren and P.J. Zandbergen (eds), Lecture Notes in Physics, 59. 330-340.

Offshore Post, 2015. Offshore drill crew at fault for catastrophic blowout. Retrieved from http://www.offshorepost.com/offshore-drill-crew-at-fault-for-catastrophic-blowout/

Offshore Technology, 2017. Industry Projects. Retrieved from http://www.offshore-technology.com/projects/region/

Olsen, J., Skjetne, P., 2016a. Current understanding of subsea gas release: a review. The Canadian Journal of Chemical Engineering, 94. 209-219.

Olsen, J., Skjetne, P., 2016b. Modelling of underwater bubble plumes and gas dissolution with an Eulerian-Lagrangian CFD model. Applied Ocean Research, 59. 193-200.

Olsen, J., Skjetne, P., Johansen, S., 2017. VLES turbulence model for an Eulerian-Lagrangian modeling concept for bubble plumes. Applied Mathematical Modelling, 44. 61-71.

OpenFOAM Foundation, 2018. Retrieved from https://openfoam.org/

Osher, S., Fedkiw, R.P., 2001. Level set methods: and overview and some recent results. Journal of Computational Physics, 169. 463-502.

Osher, S., Sethian, J., Fronts propagating with curvature dependent speed. Journal of Computational Physics, 79. 12-49.

Ovsyannikov, A., Sabel'nikov, V., Gorokhovski, M., 2010. A new level set equation and its numerical assessments. Center of Turbulence Research, proceedings from the summer program 2012. 315-324.

Padoin, N., Dal'Toé, A., Rangel, L., Ropelato, K., Soares, C., 2014. Heat and mass transfer modeling for multicomponent multiphase flow with CFD. International Journal of Heat and Mass Transfer, 73. 239-249.

Palomar, P., Lara, J.L., Losada, I.J., Rodrigo, M., Alvárez. A., 2012a. Near field brine discharge modelling part 1: Analysis of commercial tools. Desalination, 290. 14-27.

Palomar, P., Lara, J.L., Losada, I.J., 2012b. Near field brine discharge modeling part 2: Validation of commercial tools. Desalination, 290. 28-42.

Pan, H., Chen, X., Liang, X., Zhu, L., Luo, Z., 2016. CFD simulations of gas-liquid-solid flow in fluidized bed reactors – A review. Powder Technology, 299. 235-258.

Panneerselvam, R., Savithri, S., Surender, G., 2008. CFD modeling of gas-liquid-solid mechanically agitated contactor. Chemical Engineering Research and Design, 86. 1331-1344.

Park, S., Yang, H., 2017. Experimental investigation on mixed jet and mass transfer characteristics of horizontal aeration process. International Journal of Heat and Mass Transfer, 113. 544-555.

Parker, S., Nally, J., Foat, T., Preston, S., 2010. Refinement and testing of the drift-flux model for indoor aerosol dispersion and deposition modelling. Journal of Aerosol Science, 41. 921-934.

Parsi, M., Agrawal, M., Srinivasan, V., Vieira, R., Torres, C., McLaury, B., Shirazi, S., Schleicher, E., Hampel, U., 2016. Assessment of a hybrid CFD model for simulation of complex vertical upward gas-liquid churn flow. Chemical Engineering Research and Design, 105. 71-84.

Pathak, A., Raessi, M., 2016. A three-dimensional volume-of-fluid method for reconstructing and advecting three-material interfaces forming contact lines. Journal of Computational Physics, 307. 550-573.

Peña-Monferrer, C., Muñoz-Cobo, J., Monrós-Andreu, G., Martinez-Cuenca, R., Chiva, S., 2014. An Eulerian-Lagrangian open source solver for bubbly flow in vertical pipes. 40th Reunión Annual, Sociedad Nuclear Española.

Perry, R. H., Green, D. W., 1997. Perry's Chemical Engineers' Handbook, 7th Edition, McGraw-Hill.

Pilliod, J.E., Puckett, E.G., 2004. Second-order accurate volume-of-fluid algorithms for tracking material interfaces. Journal of Computational Physics, 199. 465-502.

Planete Energies, 2015. Offshore oil and gas production. Retrieved from http://www.planete-energies.com/en/medias/close/offshore-oil-and-gas-production

Popinet, S., 2013. Gerris Flow Solver. Retrieved from http://gfs.sourceforge.net/wiki/index.php/Main_Page

Pourtousi, M., Sahu, J., Ganesan, P., 2014. Effect of interfacial forces and turbulence on predicting flow pattern inside the bubble column. Chemical Engineering and Processing, 75. 38-47.

Price, G.R., 2000. A piecewise parabolic volume tracking method for the numerical simulation of interfacial flows. Thesis from the University of Calgary.

Prosperetti, A., Tryggvason, G., 2007. Computational Methods for Multiphase Flow. Cambridge University Press, United Kingdom.

Qian, L., Causon, D.M., Mingham, C.G., Ingram, D.M., 2006. A free-surface capturing method for two fluid flows with moving bodies. Proceedings of the Royal Society A, 462. 21-42.

Quan, S., Schmidt, D., 2007. A moving mesh interface tracking method for 3D incompressible two-phase flows. Journal of Computational Physics, 221. 761-780.

Quan, S., Lou, J., Schmidt, D., 2009. Modeling merging and breakup in the moving mesh interface tracking method for multiphase flow simulations. Journal of Computational Physics, 228. 2660-2675.

Quan, S., 2011. Simulations of multiphase flows with multiple length scales using moving mesh interface tracking with adaptive meshing. Journal of Computational Physics, 230. 5430-5448.

Queutey, P., Visonneau, M., 2007. An interface capturing method for free-surface hydrodynamic flows. Computers & Fluids, 36. 1481-1510.

Ramkrishna, D., 2000. Population Balances: Theory and Applications to Particulate Systems in Engineering. Academic Press.

Ranz, W.E., Marshall, W.R., 1952a. Evaporation from drops – Part I. Chemical Engineering Progress, 48. 141-146.

Ranz, W.E., Marshall, W.R., 1952b. Evaporation from drops – Part II. Chemical Engineering Progress, 48. 173-180.

Rauschenberger, P., Weigand, B., 2015. A Volume-of-Fluid method with interface reconstruction for ice growth in supercooled water. Journal of Computational Physics, 282. 98-112.

Reed, M., Hetland, B., 2002. DREAM: A dose-related exposure assessment model technical description of physical-chemical fates components. SPE 73856.

Rehder, G., Leifer, I., Brewer, P.G., Friederich, G., Peltzer, E.T., 2009. Controls on methane bubble dissolution inside and outside the hydrate stability fields from open ocean field experimetns and numerical modeling. Marine Chemistry, 114. 19-30.

Renze, P., Buffo, A., Marchisio, D., Vanni, M., 2014. Simulation of coalescence, breakup and mass transfer in polydisperse multiphase flows. Chemie Ingenieur Technik, 86 (7). 1088-1098.

Rek, Z., Gregorc, J., Bouaifi, M., Daniel, C., 2017. Numerical simulation of gas het in liquid crossflow with high mean jet to crossflow velocity ratio. Chemical Engineering Science, 172. 667-676.

Renardy, Y., Renardy, M., 2002. PROST: a parabolic reconstruction of surface tension for the volume-of-fluid method. Journal of Computational Physics, 183, 400-421.

Rew, P.J., Gallagher, P., Deaves, D.M., 1995. Dispersion of Subsea Releases: Review of Prediction Methodologies, HSE – Offshore Technology Report. OTH-95-465.

Rider, W.J., Kothe, D.B., 1998. Reconstructing volume tracking. Journal of Computational Physics, 141. 112-152.

Roghair, I., Lau, Y., Deen, N., Slagter, H., Baltussen, M., Van Sint Annaland, M., Kuipers, J., 2011. On the drag force of bubbles in bubble swarms at intermediate and high Reynolds numbers. Chemical Engineering Science, 66. 3204-3211.

Roghair, I., Van Sint Annaland, M., Kuipers, H., 2012. Drag force and clustering in bubble swarms. American Institute of Chemical Engineers Journal, 59 (5). 1791-1800.

Roghair, I., Baltussen, M., Van Sint Annaland, M., Kuipers, J., 2013. Direct numerical simulations of the drag force of bi-disperse bubble swarms. Chemical Engineering Science, 95. 48-53.

Roghair, I., Van Sint Annaland, M., Kuipers, J.A.M., 2016. An improved front-tracking technique for the simulation of mass transfer in dense bubbly flows. Chemical Engineering Science, 152. 351 – 369.

Roohi, E., Zahiri, A., Passandideh-Fard, M., 2013. Numerical simulation of cavitation around a two-dimensional hydrofoil using VOF method and LES turbulence model. Applied Mathematical Modelling, 37. 6469-6488.

Rudman, M., 1997. Volume-tracking methods for interfacial flow calculations. International Journal for Numerical Methods in Fluids, 24. 671-691.

Russo, G., Smereka, P., 2000. A remark on computing distance functions. Journal of Computational Physics, 163. 51-67.

Rzehak, R., 2016. Modeling of mass-transfer in bubbly flows encompassing different mechanisms. Chemical Engineering Science, 151. 139-143.

Rzehak, R., Krepper, E., 2016. Euler-Euler simulation of mass-transfer in bubbly flows. Chemical Engineering Science, 155. 459-468.

Saad, S., Gentric, C., Fourmigué, J., Clément, P., Leclerc, J., 2014. CFD and experimental investigation of the gas-liquid flow in the distributor of a compact heat exchanger. Chemical Engineering Research and Design, 92. 2361-2370.

Samkhaniani, N., Ansari, M., 2016. Numerical simulation of bubble condensation using CF-VOF. Progress in Nuclear Energy, 89. 120-131.

Sander, R., 2015. Compilation of Henry's law constants for water as solvent. Atmospheric Chemistry and Physics, 15. 4399-4981.

Scardovelli, R., Zaleski, S., 1999. Direct numerical simulation of free-surface and interfacial flow. Annual Review of Fluid Mechanics, 31. 567-603.

Schaefer, K., 2016. The offshore oil business is crippled and it may never recover. Retrieved from http://oilprice.com/Energy/Crude-Oil/The-Offshore-Oil-Business-Is-Crippled-And-It-May-Never-Recover.html

Schlottke, J., Weigand, B., 2008. Direct numerical simulation of evaporating droplets. Journal of Computational Physics, 227. 5215-5237.

Sellami, N., Dewar, M., Stahl, H., Chen, B., 2015. Dynamics of rising CO2 bubble plumes in the QICS field experiment: Part 1- the experiment. International Journal of Greenhouse Gas Control, 38. 44-51.

Sethian, J.A., Smereka, P., 2004. Level set methods for fluid interfaces. Annual Review of Fluid Mechanics, 34. 341-372.

Shaikh, J., Sharma, A., Bhardwaj, R., 2016. On sharp-interface level-set method for heat and/or mass transfer induced Stefan problem. International Journal of Heat and mass Transfer, 96. 458-573.

Shi, X., Xiang, Y., Wen, L., Chen, J., 2013. CFD analysis of liquid phase flow in a rotating packed bed reactor. Chemical Engineering Journal, 228. 1040-1049.

Simano, M., 2005. Experimental investigation of large-scale three-dimensional bubble plume dynamics. ETH Zurich Research Collection. Doctorial Thesis at Palermo University, Italy.

Simonnet, M., Gentric, C., Olmos, E., Midoux, N., 2008. CFD simulation of the flow field in a bubble column reactor: Importance of the drag force formulation to describe regime transitions. Chemical Engineering and Processing, 47. 1726-1737.

Skogdalen, J., Utne, I., Vinnem, J., 2011. Developing safety indicators for preventing offshore oil and gas deepwater drilling blowouts. Safety Science, 49. 1187-1199.

Smith, J., Van Ness, H., Abbott, M., 2005. Introduction to Chemical Engineering Thermodynamics, 7th Edition. Mc-Graw Hill, Avenue of the Americas, New York, NY.

Socolofsky, S.A., Adams, E.E., 2002. Multi-phase plumes in uniform and stratified crossflow. Journal of Hydraulic Research, 40(6). 661-672.

Soh, G.Y., Yeoh, G.H., Timchenko, V., 2016. An algorithm to calculate interfacial area for multiphase mass transfer through the volume-of-fluid method. International Journal of Heat and Mass Transfer, 100. 573 – 581.

Sokolichin, A., Eigenberger, G., 1997. Dynamic numerical simulation of gas-liquid two-phase flows: Euler-Euler vs. Euler-Lagrange. Chemical Engineering Science, 52 (4). 611-626.

Sokolichin, A., Eigenberger, G., 1999. Applicability of the standard k-ε turbulence model to the dynamic simulation of bubble columns: Part I. Detailed numerical simulations. Chemical Engineering Science, 54. 2273-2284.

Starinshak, D., Karni, S., Roe, P., 2014. A new level set model for multimaterial flows. Journal of Computational Physics, 262. 1-16.

Sridher, P.C., 2012. Validating sub-sea gas pipeline leaks discharge model for Arabian Sea conditions. Ph.D. Thesis, University of Petroleum & Energy Studies, Dehradun, India.

Ström, H., Sasic, S., Holm-Christiansen, O., Shah, L., 2016. Atomizing industrial gas-liquid flows – Development of an efficient hybrid VOF-LPT numerical framework. International Journal of Heat and Fluid Flow, 62. 104-113.

Sungkorn, R., Derksen, J., Khinast, J., 2011. Modeling of turbulent gas-liquid bubbly flows using stochastic Lagrangian model and lattice-Boltzmann scheme. Chemical Engineering Science, 66. 2746-2757.

Sussman, M., Smereka, P., Osher, S., 1994. A level set approach for computing solutions to incompressible two-phase flow. Journal of Computational Physics, 114. 146-159.

Talebi, S., Kazeminejad, H., Davilu, H., 2012. A numerical technique for analysis of transient two-phase flow in a vertical tube using the drift-flux model. Nuclear Engineering and Design, 242. 316-322.

Talvy, S., Cockx, A., Liné, A., 2007. Modeling of oxygen mass transfer in a gas-liquid airlift reactor. American Institute of Chemical Engineers, 53 (2). 316-326.

Tanguy, S., Ménard, T., Berlemont, A., 2007. A level set method for vaporizing two-phase flows. Journal of Computational Physics, 221. 837-853.

Tamim, N., Laboureur, D., Mentzer, R., Hasan, A., Mannan, M., 2017. A framework for developing leading indicators for offshore drillwell blowout incidents. Process Safety and Environmental Protection, 106. 256-262.

Teixeira, R., Secchi, A., Biscaia Jr., E., 2017. Differential-Algebraic numerical approach to the one-dimensional drift-flux model applied to a multicomponent hydrocarbon two-phase flow. Computers and Chemical Engineering, 101. 125-137.

Terashima, H., Tryggvason, G., 2010. A front-tracking method with projected interface conditions for compressible multi-fluid flows. Computers & Fluids, 39. 1804-1814.

Tian, X., Zhao, H., Liu, H., Li, W., Xu, J., 2015. Three-dimensional large eddy simulation of round liquid jet primary breakup in coaxial gas flow using the VOF model. Fuel Processing Technology, 131. 396-402.

Tomiyama, A., Kataoka, I., Zun, I., Sakaguchi, T., 1998. Drag coefficients of single bubbles under normal and micro gravity conditions. JSME International Journal, 41 (2). 472-479.

Tryggvason, G., Bunner, B., Esmaeeli, A., Juric, D., Al-Rawahi, N., Tauber, W., Han, J., Nas, S., Jan, Y.-J., 2001. A front-tracking method for computations of multiphase flow. Journal of Computational Physics, 169. 708-759.

Tryggvason, G., Thomas, S., Lu, J., Aboulhasanzadeh, B., 2010. Multiscale issues in DNS of multiphase flows. Acta Mathematica Scientia, 30B (2). 551-562.

Tryggvason, G., Scardovelli, R., Zaleski, S., 2011. Direct Numerical Simulations of Gas–Liquid Multiphase Flows. Cambridge University Press, United Kingdom.

Tukovic, Z., Jasak, H., 2008. Simulation of free-rising bubble with soluble surfactant using moving mesh finite volume/area method. 6th International Conference on CFD in Oil & Gas, Trondheim, Norway.

Unverdi, S.O., Tryggvason, G., 1992. A front-tracking method for viscous, incompressible, multi-fluid flows. Journal of Computational Physics, 100. 25-37.

U.S. Energy Information Administration, 2016. Offshore production nearly 30% of global crude oil output in 2015. Retrieved from https://www.eia.gov/todayinenergy/detail.php

Wang, T., Wang, J., 2007. Numerical simulations of gas-liquid mass transfer in bubble columns with a CFD-PBM coupled model. Chemical Engineering Science, 62. 7107-7118.

Wang, J., Lu, P., Wang, Z., Yang, C., Mao, Z., 2008. Numerical simulation of unsteady mass transfer by the level set method. Chemical Engineering Science, 63. 3141-3151.

Wang, Y., Wang, X., Chen, H., Taylor, R., Zhu, Y., 2017. A combined CFD/visualized investigation of two-phase heat and mass transfer inside a horizontal loop thermosiphon. International Journal of Heat and Mass Transfer, 112. 607-619.

Wardle, K., Weller, H., 2013. Hybrid multiphase CFD solver for coupled dispersed/segregated flows in liquid-liquid extraction. International Journal of Chemical Engineering, 2013.

Weiland, C., Vlachos, P., 2013. Round gas jets submerged in water. International Journal of Multiphase Flow, 48. 46-57.

Weiss, R., 1974. Carbon dioxide in water and seawater: the solubility of a non-ideal gas. Marine Chemistry, 2. 203-215.

Wörner, M., 2012. Numerical modeling of multiphase flows in microfluidics and micro process engineering: a review of methods and applications. Microfluid Nanofluid, 12. 841-886.

Wu, P., Chen, J., 2016. Numerical study on cavitating flow due to a hydrofoil near a free surface. Journal of Ocean Engineering and Science, 1. 238-245.

Wutz, J., Lapin, A., Siebler, F., Schäfer, Wucherpfennig, T., Berger, M., Takors, R., 2016. Predictability of kLa in stirred tank reactors under multiple operating conditions using an Euler-Lagrange approach. Engineering Life Science, 16. 633-642.

Xi, J., Longest, P., 2008. Numerical predictions of submicrometer aerosol deposition in the nasal cavity using a novel drift-flux approach. International Journal of Heat and Mass Transfer, 51. 5562-5577.

Xiao, Q., Yang, N., Li, J., 2013. Stability-constrained multi-fluid CFD models for gas-liquid flow in bubble columns. Chemical Engineering Science, 100. 279-292.

Xiao, Q., Yang, N., Li, J., 2013. Stability-constrained multi-fluid CFD models for gas-liquid flow in bubble columns. Chemical Engineering Science, 100. 279-292.

Xiao, F., Wang, Z., Sun, M., Liang, J., Liu, N., 2016. Large eddy simulation of liquid jet primary breakup in supersonic air crossflow. International Journal of Multiphase Flow, 87. 229-240.

Xie, B., Jin, P., Xiao, F., 2017. An unstructured-grid numerical model for interfacial multiphase fluids based on multi-moment finite volume formulation and THINC method. International Journal of Multiphase Flow, 89. 375-398.

Xue, X., Yu, Y., Zhang, Q., 2014. Study on the effect of distance between the two nozzle holes on interaction of high pressure combustion-gas jets in liquid.

Yan, X., Jia, Y., Wang, L., Cao, Y., 2017. Drag coefficient fluctuation prediction of a single bubble rising in water. Chemical Engineering Journal, 316. 553-562.

Yang, C., Mao, Z., 2005. Numerical simulation of interphase mass transfer with the level set approach. Chemical Engineering Science, 60. 2643-2660.

Yang, N., Wu, Z., Chen, J., Wang, Y., Li, J., 2011. Multi-scale analysis of gas-liquid interaction and CFD simulation of gas-liquid flow in bubble columns. Chemical Engineering Science, 66. 3212-3222.

Yang, X., Liu, J., Liu, J., Chen, N., Yan, J., 2017. Interface dynamics and pressure oscillation of stable steam jet condensation in water flow in a confined channel with the presence of non-condensable gas. International Journal of Multiphase Flow, 111. 1157-1171.

Yapa, P.D., Zheng, L., 1997a. Modeling oil and gas release from deep water: a review. Spill Science & Technology Bulletin, 4. 189-198.

Yapa, P.D., Zheng, L., 1997. Simulation of oil spills from underwater accidents I: Model development. Journal of Hydraulic Research, 35. 673-688.

Yapa, P.D., Zheng, L., Chen, F., 2001. A model for deepwater oil/gas blowouts. Marine Pollution Bulletin, 43. 234-241.

Yapa, P.D., Wimalaratne, M.R., Dissanayake, A.L., DeGraff Jr., J.A., 2012. How does oil and gas behave when released in deepwater? Journal of Hydro-environmental Research, 6. 275-285.

Yaws, Carl L., 2003. Yaws' Handbook of Thermodynamic and Physical Properties of Chemical Compounds. Knovel. Online version available at:

https://app.knovel.com/hotlink/toc/id:kpYHTPPCC4/yaws-handbook-thermodynamic/yaws-handbook-thermodynamic

Yaws, Carl L., 2009. Yaws' Handbook of Thermodynamic Properties for Hydrocarbons and Chemicals. Knovel. Online version available at:

https://app.knovel.com/hotlink/toc/id:kpYHTPHC09/yaws-handbook-thermodynamic/yaws-handbook-thermodynamic

Yi, C.H., Ye, Z.T., Sheu, T.W.H., Lin, Y.T., Zhao, X.Z., 2016. An improved interface preserving level set method for simulating three dimensional rising bubble. International Journal of Heat and Mass Transfer, 103. 753 – 772.

Youngs, D.L., 1982. Time-dependent multi-material flow with large fluid distortion, in K.W. Morton and M.J. Banes (eds), Numerical Methods for Fluid Dynamics, Academic, New York. 273-285.

Zhang, D., Jiang, C., Liang, D., Chen, Z., Yang, Y., Shi, Y., 2014. A refined volume-of-fluid algorithm for capturing sharp interfaces on arbitrary meshes. Journal of Computational Physics, 274. 709-736.?id=28492

Zhang, C., Sa, R., Zhou, D., Jiang, H., 2017. Effects of gas velocity and break size on steam penetration depth using gas jet into water similarity experiments. Progress in Nuclear Energy, 98. 38-44.

Zhao, B., Chen, C., Tan, Z., 2009. Modeling of ultrafine particle dispersion in indoor environments with an improved drift flux model. Aerosol Science, 40. 29-43.

Zhao, Y., Lu, B., Zhong, Y., 2013. Euler-Euler modeling of gas-solid bubbling fluidized bed with kinetic theory of rough particles. Chemical Engineering Science, 104. 767-779.

Zhao, L., Torlapati, J., Boufadel, M., King, T., Robinson, B., Lee, K., 2014a. VDROP: A comprehensive model for droplet formation of oils and gases in liquids – Incorporation of the interfacial tension and liquid viscosity. Chemical Engineering Journal, 253. 93-106.

Zhao, L., Boufadel, M., Socolofsky, S., Adams, E., King, T., Lee, K., 2014b. Evolution of droplets in subsea oil and gas blowouts: Development and validation of the numerical model VDROP-J. Marine Pollution Bulletin, 83. 58-69.

Zhao, L., Boufadel, M., Adams, E., Socolofsky, S., King, T., Lee, K., Nedwed, T., 2015. Simulation of scenarios of oil droplet formation from the Deepwater Horizon blowout. Marine Pollution Bulletin, 101. 304-319.

Zhao, L., Boufadel, M., Lee, K., King, T., Loney, N., Geng, X., 2016. Evolution of bubble size distribution from gas blowout in shallow water. Journal of Geophysical Research: Oceans, 121. 1573-1599.

Zhao, J., Yu, Y., 2016. The interaction between multiple high pressure combustion gas jets and water in a water-filled vessel. Applied Ocean Research, 61. 175-182.

Zheng, L., Yapa, P.D., 1998. Simulation of oil spills from underwater accidents II: Model verification. Journal of Hydraulic Research, 36. 117-134.

Zheng, L., Yapa, P.D., 2002. Modeling gas dissolution in deepwater oil/gas spills. Journal of Marine Systems, 31. 299-309.

Zheng, L., Yapa, P.D., Chen, F., 2002. A model for simulating deepwater oil and gas blowouts – Part I: Theory and model formulation. Journal of Hydraulic Research 41. 339-351.

Zhou, L., Yu, Y., 2017. Study on interaction characteristics between multi gas jets and water during the underwater launching process. Experimental Thermal and Fluid Science, 93. 200-206.

Zou, L., Zhao, H., Zhang, H., 2017. Application of high-order numerical schemes and Newton-Krylov method to two-phase drift-flux model. Progress in Nuclear Energy, 100. 427-438.